Craniofacial system under external loads: Wild type and Crouzon mice

A thesis submitted in fulfilment of

the requirements for the degree of

Doctor of Philosophy

By

Marius Didziokas

Department of Mechanical Engineering

University College London

2025

Declaration

I, Marius Didziokas, confirm that the work presented in this thesis is my own. Where information has been derived from other sources, I confirm that this has been indicated.

Signature: 

Date: 09/06/2025

This work is dedicated to my wife *Ugnė* and our four-legged friend *Fiesta*. They have given me the energy, support and understanding that I need to complete this PhD. My heartfelt gratitude is given to my parents, grandparents, parents-in-law and grandparents-in-law, as well as other family and friends in Lithuania and beyond for continued support throughout my academic journey.

Abstract

Cranial sutures permit postnatal craniofacial growth and absorb external forces. Craniosynostosis, the premature fusion of these joints, can cause craniofacial abnormalities including dysmorphology and increased intracranial pressure, typically requiring multiple invasive surgeries. Our previous research suggested that external cyclic loading of the frontal bone in Crouzon mouse models might improve suture patency and skull shape.

This study aimed to investigate the biomechanical responses during external loading and evaluate morphological effects following treatment regimes.

Biomechanical investigations demonstrated that static loading adequately represented cyclic loading for mechanical suture deformation analysis. Substantial strains (~0.6 to ~0.8) were observed in coronal sutures during frontal bone loading, along with post-loading plastic deformation. The development of BounTI allowed the investigations to be expanded. The interparietal and lambdoid sutures and additional loading locations were included. These investigations revealed that skull deformation is highly location-dependent, with posterior loading producing greater deformation. BounTI facilitated rapid finite element model development for comparison with experimental data.

Morphological investigations revealed significantly higher inter-litter variation compared to intra-litter variation, suggesting that litter-based treatment groups may introduce statistical artefacts and false positive results. Our findings indicated that each litter should be randomly divided into equal control and treatment groups, reducing erroneous statistical significance to the expected 5%. Further *in vivo* experiments, including the original treatment regime and five variations, showed no clear loading effects on skull morphology or suture patency. Importantly, effects that appeared statistically significant when comparing individual treatment groups to all controls disappeared when treatment groups were compared to littermate controls.

While our biomechanical investigations established the groundwork for treatment translation to larger animal models, the morphological investigations demonstrated milder therapeutic benefits than previously reported. Further experimental work with robust morphological and statistical study design is essential to definitively establish the efficacy of the original treatment regime.

Impact Statement

This project was a part of a larger project (CranioMech, led by Prof. Mehran Moazen), focusing on investigating craniofacial system biomechanics for the purposes of developing a new cyclic loading therapy for craniosynostosis. Work by Ms Hejazi, primarily available in Moazen et al. (2022), had set a solid foundation for this project. External cyclic loading was shown to potentially prevent or delay suture fusion and reduce craniofacial dysmorphology in $Fgfr2^{C342Y/+}$ Crouzon mutant mice. This work investigated the mouse craniofacial system considering these findings, focusing on mechanical response during external loading (Chapters 3 and 4), skull phenotype (Chapter 5), and direct therapeutic effects (Chapter 6).

The investigations available in this work were presented at various inter/national scientific conferences, including, but not limited to the 28th/29th Congress of the European Society of Biomechanics, 2022/2024 Meeting of Craniofacial Morphogenesis and Tissue Regeneration GRC/GRS, and the 21st Congress of the International Federation of Associations of Anatomists. Several of the chapters are already published or are under peer review, including Chapter 3 in Biomechanics and Modeling in Mechanobiology, Chapter 4 in Biomechanics and Modeling in Mechanobiology, and Chapter 5 in preparation for submission. Data from Chapter 6 is partially included in a joint first author manuscript in preparation for submission and Appendix I (BounTI) is published in the Journal of Anatomy and featured on the front cover of a special issue on Craniosynostosis.

Response to external loading in terms of suture strains across the craniofacial system, as outlined in Chapters 3 and 4, has been employed to design new pig experiments investigating the translation of the treatment to larger animal models. Additionally, methodological developments in these chapters are being used to estimate the strains in pig sutures during comparable loading by Dr Vithanage in the lab. The study design implications found in Chapter 5 have been disseminated across the group with future experiments by lab members (Ms Steacy and Dr Qiu), paying particular attention to the choice of control animals. Lastly, BounTI has enabled research across the group and beyond to investigate craniofacial CT scans in previously unavailable detail. Beyond being used as a tool by other groups, the simple methodology of BounTI has led to the development of novel segmentation tools. Namely, SPROUT (under review in Nature

Methods) developed in collaboration with the Natural History Museum, UK, primarily expanding the seed creation for threshold iteration developed in BounTI.

Acknowledgements

Firstly, I would like to express my gratitude to my PhD supervisor Prof Mehran Moazen for all the support, patience, and expertise throughout both my MSc (2020-2021) and PhD (2021-2025). Equally, my gratitude goes out to Dr Erwin Pauws (secondary supervisor) for his continued support and meaningful discussions. A special thanks goes out to Dr Ali Alazmani for developing the loading set-up used in this work in collaboration with Dr Dominic Jones and helping maintain its working order.

My heartfelt gratitude goes out to Ms Rosa Hejazi, who has played a critical role in establishing the foundational findings upon which this work was built. Similarly, I would like to thank Ms Miranda Steacy, Dr Tengyang Qiu, Dr Ce Liang, Dr Arsalan Marghoub and Dr Damith Vithanage for the continued support in carrying out *in/ex vivo* experiments and other technical help.

Possibly most importantly, I would like to thank all the aforementioned people and other members of our lab including Dr Louise Souquet, Dr Katherine Wang, Dr Anastasiia Maliuk, Mr Yunus Samiepour, and Ms Rounan Dong for allowing me to endlessly ramble on about my work and for how much fun this time has been.

Special thanks to all the collaborators beyond our lab who have allowed me the opportunity to contribute to their work including Dr Marco Camaiti, Dr Yishen He, Prof Anjali Goswami at the Natural History Museum, Dr Andrea Mazzolani, Prof Sandro Olivo at the Department of Medical Physics at University College London, Dr Ieva Gendviliene and Dr Egidijus Simoliunas at the Vilnius University, and Dr Kei Katsura at University of California, San Francisco.

Finally, I would like to thank the sponsors of this project, namely MoazenLab. This work was also supported by the Engineering and Physical Sciences Research Council grant (EP/W008092/1; EP/R513143/1 – 2592407 and EP/T517793/1 - 2592407) and the NIHR Great Ormond Street Hospital Biomedical Research Centre.

List of Abbreviations

2D,3D	Two-, Three- Dimensional	ISS	Inter-Sphenoid Synchondrosis
3Rs	Replacement, Reduction, and Refinement	Lambd	Lambdoid suture
ANOVA	Analysis of Variance	LM	Landmark
ARRIVE	Animal Research: Reporting of In Vivo Experiments	LOF	Loss of Function
BounTI	Boundary preserving Threshold Iteration	LSD	Fisher's Least Significant Difference
CC	Collaborative Cross	MANOVA	Multivariate analysis of variance
CCC	Lin's Concordance Correlation Coefficient	MRI	Magnetic Resonance Imaging
CorL	Coronal Left suture	MT	Mutant type
CorR	Coronal Right suture	n	number
CS	Craniosynostosis	NDP	Neural Deformation Pyramid
CT	Computer Tomography	OMIM	Online Mendelian Inheritance in Man
DO	Diversity Oubred	P#	Postnatal day
DVC	Digital Volume Correlation	PC	Principal Component
E	Elastic Modulus	PCA	Principal Component Analysis
E#	Embryonic day	Q-static	Quasi static
FE	Finite Element	QTL	Quantitative Trait Loci
FEA	Finite Element Analysis	R2	Coefficient of Determination
FEM	Finite Element Method	Sag	Sagittal suture
GM	Geometric Morphometric	WP	Work Package
GOF	Gain of Function	WT	Wild type
ICC	Intraclass Correlation Coefficient	Y	Best fit line
IntL	Interparietal Left suture	ε1	1st principal strain
IntR	Interparietal Right suture	ε3	3rd principal strain

Contents

Chapter 1 Introduction

1-1 Overview

The mammalian cranial vault largely consists of five bones connected at their edges with soft tissues known as sutures. Each suture connects different skull bones together. The metopic suture lies between the frontal bones, while the sagittal suture lies between the parietal bones. The left and right coronal sutures connect the frontal and parietal bones on each side. The parietal bones are then attached to the interparietal bone (in mice via the interparietal suture) and occipital bone (in humans via the lambdoid suture). Sutures facilitate birth and postnatal brain growth and can act as shock absorbers (Opperman 2000; Johnson and Wilkie 2011). During the early postnatal craniofacial growth, the brain gradually grows in volume. The sutures facilitate the radial expansion of the skull with the mesenchymal stem cells differentiating progressively into bone cells while also depositing bone at the edges of the sutures. Once the brain reaches its maximum volume, bone forms at the sutures and while most of the sutures remain open throughout adulthood, some completely fuse. The timing of the suture closure can vary significantly from 8 months after birth for the metopic suture to ca. 18 years of age for the coronal sutures in humans (Wilkinson et al. 2020).

Premature fusion of the sutures is a medical condition known as craniosynostosis. In this condition, one or more sutures can be fused too early, leading to abnormal skull growth (Figure 1.1). This condition affects approximately 1 in 2000 live births (van der Meulen et al. 2009; Cornelissen et al. 2016) and can be devastating for patients and their families. Current treatments for this condition can vary depending on its severity and, in complex cases, can involve multiple invasive surgeries, in which large sections of the skull are removed and remodelled. Nonsyndromic craniosynostosis is where the suture is prematurely fused but the fusion itself is not part of a syndrome, typically producing less severe and more predictable craniofacial abnormalities. The other cases are syndromic and include syndromes such as Crouzon and Apert, where usually more than a single suture is found prematurely closed. The condition is part of a larger syndrome that includes other clinical features and usually has a genetic basis, while non-syndromic cases

do not. These syndromes can cause substantial skull abnormalities. The effects of single and multiple suture fusion can be seen in Figure 1.1.

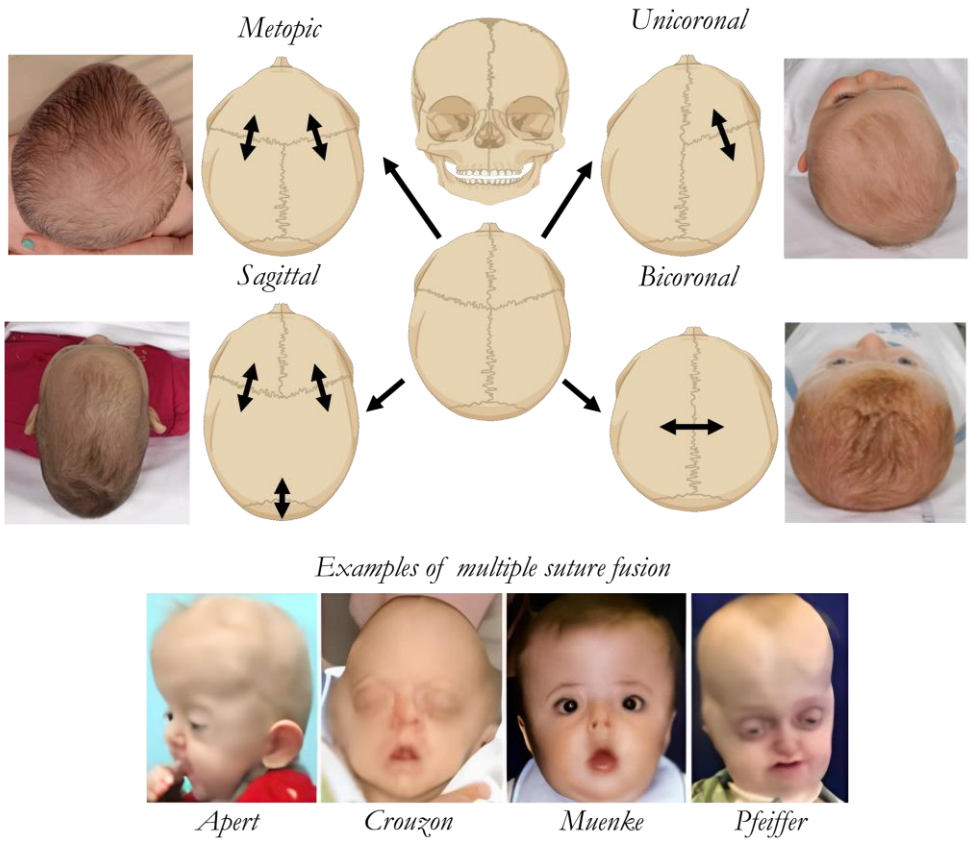

Figure 1.1 Single and multiple suture fusion (craniosynostosis) in children. Arrows indicate the growth direction due to the early fusion of the affected suture (Alden et al. 1999).

There exist a variety of invasive and minimally invasive techniques available for the management of craniosynostosis for both syndromic and nonsyndromic types. The adoption of a management plan through diagnoses to surgery is key for successfully treating the condition because different types of craniosynostosis may require different treatment techniques (Mathijssen 2015; Buchanan et al. 2017). While most techniques are applicable to the majority of suture fusion corrections, they are applied differently to the different sutures. For Crouzon syndrome craniotomy, spring-assisted and distraction cranioplasties are available. The craniotomy requires the removal of a significant part of the skull bone to accommodate the growing brain and restore normal head shape, both spring-assisted and distraction cranioplasties can achieve a comparable restorative effect with minimal surgery as both the spring and the distractor apply an additional force to normalise the skull shape (David and Sheen 1990; Rahimov et al. 2016; Breakey et al. 2021). Helmet moulding therapy may be used following these techniques to further normalise the skull shape and generally allows for non invasive remodelling of the skull shape (Delye et al. 2018).

Mice have been widely used to understand the genetic basis of craniosynostosis and the mechanics of the craniofacial system (Lee et al. 2019). This is due to the similarity of the calvaria between the mouse and human, but also the close parallels between their genomes (Monaco et al. 2015). Indeed, a number of genes responsible for various syndromic forms of craniosynostosis were discovered following experiments in mice (Barrell et al. 2022). For example, the Crouzon mouse ($Fgfr2^{C342Y/+}$), primarily presenting shortened midface, calvarial bulge and suture fusion, was established following the discovery of genes responsible for the Crouzon syndrome in Humans (Perlyn et al. 2006). Other common models include models of Pfeiffer, Apert, Beare-Stevenson, Muenke, Saethre-Chotzen syndromes amongst others, which present with varied craniosynostosis severity and progression.

It has been demonstrated that the application of external forces can help affect suture morphology, namely leading to increased width in rat premaxillomaxillary sutures (Vij and Mao 2006). More recently, Moazen et al. (2022) showed that the dynamic loading of the frontal bone in the dorsoventral direction, to load the coronal suture under tension may partially prevent early fusion of the coronal suture in Crouzon mice. This effect can be observed in Figure 1.2.

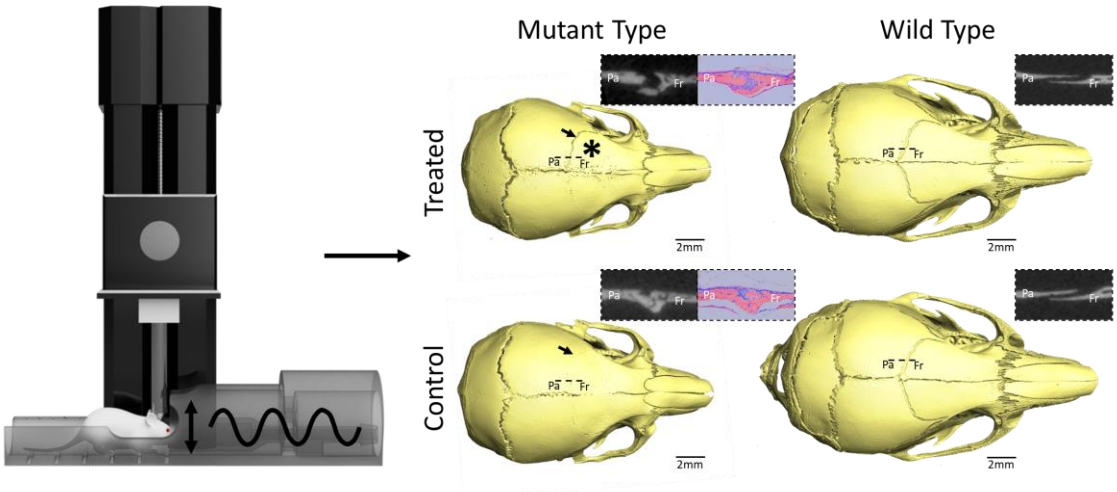

Figure 1.2 Effects of external cyclic in vivo frontal bone loading in the dorsoventral direction on coronal suture patency in Crouzon and wild-type mice. Loading set-up schematic and coronal suture patency results at P21 including CT and histological slices through the coronal suture, * indicates the approximate loading location and arrows highlight the left coronal suture. Interpreted from Moazen et al. (2022).

1-2 Aims and objectives

This project forms a part of a larger project (CranioMech) investigating the role of external dynamic loading as an avenue for craniosynostosis treatment. Dynamic loading on the frontal bone potentially leads to an increased coronal suture patency in Crouzon mice. While this represents a significant opportunity for the development of a new treatment approach and for expanding understanding on the biomechanics of the craniofacial system, the mechanical suture strains involved in this treatment approach and the suitability of the Crouzon mouse model as a general model for craniosynostosis are not clearly understood. Similarly, the general variability of the Crouzon phenotype and effects of varied loading parameters are unclear.

The overall aim of this project is to unravel the biomechanics of the craniofacial system in mice during external loading (*ex vivo* – suture strains and *in vivo* – phenotypic rescue effects) enabling the translation of the aforementioned treatment approach to other mice models of craniosynostosis, larger animal models, and eventually clinical applications.

The specific aims of this project were to:

1. Establish a validated methodology for suture strain estimation during external loading and investigate the effects of *ex vivo* frontal bone loading;

2. Characterise the loading location effects on suture strain during external *ex vivo* and *in silico loading*;

3. Characterise normal phenotypic variation (skull shape and suture patency) in Crouzon mice as it relates to inter-litter variation and suture patency.

4. Characterise in detail the *in vivo* treatment effects on the skull and suture phenotype in Crouzon mice across different treatment regimes.

1-3 Methodology

Figure 1.3 shows an overview of the methodology used to address the aims and objectives of this project. It can be divided into four parts:

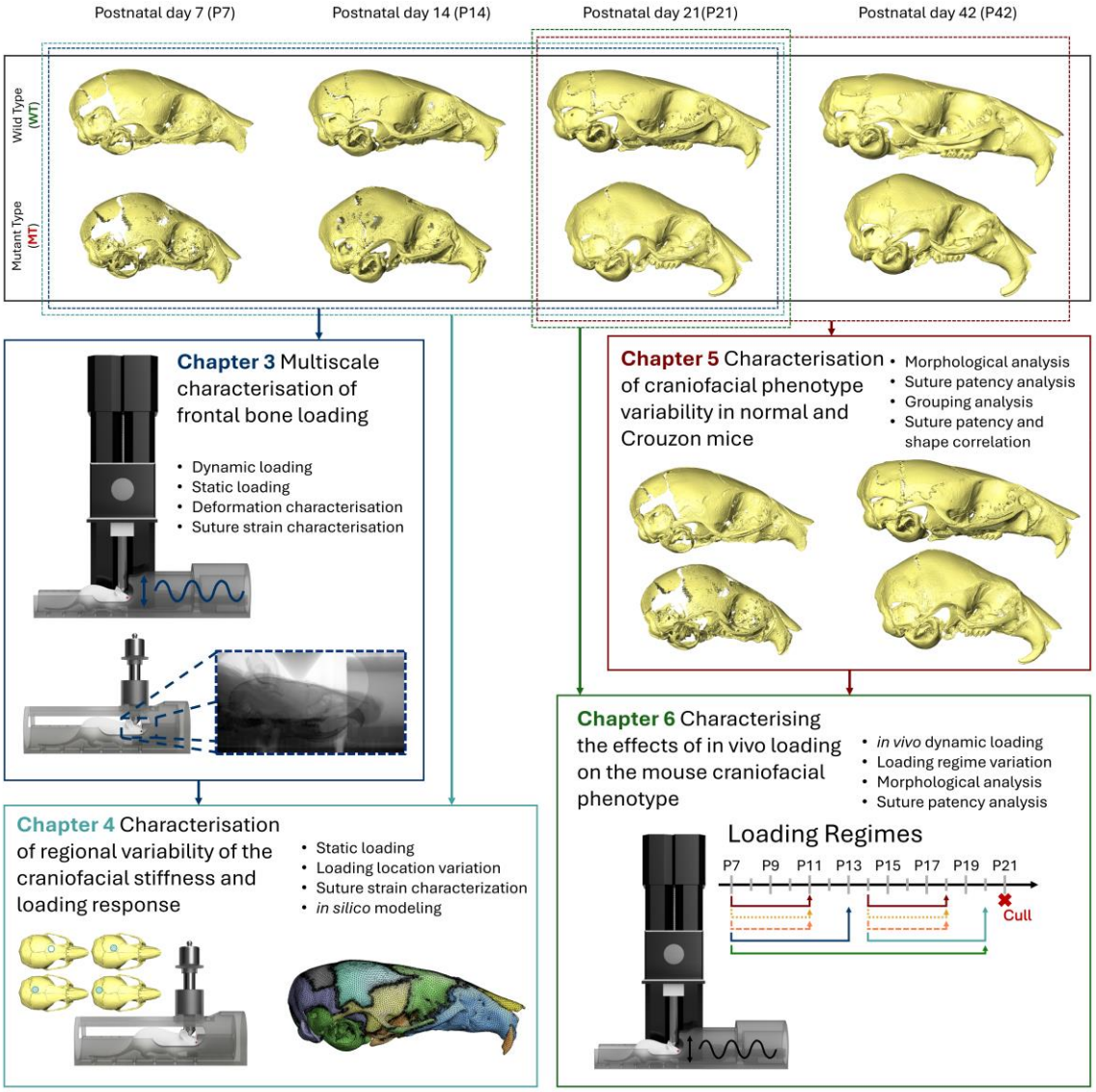

Figure 1.3 The overall methodology of the thesis. Included in the bullet points are the key investigations and analyses for each chapter. The boxes around the specimens highlight the ages at which the investigations were carried out. Regarding Chapter 6, the treatments were carried out at the ages presented in the figure and later in the chapter, but the analysis following the treatments was carried out at P21.

Chapter 3 – Frontal bone loading suture strain analysis: The effects of frontal bone loading were investigated across ages P7, P14, and P21 (early postnatal ages for reference P42 is generally considered adult) in normal and Crouzon mice (3 animals per age, per genotype). A novel methodology for suture strain estimation during *ex vivo in situ* static loading was established following the principles of Digital Volume Correlation. The

critical limitation of the developed methodology was the inability to characterise strain in partially fused sutures. Thus, only sagittal sutures were investigated in MT animals and all cross-technique comparisons were conducted on WT animals. To establish the suitability of investigated *ex vivo* suture strains, a comparative investigation was carried out between *in vivo* dynamic loading, *ex vivo* dynamic loading, and *ex vivo static loading* in WT P7 animals, focusing on the deformation retained after loading in the coronal suture. The comparison was used to establish the suitability of *ex vivo* static loading as a proxy for *in vivo* dynamic loading in terms of resulting suture strains. The work package established coronal and sagittal suture strain values during development which were later leveraged in translation to larger animal models and development of *in silico* models. The developed suture strain estimation methodology allowed for previously unknown suture deformation to be quantified during loading.

Chapter 4 – Loading location dependent suture strain in* ex vivo *and* in silico *investigations: The effects of varied loading locations (frontal bone, anterior parietal bone, posterior parietal bone, interparietal bone) were investigated across ages P7, P14, and P21 in normal and Crouzon mice (1 animal per loading location, per age, per genotype). The development of BounTI (See Appendix II) allowed more sutures to be investigated following the suture strain estimation methodology developed in **Chapter 3** and expanded to include coronal, sagittal, interparietal, and lambdoid sutures. Similarly, BounTI enabled rapid development of *in silico* models and the loading responses of P7, P14, and P21 WT animals were investigated *in silico* with fully disarticulated craniofacial models. To combat similar issues, namely the lack of investigation of the MT response, the deformations were investigated qualitatively across all ages. Additionally, a direct comparison of suture gap width at P7 was made between MT and WT animals. Optimisation of the linear isotropic material properties (of suture, brain, and bone) was carried out for the *in silico* models. Material properties of the sutures, brain, and bones were considered in this work, but the model did not include the surrounding soft tissues.

Chapter 5 – Intra- vs inter-litter and suture patency effects on the mouse craniofacial phenotype: In total, 144 cadavers were investigated for P21 and P42 WT and MT animals (30 P21 MT – across 9 litters, 75 P21 WT – across 11 litters, 32 P42 MT – across 5 litters and 7 P42 WT – across 2 litters). Linear measurements across the skull including length, width, and height among others were taken, further morphological characterisation was carried out by PCA. Additionally, a novel methodology was used to determine the quantitative level of patency across each suture in each individual for the MT animals. A novel grouping analysis was carried out across the investigated phenotypic characterisers

to determine the potential intra- vs inter-litter variation effects on treatment study design. Correlations between suture patency and linear measurements, and suture patency and the PC scores were investigated to determine the effects suture fusion has on the skull shape in the Crouzon mice.

Chapter 6 – External cyclic loading as treatment for craniosynostosis: Finally, the *in vivo* treatment effects were investigated following the same linear measurements, PCA and suture patency analyses established in **Chapter 5**. In total, 159 cadavers were investigated (69 P21 MT – with 39 animals treated, 90 P21 WT – with 15 animals treated) across six different treatment regimes, including the original treatment set out by Moazen et al. (2022). All the treatment regimes were compared individually with the control animals. Additionally, comparisons with littermate controls were produced for groups where littermate controls were available, and all treatment regimes were combined into a meta-group and compared directly to the control animals in the hope of establishing the general effects of loading.

1-4 Chapter organisation

The thesis is organised as follows:

Chapter 2: provides a brief review of previous works related to various aspects of this project. This includes: (1) animal models of craniosynostosis, (2) mechanical properties of craniofacial bones, sutures, and brain, (3) external loading of craniofacial sutures, (4) point alignment techniques and strain estimation, (5) finite element models of craniofacial loading, and (6) craniofacial morphology in WT and MT mice.

Chapter 3: presents a novel methodology for suture strain estimation during static loading and establishes the suitability of *ex vivo* static loading as a proxy for *in vivo* dynamic loading in terms of suture strain. The quantified suture strains in coronal and sagittal sutures are presented for P7, P14 and P21 animals, highlighting large deformations during the considered loading.

Chapter 4: largely expands on **Chapter 3** (frontal bone loading) by investigating the effects of varied loading location (anterior parietal bone, posterior parietal bone and interparietal bone loading) on the suture response during *ex vivo* and *in silico* loading. To address one of the limitations of previous chapters, MT and WT coronal suture response are directly compared in this chapter. Additional sutures are considered in this chapter including interparietal and lambdoid sutures enabled by the development of BounTI.

Similarly, the *in silico* models were produced using a rapid FE (Finite Element) model development methodology primarily leveraging BounTI segmentations. Investigation into the linear elastic isotropic material properties of the *in silico* models are included in this chapter. This chapter highlighted large differences in the response when more posterior parts of the skull are loaded.

Chapter 5: characterises the intra- vs inter-litter variation in both the WT and MT mice in term of linear measurements across the skull, PCA, and novel measurements of CT based quantitative suture patency. In the MT animals, suture patency and morphology correlations are investigated. A novel grouping analysis was carried out to investigate the incidence of statistical significance between different permutation of control and "treated" groups. Significant treatment study design implications are uncovered in this chapter particularly highlighting the unsuitability of non-littermates as control comparison for the craniofacial phenotype both in terms of morphology and suture patency. Additionally, the chapter highlights that suture fusion does not appear to be a significant factor in the craniofacial dysmorphology of the Crouzon mice.

Chapter 6: presents further investigation into the therapeutic effects of craniofacial loading in Crouzon mice. Six different treatment regimes were investigated including the original regime set out by Moazen et al. (2022) with others largely following the original regime with changes to the number of loading sessions, frequency and loading location. The effects were analysed following the analyses set out in **Chapter 5**. Following the study design implications of the previous chapter, littermate controls were included for comparison when available and all loading regimes combined were compared to the full control cohort in addition to direct comparisons of individual loading regimes to the full control cohort. The chapter highlights little to no effects of the treatment on the craniofacial phenotype severity (morphology or suture patency), where statistically significant differences were observed they were accounted for by littermate comparisons.

Chapter 7: summarises the main findings of this thesis. The chapter is organised with one key finding from each work chapter discussed in detail and the overall limitations of this work presented.

Chapter 8: outlines the future work that can be carried out to expand the characterisation and modelling approaches presented here. Two main avenues of future work are considered and included in this chapter. First, with significant limitations established across the work chapters and **Chapter 7,** a potential future direction is directly tackling

these limitations. Secondly as part of a larger project, the findings presented in this work thesis are already being built upon by other group members for future investigations.

Chapter 2 Literature review

2-1 Introduction

This chapter aims to review the key aspects of the literature relating to this thesis. As a significant part of the work is concerning both wild and craniosynostotic type mice, the animal models of craniosynostosis are first reviewed, as understanding the animal to human comparison is critical in developing clinically translatable treatment techniques. In this work, Crouzon Fgfr2$^{C342Y/+}$ mice were used. A large part of the thesis focuses on phenotypic variation and analysis, specifically on morphometrics and suture patency investigations (**Chapter 5** and **Chapter 6**). Thus, beyond the general discussion of the animal models of craniosynostosis, direct investigation into the literature available on craniofacial morphology in mutant and wild type mice was carried out. As the interest lies in the mechanical response of the craniofacial system, the chapter introduces the material properties of cranial sutures and bones and summarises the work previously conducted on external craniofacial loading. Additionally, this chapter lays out the methodologies commonly used for strain analysis using *in situ* microCT loading data which form the backbone of **Chapter 3** and **Chapter 4**. An introduction to FE modelling of craniofacial systems will also be included as the topic is a significant part of **Chapter 4**.

2-2 Animal models of craniosynostosis

Molecular biologists have extensively investigated the syndromic and nonsyndromic origins of craniosynostosis (Rice 2003; Ishii et al. 2015; Flaherty et al. 2016; Katsianou et al. 2016; Merkuri and Fish 2019; Lee et al. 2019). These investigations have led to the development of genetically modified animal models that can help us further understand the hereditary component of this complex condition. Typically, rodents have been used for these experimental studies, and many mutant rodents displaying craniosynostosis

have been bred, including rats, mice, and rabbits (Holmes 2012; Lee et al. 2019). This section will introduce a sample of the animal models used for craniofacial research.

Large and small animals are used for animal work, each with their distinct benefits and shortcomings. While species such as mice, rats, and rabbits are relatively inexpensive to maintain and have short gestation periods, it can be challenging to perform surgical techniques on them. Additionally, their particularly short lifespans of these animals makes it hard to accurately equate their age to humans when considering translational research (Dutta and Sengupta 2016).

Large animals such as pigs, sheep, and goats minimise the drawback seen in small mammals, namely when it comes to clinical translation (Moran et al. 2016; Ribitsch et al. 2020; Banstola and Reynolds 2022; Dias et al. 2022). They can provide similarly sized biological analogues for humans and allow for similar surgical techniques to be used. Biomechanically, the comparable size can play a significant role in mechanical response to external loads. However, the large cost of maintenance and long gestation periods makes it a difficult choice between the two groups (Miller and Chinzei 2002).

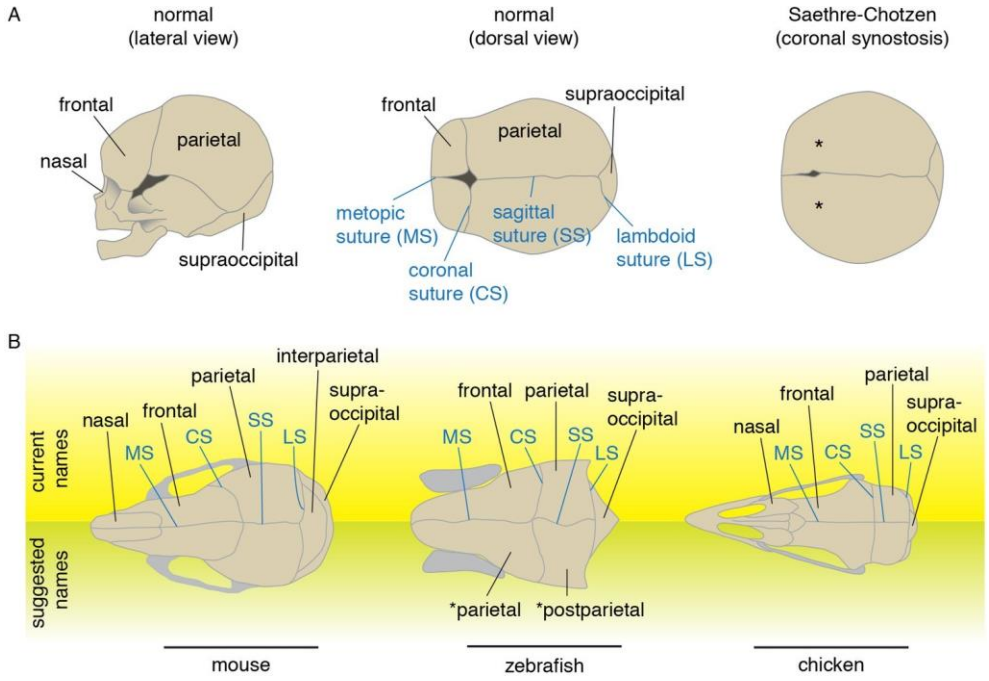

Figure 2.1 a) Diagrams of normal and synostotic human skulls. Bones are labelled in black and sutures in blue. Asterisks denote the missing coronal suture in Saethre-Chotzen Syndrome skulls. b) Major skull vault bones and sutures in dorsal views (anterior to the left) in mice, zebrafish, and chicken (Teng et al. 2019).

Most animals have similar craniofacial structures, yet some differences still exist. Apart from the variation in the shape of the skull, differences in the number of bones comprising the cranial vault can be observed. Similarly, the origin of the skull bones can be different, namely, when comparing the zebrafish partly mesoderm-derived frontal bone to mice

fully neural crest-derived frontal bone (Ferguson and Atit 2019; Teng et al. 2019). Even though there are differences between the mouse and human skulls, namely the lack of the interparietal bone in the human calvaria, these animals have still been widely used in studies of human diseases for two main reasons.

Firstly, key similarities are present between the mouse and human genomes as well as the signalling pathways during craniofacial development, which translates well to the development of genetically modified and gene "knockout" animals, which historically were developed in mice (Grova et al. 2012). Secondly, the short gestation period, combined with relatively low maintenance costs for mice makes them an ideal choice for these studies.

The mouse skull is relatively similar to the human skull, comprised of mostly the same bones in the same relative positions as seen in Figure 2.2. Similarly, the mechanical material properties of the skull bones are not too dissimilar between mice and humans (Delille et al. 2007; Moazen et al. 2015). These are particularly important in experimental loading to be able to confidently translate the findings from mouse to human and are just as key when developing validated finite element (FE) models. These properties will be further discussed in the following section.

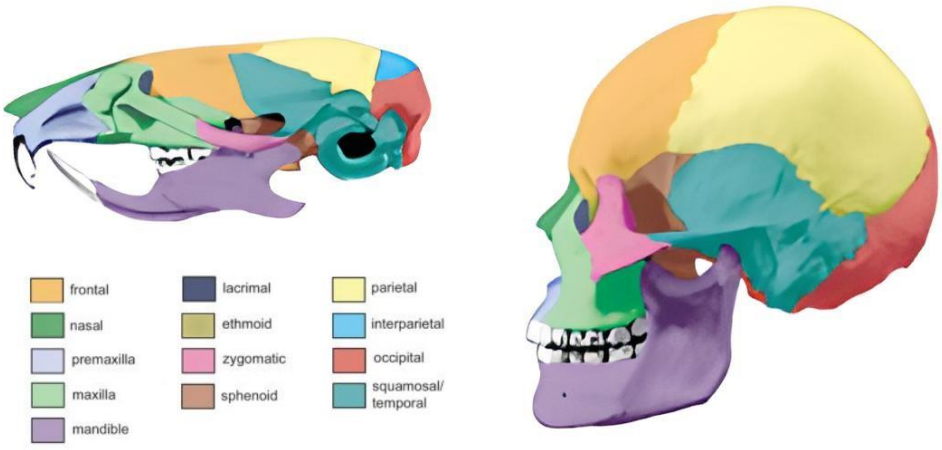

Figure 2.2. Individual bony elements are conserved between mouse (top) and human (bottom) skulls. Colour coding shows the correspondence of structures between the species. The interparietal bone (bright blue on the mouse skull) is an example of a skull bone that exists in mice but not in human.

2-3 Craniofacial morphology

Understanding craniofacial morphology of the wild type and CS model mice as well as the suture fusion patterns in the CS mice and namely the Crouzon mice used in this work

is critical for robust evaluation of treatment effects. This section will introduce available literature on craniofacial phenotype in normal and craniosynostotic mice, focusing on gross morphology and suture patency in the mutant animals during development.

2-3-1 Wild type mice

Wild type (WT) is a nebulous term often used to refer to normal mice, however, the term can refer to any mouse strain. These strains generally are either inbred – developed through brother-sister or parent-offspring mating over > 20 generations (approx. 99% homozygous at all genetic loci, Beck et al. 2000) or outbred – developed through careful rotational breeding schemes to avoid inbreeding (no two individuals are genetically identical, Olson and Graham 2014).

For the inbred mouse strains, a common choice is C57BL/6 background, while for the outbred strains, CD-1 background is commonly used (Campos-Ordoñez and Buriticá 2024). Significantly, higher phenotypic variation in normal outbred mice is observed compared to inbred mice of different backgrounds. This can represent improved experimental quality, establishing how individuals react to specific conditions. Nevertheless, in genetically engineered mice work, this variability may represent a drawback, resulting in highly variable phenotypic penetrance (Tuttle et al. 2018).

C57BL/6 and CD-1 backgrounds are commonly used in animal work, and specifically, CD-1 is used in this thesis. The key investigations of craniofacial morphology are hence summarised in Table 2.1. While direct CD-1 background, WT developmental studies were not found in the literature, the background is used in WT-MT comparison work and will be discussed in greater detail in the CS model mice **section 2-3-2**.

The literature on the WT craniofacial morphology clearly suggests strain-specific effects on craniofacial shape highlighting genotype-dependent variations (Percival et al. 2016, 2017). For outbred mice specifically, Katz et al. (2020) highlight facial phenotype correlation with the genetic variations of the animals, such effects may be further compounded by the introduction of CS to the models. Bailon-Zambrano et al. (2022) have highlighted how the paralogs of CS genes can influence the phenotypic penetrance of craniosynostosis in zebrafish models of CS. These findings suggest the possibility of genetic diversity, especially in outbred strains, significantly affecting phenotypic penetrance in specific strains and possibly in individuals/littermates.

Table 2.1 List of previous key studies investigating the WT mouse craniofacial morphology.

Author	Mouse strain	Number of specimens	Analysis type	Ages investigated	Key findings
Percival et al. 2016	A/J, C57BL/6J, 129S1/SvimJ, NOD/ShiLtJ, NZO/HILtJ, CAST/EiJ, PWK/PhJ, WSB/EiJ and their F1 hybrids.	1211	CT imaging, size-adjusted linear dimensions and PC analysis	Adult	Identified defining craniofacial characteristics that vary among CC founder strains; found stronger additive genetic effects associated with specific strain characteristics; estimated genetic contributions to craniofacial phenotypes.
Maga 2016	C57BL/6J (male)	48	CT imaging, linear dimensions and PC analysis	P0 to P90	Skull growth plateaued at ~P60; skull shape stabilised after P60; asymmetry peaked at birth; high frequency of spontaneous craniofacial malformations (~5.7%).
Vora et al. 2016	C57BL/6J (male)	36	CT imaging, linear dimensions and histology.	P7 to P112	Complex and unique growth patterns of individual bones and cranial regions; documented timing and pattern of closure of cranial base synchondroses; cranial vault and base behave developmentally as one integrated complex
Wei et al. 2017	C57BL/6NCrl (female)	40	CT imaging, linear dimensions and bone mineralisation analysis	P7 to P390	Unique craniofacial skeletal development pattern; differentiated early vs. late growth patterns; documented complex differential changes in bone parameters of various craniofacial bones with different embryonic origins and ossification mechanisms
Katz et al. 2020	Diversity Outbred (DO) mice	1147	CT imaging, linear dimensions, PC analysis and marker effects on shape	Adult	Study found 37 facial shape QTLs in Diversity Outbred mice, with intervals enriched for skeletal/facial development genes. Effects were small, suggesting facial shape is polygenic yet influenced by key genes.
Devine et al. 2022	Multiple strains in MusMorph database	10056	Standardized morphometric data collection	E10.5 to E18.5 and adult	Created standardized mouse morphology database (MusMorph) for meta-analyses of morphological variability across different strains and developmental stages.

F1 hybrid – cross of two different inbred strains,

2-3-2 Craniosynostosis model mice

To date, a number of mouse models have been developed for modelling craniosynostosis. A subsample of the available models is included in Table 2.2, which were adapted from Lee et al. (2019) who explicitly focused on syndrome models and investigations, including at least some level of suture analysis. Only about 15-30% of craniosynostosis cases are syndromic (Ko 2016). The most prominent syndromes include Apert, Crouzon, Pfeiffer, Muenke, and Saethre-Chotzen syndromes (Katouni et al. 2023). All of which have corresponding mouse models.

Morphology of the skull, suture patency, and their interplay with the mouse background strain and developmental timings are critical to developing robust treatment regimes. Specifically, in this work the Crouzon mouse – $Fgfr2^{C342Y/+}$ mice on the CD-1 background – were used; however, limited literature is currently available on this specific mutation/background combination. Thus, this section investigates the literature available on CS mouse models in general. A list of key studies is made available in Table 2.3.

Critically, the effects of mouse background play a key role in the severity of craniosynostosis (Liu et al. 2013; Dudakovic et al. 2020). Specifically, these investigations have highlighted reduced phenotypic severity in BALB/c background mice compared to the most used C57BL/6 background. The background specific phenotype suggests the need for comprehensive investigation of phenotype-genotype interaction for established mouse models in new strain backgrounds. This suggests there is limited translation between different background studies, specifically in terms of phenotypic timing, penetrance, and severity.

Additionally, the investigations highlighted key differences between craniosynostosis (CS) models, namely, $Twist1^{+/-}$ mice exhibit craniosynostosis with limited involvement of the skull base and significant influence of fusion on the morphology of the skull (Parsons et al. 2014; Menon et al. 2021; Nuri et al. 2022). Conversely, significant effects on intersphenoid synchondrosis (ISS) patency were observed in $Fgfr2^{C342Y/+}$ with premature fusion of the ISS possibly contributing significantly to the craniofacial phenotype (Hoshino et al. 2023). Studies have also suggested that craniofacial dysmorphology in the Fgfr2 Apert mutants precedes the suture fusion, further

highlighting the potentially limited role the suture fusion plays in the Crouzon mouse model skull morphology (Martínez-Abadías et al. 2010).

The literature investigations suggest a need for a detailed phenotypic investigation of the CD-1 background $Fgfr2^{C342Y/+}$ mutants. Specifically, the outbred background suggests an increased phenotypic variability in the model. Additionally, to date, the relationship between suture fusion and craniofacial morphology has remained unexplored in the mouse model. Both unexplored areas are critical for the development of robust treatment techniques in the mouse model. Without this detailed phenotypic evaluation, general phenotypic variability may be confused with treatment effects. Similarly, without a clear understanding of the relation between suture patency and craniofacial morphology suture patency treatment effects on the overall morphology are difficult to directly link

Table 2.2 List of mouse models of craniosynostosis updated (only syndrome-associated models and models with clearly reported affected sutures are included and the affected sutures updated) from Lee et al. (2018).

Gene	Mutation/transgene allele	Human syndrome (OMIM)	Affected sutures	Mechanism	Reference
Fgf3	Mutagenesis	Crouzon (123500)	Coronal, sagittal, squamosal. lambdoid	Overexpression	Carlton et al. 1998
Fgf4	Mutagenesis	Crouzon (123500)	Coronal, sagittal, squamosal. lambdoid	Overexpression	Carlton et al. 1998
Fgf9	N143T	SYNS3 (612961)	Coronal (only investigated suture)	LOF	Harada et al. 2009
Fgfr1	P250R	Pfeiffer (101600)	Metopic, sagittal, coronal	GOF	Zhou 2000
Fgfr2	C342Y	Crouzon (123500)	Coronal, sagittal, squamosal. Interparietal, lambdoid	GOF	Eswarakumar et al. 2004
	S252W	Apert (101200)	Coronal, sagittal, interparietal, lambdoid and facial	GOF	Wang et al. 2005
	S250W	Apert (101200)	Coronal (only investigated suture)	GOF	Chen et al. 2003
	Y394C	Beare-Stevenson (123790)	Coronal, zygomaxillary, squamosal	GOF	Wang et al. 2012
Fgfr3	P244R	Muenke (602849)	Zygomaxillay, zygomatic, premaxillary	GOF	Twigg et al. 2009
Gli3	Gli3Xt-J/Xt-J	Carpenter (201000)	Interparietal	LOF	Hui and Joyner 1993; Rice et al. 2010
Hdac4	Hdac4−/−	Brachydactyly mental retardation (600430)	In text referred to a “occipital sutures”	LOF	Vega et al. 2004
Jag1	Jag1flox/−, Twist1+/−, Mesp1CRE/+	Alagille (118450)	Coronal, Sagittal, interparietal	LOF	Yen et al. 2010
Msx2	Timp1-P7H	Boston-type craniosynostosis (604757)	Coronal, sagittal, interparietal	GOF	Liu et al. 1995
	CMV-P7H	Boston-type craniosynostosis (604757)	Coronal, sagittal, interparietal	GOF	Liu et al. 1995
	CMV-WT	Boston-type craniosynostosis (604757)	Coronal, sagittal, interparietal	Overexpression	Liu et al. 1995
Tcf12	Tcfl2flox/−, Twist1+/−, EIIaCRE/+	Saethre-Chotzen (101400)	Coronal, sagittal, interparietal	LOF	Sharma et al. 2013
Twist1	Twist1+/−	Saethre-Chotzen (101400)	Coronal, sagittal, interparietal	LOF	Chen and Behringer 1995; Behr et al. 2011

OMIM – Online Mendelian Inheritance in Man, LOF – loss of function , GOF – gain of function.

Table 2.3 List of previous key studies investigating the CS model mouse craniofacial morphology.

Author	Mouse strain	Syndrome/Affected Gene and Allele	Number of specimens	Analysis type	Ages investigated	Key findings
Carver et al. 2002	mixed C57BL/6J X 129S1/SvImJ	Saethre-Chotzen/Twist +/-	28	Skeletal staining	P18, P122 and P304	Coronal craniosynostosis in 57% mice; both complete and partial fusion observed; skulls with coronal synostosis usually had fusion of distal lambdoid suture.
Perlyn et al. 2006	Not available	Crouzon/FGFR2 C342Y/+	20	Micro-CT, linear measurements	P42	0% bilateral coronal suture fusion; 70% sagittal suture synostosis; all had fused ISS; brachycephalic skull shape; increased interorbital distance; shorter jaw length.
Liu et al. 2013	BALB/c	Crouzon/FGFR2 C342Y/+	56	Micro-CT, linear measurements, skeletal staining	P42 and P84	BALB/c FGFR2C342Y/+ mice exhibited selective and comparatively milder craniosynostosis phenotype; frontal bones showed reduced volume and density due to increased osteoblast apoptosis, impaired maturation, and altered gene expression; midface hypoplasia and mild craniofacial dysmorphology resembling human Crouzon syndrome were observed.

(continued…)

Parsons et al. 2014	C57BL/6J	Saethre-Chotzen/ Twist1 +/-	43	Micro-CT, linear measurements, principal component analysis	P15	Among the Twist1+/− mice, 82.4% showed premature coronal suture fusion (53% bilateral, 30% unilateral). Mice with patent coronal sutures displayed craniofacial shapes more similar to WT, suggesting that suture patency mitigates the severity of dysmorphology. However, even Twist1+/− mice without fusion exhibited intermediate phenotypes, indicating that Twist1 haploinsufficiency affects skull shape independently of fusion.
Dudakovic et al. 2020	C57BL/6 vs BALB/c	Crouzon/FGFR2 C342Y/+	125	Micro-CT, linear measurements	P3, P12 and P21	C57BL/6 FGFR2+/C342Y mice showed coronal suture fusion (88% incidence) while BALB/c showed no fusion; C57BL/6 mutants had more severe midface hypoplasia, dome-shaped skull; greatest variance was in cranial height, intercanthal distance, and nasal bone length.
Menon et al. 2021	CD-1 and C57BL/6	Saethre-Chotzen/Twist +/-	200	Micro-CT, histology, RNA-seq	P7, P8, P9, P11, P15, P17	CD51+;CD200+ skeletal stem/progenitor cell frequencies were significantly reduced in fusing (posterior frontal suture) compared to patent (coronal and sagittal) sutures, and were markedly decreased in syndromic (Twist1+/-) and induced non-syndromic (SB431542-treated) craniosynostosis models. Canonical Wnt signaling activation via Wnt3a increased CD51+;CD200+ cell populations and maintained suture patency, whereas Wnt inhibition (sFrp-1/Dkk-1) decreased these cells, inducing suture fusion.

(continued…)

Nuri et al. 2022	C57BL/6J	Saethre-Chotzen/Twist1 +/-	57	Micro-CT, linear measurements	P14, P28, P42, P56	Twist1+/- mice showed partial coronal suture fusion starting by P14 (100% incidence), progressing to complete fusion by P56 (86% bilateral, 14% unilateral); skulls exhibited reduced anteroposterior dimensions, shortened frontal bones, increased skull height (top-basal axis), and significantly reduced zygomatic arch lengths on affected sides, with asymmetry observed even in bilateral fusion; no differences in skull width nor fusion of spheno-occipital and intersphenoidal synchondroses were observed.
Perrine et al. 2022	CD-1	Crouzon/FGFR2 C342Y/+	~100	Bone scan, PTA scan, morphological integration, histology	E15.5, E16.5, E17.5, P0 and P2	Fgfr2C342Y/+ mice showed partial coronal suture bridging prenatally, but all (100%) presented partial or complete coronal suture fusion at birth (P0); prenatal skull and chondrocranial sizes were significantly larger than Fgfr2c+/+ littermates with the greatest differences localised to the lateral walls, roof of the cranial vault, and olfactory regions; early postnatal skulls (P2) showed reversal to relatively smaller dimensions compared to controls, especially reduced rostrocaudal length.
Yue et al. 2024	C57BL/6JGpt	Crouzon/FGFR2 C361Y/+	46	Micro-CT, skeletal staining, histology, behavioral assays	P42 and P70	Fgfr2C361Y/+ mice exhibited brachycephaly, bilateral coronal synostosis, midface retrusion, shallow orbits with exophthalmos, and skull base shortening; behavioural deficits included impaired learning, memory, social interaction, and motor skills without anxiety-related disorders; histological analysis revealed hippocampal neuron abnormalities potentially secondary to craniosynostosis.

2-4 Cranium mechanical properties

Understanding the mechanical material properties of the cranial sutures, bones and brain is key to developing a robust Finite Element (FE) model as well as confidently translating the findings from mice to humans. Several methodologies exist for determining the material properties of biological tissues, which include but are not limited to three-point bending, tensile, compressive, and indentation tests. The latter is a particularly attractive technique as it can be used on significantly smaller samples and local material properties can be obtained, while the former techniques provide global material properties for the considered specimen.

Limitations exist when employing material indentation analysis, as more sample points may be needed and section preparation can have a significant effect on the results. Additionally, local bone properties may be difficult to translate and compare to global properties commonly used in FE models (Rodriguez-Florez et al. 2013; Managuli et al. 2023). Thus, when considering the material properties of the mouse craniofacial system, local and global material properties should be taken into account. This section will aim to review some of the key studies that have quantified the material properties of cranial sutures and bones, as well as the brain. A schematic of the working principles of mechanical material properties testing is available in Figure 2.3.

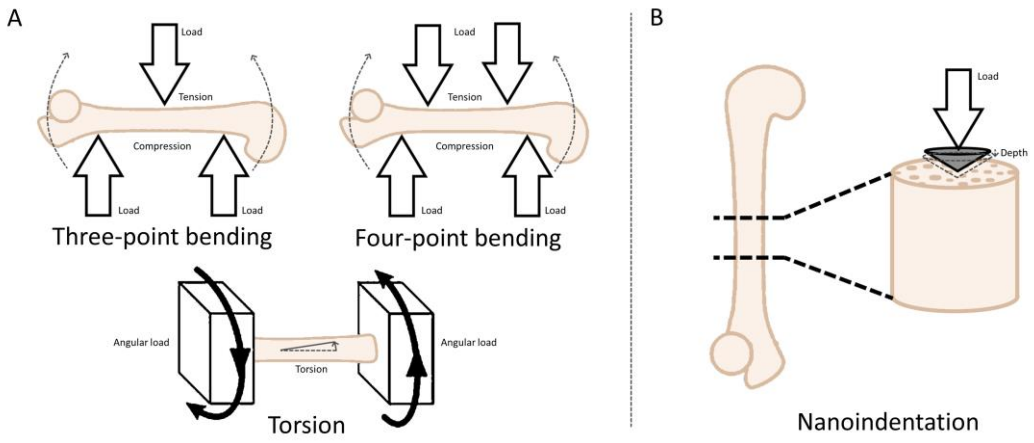

Figure 2.3 A schematic of the testing conditions for different material characterisation techniques. a) sample-wide testing methods and a) localised testing methods.

2-4-1 Cranial sutures

Several studies have been carried out on different animals across different sutures to quantify their material properties. Some of the key studies are available in Table 2.4. The most relevant study for this specific work is the study by Moazen et al. (2015). They quantified the material properties of the cranial sutures and bones of the mouse model that will be used in this study. This study included nanoindentation across sagittal, coronal, and posterior frontal sutures at P10 and P20 (comparable ages to the ages investigated in this work at P7 to P21, highlighting postnatal development). The average elastic modulus of the sutures was found to be ca. 32 ± 32 MPa. Here, it should be noted that the extreme variation indicated by the standard deviation observed may highlight the potential difficulty in accurately capturing the material properties of the sutures, and variations in the orders of magnitude range. This may be reflected in the variation observed across different studies in the broader literature.

The values available in the literature for suture material properties are inconsistent at best; large variations are present even within the same species. The variations between species, within species, and between ages are all pronounced. For example, Coats and Margulies (2006) reported that the elastic modulus for the coronal suture at 8 MPa for 1-month old human, while Wang et al. (2014) reporting 354.83 ± 44.86 MPa for a 1.5-year human. These variations might be explained by viscoelastic effects, as the suture have been shown to exhibit time-dependent behaviour and the loading rates vary significantly between studies. Other sample differences such as differences in size and shape as well as the level of mineralisation at the considered sutures, may further contribute to the observed differences (Jaslow 1990; Rahmoun et al. 2014; Moazen et al. 2015). Most of the values reported range from 10 to 100 MPa. Importantly, the values reported by Moazen et al. (2015) lie within this range and thus can be taken with some confidence.

However, the mechanical properties presented only include the elastic modulus, meaning that these are only true in the elastic regime of deformation. Thus, further consideration is required for non-elastic deformation modes. When considering the craniofacial biomechanics and its response to external loading, fracture and plastic deformation are of particular interest. The former has been investigated by (Chien et al. 2008) where the Young's modulus was reported to be 0.58 ± 0.22 MPa. Significantly lower than expected for the mouse sagittal suture at 4 months old, however, the study also reports on the

viscoelastic properties that may be key to accurately estimate the loading deformation. For the latter form of deformation, the three-point bending test data provides the stress-strain curves, but nanoindentation does not. Therefore, the results presented by Moazen et al. (2015) are not complete in that sense.

Specific attempts at producing the stress-strain curve for rat sutures have been made by Tanaka et al. (2000). However, the results are for relaxed stress (where the load was applied over long period of time) and the experiments did not reach the yield point, which is potentially pertinent to the mechanical loading experiments conducted in this thesis. Therefore, there seems to be a lack of literature on the elastoplastic deformation of the cranial sutures. Particularly important in the work is the lack of multi-modal in-depth characterisation across the mouse suture during early postnatal development. Further characterisation could enable the development of more robust and predictive FE models.

Table 2.4 Elastic modulus of cranial sutures at post-natal ages in both human and animal studies.

Author	Method (Load rate)	Specimen	Suture and region	Age of sample	Elastic modulus (MPa)
Jaslow 1990	Three-point bending	Goat	Internasal	2 -4 Years	10 - 35
			Frontoparietal	2 - 4 Years	120 - 240
McLaughlin et al. 2000	Tensile	Rat	Posterior frontal	7 Days	2.3
			Coronal	7 Days	14
			Sagittal	7 Days	13
Henderson et al. 2005	Three-point bending	Rat	Sagittal	20 - 60 Days	5 - 13
Coats and Margulies 2006	Three-point bending	Human	Coronal suture (Cranial vault)	<1 Month	8

(continued…)

Grau et al. 2006	Nano-indentation	Human	Synostosed sagittal suture (Cranial vault)	9.2 ± 3.0 Months	0.7 ± 0.2
			Synostosed metopic suture (Cranial vault)	9.0 ± 2.9 Months	0.5 ± 0.1
Popowics and Herring 2007	Compression	Pig	Nasofrontal	3 - 6 Weeks	68 ± 32
				5 - 6 Months	115 ± 45
	Tension	Pig	Nasofrontal	3 - 6 Weeks	43 ± 16
				5 - 6 Months	70 ± 33
Maloul et al. 2013	Three-point bending	Human	Bone-suture composite	81 ± 15 Years	213 ± 93
Wang et al. 2014	Three-point bending	Human	Coronal	1.5 ± 0.5 Years	354 ± 45
Rahmoun et al. 2014	Three-point bending	Human	Coronal	88 Years	2038 ± 923
Moazen et al. 2015	Nano-indentation	Mouse	Sagittal, coronal and posterior frontal	10 and 20 Days	32 ± 32

2-4-2 Cranial bones

The literature on the mechanical properties of cranial bones is more extensive than that on cranial sutures. The reported values are more consistent for both studies of the same species and between species. The collected summary for these reported values can be found in Table 2.5. A large majority of the reported values for the calvarial bones lie within the range of 1 to 10 GPa in Young's modulus. While larger deviations are reported, these are likely due to the use of different sampling techniques such as that reported by Gefen et al. (2008) or the significant age differences, particularly in early development (Margulies and Thibault 2000; Li et al. 2011, 2019b).

Moazen et al. (2015) have characterised the mechanical properties of bone at the same ages as those presented for the suture properties. The characterised values are specifically interesting for this work as again the ages span the same early postnatal developmental time points. Thus, with the reported Young's modulus of 5.32 ±0.68 to 7.14 ±0.79 GPa for the frontal bone, and 4.33 ±0.18 to 6.3 ±0.47 GPa for the parietal bone, all lying well within the range of values reported by others in the literature, the results seem to be reliable.

The fracture and plastic properties of bone are not as important for this study in the same way as it is for the sutures because the loading expected is less likely to achieve plastic deformation of bone. However, the quantification of these properties is more widely available than what has been reported for the sutures. Namely, work has been carried out on the cranial and other bones to determine the stress-strain relationships (Sharir et al. 2008; Li et al. 2019a).

The breadth of bone material analysis is significantly more robust than the suture analysis. However, the investigations of location-based variability of material properties in the FGFR2 mutants remain scarce. This is particularly important for the loading regimes considered in this work as treatment for the Crouzon mouse model. FGFR2 mutations have been shown to reduce mineralisation and increase porosity across the skull and particularly the frontal bone in FGFR2 mutant mice (Liu et al. 2013; Percival et al. 2014; Ajami et al. 2024). Similar abnormal mineralisation patterns have been demonstrated in other FGFR mutations (Valverde-Franco et al. 2004).

The reduced mineralisation findings in addition to increased porosity and bone volume decrease observed in the Crouzon mice, strongly suggest reduced global structural

integrity of the skull or at least the frontal bone. This is particularly important for the loadings investigated in this work as the loading location happens to coincide with the most porous region of the frontal bone. The lack of localised material characterisation in the mouse model represents a significant challenge for the development of accurate and robust *in silico* models of the Crouzon mouse skull.

Table 2.5 Elastic modulus of cranial bone at pre- and post-natal ages in both human and animal studies.

Author	Method (Load rate)	Specimen	Bone and region	Age of sample	Elastic modulus (GPa)
McElhaney et al. 1970	Compression	Human	Not available	56-73 Years	2.4 ± 1.4
McPherson and Kriewall 1980	Three-point bending	Human	Frontal	40 Gestation weeks	4.2 ± 0.7
			Parietal	40 Gestation weeks	4.2 ± 0.7
Jaslow 1990	Three-point bending	Goat	Not available	2-4 Years	0.259 ± 0.043
Claessens et al. 1997	Impact response + FE	Human	Not available	Infant	6.5
Margulies and Thibault 2000	Three-point bending	Pig	Not available	2-3 Days	0.615 ± 0.096
		Human	Not available	6 Months	2.65 ± 0.59
Coats and Margulies 2006	Three-point bending	Human	Parietal	<1 Month	260
Gefen et al. 2008	Indentation + FE	Rat	Bone-suture	13 to 43 Days	0.004 to 0.011

(continued…)

Motherway et al. 2009	Three-point bending	Human	Frontal	81 ± 11 Years	10.4 ± 8.5
			Parietal	81 ± 11 Years	11.7 ± 8.3
Li et al. 2011	Optimised FE	Human	Not available	6 Months	0.171
Maloul et al. 2013	Three-point bending	Human	Not available	81 ± 15 years	0.243 ± 0.063
Wang et al. 2014	Three-point bending	Human	Frontal	1.5 ± 0.5 years	1.3 ± 0.1
			Parietal	1.5 ± 0.5 years	1.1 ± 0.1
Rahmoun et al. 2014	Three-point bending	Human	Frontal	88 years	3.3 ± 2.0
			Parietal	88 years	4.1 ± 3.9
Moazen et al. 2015	Nano-indentation	Mouse	Frontal	10 to 20 days	6.3 ± 0.7
			Parietal	10 to 20 days	5.3 ± 1
Li et al. 2019b	Tension	Pig	Frontal	8 weeks	0.4 to 0.8
			Occipital	8 weeks	0.1 to 0.2

FE - Finite element

2-4-3 Brain

The brain has been a relatively well-investigated space considering material properties. Similar to the sutures, the variation in available literature that engages with both the same species and across different species is staggering. With values for mice ranging from Young's modulus of 2 KPa (Gefen et al. 2003) to between 60 and 159 Pa (Koser et al. 2018) for age-matched samples. The measured values for Humans are in the range of MPa, representing five orders of magnitude increase from the mouse measurements. The available literature is summarised in Table 2.6.

The brain properties of mice reported in the literature are low compared to the material properties of the other constituent parts of the craniofacial system, namely bones (8 orders of magnitude) and sutures (5 orders of magnitude). This suggests a minimal impact on the deformation response of the craniofacial system in modelling if the most recent values are considered by (Koser et al. 2018). However, as larger values were measured by (Gefen et al. 2003), the correct choice of material properties may significantly impact *in silico* model accuracy.

Accurate brain properties are critical in developing robust FE models because by volume the brain represents by far the largest portion of the craniofacial system (Marghoub et al. 2019a). The literature investigated here measured linear elastic material properties of the brain. However, the wider literature on FE models of the craniofacial system, commonly investigating trauma injury, has moved away from linear elastic models in favour of viscoelastic (Hua et al. 2015; Zhou et al. 2020) or visco-hyperelastic models (Kleiven and Hardy 2002; Lyu et al. 2022).

Hyperelastic models differ from traditional elastic models capturing strain-dependent stress-strain relations and are commonly used in soft tissue modelling (Mihai et al. 2015). They typically involve strain energy functions which relate to deformation energy to the strain state (Yamashita et al. 2023). In the brain's case, allowing for low compressibility while capturing large deformation – rubberlike behaviour.

The visco-hyperelastic behaviour of the brain may be the crucial factor in such a wide range of linear elastic properties measured as observed in Table 2.6. As the material behaviour of the brain changes significantly based on the load rate, load size, among other factors. It has been shown that even viscoelastic properties may only appropriate approximate brain behaviour at low strains of $< 0.1\%$ (Bilston 1997).

Hyperelastic models largely address these limitations (de Rooij and Kuhl 2016). The low strain limit of traditional linear elastic models is particularly important in investigations of external craniofacial loading, especially at large calvarial deformations. However, currently such models are not available for mice brain properties at early developmental stages.

Until these material characterisations are made for the hyperelastic brain properties in early postnatal mouse brain tissue, linear elastic models may still prove to be a useful tool in rough approximation. However, as linear elastic models are clearly inappropriate at large deformations, the results need to be interpreted carefully with these literature findings in mind.

Table 2.6 Material properties of brain at postnatal stage in both human and animal studies.

Author	Method (Load rate)	Specimen	Age of sample	Tissue type	Elastic modulus (kPA)
McElhaney et al. 1970	Compression test	Human	56-73 Years	Dura mater	31500
Zhou et al. 1995	FE validated	Human	Not available	Grey matter	500
			Not available	White matter	800
Claessens et al. 1997	FE validated by the transient response to impact	Human	Infant	Brain (no specified component)	1000
Miller et al. 2000	Nano-indentation	Pig	100 days	Brain (no specified component)	3.24
Gefen et al. 2003	Nano-indentation	Mouse	13 to 43 Days	Brain (no specified component)	2 - 1.3
Christ et al. 2010	Scanning force microscopy	Mouse	2 to 3 Months	Grey matter	0.454 ± 0.053
				White matter	0.294 ± 0.074

(continued…)

Author	Method (Load rate)	Specimen	Age of sample	Tissue type	Elastic modulus (kPa)
Budday et al. 2015	Nano-indentation	Cow	16 Months	Grey matter	1.4 ± 0.3
				White matter	1.9 ± 0.6
Koser et al. 2015	Atomic force microscopy	Mouse	> 3 Months	Grey matter	0.123 ± 0.009
				White matter	0.055 ± 0.009
Koser et al. 2018	Atomic force microscopy	Mouse	4 - 7 Weeks	Grey matter	0.159 ± 0.026
				White matter	0.060 ± 0.007
Zwirner et al. 2019	Tension	Human	50 ± 23 Years (range 2 – 94 Years)	Dura mater	70000 ± 44000

2-5 External loading of craniofacial sutures

Sutures are loaded naturally during mastication and other physical activities. Thus, their morphologies often correspond to the loads they are subjected to during these processes (Rafferty and Herring 1999; Herring 2008). This indicates that the forces applied externally can potentially affect the suture structure and patency (Herring 2008). It is well known that external forces and restrictions can have a pronounced effect on the skull shape as ritualistic practices have had humans practising artificial cranial deformation for thousands of years across the world (Meiklejohn et al. 1992; Schijman 2005; Khudaverdyan 2011; Palomo et al. 2017). A subsample of the types of deformation is available in Figure 2.4.

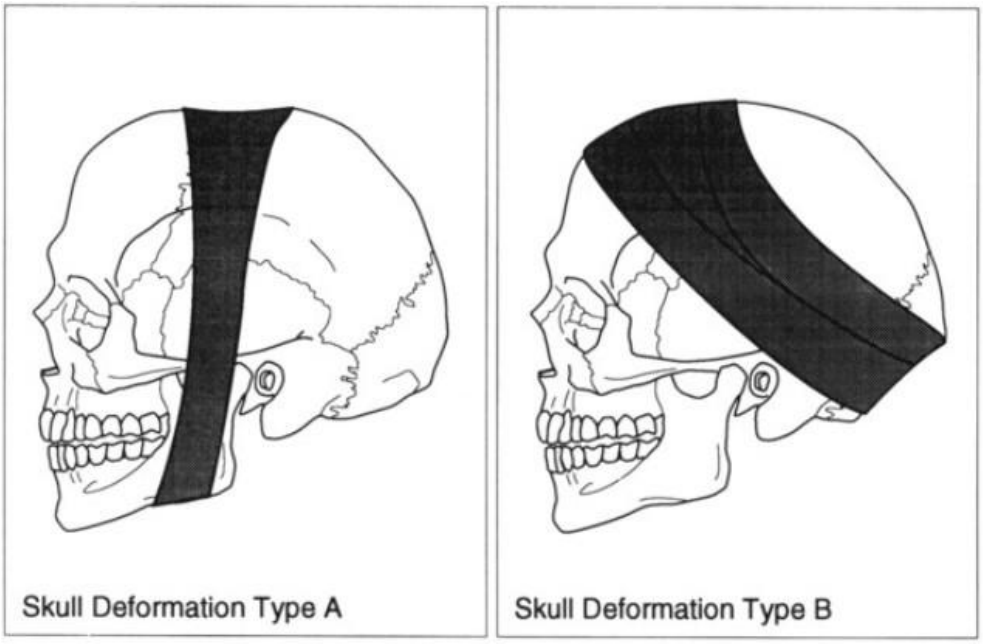

Figure 2.4 Types of deformation practiced in the proto-neolithic and neolithic near east (Meiklejohn et al. 1992).

Several groups have investigated the effect of external loading on craniofacial sutures using a variety of techniques and tools. Both *in vitro* and *in vivo* studies have been conducted on a variety of different species. *In vitro* studies are conducted on sections of the cranial bone, in which sutures removed and loading is applied to the explants in dishes. These types of studies can report cellular changes during loading, however, they alone do not provide a complete understanding of the processes due to their inherent limitation i.e. the lack of interaction with the rest of the organism. Early studies have been conducted by (Meikle et al. 1979) that were then followed by several other researchers (Opperman 2000; Yu et al. 2001; Tholpady et al. 2007; Oppenheimer et al. 2012).

In vivo studies can bridge this translational gap between the *in vitro* studies and clinical applications. Similarly, these experiments have significant limitations, namely due to the biomechanical complexity of the craniofacial system. It can be particularly difficult to design experiments where all confounding variables are accounted for. Thus, the *in vitro* and *in vivo* must be investigated simultaneously to negate the limitations of both.

Two primary load types have been studied i.e. quasi-static and dynamic loading. The former type of load has been done during artificial cranial deformation, while the latter is what the sutures experience due to the cyclical nature of mastication loads. Both can be either tension or compression loads or a combination, depending on the force direction and suture morphology. This section will review the key literature in this area, and a summary of the key investigations conducted can be found in Table 2.7 for both quasi-statically and dynamically loaded animals.

2-5-1 Static loading

There is no doubt that static or more accurately quasi-static loading can affect the shape of the skull. This has been practiced through artificial cranial deformation since the ancient times. More recently clinical work has shown the efficacy of helmet therapy as a treatment for various forms of craniosynostosis (Seymour-Dempsey et al. 2002; Marupudi et al. 2016; Iyer et al. 2018). However, it is important to understand how much this type of treatment affects bone formation and remodels the bones as opposed to affecting the suture morphology and its mechanics. Thus, *in vitro* studies allow for a deeper understanding of directed suture loading, while *in vivo* studies can help us understand the larger effects on the craniofacial sutures present during such treatment in patients.

Spring-assisted cranioplasty is a much more directed clinical treatment method that relies on quasi-static loading; however, often the springs are applying loads across a surgically removed strip of bone instead of a patient's suture. It should be noted that while showing clinical success, this approach inevitably requires surgical intervention (Shen et al. 2015; Yan et al. 2020). A comparison of these two treatment approaches is available by Skolnick et al. (2021) with the application methods seen in Figure 2.5.

The two treatment techniques included here represent clinically available external loading as treatment for craniosynostosis. Highlighting two different modes external loading with passive (helmet) and active load (spring) quasi-static loading methods.

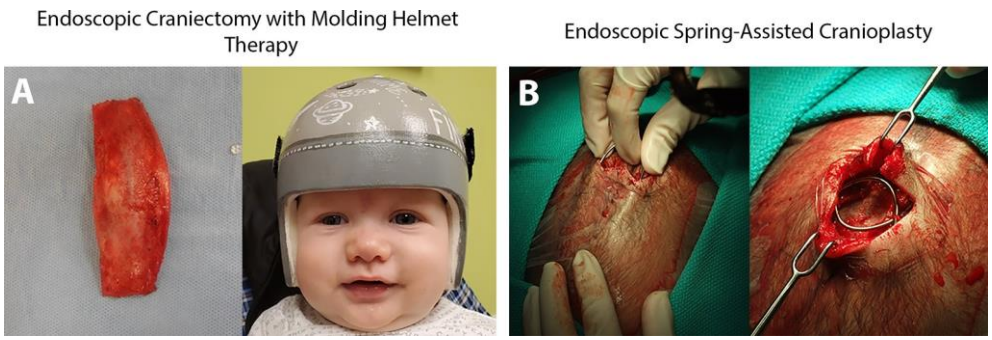

Figure 2.5 a) Endoscopic craniectomy with moulding helmet therapy: resection of the fused suture. The patient wearing a cranial orthotic. The helmet allows expansion in the biparietal dimension. b) Endoscopic spring-assisted cranioplasty: insertion of the springs Skolnick et al. (2021).

While the helmet treatment has shown some success in treating craniosynostosis patients non-surgically, it is more often combined with surgical interventions (Sood et al. 2011; Delye et al. 2018). A study by Takeshita et al. (2017) investigated direct tensile force on the sagittal suture in mice and identified the key effects on gene regulation. However, this passive force may be limited in its ability to affect suture morphology and maintain suture patency in craniosynostosis patients. Thus, dynamic loading may be key to achieving more pronounced effects without surgical intervention.

2-5-2 Dynamic loading

Quasi-static loading has been employed clinically in both helmet therapy and various forms of cranial distraction, but there has been no application of dynamic loading in a clinical setting. However, this does not mean that no applications exist. Conversely, early animal studies suggest that dynamic loading may be able to treat severe forms of craniosynostosis without surgical intervention.

Several studies have investigated the effect of dynamic loading in rats, rabbits, and pigs (Vij and Mao 2006; Peptan et al. 2008; Soh et al. 2018; Herring et al. 2024). The work by Vij and Mao (2006) as well as Peptan et al. (2008) both indicated an effect on suture morphology due to the external dynamic forces applied. However, no difference was observed between the tension and compression of the suture, in relation to suture patency. This was not corroborated in Moazen et al. (2022) and more significant changes occurred where the coronal suture was in apparent tension during frontal bone loading. Parietal bone loading showed little effect on the overall skull shape.

The pig study conducted by Soh et al. (2018) where a 1.5 kg cyclic load was applied across the nasofrontal suture showed a positive effect on the suture width. However, further investigation highlighted that the cyclic loads failed to promote growth in Yucatan mini pigs (Herring et al. 2024). Additionally, the study highlighted the relatively large forces (1-2 kg) required to induce significant strains (600 – 4000 με) in the sutures of larger animals and linked the deformation of one suture to another. Showing that the loads are transmitted through the bone to other sutures that are not directly loaded. Work by Moazen et al. (2022) has highlighted the possible phenotype-mitigating effects of frontal bone loading in Crouzon mice with potential improvement in coronal suture patency and skull shape normalisation.

The loading regime that successfully achieved this treating effect was: 0.1N force, 10-minute loading at 1 Hz on the frontal bone per session. This was repeated for 10 days over a 2-week period with 2 days of rest in the middle. These values were originally loosely based on the rat in Vij and Mao (2006), the frequency is an approximation of normal loads during chewing. The parameters for the mouse experiments were adjusted for the animal size and other practical constraints. As these parameters had shown therapeutic effects, all the dynamic loading methodologies presented in **Chapter 3** were based on these loading conditions to help unravel the underlying mechanics contributing to the success of this treatment approach. **Chapter 6** included replication of these parameters, and all the varied regimes were based on them with minimal variations.

Table 2.7 List of previous key studies of quasi-static and dynamic calvarial loading in animals.

Author	Suture	Specimen	Loading conditions			Type
			Age	Level	Duration	
Cleall et al. 1965	Midpalatal	Rhesus monkey	30-40 Months	4mm in 2 weeks then 2mm in 4 weeks for 12 weeks	2-36 Weeks	Q-static (tension)
Tuenge and Elder 1974	Various sutures	Rhesus monkey	Not available	70M applied to the occlusal plane via headframe at 40°angle	57-72 Days	Q-static (tension)
Ten Cate et al. 1977	Sagittal	Rat	Not available - Adult	2mm deflection via wire frame	2 Hours to 42 Days	Q-static (tension)
Jackson et al. 1979	Various sutures	Southern pig-tailed macaque	40-46 Months	30N per side parallel to the occlusal plane via wire frame	63-114 Days	Q-static (tension)
Southard and Forbes 1988	Interpremaxillary	Rat	53-58 Days	5 to 30N tension in the suture	12 Hours to 4 Days	Q-static (tension)
Losken et al. 1999	Coronal	Rabbit	28 Days	0.33 mm distraction per loading	12 loadings in 42 Days	Q-static (tension)
Mao 2003	Premaxillomaxillary	Rabbit	42 Days	2N on incisors at 0, 0.2 and 1 Hz	10 min/day for 12 Days	Q-static/ dynamic (tension)
Vij and Mao 2006	Premaxillomaxillary, nasofrontal	Rat	17, 23, 32 Days	0.3N to maxilla at 4Hz	20 min/day for 12 Days	Dynamic
Soh et al. 2018	Nasofrontal	Pig	3 Months	800 to 1000 μstrain at 2-3Hz	30 min/day for 5 Days	Dynamic
Moazen et al. 2022	Coronal	Mice	7 Days	0.1N on the frontal bone at 1Hz	10 min/day for 10 Days	Dynamic
Herring et al. 2024	Nasofrontal	Yucatan miniature pig	4–5 Months	~2000 μstrain at 2.5 Hz	30 min/day for 5 Days	Dynamic

2-6 Image correlation

Quantifying the level of mechanical strain that the craniofacial system experiences during loading can have various implications. For example, it can enable us to scale up an experiment from a small to a larger animal model. Strain gauges have been classically used to quantify the level of strain for various mechanical and industrial applications. They have also been placed on the sutures and across the skull bones to measure the level of strain induced across the skull due to the external forces (see e.g. Soh et al. 2018). This becomes much more challenging for smaller animals as it requires considerable effort for the surgery and may influence the strain results. Thus, another approach to estimate the strain during loading is required when considering smaller animal models, e.g. mice. In this section, digital volume correlation will be introduced as a potential method for investigating strain in intact animal sutures. It will outline the common point alignment techniques used to correlate the undeformed and deformed microCT scans and introduce the methods used to obtain strain from these deformation estimations.

2-6-1 Point alignment techniques

A number of approaches for point alignment exist as this technique can be used for aligning partial scans, estimating manufacturing errors, and various other engineering applications, in addition to its use in digital image correlation. This alignment is also known as point registration. Three main point cloud alignment approaches exist: rigid - where the points are aligned without changing their position within the cloud or scaling all axes equally; affine - where the relative position of the points within the cloud can be scaled non-uniformly, but only scaling can be applied; and non-rigid registration - where the points can align arbitrarily (usually constrained by specific equations) to best fit the target cloud. This is illustrated in Figure 2.6.

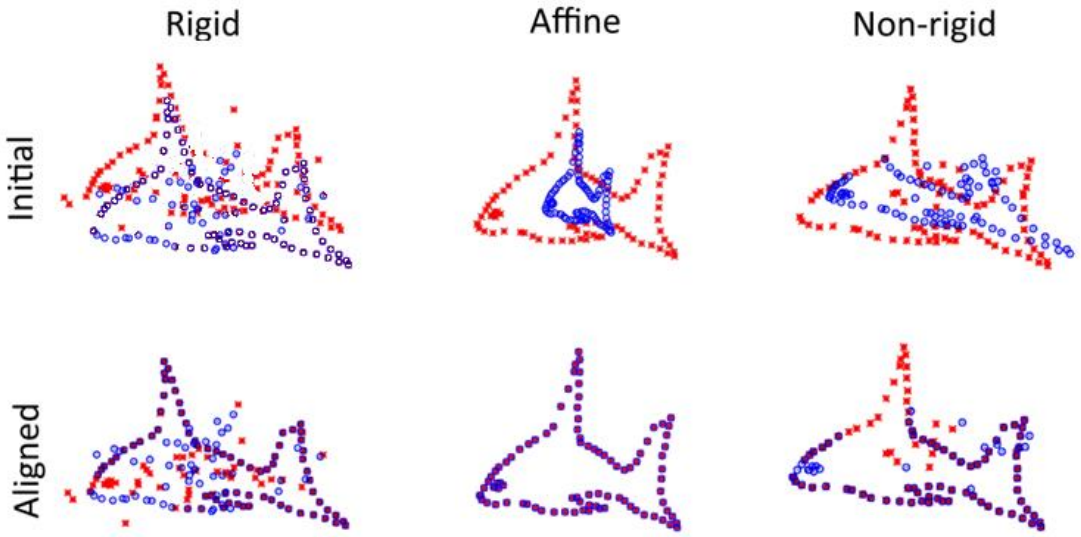

Figure 2.6 Point set registration approach comparison reinterpreted from Myronenko and Xubo Song (2010).

As point cloud registration is crucial in computer vision, published research on this topic has increased exponentially over the years due to the meteoric increase in the use of computer vision in daily life (Pomerleau et al. 2015). Thus, many different techniques have been developed to achieve the desired effect in various fields (Chebrolu et al. 2020; Zampogiannis et al. 2021; Li and Harada 2022; Huang et al. 2023). While conventional registration algorithms produce good results, but require large computational resources. Newer algorithms employing the capabilities of neural networks have significantly reduced the computation time while simultaneously introducing new features. This is particularly well showcased in the work by Li and Harada (2022), in an approach they called "neural deformation pyramid", which is able to capture large deformation while preserving small topological features, as seen in Figure 2.7.

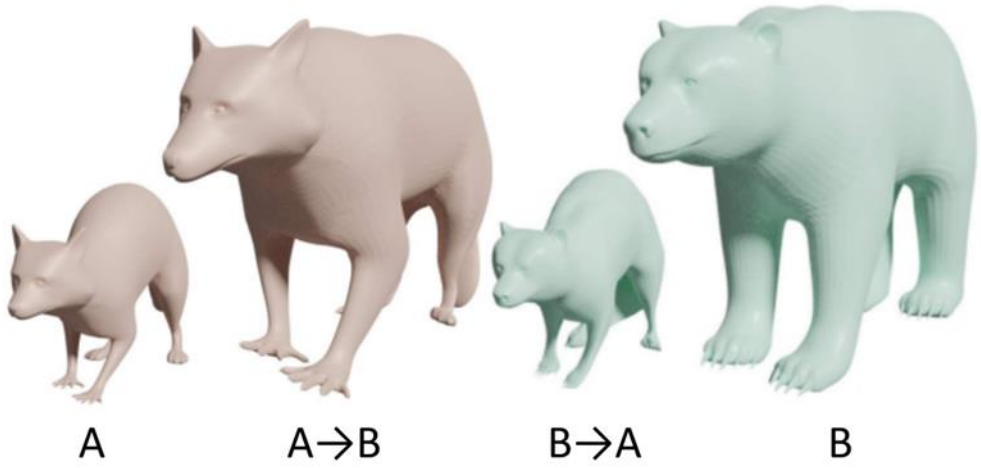

Figure 2.7 Shape transfer using NDP. The arrows indicate the directions of alignment Li and Harada (2022).

The approach works particularly well when deformations of the same object are to be quantified. This is indeed useful to determine the mechanical strain induced on an object by comparing its undeformed and deformed states because the former model can be forced to take the position and shape of the deformed model. Obtaining the deformed shape using the original models allows the points of the original model to be tracked from undeformed shape to the deformed shape.

2-6-2 Strain estimation

Point cloud registration allows for the deformation of a structure to be examined without strain gauges (Yuan et al. 2023). If the loaded and unloaded states of a structure can be imaged, point cloud registration can be used to obtain the deformation and thus, to determine the strain in the structure. Thus, Digital Volume Correlation (DVC) has been employed to estimate the local shifts between two states of the same structure that has been scanned most often using CT (Wang et al. 2019; Olufsen et al. 2020; Kim et al. 2020; Nogatz et al. 2022). A number of algorithms are available to obtain these strain results, which have shown varying degrees of success (Powierza et al. 2019).

DVC works by subdividing the structure into smaller elements, which can then be individually aligned to the reference volume, obtaining the shift for that element (Bar-Kochba et al. 2015). These shifts between the elements can then be used to estimate the strain in the structure. The general approach for the methodology is seen in Figure 2.8.

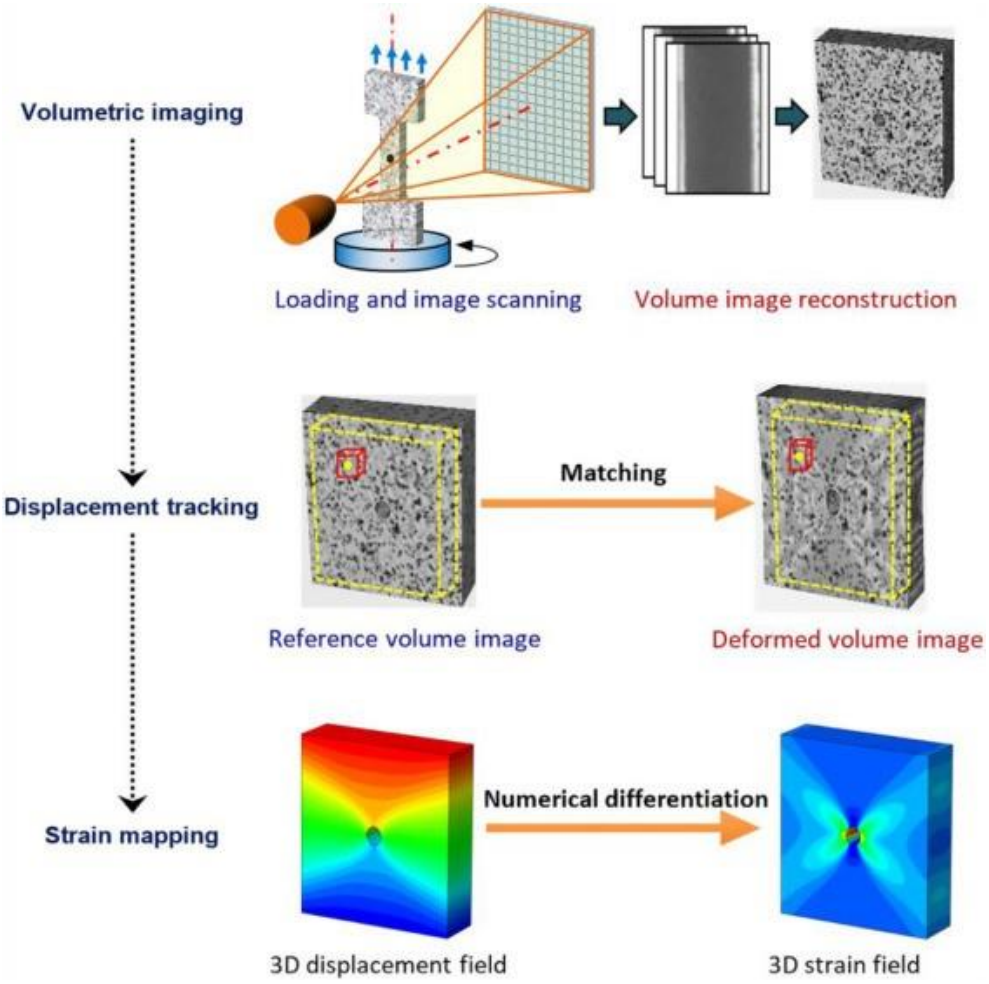

Figure 2.8 Basic procedure of DVC approach for internal deformation measurement (Pan and Wang 2020).

As the element size is decreased, the algorithms are more prone to errors and noise becomes an important issue, because the elements become harder to accurately register with the deformed body. Thus, the approach is best suited for determining the inner strains in a structure that takes up most of the scan volume, which has good features to be used for registration. This suits extracted bone samples, especially for larger species (Roberts et al. 2014). The DVC studies presented in Table 2.8 follow these basic principles and encompass the conditions for the standard use of DVC when mapping bone strain. However, DVC falls short for scenarios where small parts of the volume are of interest and do not have high resolution. In mice microCT scans the bone of interest is thin and poorly resolved compared to the whole scan volume including the full craniofacial system. However, while the point registration methodology of DVC might not apply, the strain estimation can still be used if a modified approach for determining the local shifts could be obtained.

Table 2.8 List of some of the key previous studies using digital volume correlation in animal bone. Partially reinterpreted from Dall'Ara and Tozzi (2022).

Author	Bone	Animal	DVC algorithm
Bay et al. 1999	Femur	Human	Local (custom)
Gillard et al. 2014	Femur	Pig	Local (DaVis)
Palanca et al. 2016	Vertebrae	Pig	Global (BoneDVC)
Joffre et al. 2017	Femur	Human	Local (custom)
Costa et al. 2017	Vertebrae	Pig	Global (BoneDVC)
Fernandez et al. 2018	Femur	Sheep	Local (DaVis)
Oliviero et al. 2018	Tibia	Mouse	Global (BoneDVC)
Giorgi & Dall'Ara, 2018	Tibia	Mouse	Global (BoneDVC)
Turunen et al. 2020	Femur	Human	Local (TomoWarp2)
Le Cann et al. 2020	Tibia	Rat	Local (TomoWarp2)
Kusins et al. 2020	Humerus	Human	Global (BoneDVC)
Ryan et al. 2020	Femur	Human	Global (BoneDVC)
Palanca et al. 2021	Vertebrae	Pig	Global (BoneDVC)
Martelli et al. 2021	Femur	Human	Global (BoneDVC)

2-7 Craniofacial system FE modelling

Finite element analysis has been extensively employed by various engineering disciplines. It allows for low costs estimation of experimental results, which can be particularly important in industry as cost reduction is always a priority. For animal research, FE models can help reduce the number of animals needed for animal studies (in line with the 3Rs of animal research - Replacement, Reduction, and Refinement) as well as provide robust results and quantify values that could not be obtained in other ways (Madden et al. 2020). In addition to this, FE can be used to modify the initial conditions of the analysis setup and test hypotheses. This has made *in silico* techniques of all types gain traction in the biomechanics field from head impact trauma to tendon analysis (Deck and Willinger 2008; Shim et al. 2018).

When considering *in silico* techniques, there are several different approaches each best suited for different applications. FEA (Finite Element Analysis) tools, for instance, are designed for deformation analysis based on material properties, which allow for obtaining stress and strain contours. Most FE studies in the biological field fall into one of three categories: developmental modelling, impact modelling, and functional modelling (Rayfield 2007; Fernandes and Sousa 2015; Cross et al. 2022). When considering the craniofacial system, two distinct FE approaches exist: static and transient models. The former is where the external loads and boundary conditions do not change with time, while for the latter the boundary conditions and external loads can change. While transient models can capture the complexities of the craniofacial system more accurately, the static models can be used in certain cases where the increased accuracy is not worth the exponential increase in the computational resources (Ming Tse et al. 2014).

When considering FE or any other *in silico* technique, validation and verification should be provided. While FEA is a powerful tool that allows for cheap quantification of difficult-to-get otherwise quantities in biomechanical fields, it can easily mislead the researchers if not properly validated. Thus, experiments need to be included and compared to confidently assert the validity of the FE results or establish error levels (Oefner et al. 2021).

A summary of key studies, including both static and transient FE models, is available in Table 2.9. Included in the summary are key studies of external loading of the craniofacial system and sutures. Growth models are omitted from the summary.

2-7-1 Static models

While static models may not be the most accurate, they can still provide valuable insights into the biomechanics of craniofacial development. Marghoub et al. (2019) developed a validated FE model for calvarial growth in mice. By using some of the material properties presented earlier in this chapter, they were able to accurately predict the growth patterns of neonatal mice skulls. This work was then built upon by Cross et al. (2022) to predict skull growth in humans during both normal and abnormal (craniosynostotic) development. More recently, (Liang et al. 2024) have further expanded the FE models for craniofacial growth by introducing facial growth modelling.

In addition to this, Moazen et al. (2022) have attempted to use FE models to estimate the strain during external loading used as a novel approach for craniosynostosis treatment. The model used closely resembles the material properties and boundary conditions used by Marghoub et al. (2019). The research available for external calvarial loading FE models in mice is extremely scarce, however, numerous FE models have been developed for craniofacial loading in other animals and most abundantly in humans.

FE models of animals other than mice may help develop a more robust model than previously available in mice, and while some of the findings may not be directly applicable, the methods used in the past should be carefully considered when developing new FE models. The static FEA work done by Godinho et al. (2017) in humans shows that although the models often failed to reproduce the absolute strain magnitudes, the relative magnitudes were approximated well enough when compared to the experimental results as seen in Figure 2.9.

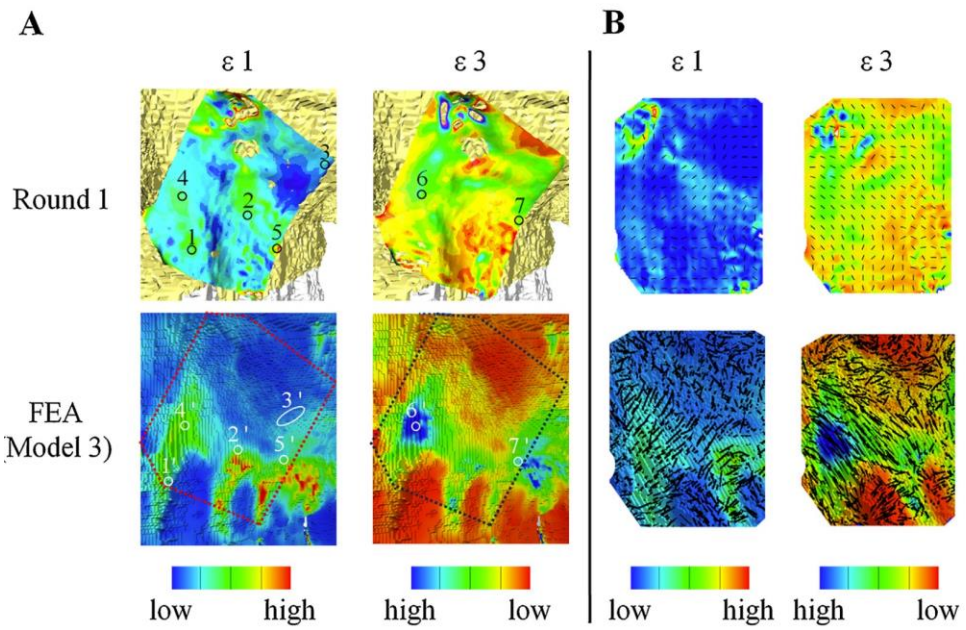

Figure 2.9 a) strain contour for first (ε1) and third (ε3) principal strains. Experimental results at the top and FE results are at the bottom. Numbered points indicate matching absolute values. b) strain vector direction map (Godinho et al. 2017).

This can mean that in some cases the relative strain results may be a more useful quantity than the absolute results and be potentially closer to the real system. However, this model did not include the sutures, thus, the work by (Watson et al. 2021) may be more comparable to the work for this study because the sutures are included and the work has been done on rodents. The authors were able to determine the strain contours on the rabbit skull during mastication and identified the compression and tension areas of the bones. These static models can be used as a basis for building an experimentally validated mouse FE model during external cranial loading.

2-7-2 Transient models

One common theme in human transient FE models is the omission or significant simplification of the sutures (Hosseini-Farid et al. 2020; Kiriyama et al. 2022). However, this makes the studies less directly applicable to this work. Jasinoski and Reddy (2012) and Zhang and Yang (2015) have developed transient models for the sutures themselves. To investigate their response to dynamic loading, the duration of the loading, and the overall influence of suture geometry. While these models are grossly simplified, they provide useful insights into the total strain induced in the suture. From this work, it is clear that butt-end sutures can including the sagittal suture, experience more strain from the same load than interdigitated sutures, such as a nasofrontal suture. Additionally, these

studies specify the viscoelastic material properties of the sutures, which can be adopted for more inclusive models.

The majority of human transient studies investigate head injury by impact. However, the methodologies applied can be replicated for estimating the effects of external dynamic loading because the largest difference between these is the force applied. Work by Hosseini-Farid et al. (2020) and Kiriyama et al. (2022) introduce fast-moving impact balls, ranging from 7.2m/s to 20m/s. The strain rate during the impact on the brain can be seen in Figure 2.10.

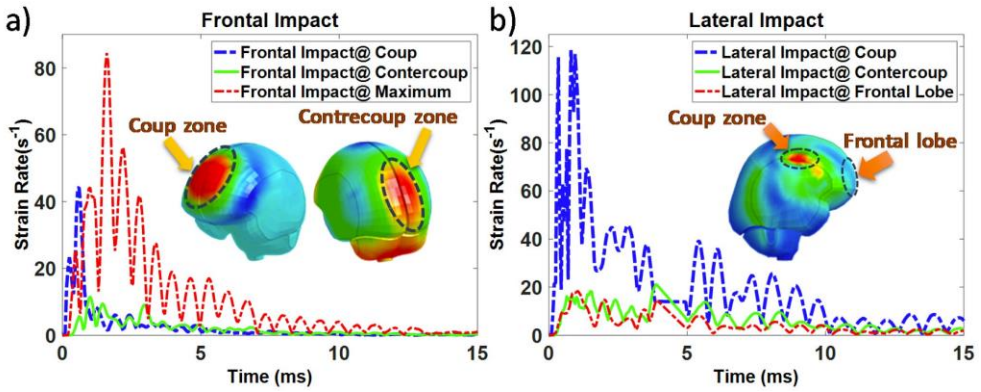

Figure 2.10 a) strain rate during a frontal impact and b) strain rate during a lateral impact (Hosseini-Farid et al. 2020).

Table 2.9 List of previous key studies of static and transient cranial loading in FE models.

Author	Suture	Specimen	Loading conditions			Type
			Location	Level	Boundary conditions	
Jasinoski and Reddy 2012	Idealised	Not available	Simplified suture joint, from side	100KPa compressive static and up to 5Hz	Bone on the opposite side of the loading	Static and Transient
Zhang and Yang 2015	Idealised	Not available	Simplified suture joint, from side	50KPa rectangular pulse, 0.04μs	Bone on the opposite side of the loading	Transient
Godinho et al. 2017	Not included	Human	Maxilla (side)	Static 425.61N	The two mastoid processes and the meso-lingual cusp of the first left molar	Static
Hosseini-Farid et al. 2020	Not included	Human	Calvaria (front and side)	Impact loading at 10, 15, and 20 m/s, 42.7mm ball	Fixed at the neck	Transient
Watson et al. 2021	Included	Rabbit	Cranium (muscle attachments)	Application of predicted loads during mastication	Tip of the tooth	Static
Kiriyama et al. 2022	Simplified	Human	Calvaria (top, side, back)	Impact loading at 7.2 m/s, 2mm sphere from different directions	Fully fixed diagonal plane	Transient

2-8 Summary

This chapter presented an overview of key literature related to craniofacial biomechanics and specifically here during normal and abnormal (craniosynostotic) development, focusing on the normal and Crouzon mouse skull phenotype, material properties, external loading, deformation analyses and computational modelling.

Investigation into the literature on WT and MT phenotypes highlights the variability of the craniofacial morphology in both normal and craniosynostotic mice. Literature clearly shows a link between mouse strain and craniofacial phenotype as well as suture fusion patterns in mutant animals. These findings suggest increased phenotypic variability in outbred mice backgrounds, such as CD-1. **Chapter 5** characterises the craniofacial phenotype, specifically focused on intra- vs inter-litter variation and suture patency correlations to skull shape. In this chapter, the implications of increased inter-litter variation on craniosynostosis treatment study design are examined.

Cranium mechanical properties, including sutures, bones and brain, were examined in this literature review. The literature highlights significant variations between studies in the measured material properties across all three investigated domains. **Chapter 4** investigates the effects of these material properties on the craniofacial response to external loading in FE simulations based on the literature summarised in this review on craniofacial system FE modelling. The computational results are compared to experimental results originally established in **Chapter 3.** The investigations in the chapter followed the literature investigation on external loading of the craniofacial system and specifically investigated the loading conditions shown as a potential craniosynostosis treatment by Moazen et al. (2022). External loading is further investigated experimentally in **Chapter 4**. Both chapters significantly focused on suture strain analysis obtained through image correlation, highlighted in this chapter as a powerful tool for deformation analysis.

Following these investigations and the literature available on external loading, both the original loading regime described by Moazen et al. (2022), and five more modified loading regimes are investigated in **Chapter 6**. The investigations are focused on detailed characterisation and phenotype variability implications available in this review, and confirmed by **Chapter 5**.

Chapter 3 Multiscale characterisation of frontal bone loading

3-1 Introduction

As described in the literature review, the work by Moazen et al. (2022) highlighted that the cyclic loading of the frontal bone in the Crouzon mouse can potentially prevent early fusion of coronal sutures in this mouse model. However, we do not understand the underlying mechanics of this treatment and the level of mechanical strain that needs to be induced across the coronal suture, to achieve the observed therapeutic effects. Understanding the underlying mechanism may help inform the feasibility of this treatment in larger animal models and potentially humans. Thus, this chapter aims to quantify the level of deformation and mechanical strain across the skull during the calvarial loading of Crouzon (MT) and normal (WT) mice.

Aim: Quantify the level of strain the in the coronal and other calvarial sutures during external loading.

Objectives: Establish comparability between *in vivo* and *ex vivo* loading in terms of induced suture strain, quantitatively investigate the suture strain during *ex vivo* loading and investigate the differences between WT and MT animals and the effects of age.

3-2 Materials and methods

A series of *in vivo* experiments were carried out on wild-type and Crouzon $Fgfr2^{C342Y/+}$ mice at specific ages (P7, P14, and P21). These experiments were force-controlled, and the loading tip displacement was quantified as a measure of the whole head displacement. Then, a series of *in/ex vivo* dynamic and static loading experiments were carried out (using P7 WT specimens) to quantify the level of loading tip displacement and the lasting size change across the coronal suture (via quantification of suture thickness changes) as a result aforementioned tests. This investigation enabled us to understand to what extent an *ex vivo* static loading scenario on fresh cadavers may differ from an *in vivo* dynamic

loading experiment. Lastly, a series of *ex vivo* static loading experiments were carried out (at P7, P14, and P21), and a novel algorithm was developed to quantify the level of mechanical strain induced across the calvarial sutures. The loading for the strain analyses was carried out *ex vivo* and under static loading due to the necessity for micro-CT imaging. The scans lasted 2hrs, the anaesthesia and radiation dose prohibited these measurements *in vivo*. Note that in all cases, the left frontal bone was loaded in the dorsoventral direction (see Figure 3.1).

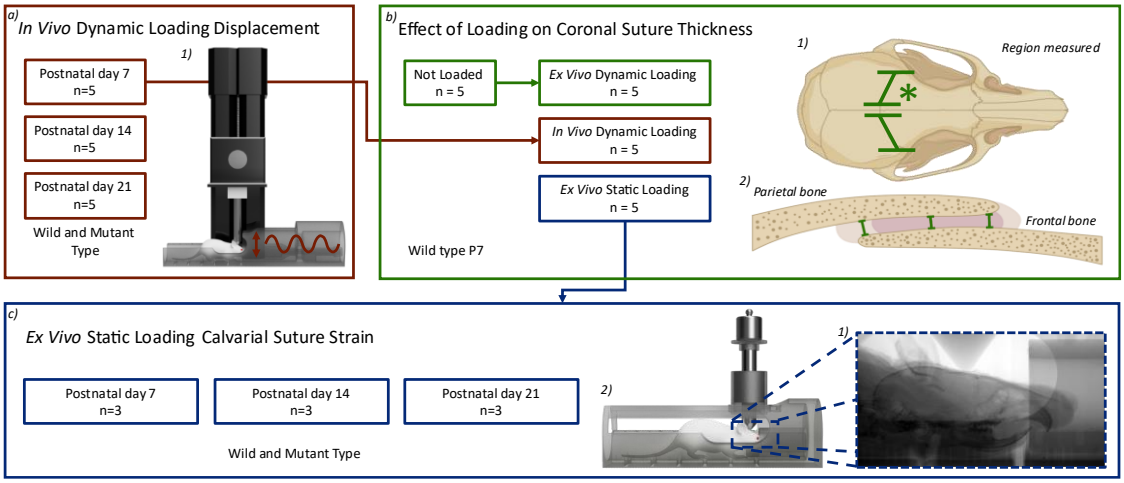

Figure 3.1 An overview of various experiments and analyses performed in this chapter. This includes the type of experiments conducted and the number and type of animals used for each experiment. a) *In vivo* dynamic loading displacement characterisation 1) dynamic loading set-up schematic, b) suture thickness after static and dynamic loading 1) region measured with * denoting the loading location for all experiments, 2) measurements taken across the coronal suture and c) *ex vivo* static loading suture strain quantification 1) radiography image during loading, 2) static loading set-up schematic.

3-2-1 Specimens

Wild-type and mutant mice were investigated. For the latter, the $Fgfr2^{C342Y/+}$ Crouzon mouse model was used. The mutant animals were derived from the European Mouse Mutant Archive (EMMA) at MRC Harwell, as described by Peskett et al. (2017). *Ex vivo* studies were carried out on fresh, refrigerated (4°C) cadavers, i.e. the analyses were carried out within four days of the animals being culled.

Figure 3.1 summarises the number of animals used in different experiments carried out in this study. In total, 63 animals were used. For the *in vivo* dynamic loading, 5 animals were used per group (P7 WT, P14 WT, P21 WT and P7 MT, P14 MT, P21 MT). For the lasting suture thickness analysis, 5 animals were used per group (P7 WT not loaded/*ex vivo* dynamic loading, P7 WT *in vivo* dynamic loading and P7 WT *ex vivo* static loading).

Lastly, for the suture strain analysis during *ex vivo* static loading, 3 animals were used per group (P7 WT, P14 WT, P21 WT and P7 MT, P14 MT, P21 MT).

In all analyses, the sex of the animals was not controlled for and was randomly distributed across the investigated groups. This was deemed appropriate as mouse skull morphology does not show statistically significant sexual dimorphism even in adulthood (Csanady & Mosansky, 2017). Any sexual differences are expected to be smaller in early postnatal ages, pertinent to the animals investigated in this work.

Note: all animal experiments were approved by the UK Home Office and performed as part of a Project License (number: PP8161503) under the UK Animals (Scientific Procedures) Act 1986. Animal procedures complied with the ARRIVE guidelines and were performed under the supervision of UCL Biological Services.

3-2-2 Loading setups

Dynamic loading: this was applied using a custom-built test system (mock-up in Figure 3.1a1). Here, an actuator (Newmark Systems, Inc: res. 0.04µm with Maximum velocity of 25mm/sec) and a force sensor (GSO Series, Transducer Techniques: res. 0.01 N with 1.5 N capacity) were used with a custom developed LabVIEW program (National Instruments Corp, Austin, TX, USA). The dynamic loading was force-controlled and conducted following the protocols used by Moazen et al. (2022). The mice were loaded for 10 minutes at 1Hz with 0.1N maximum load (reported parameters from the aforementioned loading study, that showed therapeutic effects).

Static loading: this was applied using a custom-built setup mimicking the dynamic loading setup (mock-up in Figure 3.1c2) to ensure the loading position and force remained as close as possible to the *in vivo* setup. Here, the animals were placed in a simplified anaesthetic tube to preserve the same points of contact during loading, and a 10g (0.1N) weight was placed on a plunger with the same diameter tip as in the dynamically loaded specimens. The static loading was conducted in a micro-CT scanner (XT H 225ST, Nikon, Herts., UK), and the specimens were scanned in place before and during the loading. All the CT scans were taken at 90kV for 2 hours with a voxel size of 9.5µm.

Animal positioning: the principal consideration when developing the loading setups was maintaining the loading conditions originally established in Moazen et al. (2022). To

reproduce the loading position, the same anaesthetic tube design from the previous study was used. The animals were loosely placed in the anaesthetic tube, with the upper incisors in contact with the tube as shown in Figure 3.1c1. The animals were not further constrained. Regarding all experiments the positioning of the animals as well as the load was conducted by a single operator.

In the *in vivo* experiments carried out in both Moazen et al. (2022) as well as here, the placement of the loading tip is carried out following external anatomical landmarks, specifically the posterior-anterior position is defined by the imaginary line between the posterior corners of the eyes. The tip is then position one tip diameter (1 mm) away from the midline. In the *ex vivo static* experiments the consistency of the load positioning is improved by the radiography images available prior to the application of the load.

Load-relaxation: a load-relaxation test was carried out using the setup inside the micro-CT scanner. Here, the skull was loaded at 0.1N, and radiography images were taken every 15 seconds for 180 min. It was found that after 120 min there was minimum deformation across the skull (Appendix I-A1.1). Hence, all static loading experiments inside the CT scanner lasted 240 min with 120 min of relaxation and 120 min of continuous scanning time with the load applied throughout the 240 min period. A 120 min scan prior to the loading and relaxation was also carried out. This was the major difference compared to dynamic loading and a limitation of this work.

3-2-3 Measurements

Loading tip displacement: the dynamic loading setup had an encoder built into it. Hence, the loading tip's displacement data during the dynamic loading was measured directly from the linear motor in the custom developed loading setup. Here, two parameters were quantified: (1) the maximum displacement of the head and (2) the difference between the maximum and minimum displacement for each oscillation cycle in the last 30 seconds of the loading. The aforementioned time period was used to reduce the variability in the results, especially as the oscillation max-min values were significantly affected by the animal's breathing patterns. In the static loading, tip displacement data was measured from the CT data obtained before and during the loading.

Suture thickness: Coronal suture thickness was measured using the micro-CT data. The measurements were taken over 250 slices (in the mediolateral plane) on each side (i.e. left

and right coronal suture) at three points: the edge of the frontal bone, the midpoint and the edge of the parietal bone in the sagittal plane (Figure 3.1b). The average distance for each of the three measurements for each specimen was recorded. Note that coronal suture thickness was measured only in wild-type P7 animals.

Mechanical strain across the sutures: A custom program was written in Python (Python Software Foundation, USA) to calculate the deformation patterns across the bones using the CT data before and after the loading. The program was based on the digital volume correlation concept (Buljac et al. 2018; Dall'Ara and Tozzi 2022). Commercially available digital volume correlation algorithms could not be used due to the extremely small thickness of bone when compared to the scan volume that included the whole craniofacial system (Aggarwal et al. 2009). The displacement data across the bones could then be used to calculate the strains present in the calvarial sutures.

Several tests were performed to assess the validity of the program developed here. Two geometries were investigated, a simplified suture geometry of two offset plates sandwiching a softer material and the actual frontal and parietal bones with the coronal sagittal and interfrontal sutures. FEA was carried out on the two geometries, with material properties tuned to produce qualitatively similar levels of deformation as observed during the external loading experimentally (~0.6 von Mises average strain in the coronal sutures). The deformed surfaces of the bone were then extracted, and the surfaces were remeshed. The developed methodology was then applied to the artificially deformed bones from the unloaded bones to estimate the suture strains. The FEA results of the suture strains were then compared to the estimated values (see Appendix I-A1.2).

The overall workflow for the proposed approach here is summarised in Figure 3.2. In brief, firstly, the loaded and unloaded scans were segmented using common thresholds (Figure 3.2a). This was to minimise variability due to manual segmentation. This was possible because all the animals were scanned using the same machine with identical scanning parameters. The segmented unloaded scan was then divided into square elements, where each element was rigidly aligned individually to the loaded surface (Figure 3.2b). 100 elements per bone were used, as this was found to best capture the deformation. More elements could not be used as the features in each would not be sufficient to confidently align with the deformed body. Figure 3.2c illustrates the differences in accuracy between direct and element alignment. The displacement at the boundaries between the elements was then smoothed using a centred average for each node 0.25 times the element size to obtain the deformation pattern. The displacement data

for each node of the bone surface was then imported into a commercial FE solver (ANSYS, V2022 R2, ANSYS Inc., Canonsburg, PA, USA) as boundary conditions to estimate the strain in the sutures.

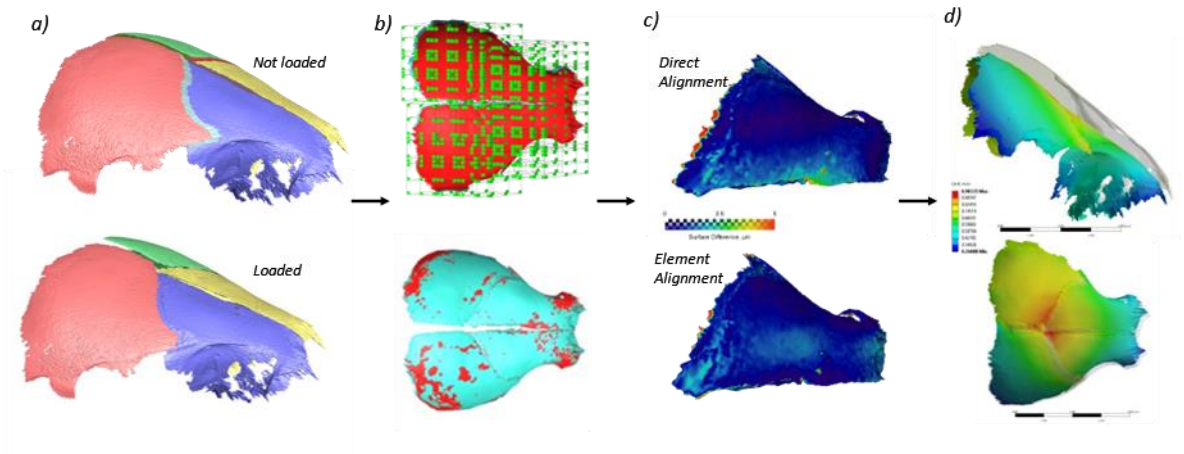

Figure 3.2 Strain estimation during calvarial loading methodology. a) Not loaded and loaded states of the same individual, b) separation of the surfaces to square elements, c) comparison between direct alignment of surfaces and element separated alignment of surfaces and d) visualisation of displacement and calculation of strain field using FE (ANSYS).

It should be noted that (i) while the program developed here provided an accurate estimation of the strain across the sutures, it overestimated the strain in the calvarial bones; hence, the strain data on the bone is not reported here (see Appendix I-A1.2); (ii) a significant limitation of the program developed here was that the sutures had to be continuous to provide full disarticulation between the bones in the CT data. This was not the case for the coronal suture in the Crouzon mice. Nonetheless, the level of strain in other sutures was quantified.

3-2-4 Statistical analysis

Statistical analysis was performed in SPSS (IBM SPSS, NY, USA). One-way analysis of variance (ANOVA), with Levene's test used to test for equal variances. The significance level was set at $p < 0.05$.

3-3 Results

3-3-1 *In vivo* loading displacement (P7, P14, and P21 - MT and WT)

The maximum head displacement across all considered cases was in the range of 2.2-3.7mm, while the displacement within each oscillation (oscillation max-min) was in the range of 0.13-0.32mm (Figure 3.3). It was clear that the maximum displacement was primarily linked with the initial position of the animal in the anesthetic tube, while the displacement within one oscillation may be reflecting the level of loading applied to the craniofacial system (see Appendix I-A1.3 for the displacement data over 10 min of loading).

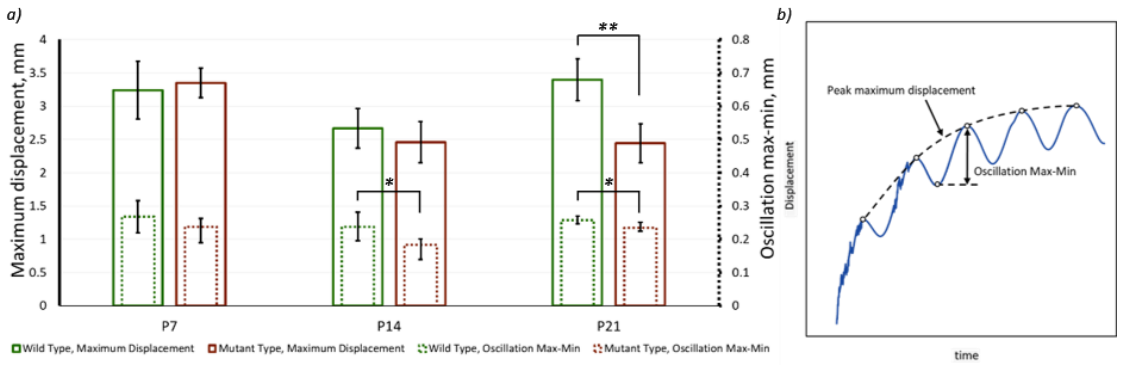

Figure 3.3 a) Maximum oscillation displacement (left value bar) and Max-Min oscillation (right value bar) values for the final 30 seconds of loading comparing wild-type and mutant-type animals. * and ** mark differences between the groups at $p < 0.05$ and $p < 0.01$, respectively and b) explanation of the values presented in a).

The differences in both recorded displacement quantities were more apparent between the WT and MT mice as the animals became older. There was no significant difference in the displacement quantities between the WT and MT animals at P7. Still, there was a significant difference ($p < 0.05$) in oscillation displacement between the WT and MT animals at P14 and P21.

3-3-2 Comparison between the *in vivo* and *ex vivo* loading (P7 - WT)

The whole head displacement was compared between the *in vivo* dynamic, *ex vivo* dynamic, and *ex vivo* static loading experiments (Figure 3.4). This data highlighted that the head displacement in the ex vivo static loading scenario was lower than the two other considered loading scenarios. This was statistically significant when comparing the *ex vivo* static loading vs. *in vivo* dynamic loading scenarios (1.65mm ± 1.05mm vs. 3.34mm ± 0.25mm – $p < 0.01$).

In addition to the whole head displacement, suture thickness was also quantified across the aforementioned loading scenarios and compared to an unloaded control group (Figure 3.4B). This data highlighted that:

1) Coronal suture thickness across all loading scenarios was significantly larger than the control group ($p<0.05$). The only exception was at the right coronal suture (i.e. unloaded side) for the *in vivo* dynamically loaded ($p=0.085$) at the frontal edge. This suggested a permanent deformation across the sutures under all considered loading scenarios.

2) The coronal suture thickness on the loaded side (left) was slightly higher than on the unloaded side. However, this was not statistically significant when comparing left to right sides' results within each group.

3) There was no statistically significant difference in the thickness of the coronal suture between the considered loading scenarios. The only exception was the left coronal suture thickness across the frontal edge, where the *ex vivo* static loading scenario significantly differed from the *in vivo* dynamic loading ($p=0.047$). Nonetheless, there was a clear albeit not statistically significant, pattern of higher thickness being measured for the *ex vivo* static loading compared to the *in/ex vivo* cyclic loading scenarios. For example, the ratio of the coronal suture measured between the mean increase from the control unloaded group were 0.38 ± 0.09, 0.51±0.10, and 0.70±0.10 times the unloaded thickness for the *ex vivo* dynamically, *in vivo* dynamically, and *ex vivo* statically loaded groups respectively.

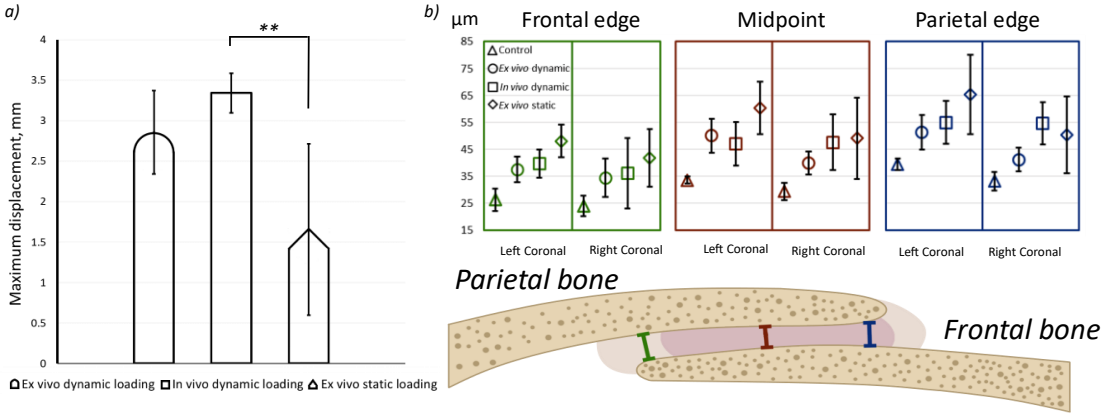

Figure 3.4 a) Comparison of the maximum displacement of the loading tip for *ex vivo/in vivo* dynamic and *ex vivo* static loading regimes for P7 WT mice. ** - $p < 0.01$ and b) suture thickness as measured after loading at 3 different points in the coronal suture (edge of the frontal bone, midpoint, and edge of the parietal bone) over 250 slices laterally on each side for P7 WT mice after each loading regime.

3-3-3 *Ex vivo* static loading - suture strain (P7, P14 and P21 – MT and WT)

The pattern and level of mechanical strain induced across the calvarial sutures because of unilateral loading on the frontal bone (at 10g) are shown in Figure 3.5 and Figure 3.6. Additional data as per individual variation in the three considered specimens for each WT group is included in Appendix I-A1.4. Overall, this data highlighted that:

1) The coronal suture on the loaded side was under higher mechanical strain compared to the unloaded side across the considered ages (e.g. 0.73 ± 0.08 vs. 0.49 ± 0.07 von Mises strain at P7– Figure 3.6c). This suture was predominantly loaded under tension across the considered ages; however, this was not as clear on the unloaded side, e.g. considering the P7, there was a similar level of 1st and 3rd principal strain across the coronal suture in the unloaded side (Figure 3.6a and b at P7).

2) A direct comparison between the WT and MT mice across the coronal suture was not possible; however, considering the sagittal suture, a lower level of strain was recorded in the MT compared to the WT mice across the considered ages (e.g. 0.26 ± 0.07 vs. 0.50 ± 0.25 von Mises strain at P7– Figure 3.6a).

3) There was no clear pattern of increase or decrease in the strain level from P7 to P21 across the coronal suture. However, the strain level across the sagittal suture significantly decreased from P7 to P14 in both WT and MT (e.g. 0.50 ± 0.25 vs. 0.29 ± 0.05 for von Mises strain in the WT; $p<0.05$ – Figure 3.6c).

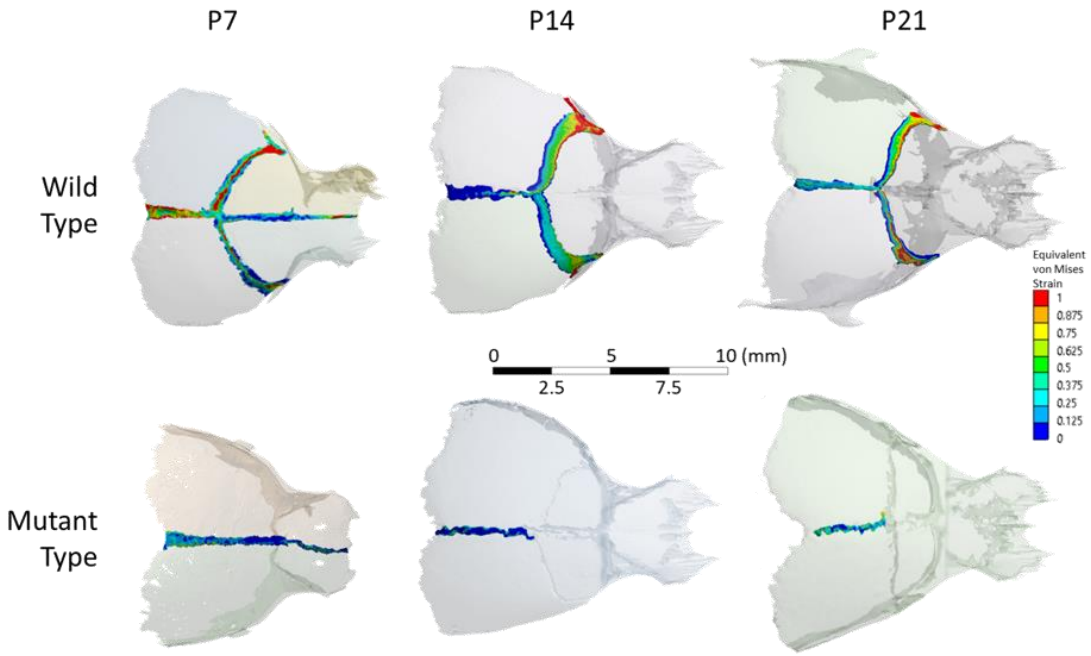

Figure 3.5 von Mises strain contours for mutant and wild-type specimens at P7, P14, and P21 during *ex vivo* static loading.

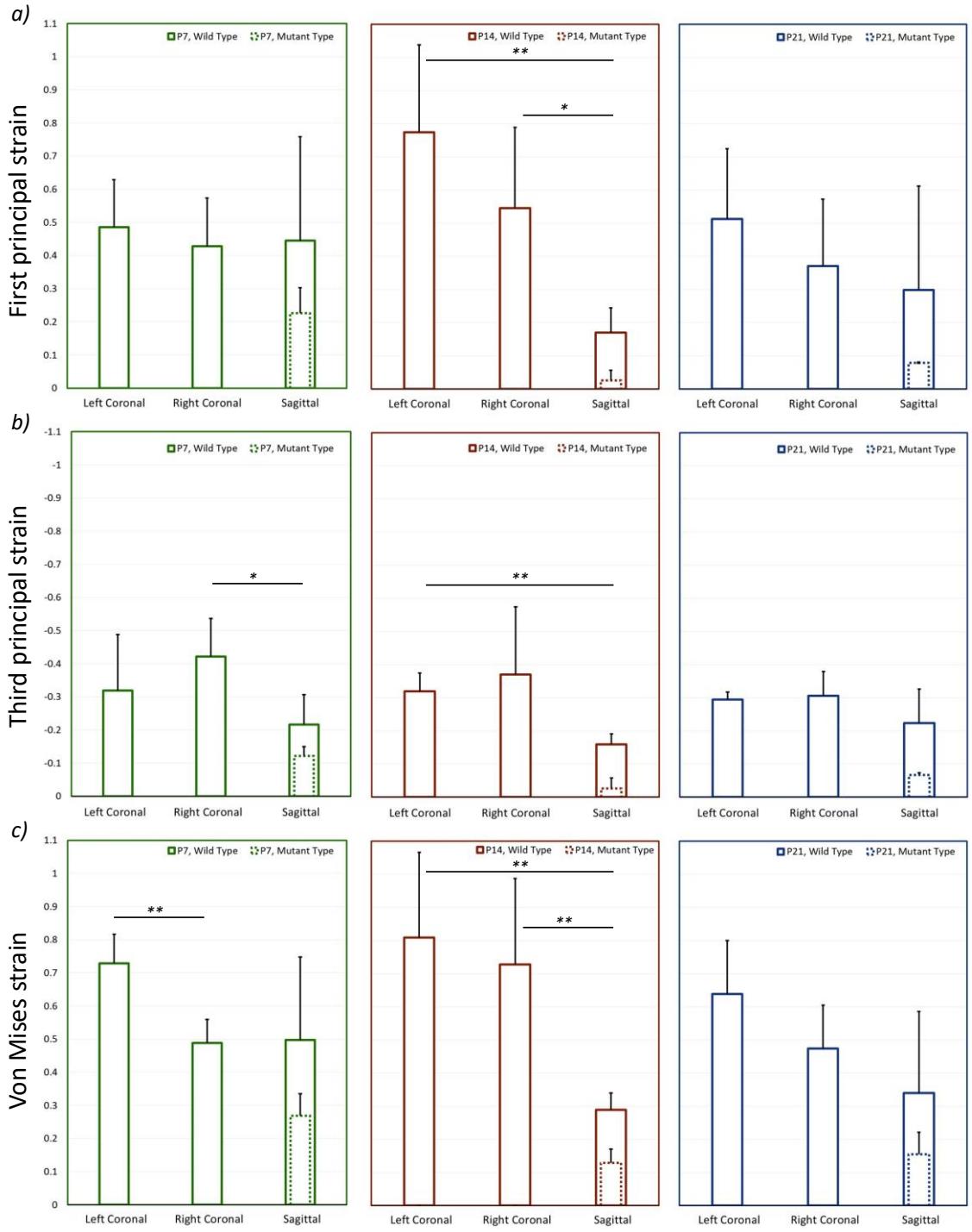

Figure 3.6 Average strain across each suture for mutant and wild-type specimens at P7, P14, and P21 during *ex vivo* static loading. a) First principal strain, b) third principal strain and c) von Mises strain. * - $p < 0.05$ and ** - $p < 0.01$.

3-4 Discussion

A previous study by Moazen et al. (2022) discovered that through the external, cyclic unilateral loading of the frontal bone in the dorsoventral direction, the early fusion of the coronal suture (unilaterally) in the Crouzon mouse (MT) could be delayed. Here, a series of *in/ex vivo* experiments were carried out to provide insight into the level of mechanical strain induced across the coronal suture in the aforementioned study. This data was crucial to optimise this approach in mice and scale it up for larger animal models in preparation for potential clinical translation to humans.

Three sets of experiments were carried out to establish the difference between the *in vivo* dynamic and *ex vivo* static loading experiments, which were eventually used to quantify the strain level across the calvarial sutures. Initially, the level of whole head movement during the in vivo experiments was quantified at P7, P14, and P21 (Figure 3.3). Given that the maximum deformation was expected to occur at P7, this age was then used to compare the effect of *in vivo* dynamic loading vs. *ex vivo* dynamic loading and *ex vivo* static loading (Figure 3.4 and Figure 3.5a). These results highlighted that the overall head displacement during the ex vivo static loading was significantly smaller than during in vivo dynamic loading. This likely occurs as the parameter is more likely to have been impacted by the dynamic vs. static nature of these experiments.

The whole head displacement for *in vivo* dynamically loaded animals is difficult to interpret. An unclear age-related pattern was observed with the displacement reducing from P7 to P14, but increasing from P14 to P21. This was not the case in the MT animals, with the whole head displacement reducing from P7 to P14 and remaining relatively stable at P21. Some of the differences may be attributed to malocclusion in the MT animals. The primary point of contact is at the incisors, with the anaesthetic tube acting as the only fixed constraint. Thus, the curved teeth of the MT animals main not permit a sufficiently constraining contact.

Similarly, the cause of the lower whole head displacement of the *ex vivo* statically loaded animals compared to their *in vivo* dynamically loaded counterparts is unclear. One possible explanation may be that the static loading does not allow for the same adjustments to be made during loading that the dynamic allows by removing the load every oscillation. Another possible explanation may be that during dynamic loading, more of the load is transferred towards moving the body. The latter is supported by a larger

increase in the coronal suture thickness after loading in the ex vivo statically loaded animals.

A larger coronal suture thickness and higher variation in this measurement were observed for the *ex vivo* static experiments as opposed to the *in vivo* dynamic loading experiments, albeit not statistically significant. This may be due to the higher loading duration in the ex vivo static experiment, i.e. 4hr to adjust for the relaxation as opposed to 10min in vivo experiments. It may also be explained by more of the force of the dynamic loading being absorbed by the body, leading to the aforementioned higher whole head displacement.

The suture thickness analysis and the comparison with an unloaded control group at P7 highlighted that: 1) a permanent deformation had occurred in the coronal suture as a result of 10min in *vivo* dynamic loading; 2) the level of mechanical strain induced at the coronal sutures during the *in vivo* loading was likely at least 0.51 ± 0.10 based on the permanent mean thickness increase across the coronal suture after the loading observed in data presented in Figure 3.4b; 3) *ex vivo* static loading experiments may overestimate the level of minimum mechanical strain induced across the coronal suture during dynamic loading. A higher estimated strain of at least 0.70 ± 0.10 based on the mean increase in thickness across the coronal suture was observed (Figure 3.4b).

The *ex vivo* and *in vivo* dynamically loaded animals showed a comparable increase in the coronal suture thickness with no statistically significant differences. Consequently, the increase in the suture thickness cannot be a biological response of the suture to the loads instead. The sutures are likely experiencing plastic deformation. This suggests that the increase in suture thickness during the loading is at least equal to the lasting increase if not higher. Thus, the minimum strain estimations presented here were obtained by comparing the coronal suture thickness after loading to the control (not loaded) coronal suture thickness. Even with the higher increase in the coronal suture thickness observed, the differences between *ex vivo* static and *in vivo* dynamic loading coronal suture thicknesses are not statistically significant. The *ex vivo* static loading strain estimated in this work is likely a good approximation of the strains experienced during *in vivo* dynamic loading.

Ex vivo strain analysis based on the CT data and the custom code developed in this study provided a full 3D strain analysis of the strain level across the coronal suture at P7 in WT. The estimations aligned with the excepted ranges based on the 2D suture thickness analysis. The 3D analysis also provided an overview of the impact of loading across all

calvarial sutures. This provides a more holistic understanding of the impact of the loading across all calvarial sutures in 3D. For example, it highlights that unilateral loading of the frontal bone also induced a relatively high level of strain in the contralateral coronal sutures (e.g. 0.73 ± 0.08 vs. 0.49 ± 0.07 von Mises strain at P7– Figure 3.6c). This can explain the observation of bilateral coronal suture patency in some of the MT mice in the study of Moazen et al. (2022). Nonetheless, given that the coronal sutures were at least partially fused at P7, it was not possible to estimate the level of strain induced at the coronal suture in the MT mice at any of the investigated ages. This suture likely experiences a significantly lower level of strain as opposed to the WT mice at the same age, in line with the finding of a lower level of strain in the sagittal suture in the MT compared to the WT at all considered ages. The fused parts of the suture limit the relative movement between the frontal and parietal bones, contributing to the reduction in strain.

A significant decrease in the sagittal suture strain was observed between the P7 and P14 specimens in WT and MT animals. This may be because the metopic suture is patent at P7 but closed at P14. This couples the displacement of the frontal bones and, in turn, restricts relative displacement between the two parietal bones. The effect is likely magnified in the MT as, in addition to the metopic, the coronal sutures undergo fusion (Perlyn et al. 2006; Martínez-Abadías et al. 2013; Liu et al. 2013) leading to further limitations in the relative displacement between the two parietal sides. Concurrently, the patent coronal sutures in the WT likely permit increased relative displacement of the two parietal bones leading to a higher sagittal strain compared to the MT at P14. Note, lower average von Mises and first principal strains were observed in the sagittal suture than in either of the coronal sutures at P14, which was statistically significant (see Figure 3.6).

There remains a question regarding the level of strain experienced by the coronal suture in the MT mice. This requires further investigation, and computational models based on the finite element method can be a powerful tool. These models can be used to virtually segment this suture and estimate the level of strain experienced by it in the MT mice. Indeed, the data obtained in this study set a strong foundation for future validation of such studies. Our understanding of this structure's mechanical response to external loading is currently limited.

A potential explanation for the therapeutic effect observed by Moazen et al. (2022) may be that the consecutive cyclic loading disarticulates (mechanically separates) the frontal and parietal bones as they undergo fusion. The newly formed bone in the sutural space may be a mechanical weak point of the system, and continuous application of force may

prevent fusion from progressing. While this was not observed directly during static loading, the hypothesis is strengthened by the observed permanent change in the gap between the frontal and parietal bones observed after cyclic loading in P7 WT mice. Further examination of the coronal suture structure for the fully treated animals is required to understand the underlying mechanism.

Translation to larger animal models of the Moazen et al. (2022) treatment regime is an important step towards establishing the technique as a treatment option for human patients. The strain values estimated will help establish the level of loading required in larger animals. Equally important may be translation to other mice models or other suture fusion in the same model establishing the generalisability of the treatment as an option for craniosynostosis conditions. However, while the work here may present potential strain values to be matched, the strain across other sutures when the loading targets them remains unknown.

Limitations

Significant limitations are present in this chapter. Perhaps the greatest of which is 1) lack of direct investigation of the deformation of the MT coronal sutures under external loads, as this is the group with therapeutic effects observed in Moazen et al. (2022) because it is unclear how the investigated WT strains relate to the MT strains. Additional limitations include 2) P14 and P21 MT animals that underwent the dynamic loading treatment regime were not included in these investigations. Thus, the effects of treatment on the response to external loading were not investigated here. 3) The developed methodology for strain estimation fails to accurately estimate the bone strain during loading. While not the focus of the chapter, investigation of the bone strain could provide additional details on the response to external loading. 4) The static loading appeared to be an appropriate proxy for dynamic loading based on the persistent deformation of the suture observed. However, this only confirms that the minimum strain for the two loadings agrees; a possibility of significantly higher strains existing during dynamic loading remains open and difficult to directly observe. 5) The significant differences in loading durations between *in vivo* dynamic loading and *ex vivo* static loading potentially introduce further unaccounted differences between the two loading regimes and thus possible suture patency results.

3-5 Summary

In summary, this chapter provided insight into the level of displacement and mechanical strain induced during and after both *in vivo* and *ex vivo* dynamic loading, as well as *ex vivo* static loading.

As the first work chapter of this thesis, it establishes previously unknown values of suture strain during external loading, shown to have a positive effect on suture patency in Moazen et al. (2022). The chapter also highlights the efficacy of *ex vivo* static loading as a proxy for *in vivo* dynamic loading in terms of suture strain results. Levels of strain across the coronal sutures observed in this chapter are orders of magnitude higher than the FE predicted values in Moazen et al. (2022). Additionally, considering the loading one of the critical findings is the presence of plastic deformation after both the dynamic and static loadings, potentially indicating previously unconsidered mechanical means of suture patency retention.

These values are used in the larger CranioMech project to estimate the required loading levels in pig investigations. Simultaneously, the work established a validated data set for future *in silico* models and highlighted issues in MT strain estimation, which are both further investigated in **Chapter 4**. The methodology set out in this chapter for suture strain characterisation is expanded to other sutures enabled by BounTI (Appendix II) and employed in the following chapter.

Chapter 4 Characterisation of regional variability of the craniofacial stiffness and loading response

4-1 Introduction

This chapter largely focuses on the directions set out in **Chapter 3**. It investigated the location-specific responses of various sutures across the calvaria, the response of MT animals to external loads, and the efficacy and predictive power of *in silico* models. Establishing the variation in loading response as it relates to the loading location is critical for translation of the developed treatment approach to other mouse models, where other sutures may be affect and require loading. Accurate computational models could enable further optimisation of the treatment approach as well as predict the required levels of load to induce similar in other sutures.

Aim: Quantify the response of the mouse craniofacial system to external loading with varied anatomical loading locations experimentally and to compare the experimental results to fully disarticulated computational models.

Objectives: Establish the overall deformation of the skull, the deformation in the coronal suture in both WT and MT at P7, suture strains in WT mice at P7, P14 and P21 and finally test the predictive capabilities of computational models against the quantified experimental results.

4-2 Materials and methods

The experimental data for the three objectives was obtained through a series of *ex vivo in situ* experiments comparable to the ones carried out in **Chapter 3** on wild type and Crouzon $Fgfr2^{C342Y/+}$ mice at P7, P14, and P21. In addition to the loading of the frontal bone, three additional loading locations were considered: the anterior part of the parietal bone, the posterior part of the parietal bone, and the interparietal bone. The loadings were

carried out a tip diameter (1mm) away from the midline on the left side of the skull. The animal and load positioning methodology remained consistent with **Chapter 3**, as the chapter exclusively considered *ex vivo* static loading, all positioning was done considering the radiography images. The computational models for objective (4) were developed based on the CT data of the unloaded frontal bone loading WT mice at each of the investigated ages. A graphical outline of this work is presented in Figure 4.1.

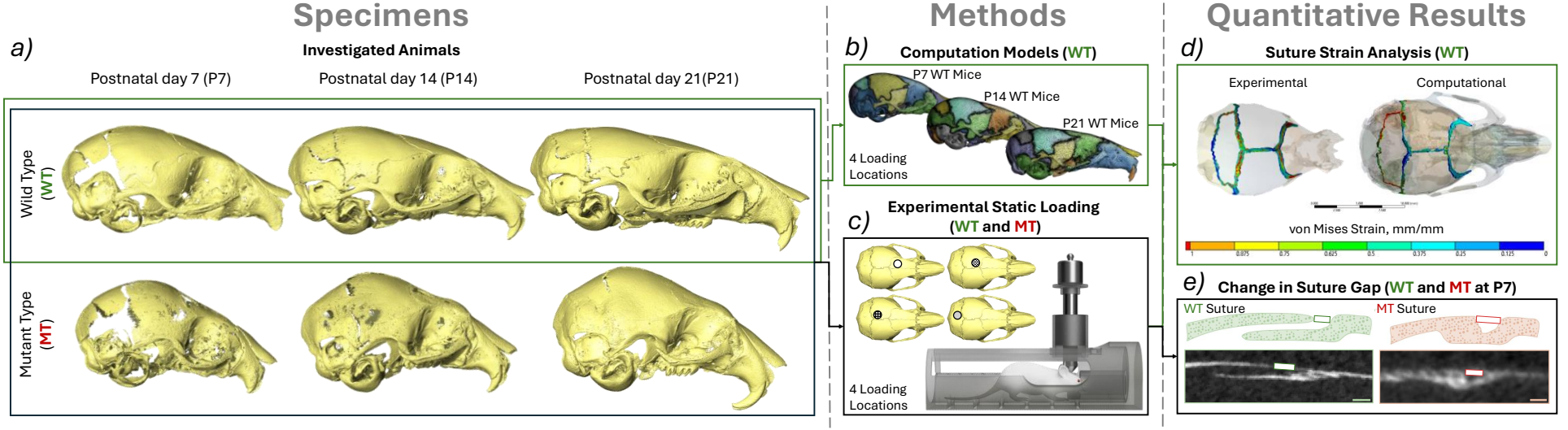

Figure 4.1 An overview of the overall workflow of this study. a) Investigated animals – P7(WT n=4, MT n=4), P14(WT n=4, MT n=4) and P21(WT n=4, MT n=4), b) computational models of WT animals developed from the unloaded scans of the frontal loading at P7, P14 and P21 investigated at 4 different loading locations (frontal bone, anterior part of the parietal bone, posterior part of the parietal bone and interparietal bone), c) Experimental static loading of both MT and WT animals at P7, P14 and P21 investigated at 4 different loading locations, d) Suture strain analysis of the experimentally loaded animals and comparison to the computational model results and e) Linear measurements of the coronal suture gap in both MT and WT animals at P7 comparing the loaded and unloaded states across 200 slices of the straight region of the suture.

4-2-1 Specimens

Mutant- and wild-type mice were investigated; for the former, the $Fgfr2^{C342Y/+}$ Crouzon mouse model was used, which were derived by the European Mouse Mutant Archive (EMMA) at MRC Harwell, as described by Peskett et al. (2017). *Ex vivo* studies were carried out on fresh, refrigerated (4°C) cadavers, i.e. the analyses were carried out within four days of the animals being culled.

In total, 24 cadavers were investigated in this work (4 P7 WT, 4 P7 MT, 4 P14 WT, 4 P14 MT, 4 P21 WT and 4 P21 MT) with one animal used per different type, different age, and different loading location. The low number of animals was justified by the large differences observed in the mechanical response to different loading locations. Additionally, the variation in the strain results was already established in **Chapter 3**. In the interest of reducing the number of animals sacrificed, it was deemed that an increased number of animals was not required (in line with the principles of 3Rs). However, the low number of animals included in this study represents a limitation of this work.

Note: all animal experiments were approved by the UK Home Office and performed as part of a Project License (number: PP8161503) under the UK Animals (Scientific Procedures) Act 1986. Animal procedures complied with the ARRIVE guidelines and were performed under the supervision of UCL Biological Services.

4-2-2 Loading setup

Static loading was carried out following the previous chapter, that originally mimicked the dynamic loading setup from Moazen et al. (2022). The animals were placed in a simplified anaesthetic tube with the same contact point preserved as in the *in vivo* loading. A 10g (0.1N) weight was then placed on the plunger attached to a 1mm diameter tip freely positioned across the skull. The loading was carried out in a micro-CT scanner (XT H 225ST, Nikon, Herts., UK) and the specimens were scanned before and during the loading. All the CT scans were taken at 90 kV for 2 hours with a voxel size of 9.5 µm. Each animal was only used for one loading.

Initially, a load relaxation test was carried out which identified 120 minutes as the required time for the relaxation (Appendix I-A1.1). However, during the development of this investigation, the significantly larger deformation of the other loading locations led

to a significantly longer relaxation period. At P7, 12 Hours were required for the specimen to fully relax under the load, at P14, 4 hours, and at P21, the original 2 hours were sufficient. While the relaxation times were different, it should be noted that past this time no deformation occurred; for example, the frontal P7 loading deformation remained the same after 12 hours as it was after 2 hours. Thus, all the animals were scanned at the same state of cessation of deformation under a 0.1 N load.

4-2-3 Computational models

The computational models were developed using a novel rapid development workflow presented in Figure 4.2. The unloaded scans of the frontal bone loading WT cases were used for the generation of the computational models. A novel automated segmentation tool BounTI (Appendix II) was used to obtain the fully disarticulated segmentation of the craniofacial system (Figure 4.2b) for the three specimens. With all the specimens scanned using the same parameters, the same BounTI parameters were used to produce the segmentations (number of segments – 51, number of iterations – 100, initial threshold – 19000, target threshold – 17000).

To generate the sutures the disarticulated segmentation was expanded 5 voxels where most of the bones were in full contact with the adjacent bones. Expansion of 5 voxels produced the best results as it ensured the contact of all the bones, but did not over expand the bones. The contact voxels were assigned to sutures. These suture segments were expanded by 5 voxels and imported to the disarticulated segmentation. A series of smoothing and expansion only on the suture segments were carried out (smoothing of 9 voxels, expansion of 1 voxel, smoothing 9 voxels) until the suture segmentation followed the shape of the skull smoothly and did not extrude over the bone while at the same time capturing the full depth of the suture (Figure 4.2c).

The disarticulated segmentation was then converted to a tessellated mesh. Smoothing of 3 voxels was applied in Avizo (Thermo Fisher Scientific, MA, USA) and the mesh was reduced to 500000 surface triangles. Using Icex (Buzi et al. 2023), an R package for the extraction of endocast, the intracranial volume was extracted based on the surface mesh of the skull (Figure 4.2d). The intracranial volume mesh was then converted to segmentation and combined with the disarticulated segmentation of the skull. Additionally, the intracranial volume surface was non-rigidly aligned to the outside surface of the skull. This was used to generate the covers at the larger gaps in the skull

such as the foramen magnum, which were later assigned the same material properties as the sutures.

Lastly, the combined segmentation was again smoothed with the extent of 3 voxels in Avizo and the generated surface mesh was reduced to 500000 surface mesh and remeshed with a high regularity objective (vertex valence option of 3 passes and triangle quality option of 30 passes). The process was identical to the generation of bone surfaces for strain estimation with the only differences of inclusion of the intracranial volume and more bones (only the frontal, parietal, interparietal, and lambdoid bones were included for the strain estimation). The generated surfaces were imported to ANSYS SpaceClaim (ANSYS Inc., Canonsburg, PA, USA), where they were converted to parametric bodies and a tetrahedral mesh was generated in the mesh module (Figure 4.2e). The meshing parameters were again identical to those for the strain analysis originally established in Chapter 3. Adaptive size function was used for the mesh with the maximum set to 0.2 mm resulting in the average element size in the bone of 0.1 mm and 0.03 mm for the sutures. This represented at least 2 elements over the thickness of the bone and at least 3 elements over the bone-to-bone direction of the sutures.

The models were then displacement-constrained at the maxillary incisors i.e. contact with the anaesthetic tube and basioccipital bone where most posterior ventral nodes were fixed in all degrees of freedom. Preliminary test were carried out with varied boundary conditions, specifically, the number of nodes constrained (all dorsal bone surfaces at the foramen magnum) and constraint axes were varied, all producing <5% changes in the suture strain predictions. The forces were applied on a 1 mm diameter disc of nodes in locations corresponding to the experiments on the frontal, parietal (anterior and posterior regions), and interparietal bones in the dorsoventral direction (see Figure 4.1c for the loading locations).

All material properties investigated were elastic isotropic and a consistent Poisson's ratio of 0.3 was used. The Young's modulus was varied for the different scenarios investigated. For the brain value, 150 MPa (Marghoub et al., 2019) and 3 Pa (assuming no contribution of the brain) were used, for the suture's values of 30 MPa (Moazen et al, 2015) and 30 KPa (optimised for similarity in maximum deformation during frontal bone loading at P7) were used, and the values for bone ranged from 10 MPa to 7000 MPa. The reasoning behind the investigation of these specific values is detailed in the following section of the methodology i.e. 4-2-4 . A significant limitation of this work is the use of linear isotropic elastic material properties for all of the constituent parts of the model; however, no other

values were available in the literature, especially for the early developmental time points investigated here. This limitation is extensively discussed later on.

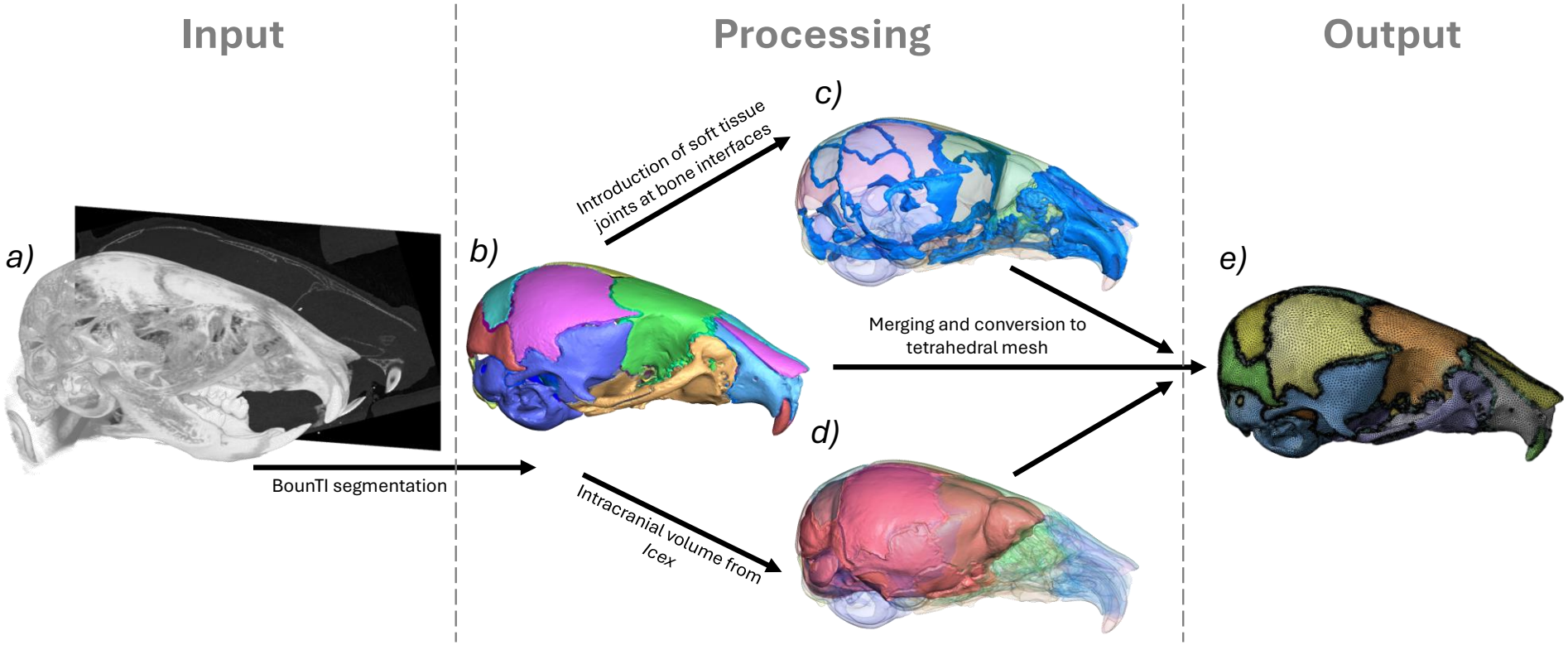

Figure 4.2 Rapid computational model development methodology. a) CT data (P7, P14, P21 WT), b) fully disarticulated segmentation of the craniofacial system using BounTI (Didziokas et al. 2024), c) generated soft tissue joints from the contacts regions of the separated bone, d) extracted intracranial volume using Icex (Buzi et al. 2023) and e) combined and tetrahedrally meshed model.

4-2-4 Analyses

Coronal suture gap (P7 WT and MT): To understand the impact of the external location varied loading on the coronal suture, the coronal suture gap between the frontal and parietal bones was measured using the micro-CT data. The gap was measured instead of the previously laid out suture thickness measurements in **Chapter 3** to allow comparison between MT and WT animals, which was not available in the previous chapter. The measurements were taken every 10 slices over 200 slices (in the mediolateral plane) with only the straight part of the coronal suture included on each side (i.e. left and right coronal suture). The measurement was taken from the dorsal edge of the frontal bone to the dorsal edge of the parietal bone (Figure 4.1e). The analysis was carried out for WT and MT animals of the four investigated loading conditions at P7. The MT measurements were only taken where the gap was present, the slices that had full fusion (no discernible gap visible, effectively 0mm gap) were not included. The unloaded and loaded states of the same animal were compared. Note: the voxel size was 9.5 μm, and the measurements ranged from 9 to 19 times the voxel size for the unloaded WT, and from 4 to 9 times for the unloaded MT.

Mechanical strain across the sutures (P7, P14, and P21 WT): To quantify the level of mechanical strain induced across the calvarial sutures due to varied loading locations, the methodology developed and validated in **Chapter 3** for strain analysis was used. In brief, the unloaded bone surfaces were aligned to the loaded bone surfaces from which the strain in the sutures was estimated. The only departure from the previously developed methodology was the use of a non-rigid deformation algorithm by (Li and Harada 2022) known as the neural deformation pyramid instead of the previously proposed element-based rigid alignment. This was changed as the bone experienced significantly higher local deformations during the more parietal loading conditions than the frontal bone loading originally investigated. Additionally, with the development of an automatic segmentation tool BounTI, it was now possible to carry out the same analysis but include more sutures. Thus, while originally only the coronal and sagittal sutures were included, here the strain investigation was expanded to include interparietal as well as the lambdoid sutures. This methodology enabled estimation of the mechanical strain across the

individual sutures (in response to external loading on the skull bones) for which the von Mises as well as 1st and 3rd principal strains were recorded.

Comparison of computational and experimental strain across the sutures (P7, P14 and P21 WT): To investigate the sensitivity and validity of the computational models, their results were compared with the experimental data considering the choice of key input parameters to the models. Here, three different conditions were investigated for the brain and suture material properties. Originally Young's moduli of 150 MPa and 30 MPa for brain and suture, respectively were used in line with the computational study carried out by Marghoub et al. (2019). However, the physical phenomena estimated in the previous study were different to the external loading considered here. Thus, the high brain Young's modulus was deemed inappropriate. Previously, 10 MPa value was used by Moazen et al. (2022); however, the literature suggests that the linear elastic material model may be unreliable, especially at large deformations as observed here (Kaster et al. 2011; Mihai et al. 2015; MacManus et al. 2016; Voyiadjis and Samadi-Dooki 2018). Thus, instead of optimising various coefficients for a hyperelastic model, it was decided to discount the brain contribution entirely using a linear elastic isotropic model with Young's modulus of 3 Pa, a value significantly closer to the measured 60 Pa value by (Koser et al. 2018). The effect of suture Young's modulus was investigated and 30 KPa (as opposed to 30 MPa) was found to produce overall directional displacement of all the bones individually closest to the experimental results at P7 with the adjusted brain modulus. Values used for the bone were: 3500 MPa, 5100 MPa, and 6700 MPa for P7, P14, and P21, respectively, as estimated from Moazen et al. (2015). The three cases described here were then compared to the experimental results at the 4 different loading locations for the 3 different ages in WT animals.

Bone Young's modulus optimisation (P7 WT optimisation and P7, P14, and P21 comparison): To investigate the effect of the bone material properties that were left unaltered in the previous comparison, additional analysis was carried out. Here, the bone Young's modulus was adjusted from 10 MPa to 7000 MPa for the P7 case (3500 MPa used in the previous investigation). All the loading locations were investigated and the magnitude of the percentage difference in average strain across the suture was recorded for each investigated suture individually and all the sutures together. The optimal value for most cases was then investigated following the same comparison from the previous investigation for all the considered ages.

4-2-5 Statistical analysis

Statistical analysis was performed in SPSS (IBM SPSS, NY, USA). One-way analysis of variance (ANOVA), with Levene's test was used to test for equal variances. The significance level was set at $p<0.05$.

4-3 Results

4-3-1 Qualitative loading comparison (P7, P14, and P21 - MT and WT)

The reconstructed loaded skulls, including the loading tip are shown in Figure 4.3 for WT and Figure 4.4 for MT animals. Firstly, for both the mutant- and wild-type animals the overall deformation of the skull during the frontal bone loading appeared to be the mildest compared to the other 3 investigated locations at P7. Additionally, the level of deformation seemed to increase the more posteriorly the skull was loaded. In general, the overall deformation of the skull across all considered locations decreased with age. However, this was more pronounced in the mutant animals where P7 animals experienced extreme levels of deformation but P14 remained relatively undeformed under the 10g load. This was not the case in the WT animals where large deformations were still present at P14. For both WT and MT animals, the deformation was significantly lower at P21.

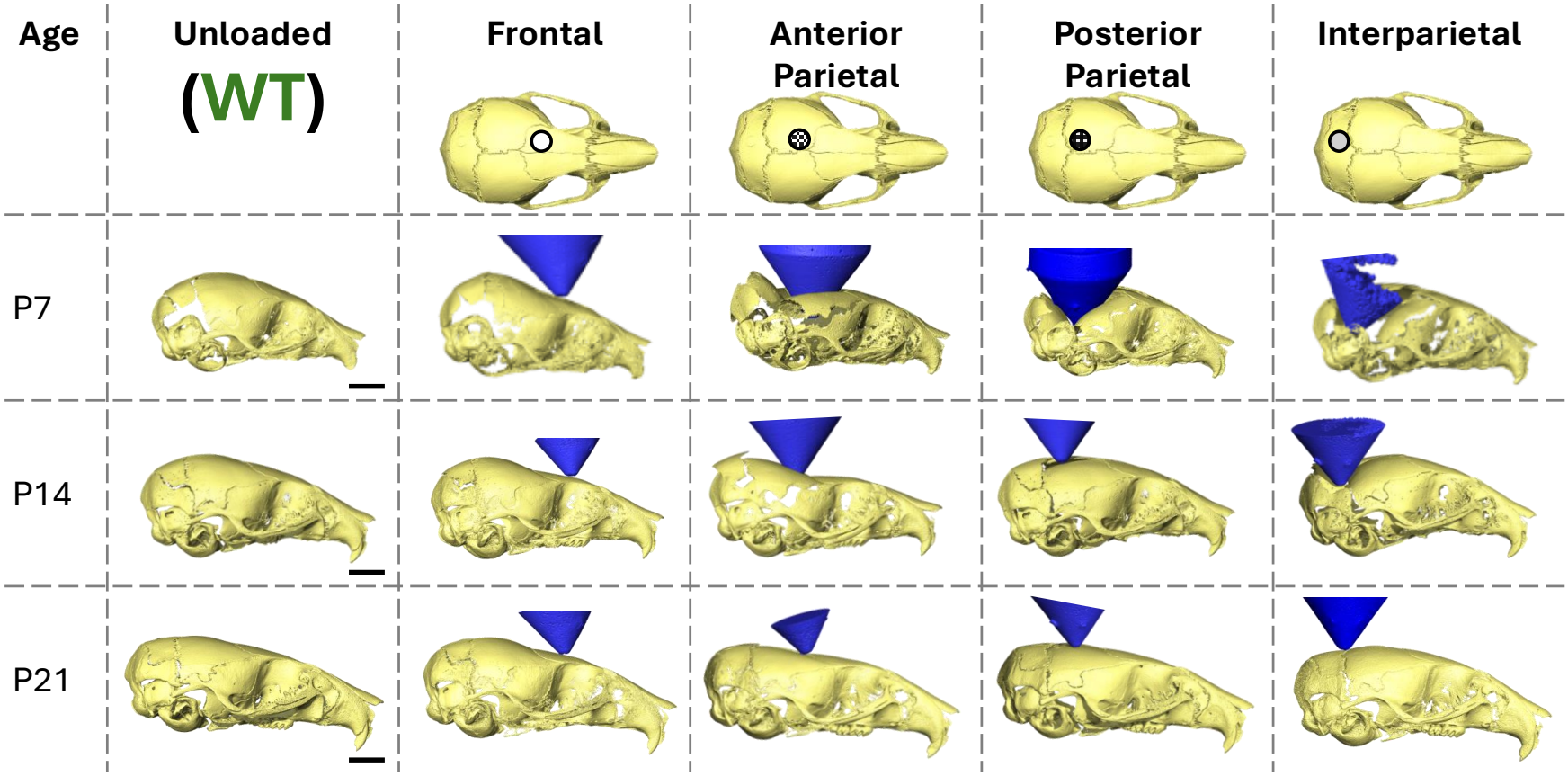

Figure 4.3 Reconstructions of deformed skull shapes of each investigated individual at 3 different ages (P7, P14 and P21) at 4 different loading locations (frontal bone, anterior part of the parietal bone, posterior part of the parietal bone, and interparietal bone) and the loading tip (blue cone) in wild type animals.

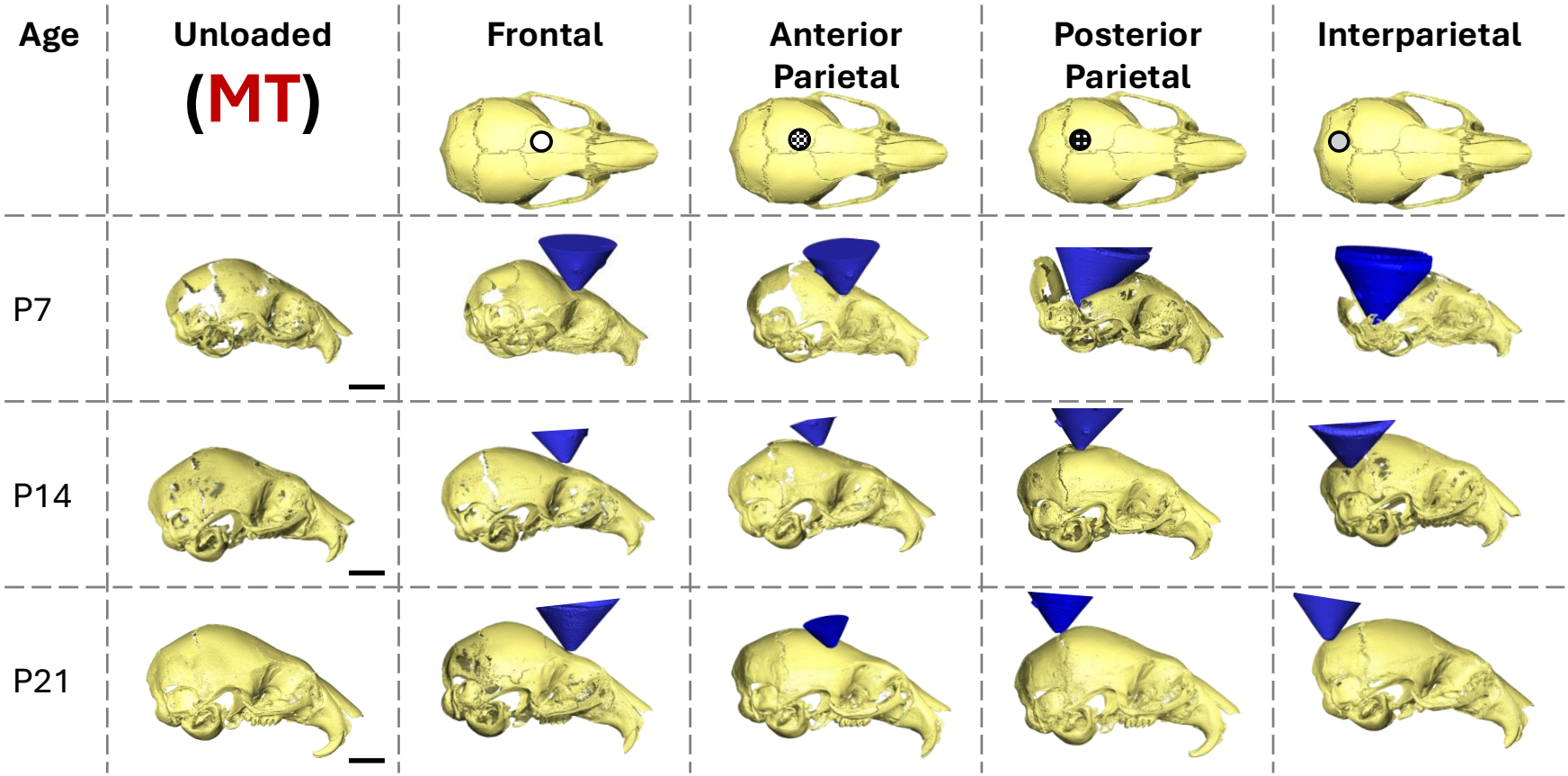

Figure 4.4 Reconstructions of deformed skull shapes of each investigated individual at 3 different ages (P7, P14 and P21) at 4 different loading locations (frontal bone, anterior part of the parietal bone, posterior part of the parietal bone, and interparietal bone) and the loading tip (blue cone) in mutant type animals.

4-3-2 Coronal suture gap (P7 – WT and MT)

The coronal suture gap was measured for all the loadings at P7 for both WT and MT animals comparing the unloaded and loaded states (Figure 4.5b). Both quantitative results as well as representative qualitative sketches of the deformed results are presented in Figure 4.5. The data gathered highlighted that:

1) The increase in the coronal suture gap from the unloaded state to the loaded state was statistically significant in all but one investigated case, the frontal bone loading, right coronal suture for WT animals. Conversely, for the MT animals, the only statistically significant change was a decrease in the gap distance for the interparietal bone loaded animal on the loaded (left) side coronal suture with no statistically significant difference for all the other sutures in all the other loadings.

2) The average increases for the WT animals for the left and right coronal sutures respectively were 0.33 ($p<0.01$) and 0, 1.89 ($p<0.001$) and 1.93 ($p<0.001$) , 1.76 ($p<0.001$) and 4.37 ($p<0.001$) and 2.13 ($p<0.001$) and 1.77 ($p<0.001$) times the original length for for the frontal, anterior parietal, posterior parietal and the interparietal bone loadings respectively. In the MT animals, the only statistically significant change was a 0.22 ($p<0.05$) times decrease of the original length for the left coronal suture in the interparietal bone loading case.

3) Qualitative differences were observed between the deformed suture gaps in the WT animals when the 4 different loading locations were compared. The coronal suture gap measured appeared to remain consistent for the frontal bone loading animal however the gap at the posterior edges of the suture widened. During the anterior parietal loading, the suture thickness remained constant, but the parietal bone moved posteriorly widening the measured gap length. During both posterior parietal and interparietal loading, the parietal bone appeared to move posteriorly widening the gap and the overall thickness of the suture increased with the parietal bone edge moving dorsally.

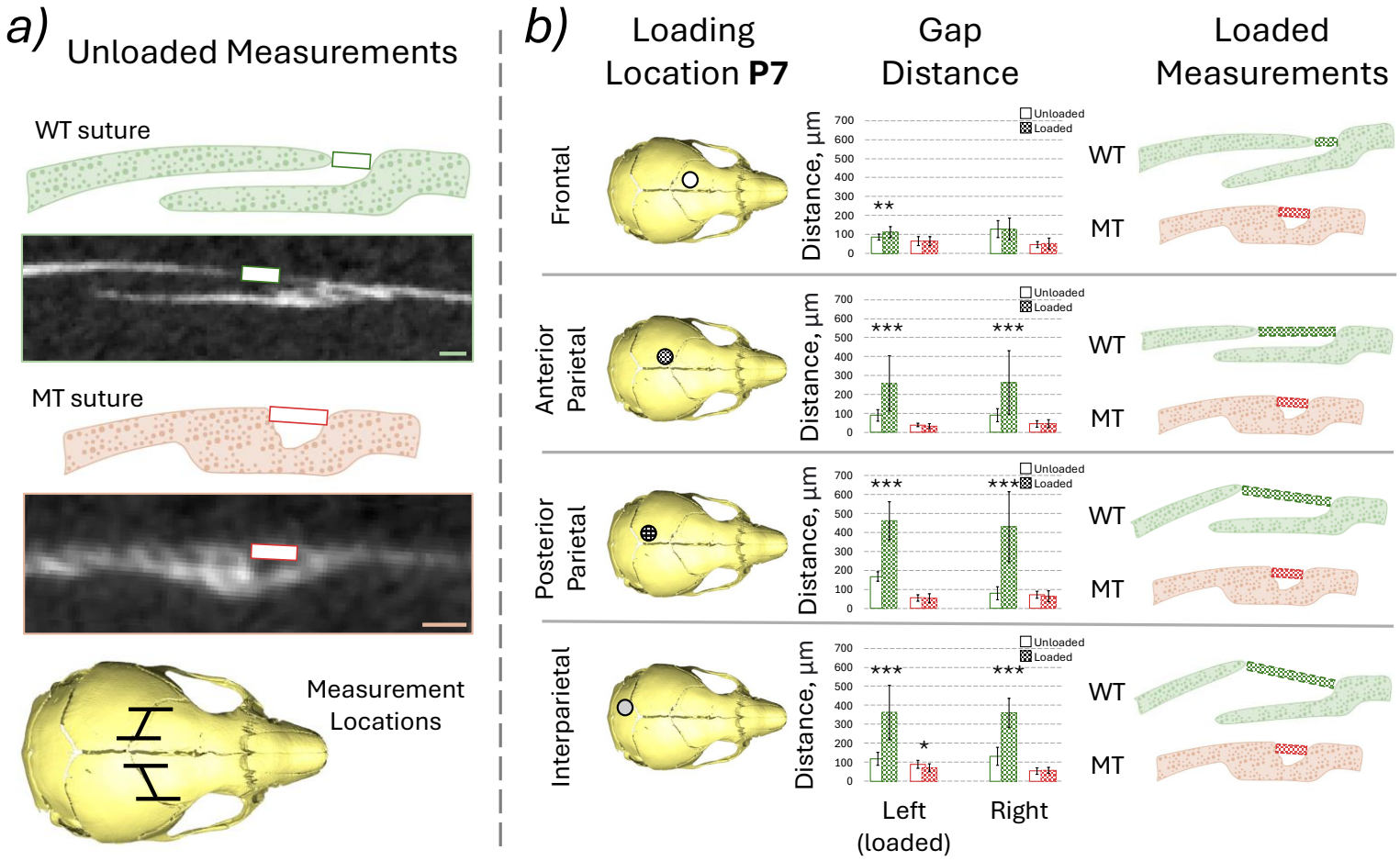

Figure 4.5 a) Measured distance and the region measured, 20 slices were investigated in each case every 10 slices of the 200 slices across the straight region of the suture at P7 for both WT and MT animals. Voxel size = 9.5µm and b) Highlighted loading locations, measured gap distance, green – WT, red – MT, empty box – unloaded and hashed box – loaded, qualitative representation of the deformation at the suture observed. *, ** and *** mark differences between the states at $p < 0.05$, $p < 0.01$ and $p < 0.001$, respectively.

4-3-3 Mechanical strain across the sutures (P7, P14 and P21 – WT)

The von Mises strain across the investigated sutures (coronal left, coronal right, sagittal, interparietal left, interparietal right, and lambdoid, see Figure 4.6c) as well as the average strain across all the investigated sutures, are presented in Figure 4.6. Complementary figures with 1st and 3rd principal strain results are included in Figure 4.7 and Figure 4.8. Overall, this data highlighted that:

1) The strain across the coronal sutures was higher in all the investigated loading conditions compared to the frontal loading at all ages. Higher strains were observed in the loaded side sutures (left) compared to the unloaded side for both coronal and interparietal sutures. This pattern was present across all ages and in all loading conditions.

2) At P7, the sagittal, interparietal, and lambdoid sutures exhibited higher strains than the coronal sutures. At P14 only, the interparietal left (loaded side) and the lambdoid suture showed increased strain. At P21, no prominent increase in strain was observed in the other sutures compared to the coronal suture.

3) The average strain across all the investigated sutures decreased with age in all the loading conditions see Figure 4.6b. However, while at P21 the strains were comparable for all 4 investigated loading locations at P7 and P14 the strains were markedly higher in the anterior parietal, posterior parietal and interparietal bone loadings compared to frontal bone loading. Similar trends were observed for both 1st and 3rd principal strains in Figure 4.7 and Figure 4.8.

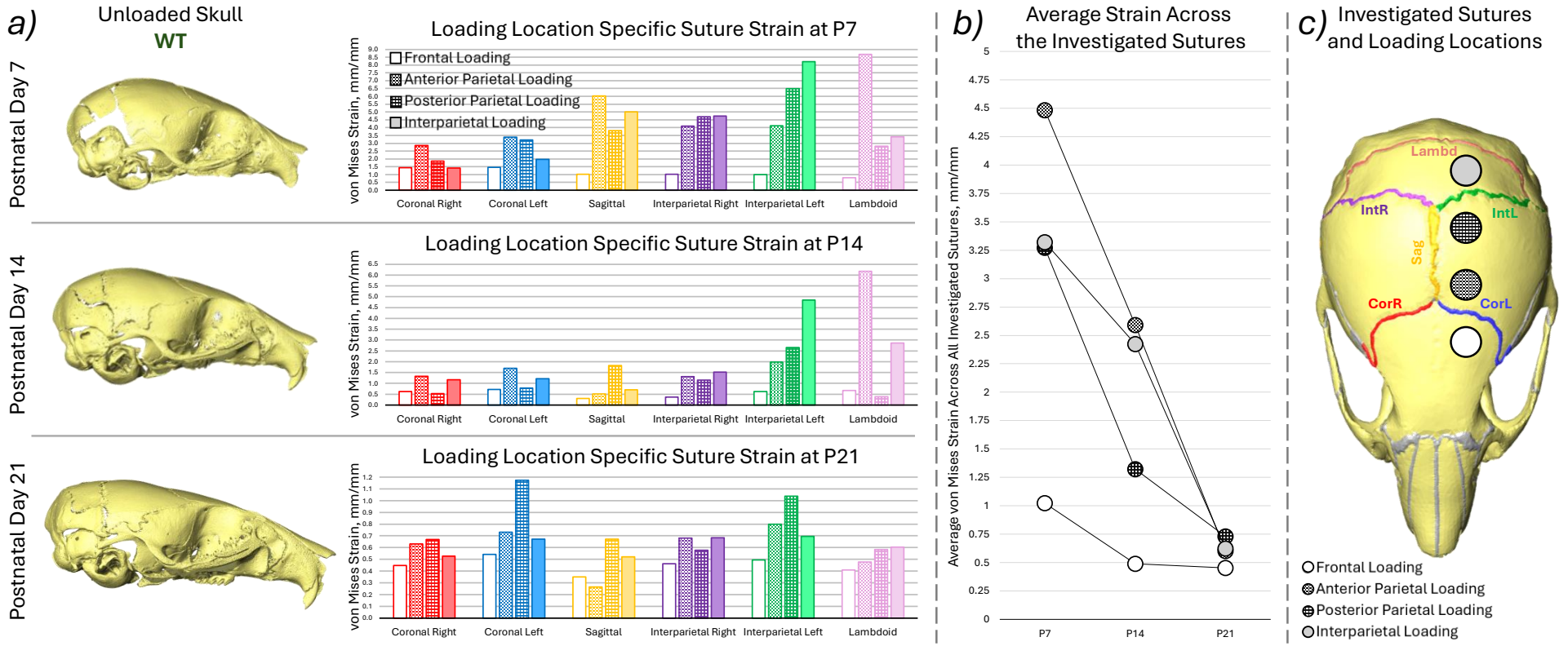

Figure 4.6 a) Representative unloaded skull shapes at the three investigated ages (P7, P14, and P21) for WT animals, average von Mises suture strain results for each investigated suture for the 4 different loading conditions (empty box – frontal bone, hashed box – anterior part of the parietal bone, dotted box – posterior part of the parietal bone and solid filled box – interparietal bone), b) average von Mises strain across all of the investigated sutures compared with age for the 4 different loading conditions and c) highlighted investigated sutures and the approximate loading locations.

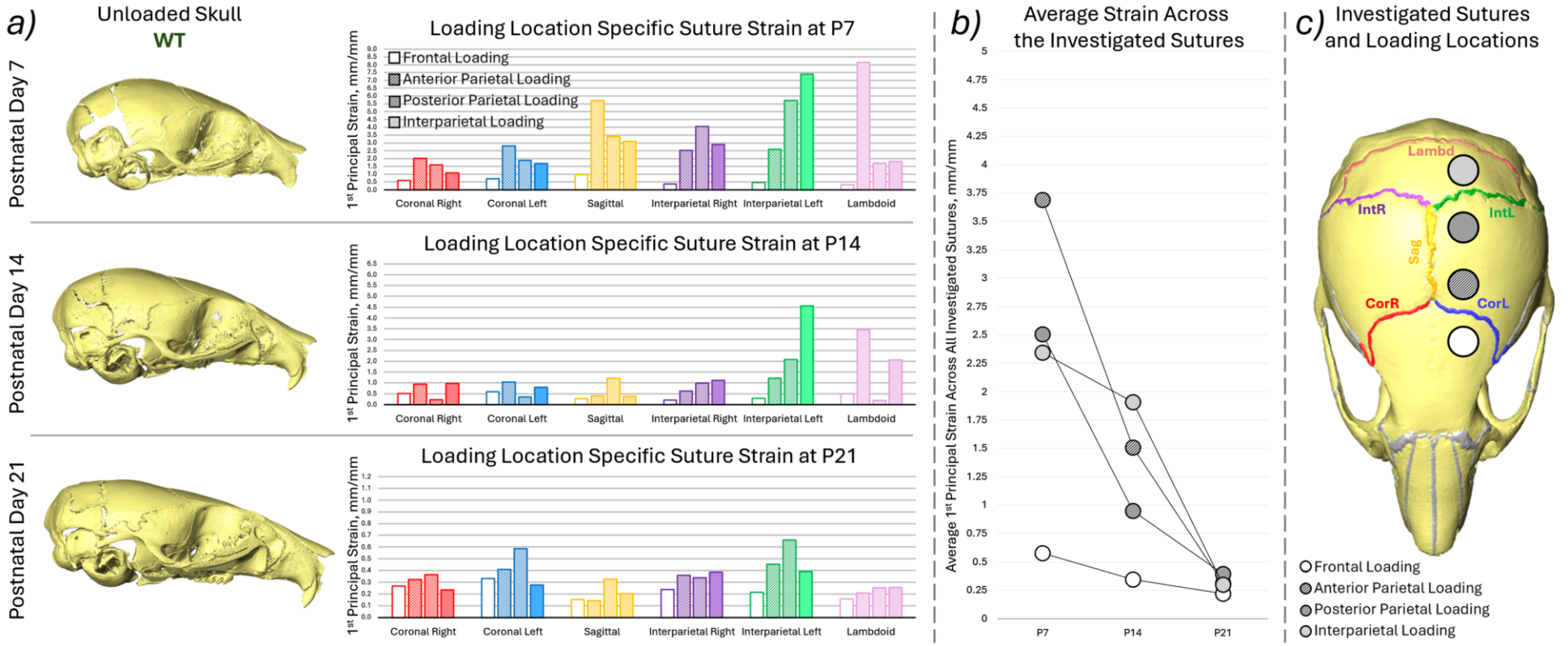

Figure 4.7 a) Representative unloaded skull shapes at the three investigated ages (P7, P14, and P21) for WT animals, average 1st principal suture strain results for each investigated suture for the 4 different loading conditions (empty box – frontal bone, hashed box – anterior part of the parietal bone, dotted box – posterior part of the parietal bone and solid filled box – interparietal bone), b) average 1st principal strain across all of the investigated sutures compared with age for the 4 different loading conditions and c) highlighted investigated sutures and the approximate loading locations.

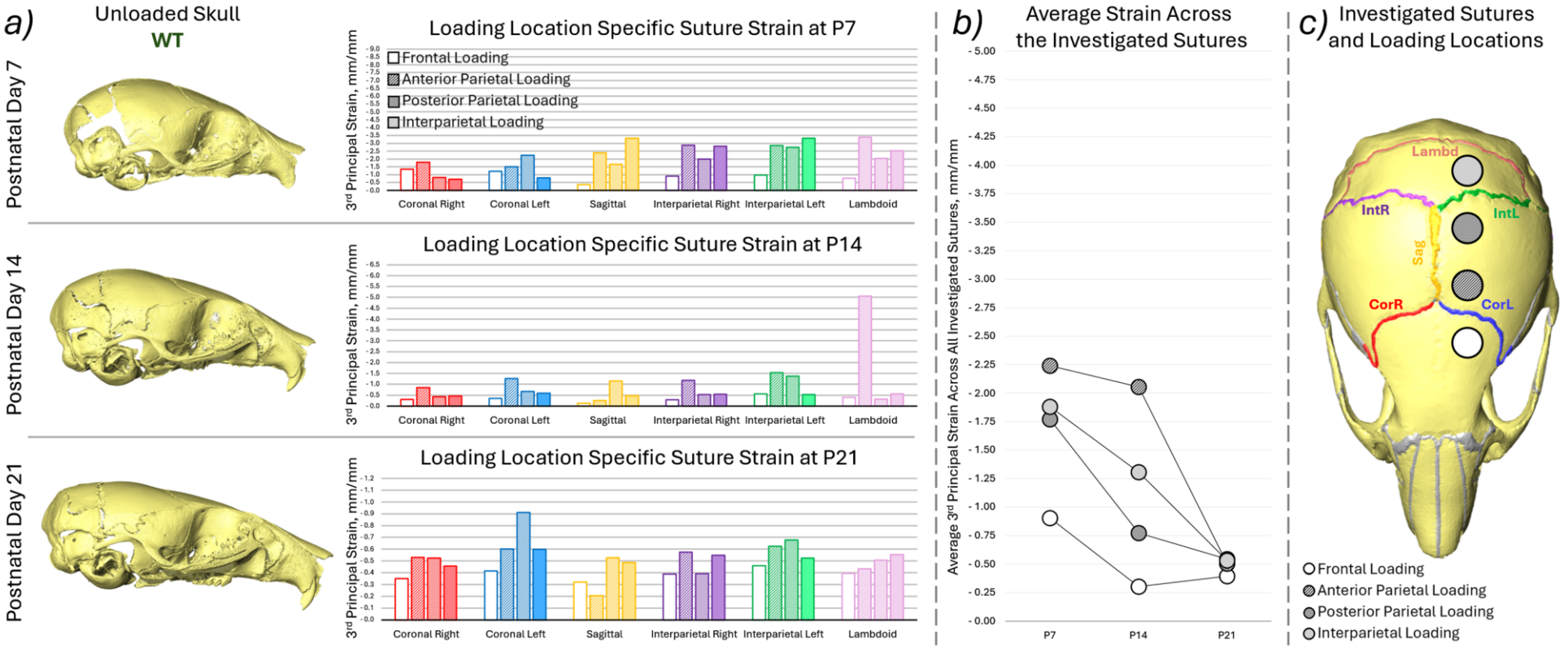

Figure 4.8 a) Representative unloaded skull shapes at the three investigated ages (P7, P14, and P21) for WT animals, average 3rd principal suture strain results for each investigated suture for the 4 different loading conditions (empty box – frontal bone, hashed box – anterior part of the parietal bone, dotted box – posterior part of the parietal bone and solid filled box – interparietal bone), b) average 3rd principal strain across all of the investigated sutures compared with age for the 4 different loading conditions and c) highlighted investigated sutures and the approximate loading locations.

4-3-4 Comparison of computational and experimental results (P7, P14 and P21 – WT)

Computational models of three different ages with varying bone properties were investigated (P7 – 3500MPa, P14 – 5100 MPa and P21 – 6700 MPa). Three different sets of Young's moduli were investigated for the brain and suture material properties (150 MPa, 30 MPa – previously used by Marghoub et al. (2019); 3 Pa, 30 MPa – no brain contribution; 3 Pa, 30 KPa – adjusted for minimal differences in overall displacement across each bone in frontal bone loading, for the brain and sutures respectively). The computational von Mises strains were plotted against the experimental von Mises strains across the same sutures in Figure 4.9 and Table 1 includes Lin's Concordance Correlation Coefficient (CCC) (Lin 1989), best-fit line equation and R2 to the best-fit line. The results highlighted that:

1) With the material properties from literature Figure 4.9 and Figure 4.10 (Table 1a and 1b), the computational strains were orders of magnitude underestimated (10000 times for the 150 MPa brain case and 1000 times for the 3 MPa case). With Young's modulus for the suture adjusted to 30 KPa, the computational strains were more in line with those obtained experimentally see Figure 4.11.

2) While the computational results were closer to the experimental values for the 30 KPa suture case, they did not significantly correlate with the experimental results with the CCC ranging from -0.3 to 0.327 for P7, from -0.0796 to 0.507 for the P14 case and from -0.5857 to 0.1282 for the P21 model see Table 4.1. The negative values indicate that as the experimental strain across the individual sutures increases the predicted computational strain for those sutures individually decreases, predicting the opposite pattern. This was observed in the best-fit lines with the negative coefficients of the x term.

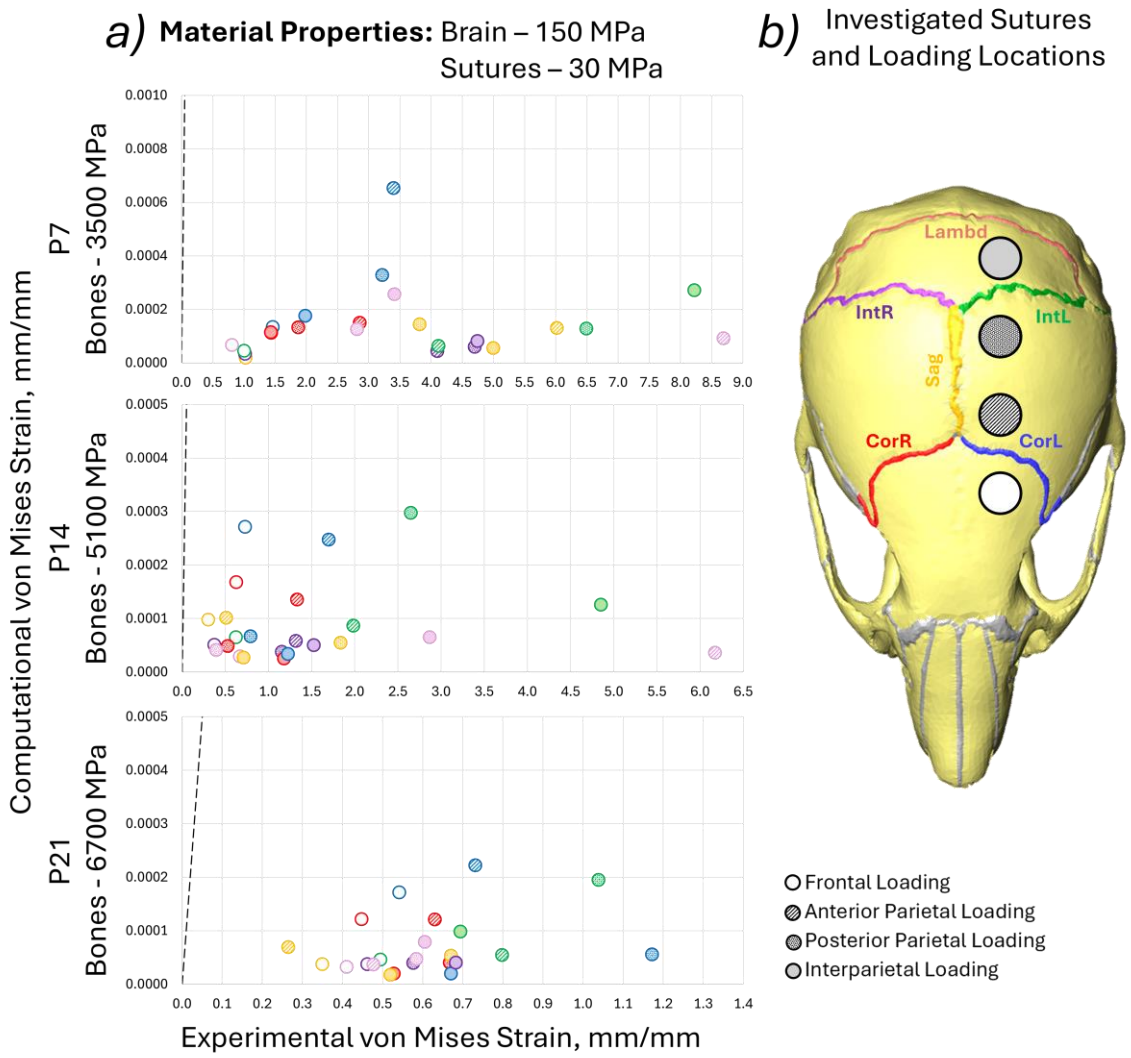

Figure 4.9 Comparison of the experimental von Mises strain results and experimental von Mises strain results for individual sutures at the 4 different loading locations for 3 different ages (P7 – bone Young's modulus 3500 MPa, P14 – bone Young's modulus 5100 MPa, P21 – bone Young's modulus 6700 MPa). The colours indicate different sutures and the marker types indicate different loading locations (i.e. the same simulation). a) 150 MPa, 30MPa, for the brain and suture Young's modulus respectively and b) highlighted investigated sutures and the approximate loading locations.

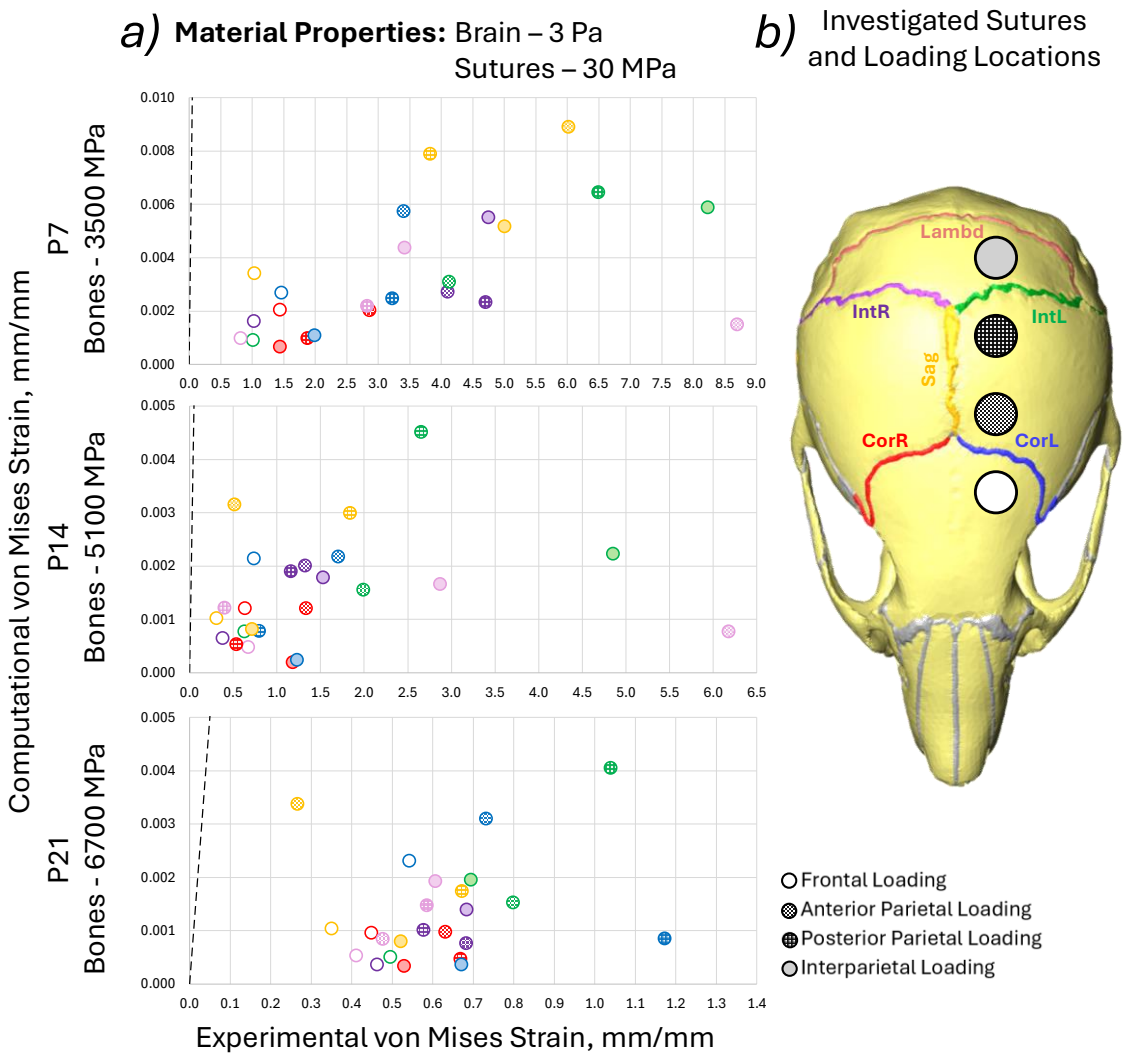

Figure 4.10 Comparison of the experimental von Mises strain results and experimental von Mises strain results for individual sutures at the 4 different loading locations for 3 different ages (P7 – bone Young's modulus 3500 MPa, P14 – bone Young's modulus 5100 MPa, P21 – bone Young's modulus 6700 MPa). The colours indicate different sutures and the marker types indicate different loading locations (i.e. the same simulation). a) 3 Pa, 30MPa, for the brain and suture Young's modulus respectively and b) highlighted investigated sutures and the approximate loading locations.

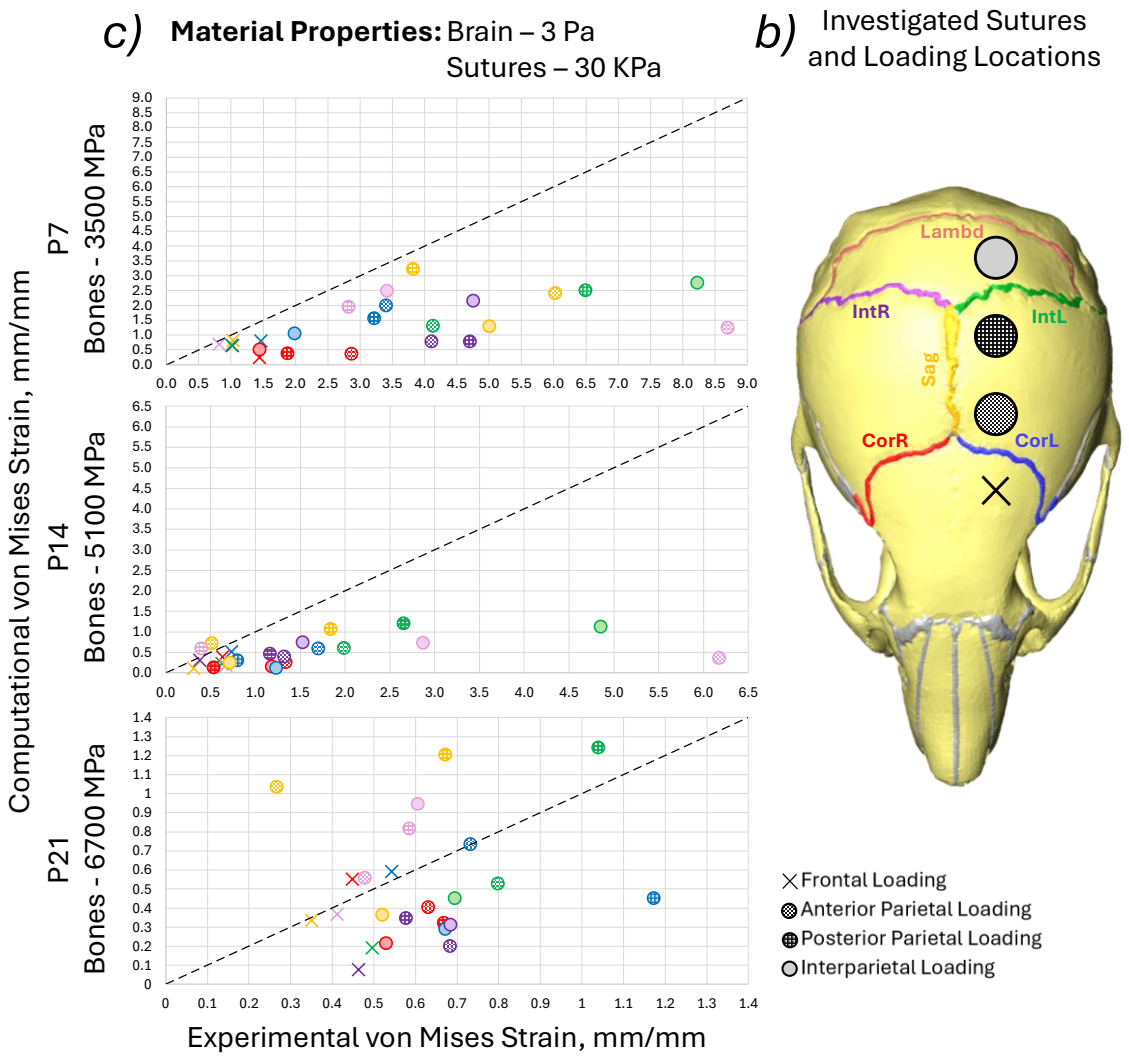

Figure 4.11 Comparison of the experimental von Mises strain results and experimental von Mises strain results for individual sutures at the 4 different loading locations for 3 different ages (P7 – bone Young's modulus 3500 MPa, P14 – bone Young's modulus 5100 MPa, P21 – bone Young's modulus 6700 MPa). The colours indicate different sutures and the marker types indicate different loading locations (i.e. the same simulation). a) 3 Pa, 30MPa, for the brain and suture Young's modulus respectively and b) highlighted investigated sutures and the approximate loading locations. Here frontal bone loading is marked with an X instead to indicate that the suture properties were optimised for this loading condition.

Table 4.1. Statistics for computational to experimental correlation. Lin's concordance correlation coefficient (CCC), best-fit line (Y), and coefficient of determination (R^2). a) Material Properties: Brain – 150 MPa, Sutures – 30 MPa, b) Material Properties: Brain – 3 Pa, Sutures – 30 MPa, c) Material Properties: Brain – 3 Pa, Sutures – 30 KPa

a) **Material Properties:** Brain – 150 MPa, Sutures – 30 MPa					
Age	Results	Frontal	Anterior Parietal	Posterior Parietal	Interparietal
P7 Bones 3500 MPa	CCC	**0**	**0**	**0**	**0**
	Y	-8.2193x + 1.0582	-2054.9x + 4.6673	-638.81x + 3.5249	11940x + 1.9538
	R^2	0.000003	0.0316	0.001	0.1878
P14 Bones 5100 MPa	CCC	**0**	**0**	**0**	**0**
	Y	537.25x + 1.0594	-13455x + 4.7958	9249.6x + 2.8699	61664x + 0.8984
	R^2	0.0113	0.325	0.0836	0.6053
P21 Bones 6700 MPa	CCC	**0**	**0**	**0**	**0**
	Y	397.26x + 0.4052	780.91x + 0.5101	1418x + 0.6554	1274.2x + 0.547
	R^2	0.2919	0.09	0.3193	0.3872

(continued…)

b) **Material Properties:** Brain – 150 MPa, Sutures – 30 MPa					
Age	Results	Frontal	Anterior Parietal	Posterior Parietal	Interparietal
P7 Bones 3500 MPa	CCC	**0.0001**	**0.0001**	**0.0005**	**0.0006**
	Y	122.2x + 3.8386	196.85x + 2.7287	449.82x + 1.9299	907.52x + 0.6857
	R^2	0.0173	0.0412	0.4772	0.8024
P14 Bones 5100 MPa	CCC	**0.0002**	**-0.0003**	**0.0011**	**0.0003**
	Y	111.05x + 0.4332	-1770.4x + 5.3872	554.47x + 0.1148	1399.5x + 0.4297
	R^2	0.1466	0.5346	0.9382	0.5967
P21 Bones 6700 MPa	CCC	**0.0002**	**-0.0004**	**0.0004**	**0.0001**
	Y	41.472x + 0.4106	-58.495x + 0.7008	72.766x + 0.6677	48.998x + 0.5609
	R^2	0.2919	0.09	0.3193	0.3872

(continued…)

c) **Material Properties:** Brain – 3 Pa, Sutures – 30 KPa					
Age	Results	Frontal	Anterior Parietal	Posterior Parietal	Interparietal
P7 Bones 3500 MPa	CCC	**-0.3**	**0.0894**	**0.2856**	**0.327**
	Y	-0.7188x + 1.5654	1.3263x + 2.5776	0.9474x + 1.9306	2.1599x + 0.341
	R^2	0.3337	0.1521	0.3288	0.6581
P14 Bones 5100 MPa	CCC	**0.2487**	**-0.0796**	**0.507**	**0.2262**
	Y	0.6734x + 0.3509	-2.3652x + 2.466	1.7847x + 0.0786	3.3186x + 0.2977
	R^2	0.3245	0.1432	0.7632	0.7647
P21 Bones 6700 MPa	CCC	**0.092**	**-0.5857**	**0.1282**	**0.0199**
	Y	0.0619x + 0.4286	-0.4314x + 0.8468	0.0885x + 0.72	0.0157x + 0.6099
	R^2	0.0342	0.3964	0.0214	0.0028

4-3-5 Bone Young's modulus optimisation (P7 – WT optimisation and P7, P14 and P21 – WT comparison)

The bone properties were investigated by optimising the Young's modulus at P7 Figure 4.12a and Figure 4.12c. The computational strain value was compared to the experimental strain values in terms of the percentage difference of the experimental value. The optimal value for most loading cases at P7 (20 MPa) was then used for the three different ages with the same comparisons as in the previous section. See Figure 4.12d, Figure 4.13 and Table 4.2. The results showed that:

1) A decrease in the bone Young's modulus resulted in a decrease in the right coronal and sagittal suture strain percentage difference for the frontal loading; however, the percentage difference increased for the other sutures. For the other loading cases, the percentage difference decreased with lower Young's modulus for most sutures with the exceptions of the lambdoid suture for the posterior parietal case and for the interparietal case. The exact value for optimal prediction of suture strain varied between loading conditions and individual sutures.

2) The average percentage difference values across all the investigated sutures were compared to find the most applicable Young's modulus. In the anterior parietal, posterior parietal and interparietal loading cases 20 MPa produced the lowest average percentage difference at 19%, 40% and 25% respectively, compared to 57%, 46%, and 53% for the original Young's modulus of 3500 MPa. However, the 20 MPa Young's modulus led to an increase in the percentage difference from 40% to 145% for the frontal loading case.

3) The adjusted 20 MPa Young's modulus represented a significant increase in the correlation of the computational results to the experimental values at both P7 and P14 and minimal change at P21 (Figure 4.12d, Figure 4.13 and Table 4.2). At P7, the CCC ranged from 0.0784 to 0.6008, at P14, from -0.2318 to 0.8759, and at P21 from -0.1076 to 0.1356. Additionally, the lambdoid suture in the anterior parietal loading and the interparietal left suture in the interparietal loading at P7 exhibited particularly high levels of strain experimentally at 8.689 and 8.222, respectively. The CCC and R^2 for these two loading locations in brackets represent the values with these sutures removed from the statistical analysis.

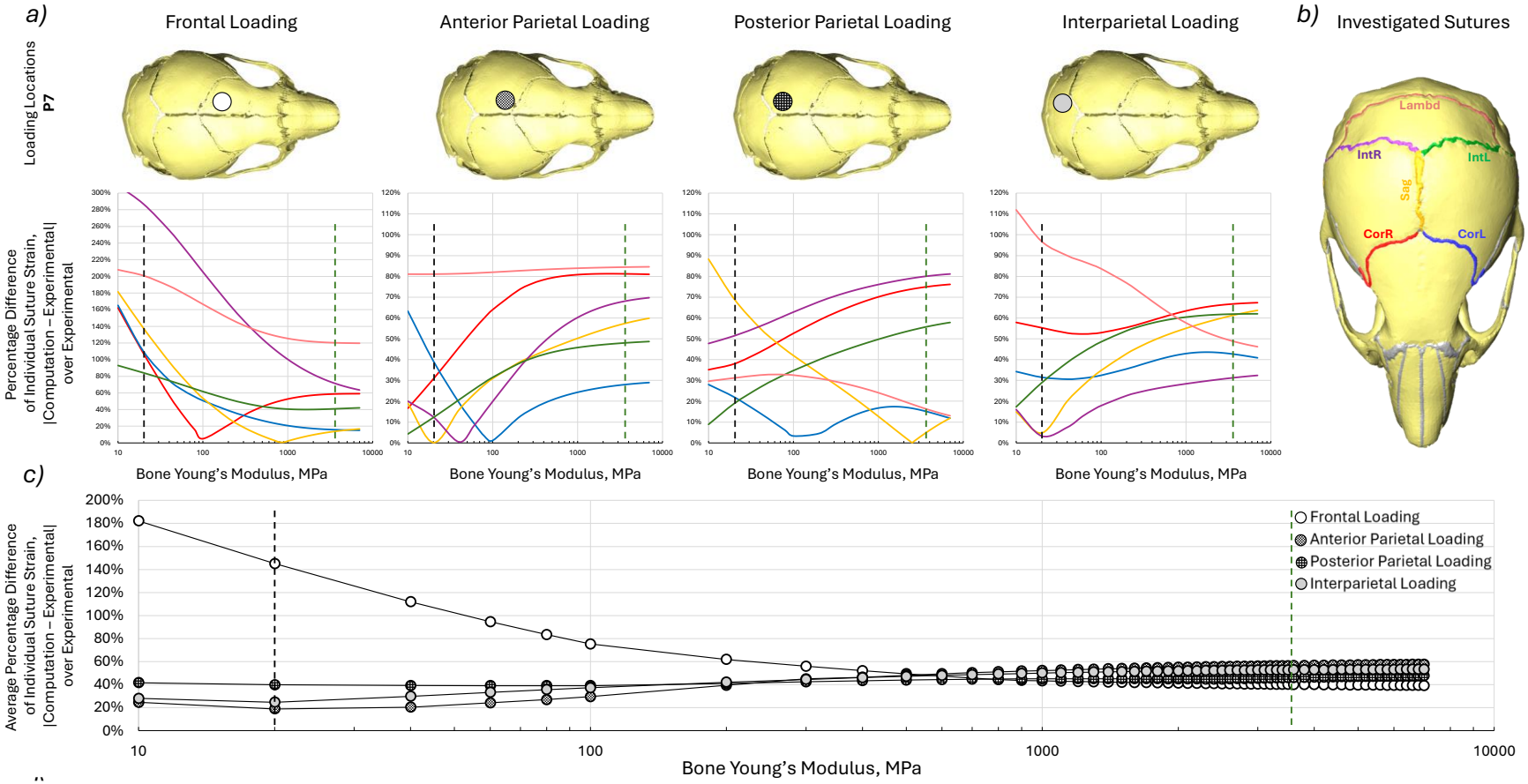

Figure 4.12 a) percentage difference of the computation von Mises strain to experimental von Mises strain at P7 for each investigated suture for the 4 different loading conditions with varying bone Young's modulus. The green dashed line indicates the literature value for the bone Young's modulus (3500 MPa) and the black dashed line indicates the optimised Young's modulus (20 MPa), b) highlighted investigated sutures, c) average percentage difference of the computation von Mises strain to experimental von Mises strain at P7 across all investigated suture for the 4 different loading conditions with varying bone Young's modulus. The green dashed line indicates the literature value for the bone Young's modulus (3500 MPa) and the black dashed line indicates the optimised Young's modulus (20 MPa)

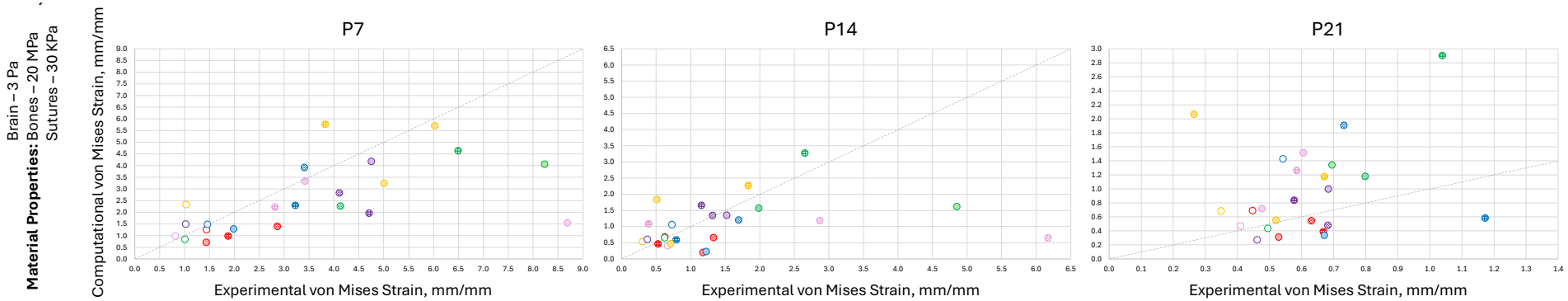

Figure 4.13 Comparison of the experimental von Mises strain results and experimental von Mises strain results for individual sutures at the 4 different loading locations for 3 different ages with minimised suture percentage strain difference at Young's moduli of 3 Pa, 20 MPa and 30 KPa for brain, bone and suture, respectively.

Table 4.2 Statistics for computational to experimental correlation. Lin's concordance correlation coefficient (CCC), best-fit line (Y), and coefficient of determination (R^2). Material Properties: Brain – 3 Pa, Sutures – 30 KPa, Bone – 20 MPa.

Material Properties: Brain – 3 Pa, Sutures – 30 KPa					
Age	Results	Frontal	Anterior Parietal	Posterior Parietal	Interparietal
P7 Bones 20 MPa	CCC	**0.0784**	**0.0037 (0.6591)**	**0.5192**	**0.6008 (0.8226)**
	Y	0.2415x + 1.1299	0.0043x + 2.9238	0.6576x + 0.4721	0.4927x + 0.7719
	R^2	0.0145	0.00003 (0.6738)	0.3411	0.6901 (0.8546)
P14 Bones 20 MPa	CCC	**0.3651**	**-0.2318 (-0.3077)**	**0.8759**	**0.3532 (0.3576)**
	Y	0.5551x + 0.3554	-0.1481x + 1.5345	1.1778x + 0.1199	0.3123x + 0.2025
	R^2	0.1887	0.3852 (0.1001)	0.9014	0.6132 (0.4207)
P21 Bones 20 MPa	CCC	**0.1132**	**-0.1076 (-0.1468)**	**0.1356**	**0.1084 (0.0737)**
	Y	2.7474x - 0.5722	-1.1592x + 1.8416	1.0924x + 0.3363	2.9064x - 0.9483
	R^2	0.2028	0.1068 (0.2117)	0.0952	0.1912 (0.0736)

4-4 Discussion

In the previous chapter (**Chapter 3**), a series of *in/ex vivo* experiments were carried out to characterise the level of mechanical strain induced across the coronal suture in mutant- and wild-type mice during the external frontal bone loading. This was carried out to understand the therapeutic effects observed in dorsoventral cyclic loading of the frontal bone in coronal suture patency retention, as observed by Moazen et al. (2022). The investigations validated a novel suture strain estimation approach during loading and provided insight into the level of strain during external loading laying the foundation for computational studies. However, several questions remained unanswered such as the effect of loading location on suture strain and the level of strain in the coronal suture of the MT animals during loading.

In this chapter, further experiments were carried out to investigate the effect of loading location on the suture strain and more sutures were included in the analysis than previously examined. Additionally, the deformation of the suture gap was measured to estimate the level of deformation and strain at the coronal sutures of the WT and MT animals, specifically comparing the response to the external load. The expanded experimental investigation was followed by an investigation of computational models. Only the WT animals were included in both the strain analysis investigations and computational models. The same limitations prevented the investigation of MT animals that were present in the previous chapter; namely, the fused coronal suture in the Crouzon mice. Additionally, only linear elastic properties were investigated for the material models in the computational models likely representing the most significant limitation of the computational part of this investigation.

Qualitatively clear differences between the responses of the skulls to the external loading at different locations are present (Figure 4.3). The previously investigated loading location (frontal bone) exhibited a significantly lower level of relative deformation compared to the other investigated loading locations (posterior parietal, anterior parietal, and interparietal bones). The significant difference observed can be explained by the anatomy of the skull. The frontal bones are structurally connected to the skull base and are overall part of a more rigid framework. Conversely, the parietal and interparietal bones at P7 are more loosely connected to the rest of the cranial skeleton and even at P14 still have significant gaps (sutures) present at their boundaries.

These anatomical differences and in turn variable rigidity of the skull may be linked to the developmental role the sutures assume. The posterior region of the skull elongates in WT animals from P14 to P21 see Figure 4.3a. Potentially, the structure of this region allows this elongation to occur by providing the least resistant growth direction for the brain, but in turn leads to a significantly less stiff structure that is more susceptible to external loading. The mutant animals appear to confirm the link between the external rigidity of the posterior skull and its elongation during development as the posterior region is significantly more rigid in the MT animals at P14 compared to the WT animals and the characteristic elongation does not occur.

The premature fusion of the sutures may account for an early stiffening of the skull to external loading. As early as P7, the frontal and posterior parietal bone loadings appeared to produce minimal levels of deformation compared to their WT counterparts. This suggests that the affected sutures may play a role in the mechanical response as early as P7. Another significant difference in the mutant loading response appeared to be the local deformation of the bone. The $Fgfr2^{C342Y/+}$ mutant mice present with decreased mineralisation of the frontal and other bones (Liu et al. 2013; Moazen et al. 2015b; Ajami et al. 2024). As the loading locations coincided with the less bony regions the deformations, they qualitatively appeared to occur across the bone as opposed to across the sutures as in the WT case. The premature fusion at the sutures that was present even at P7 may have further limited the deformability of the sutures.

With these qualitative differences between WT and MT responses to the external loading at the four different locations present, the response of the coronal suture was investigated directly for both MT and WT animals at P7, where the deformations were the greatest and the level of coronal suture fusion was the lowest. Importantly, the suture gap distance did not increase in any of the investigated cases for the MT animals, while the gap distance increased significantly ($p<0.01$ and $p<0.001$) for the WT animals in all but one case. The only statistically significant change in the MT animals was the decrease in the gap size on the loaded side for the interparietal loading. The interparietal bone loaded MT also exhibited the most patent coronal sutures and the only statistically significant difference thus, was chosen for further qualitative investigation.

Figure 4.14 compares the WT and MT, loaded and unloaded states for the interparietal bone loaded P7 animals. A clear difference in the deformation across the coronal suture was observed in the two cases. Namely, the bones appear to move freely under the load in the WT case, thus changing the sutural gap distance. Conversely, the geometry of the

affected suture in the MT case appears to remain unchanged in this case. While the overall deformation of the skull appeared to be comparable in the MT case, the deformation did not occur across the sutures and instead appeared to locally deform the frontal bone across the lower ossification region. The lack of deformation across the suture was highlighted quantitatively for the other loading locations and was observed qualitatively during measurement

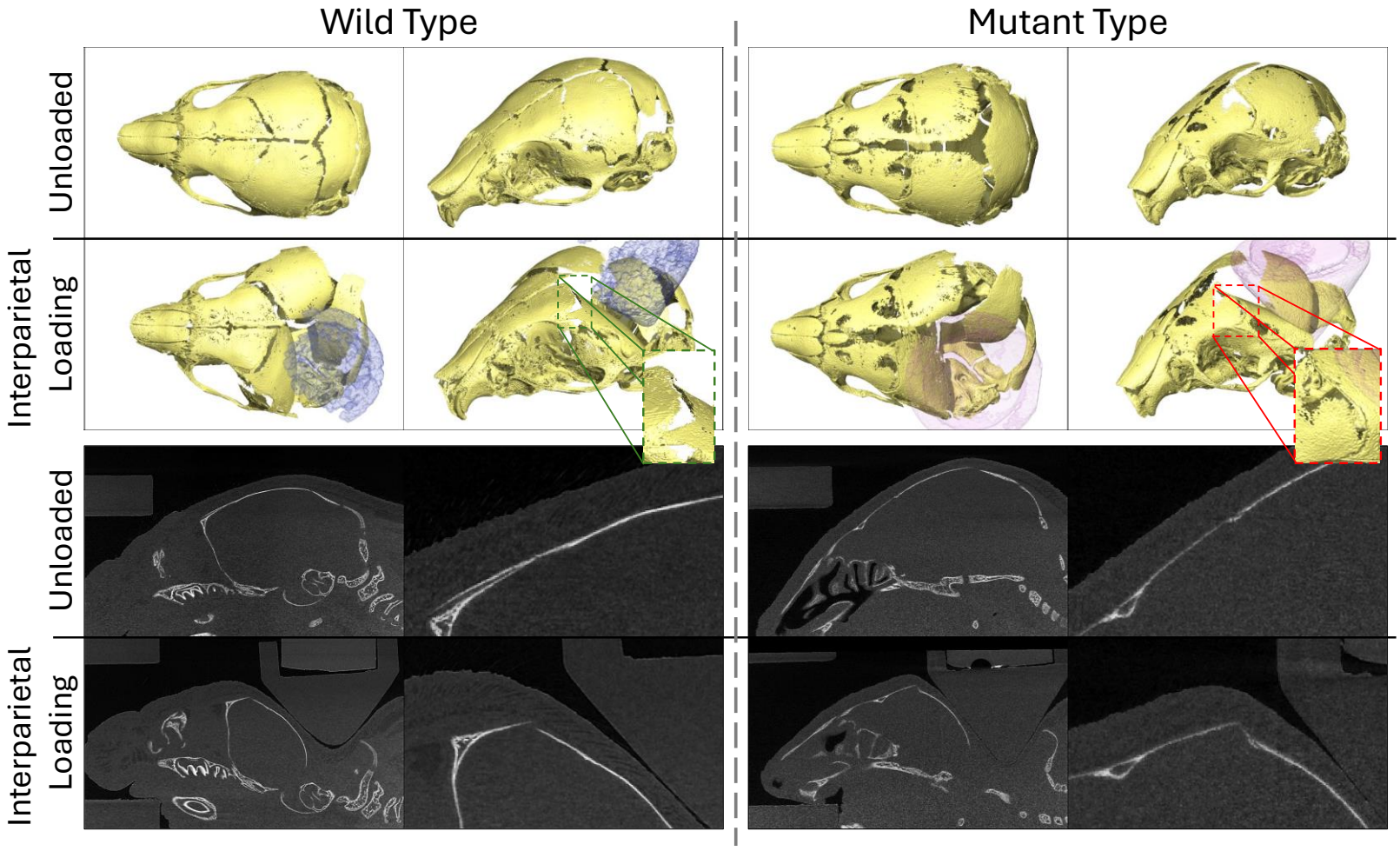

Figure 4.14 Qualitative comparison of the loaded and unloaded WT and MT skulls during interparietal loading at P7. Highlighting the different responses of the unfused (WT) suture and partially fused (MT) suture to external loading.

These findings highlight the unexpectedly large difference between the response of the coronal sutures to external loading between MT and WT animals. Specifically, no strain in the coronal sutures appeared to be present in the affected animals with the only measurable change being a 22% decrease. Whereas, for the WT animals, the majority of the deformation and, therefore, strain occurred at the sutures ranging from 33% to 437% increase from the original size. It is then unclear whether the mechanism of suture patency retention proposed by Moazen et al. (2022), where the tensile strain across the sutures maintains the suture patency applies to these animals. As little to no suture strain was observed in the MT animals, especially compared to the extreme changes in coronal suture gap observed in the WT animals. However, the cyclic nature of the *in vivo* treatments not captured in these investigations may play a significant role in the therapeutic mechanisms. Perhaps, there may be direct disarticulation of the less affected sutures at early stages of fusion as previously suggested in **Chapter 3** or the activating of mechanotransduction mechanisms differently. However, further investigations of the *in vivo* treated animals are required to answer these questions.

The early fusion of the sutures in the mutant animals prevented the strain estimation methodology used that was originally established in **Chapter 3**. Thus, the strain was investigated only in the WT animals at P7, P14, and P21 for the four different loading conditions. In addition to the expanded experimental scope in terms of loading locations, more sutures were included in the analyses than previously (coronal, sagittal, interparietal, and lambdoid), see Figure 4.6c enabled by the development of BounTI. Overall, strain patterns aligned with the patterns observed in the qualitative comparison of the loaded skulls. Namely, the significantly lower strains across the sutures during frontal bone loading compared to the other loading locations. Similarly, a decrease in suture strain was observed across all loading locations with a particularly sharp and even decrease at P21. This suggests that the skull has reached a similar stiffness for all the loading locations investigated as the strains were in range comparing the frontal bone loading to the other loading locations.

The strains across the coronal suture at P7 can be directly compared between the average strain analysis across the full suture and the change in length of the sutural gap. The measured von Mises strains (suture gap change) across the left coronal suture were 1.45 (0.33), 3.39 (1.89), 3.22 (1.76), and 1.97 (2.13) for the loading of frontal, anterior parietal, posterior parietal, and interparietal bones, respectively. For the right coronal suture, the

values were 1.43 (0), 2.85 (1.93), 1.86 (4.37), and 1.42 (1.77), respectively. The comparison highlights that the values are not the same, however, they generally fall within the same range. The suture strain analysis considered the full suture while the gap analysis only investigated the superficial part of the suture to compare the results to mutants. This is particularly apparent where strains of 0 were measured for the frontal loading while both qualitatively (in the suture gap analysis) and quantitatively (in the strain analysis) deformation across the suture was observed. Low suture gap change in the frontal loading scenario was observed because the deformation of the bones appeared to hinge around the suture gap, see Figure 4.5b.

The frontal bone and anterior parietal bone loadings can be considered as "targeting" the left coronal suture as it is the closest suture to the loading locations. Similarly, the posterior parietal bone and interparietal bone loadings can be considered as "targeting" the left interparietal suture. The von Mises strain across the "targeted" suture for the frontal and anterior parietal bone loadings were 1.45 and 3.39, 0.72 and 1.69, and 0.54 and 0.73 for P7, P14, and P21 animals, respectively. The strains across the "targeted" suture for the posterior parietal and interparietal bones were 6.48 and 8.22, 2.65 and 4.85, and 1.04 and 0.69 for P7, P14, and P21 animals, respectively. While at P21, the results across the "targeted" suture were relatively consistent between all the loading locations at P7 and P14 the interparietal left suture, strain was observed to be 2 to 5 times more than the coronal suture under the same loads. This suggests that for the treatment of other sutures by loading different bones the loading parameters established for coronal suture patency are likely inappropriate. The force should be adjusted to account for the age-variable rigidity of the posterior skull.

Considering optimisation for the treatment of other suture fusions, the loading angle (load direction) may be less appropriate due to the geometry of the suture in question. Previously, Herring et al. 2024 has used longitudinal force application across the nasofrontal suture in pigs. While this was not investigated in this work, further suture specific loading parameters are likely to include loading angle. This was not possible with the current loading setup.

The average von Mises strains of the six sutures investigated for four different loading locations at three different ages provide a solid foundation for the development of computational models and their validation. Three computational models were developed from the unloaded scans of the frontal bone loading case in WT at the three investigated ages (P7, P14, and P21). Each was loaded on the four different locations investigated

experimentally and the computational predictions were compared directly to the experimental values of the von Mises strain. With the higher Young's modulus values for the suture for both cases (150 MPa, 30 MPa and 3 Pa, 30 MPa, for brain and sutures, respectively), the computational results were orders of magnitude off the experimentally observed values. It should be noted here that the computational models lack skin, muscles, and adjoining structures such as the mandible or the spine. However, the inclusion of these structures could not account for the 1000 to 10000 times lower computational deformation compared to the experimental results and would likely only further marginally decrease the local deformation of the cranial bones. Thus, the discrepancy between the computational and experimental results suggests that the material properties of the sutures in the computational models could not capture the deformation observed physically. Hence, the suture properties were optimised to best match the individual bone directional displacement and the value of 30 KPa was found.

While the computational results with the adjusted suture Young's modulus were generally in the same order of magnitude as the experimental results they still did not correlate well (highest CCC was 0.507). Tensile tests of the sagittal suture in adult mice were previously carried out by Chien et al. (2008), where a Young's modulus of 580 KPa was reported for the aforementioned suture. This is significantly closer to the 30 KPa optimised value than the 30 MPa measured using nanoindentation by Moazen et al. (2015). Additionally, the mice investigated by the tensile study were adults and the material properties of neonatal mice are expected to be lower. This highlights that the range of material property studies for the sutures in mice specifically at early ages may be insufficient to fully capture the complexity of the loadings investigated. Lastly, the bone properties were investigated. As large local deformations of the bones were observed qualitatively and were particularly prominent at P7.

The bone Young's modulus ranging from 3500 MPa to 6700 MPa did not permit any significant local deformation of the bone under the 0.1 N load that was considered in this study. To test the effect of bone Young's modulus on the computational results the value was varied for the P7 models from 10 MPa to 7000 MPa. The investigation highlighted that Young's modulus of 20 MPa appeared to produce the best strain predictions for all but the frontal bone loading. Again, highlighting that perhaps the frontal part of the skull was significantly stiffer and responded differently when compared to the more posterior part of the skull. The adjusted bone Young's modulus produced a better correlation with the experimental results in both P7 and P14 animals and did not affect the correlation at

P21, see Table 4.2. While the correlation improved following all the adjustments, the predictive power of the models is still questionable.

The skull appears to respond differently to external loading with changing loading locations. These differences were hardly captured by the adjusted linear elastic material model of 3 Pa, 30 Kpa, and 20 MPa for the brain, suture, and bone Young's moduli, respectively. The most significant limitation of the computational part of this work is the linear elastic properties because the brain is known to behave hyperelastically, especially during large deformation. Similarly, the sutures were shown to experience plastic deformation during this loading in the previous study Chapter 3 and the complex microstructure of the sutures may require a significantly more complex material or computational model to capture. This work highlights the limitations in the understanding of the material properties of the mice craniofacial system, specifically during external calvarial loading early in development.

Limitations

The experimental and computational parts of this chapter include significant limitations in the study design. 1) For the experimental part only 1 animal per age per loading location was considered. While somewhat justified by the investigations in the previous chapter, setting out the variability of the loading response and the experimental constraints of including more animals. Only one observation per group means that statistical analysis comparing the strains are not possible and individual variation of phenotype may significantly affect the strain results. 2) Both experimental and computational investigations lack direct measurements of suture strain in mutants due to the early fusion of the sutures of interest similar to the limitations of Chapter 3. While the suture gap analysis tackles this limitation by directly comparing the MT suture coronal suture to the WT suture, further methodological development is required for deeper investigation into the response of partially fused sutures. 3) Computational investigations focused on linear isotropic material properties, likely unsuitable for the physical phenomena investigated. However, the work here highlights the limitations of these material models and the need for more investigations of the mouse brain and suture material properties especially at early developmental timepoints.

4-5 Summary

This chapter highlighted that while little trust can be put in the predictive power of the computational models developed here, the development process itself represents a significant investigation into the mechanical behaviour of the mouse skull. The experimental investigations produced in this work can help further the treatment developed by Moazen et al. (2022) and provide insight into craniofacial morphogenesis. Namely, the investigation into the suture gap represents the first direct measurement of the deformation of the coronal suture during external loading in Crouzon mice. Surprisingly, highlighting no measurable tensile deformation of the suture, that was previously assumed to contribute to the retention of suture patency. Additionally, the apparent variable stiffness of the skull to external loading with more deformation observed posteriorly could explain the mechanism of the posterior skull elongation observed from P14 to P21 in mice. With the lower stiffness providing the least resistant path for the brain to expand during growth and thus resulting in the elongation of the skull. Lastly, the investigation into the strain across the other sutures suggests that the same loading force is likely inappropriate at P7 or P14 to target the fusion of interparietal sutures and should be appropriately reduced.

Following qualitative observations of individual craniofacial variability of animals observed in **Chapters 3** and **4**. Direct analysis of phenotypic variability in terms of overall skull morphology and suture patency is carried out in the following chapter to establish study design implications and the relation between suture patency and skull shape.

Chapter 5 Characterisation of craniofacial phenotype variability in normal and Crouzon mice

5-1 Introduction

Chapter 3 and **Chapter** 4 investigated the response of the mouse craniofacial system to external loads, understanding the variability of the Crouzon phenotype is equally important when interpreting *in vivo* treatment results. Throughout the suture quantification experiments as well as the repeated *in vivo* treatment investigation, it became clear that the craniofacial phenotype was extremely varied. Animals from different litters appeared different from each other, and no clear relation between retained suture patency at P21 and the skull morphology was qualitatively observed. This chapter investigates these qualitative observations quantitatively.

Aim: Quantify the phenotypic variability in MT and WT mice as it relates to the litter and suture fusion in the MT animals.

Objectives: Establish the morphological variations of Crouzon and WT mice skulls and litter effects on these variations, the level of suture fusion in the Crouzon mice and litter effects on suture fusion and finally unravel the relations between suture fusion and skull shape in Crouzon mice.

5-2 Materials and methods

The workflow to achieve the objectives of this chapter is outlined in Figure 5.1. Untreated MT and WT animals at P21 (9 MT and 11 WT litters) and P42 (5 MT and 2 WT litters) were investigated in this Chapter. The P21 animals investigated here were also used as the control group in the following chapter in line with the principles of the 3Rs of animal research.

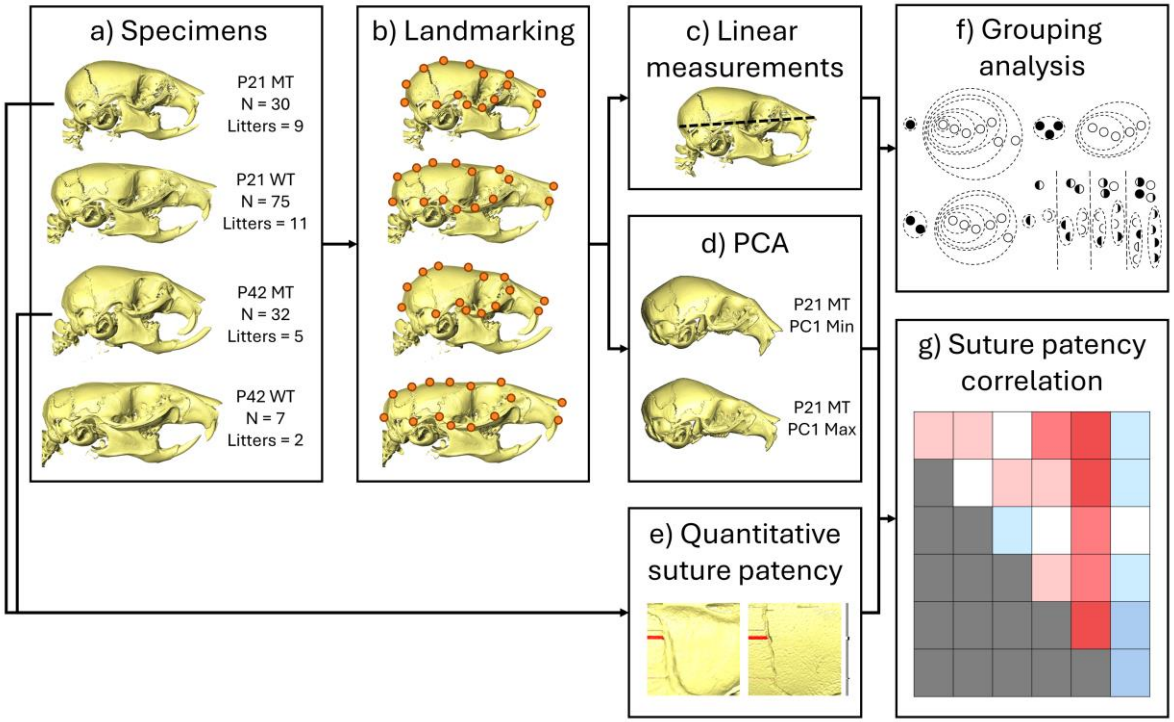

Figure 5.1 An overview of the workflow. a) Specimens used in the study including the number of animals and the number of litters, b) landmarking of the skulls, conducted for all included specimens, c) linear measurements including skull length, braincase length, frontal bone width, braincase width, and braincase height, d) principal component analysis of the landmarking data, conducted for all investigated animals for both shape and size (form) and shape (P21 MT shape PC1 min and max shape shown as examples), e) quantitative suture patency analysis carried out on P21 (metopic, coronal, sagittal, and interparietal sutures and the ISS) and P42 (sagittal and interparietal sutures) MT animals, f) grouping analysis carried out for P21 MT and P21 WT animals for all investigated measurements and P42 MT for linear measurements (available in the supplementary materials) investigating the effects of within and between litter study designs, included intraclass correlation coefficients and g) suture patency correlation with skull shape investigation carried out for P21 and P42 MT animals including correlation matrix and regression analysis.

5-2-1 Specimens

Both mutant and wild type mice were included in this study; $Fgfr2^{C342Y/+}$ Crouzon mouse model was used for the generation of both mutant and wild type mice on a CD-1 background. These were derived by the European Mouse Mutant Archive (EMMA) at MRC Harwell, as described by Peskett et al. (2017).

In total, 144 cadavers were characterised in this study (30 P21 MT – across 9 litters, 75 P21 WT – across 11 litters, 32 P42 MT – across 5 litters and 7 P42 WT – across 2 litters). The distribution of these animals across the different litters and the reconstructed skulls of the most average members of each litter are highlighted in Figure 5.2. The majority of the animals here were sacrificed as controls for other experiments thus following the reuse principle of the 3Rs.

Note: All animal experiments were approved by the UK Home Office and performed as part of a Project License (number: PP8161503) under the UK Animals (Scientific Procedures) Act 1986. Animal procedures complied with the ARRIVE guidelines and were performed under the supervision of UCL Biological Services.

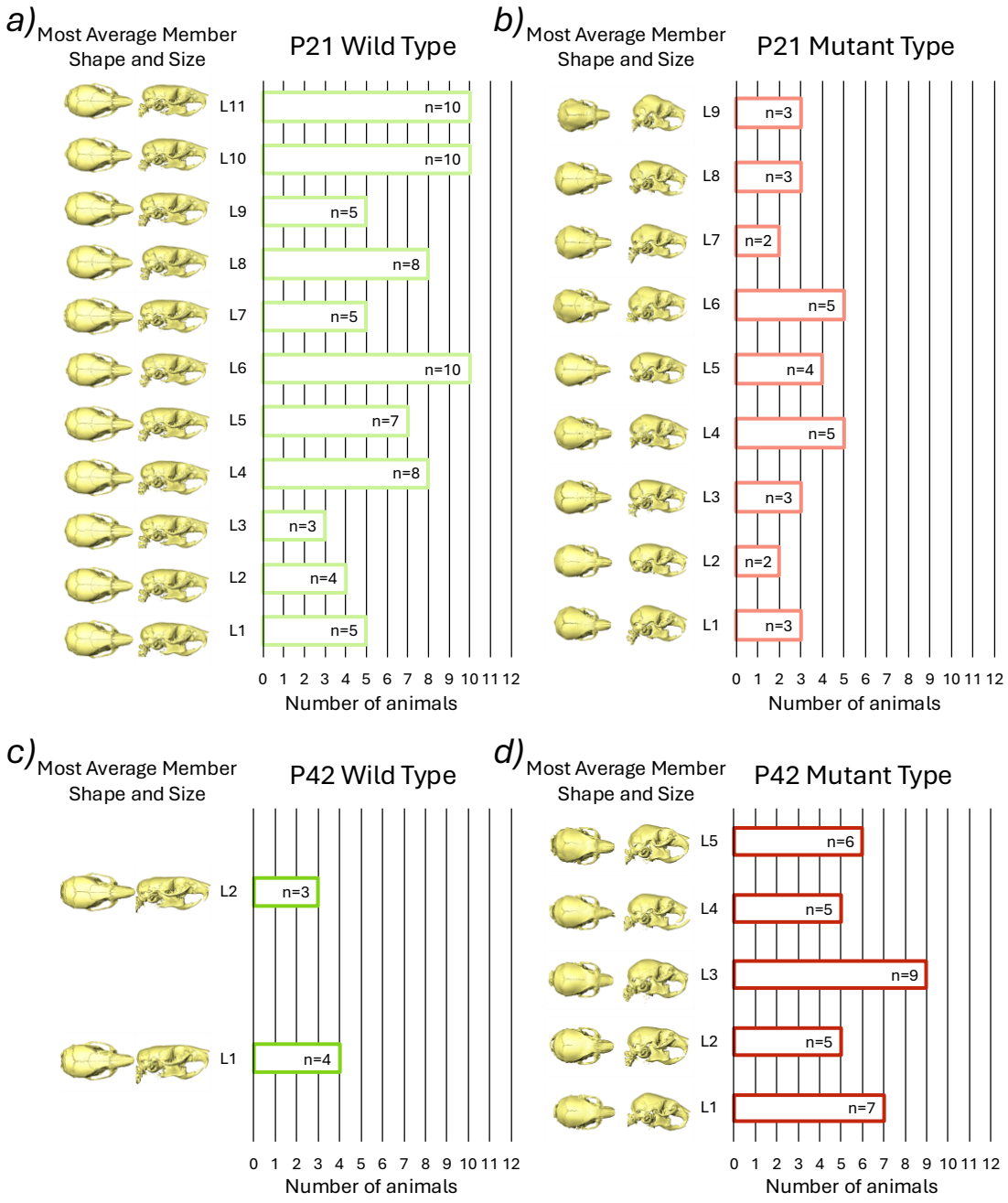

Figure 5.2 An overview of the animals used in this work, including numbers of individuals in each litter and the reconstruction of the skull of the most average member of each litter in terms of shape and size. a) P21 WT, b) P21 MT, c) P42 WT and d) P42 MT.

5-2-2 Imaging

The skulls were immediately fixed in 10% formalin at 4°C for 7 days. The fixed skulls were scanned in the micro-CT scanner (XT H 225ST, Nikon, Herts., UK). The following parameters were used for all included samples: Scan parameters – 9.6 μm × 9.6 μm × 9.6 μm, 90 kV, 90 μA, 1 s exposure. Reconstruction was done using Inspect-X (Nikon, Herts., UK) with only a beam hardening filter at strength 2 applied to all reconstructions. CT images were imported into an image processing software (Avizo 2022.1, ThermoFisher Scientific, Mass, USA), where the data was converted to 16-bit (from 0 - 300 – 32bit float input range to 0 – 65535 – 16bit int output range). The resampled data was grossly aligned between different specimens and finely aligned using the image registration tool in Avizo was carried out. Alignment produced generally consistent orientation with the cardinal axes and individual specimens. Segmentation was carried out using a consistent threshold of 19000.

5-2-3 Morphometric analysis

56 landmarks were placed across the skull as shown in Figure 5.3, Figure 5.4 and described in Table 5.1. The landmark positions were largely based on Richtsmeier et al. (2000) and Motch Perrine et al. (2014), with some changes to account for unclear boundaries due to fusion and different developmental time points investigated. Linear measurements were taken from landmarks 3 to 30 for the full length of the skull, from 8 to 30 for the length of the braincase, from 21 to 22 for the width of the frontal bone, from 25 to 26 for the width of the braincase and from 24 to 38 for the height of the braincase. Braincase curve was calculated as the sum of distances from 8 to 23, from 23 to 55, from 55 to 24, from 24 to 27 and from 27 to 30. This value was divided by the length of the braincase to obtain a curvature measurement with higher values indicating higher curvature of the braincase. A single operator carried out all imagining, processing and landmarking.

PCA (principal component analysis) was carried out for all specimens as well as age and type groups individually. Both size and shape (form), and shape differences were investigated. The analysis was carried out in R using the same code as described in Liang et al. (2023). Statistical comparison of the PCA results was carried out with MANOVA considering the first PC scores contributing to >95% of the variation. Generally, the first 14 PCs captured 95% of the variation, however, for the grouping analysis (explained in

Section 5-2-5) the number of included PCs varied significantly due to a significant reduction in the number of specimens included.

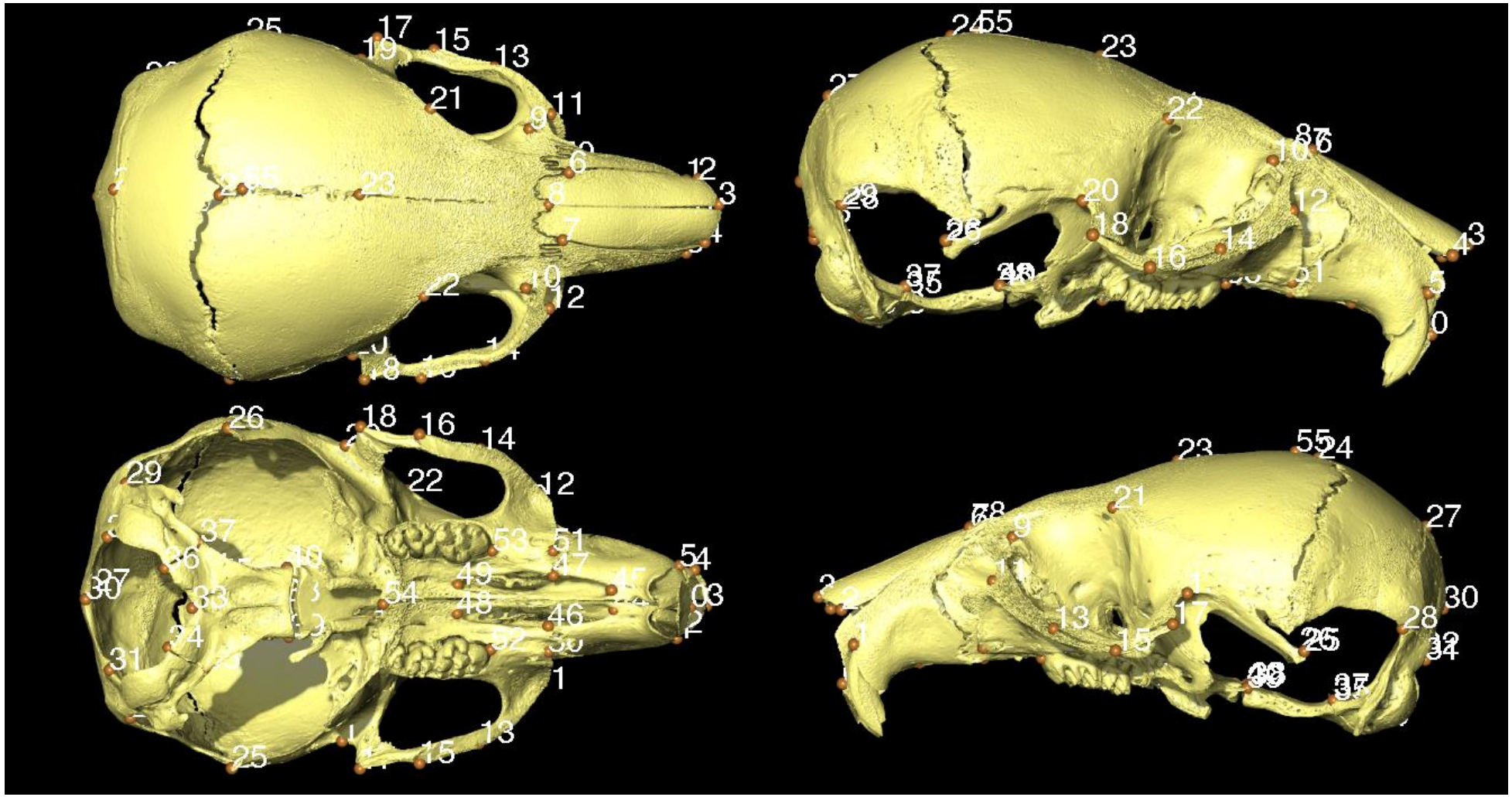

Figure 5.3 Landmark locations on intact skull.

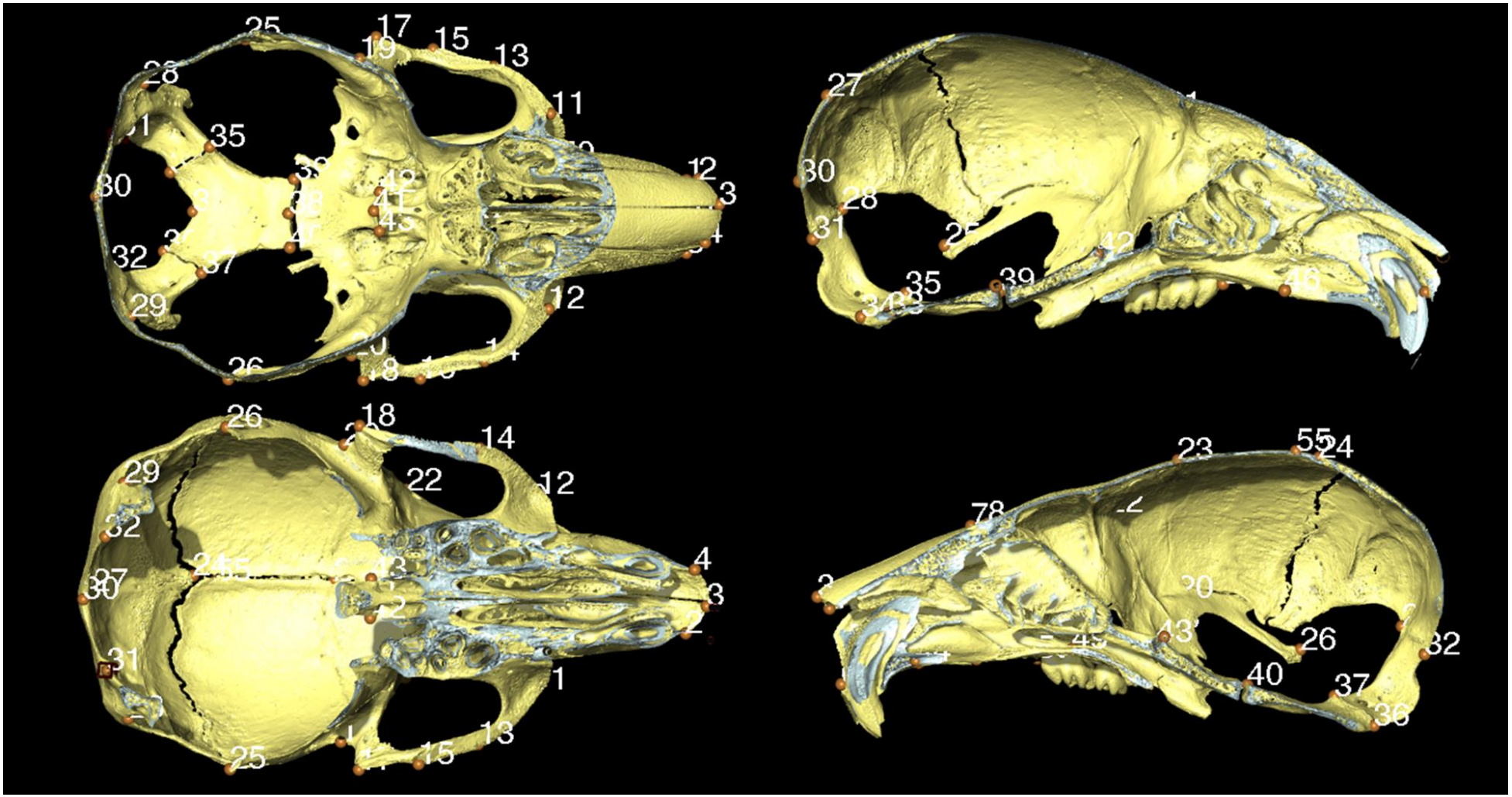

Figure 5.4 Landmark locations on cross section views.

Table 5.1 List of landmark location descriptions

0	Interdental superior, most anterior midline point on alveolar border superior to septum between central incisors
1	Center of alveolar ridge over maxillary incisor, left side
2	Anterior-most point at intersection of premaxillae and nasal bones on the nasal bone, left side
3	Nasale: Intersection of nasal bones, rostral point
4	Anterior-most point at intersection of premaxillae and nasal bones on the nasal bone, right side
5	Center of alveolar ridge over maxillary incisor, right side
6	Intersection of nasal, maxilla and frontal bones, on the nasal bone, left side
7	Intersection of nasal, maxilla and frontal bones, on the nasal bone, left side
8	Nasion: Intersection of nasal bones, caudal point
9	Intersection of frontal process of maxilla with frontal and lacrimal bones, left side
10	Intersection of frontal process of maxilla with frontal and lacrimal bones, right side
11	Anterior notch on frontal process lateral to infraorbital fissure, left side
12	Anterior notch on frontal process lateral to infraorbital fissure, right side
13	Intersection of zygomatic process of maxilla with zygoma (jugal), anterior most point of the flat part of the joint, left side
14	Intersection of zygomatic process of maxilla with zygoma (jugal), anterior most point of the flat part of the joint, right side
15	Intersection of zygomatic process of maxilla with zygoma (jugal), posterior most point of the flat part of the joint, left side
16	Intersection of zygomatic process of maxilla with zygoma (jugal), posterior most point of the flat part of the joint, right side
17	Intersection of zygoma (jugal) with zygomatic process of temporal, superior aspect, left side
18	Intersection of zygoma (jugal) with zygomatic process of temporal, superior aspect, right side
19	Joining of squamosal body to zygomatic process of squamosal, left side
20	Joining of squamosal body to zygomatic process of squamosal, right side

21	Intersection of frontal and parietal bones, anterior most point of the coronal suture process, on the frontal bone, left side
22	Intersection of frontal and parietal bones, anterior most point of the coronal suture process, on the frontal bone, left side
23	Bregma: intersection of frontal bones and parietal bones at midline
24	Intersection of parietal bones with anterior aspect of interparietal bone at midline
25	Dorsal most point on the post-tympanic hook , left side
26	Dorsal most point on the post-tympanic hook , right side
27	Intersection of interparietal bones with squamous portion of occipital bone at midline
28	Intersection of the left occipital condyle and lambdoid bone, anterior most point
29	Intersection of the right occipital condyle and lambdoid bone, anterior most point
30	Opisthion, midsagittal point on the posterior margin of the foramen magnum
31	Intersection of the left occipital condyle and lambdoid bone, posterior most point
32	Intersection of the right occipital condyle and lambdoid bone, posterior most point
33	Basion, midsagittal point on the anterior margin of the foramen magnum
34	Intersection of the left occipital condyle and occipital bone, posterior most point
35	Intersection of the left occipital condyle and occipital bone, anterior most point
36	Intersection of the right occipital condyle and occipital bone, posterior most point
37	Intersection of the right occipital condyle and occipital bone, anterior most point
38	Midline point on the edge of the spheno-occipital synchondrosis, on the occipital bone, from the superior view
39	Left most point on the lateral edge of the spheno-occipital synchondrosis, on the occipital bone, from the superior view
40	Left most point on the lateral edge of the spheno-occipital synchondrosis, on the occipital bone, from the superior view

41	Midline point on the edge of the intersphenoid synchondrosis, on the sphenoid bone, from the superior view
42	Right most point on the lateral edge of the intersphenoid synchondrosis, on the sphenoid bone, from the superior view
43	Right most point on the lateral edge of the intersphenoid synchondrosis, on the sphenoid bone, from the superior view
44	Most anterior point of the anterior palatine foramen, left side
45	Most anterior point of the anterior palatine foramen, right side
46	Most inferolateral point on premaxilla-maxilla suture, left side
47	Most inferolateral point on premaxilla-maxilla suture, right side
48	Most posterior point of the anterior palatine foramen, left side
49	Most posterior point of the anterior palatine foramen, right side
50	Most anterior point on the frontal part of the maxillary temporal process lower connection to the maxilla, left side
51	Most anterior point on the frontal part of the maxillary temporal process lower connection to the maxilla, right side
52	The anterior most point on the central ant/post axis of the left molar alveolus
53	The anterior most point on the central ant/post axis of the right molar alveolus
54	The anterior most point of the ventral intersection of maxilla bones
55	Apex of the parietal bone curve on the midline

5-2-4 Suture patency analysis (MT)

The suture patency was investigated quantitatively in the mutant animals. Six craniofacial sutures (metopic, coronal left, coronal right, sagittal, interparietal left, and interparietal right) patency scores were calculated. In addition to the sutures, the intersphenoidal synchondrosis (ISS) patency was quantified.

The landmarks were used to crop the segmented skull volumes into the suture regions. The sutures were then rotated to be as in line with the z-axis as possible. The number of slices in the XY plane with patent sutures was divided by the total number of slices across the suture length to obtain the quantitative level of suture patency with 100% representing full patency and 0% full fusion (See Figure 5.5).

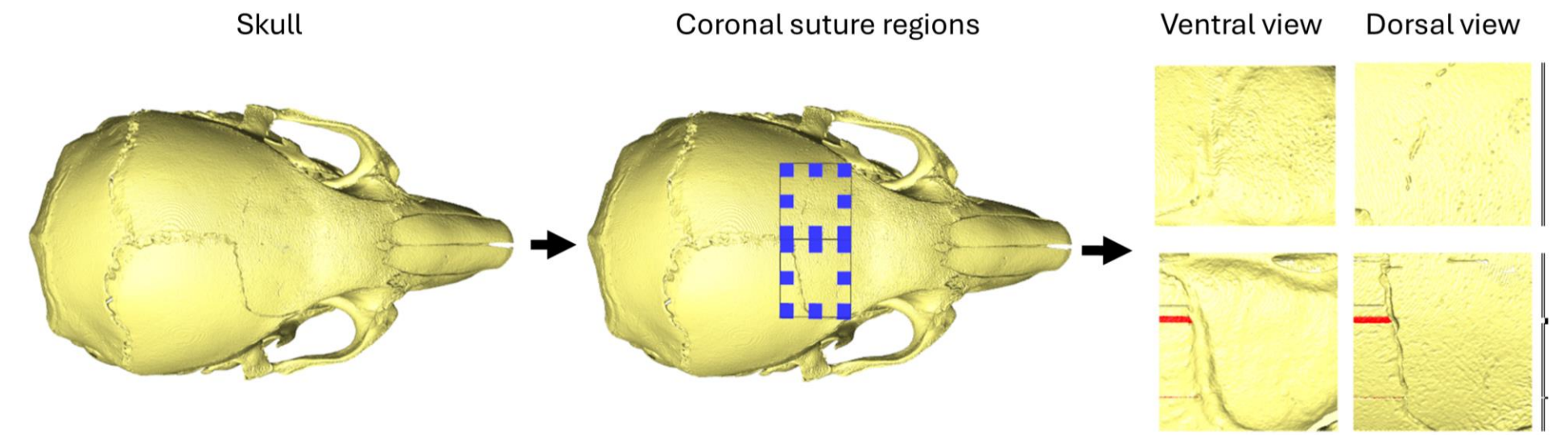

Figure 5.5 Quantitative suture patency analysis. Suture regions are selected based on landmark coordinates, the regions are separated, and each slice is checked, if the slice contains two distinct bone pieces it is selected as open (shown in red) if not it remains yellow. The percentage of slices that contain open sutures is then considered as patency percentage with 100% representing full patency and 0% full fusion. This process is carried out across all other investigated sutures.

Synchondrosis patency could not be investigated in the same way as the suture patency. Fusion was observed across the full lateral length of the synchondrosis in all animals. The depth of the unfused synchondrosis over the full depth of the synchondrosis was calculated to obtain the level of ISS patency. As these measurements are significantly different from the suture patency measurements, it is unclear how comparable their biological meaning is.

Additionally, the suture patency sum was calculated as the sum of the difference of patency from the mean in terms of the number of standard deviations. This was used in Section 5-2-6 to determine the effects of individual variation of overall patency in relation to morphology and individual suture patency.

5-2-5 Intra vs inter litter variation and study design analysis

The intra vs inter litter variation was investigated through statistical analysis of the linear measurements and group-wise principal component scores for P21 WT animals. In addition to these, the level of suture patency was included for P21 MT animals. One-way ANOVA was used to understand whether there were any statistically significant differences between the groups. Additionally, intraclass correlation coefficients were calculated to understand the intra vs inter litter effects on the suture patency and skull shape.

For all the investigated measurements including linear measurements, principal component scores, and suture patency grouping analysis - a novel investigation into the implications of litter effects on study design was carried out at P21. Here, two groups were created group 1 and group 2. The group 1 simulates a treatment control group and the group 2 simulates the treated group, both groups included only control animals. Thus, the expected incidence of statistically significant comparison should be the statistical significance level set (in this case $p < 0.05$) as in reality two control groups of different litter compositions.

Different combinations were investigated with group 2 made of 1 litter against group 1 made of 1, 2, 3, 4, 5, 6, 7 litters, group 2 made of 2 litters against group 1 made of 2, 3, 4, 5, 6 litters, and group 2 made of 3 litters against group 1 made of 3, 4, 5 litters. Visual explanation of the considered groupings is available in Figure 5.6. All possible permutations were investigated, and the statistical significance of each permutation was recorded, the significance level was set at $p < 0.05$ and the proportion of statistically

significant permutations to the total number of permutations was recorded. The number of permutations for each comparison is available in Table 5.2A for WT and Table 5.2B for MT. The investigation into form and shape was conducted for each permutation individually instead of using the available PC scores from the full comparison. This was chosen to better simulate real treatment studies where only the available animals would be included in the morphological analysis.

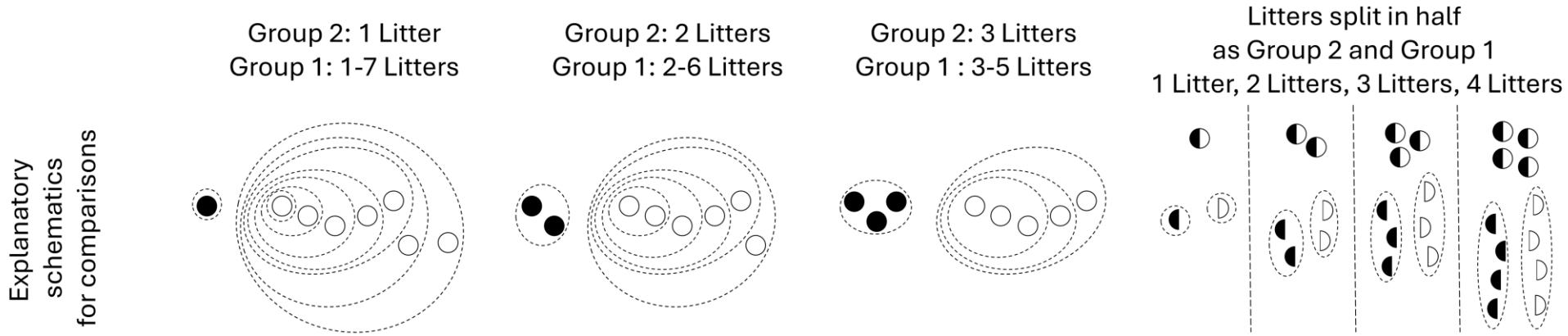

Figure 5.6 Grouping compositions for statistical comparison of grouping effects. Circles represent one litter and half circles represent a random half of a litter. Black for the group 2, white for the group 1, dotted outline highlights the considered group composition.

Table 5.2 Number of permutations of each grouping analysis comparison. a) number for permutations in P21 WT animals and b) number of permutations in P21 MT animals.

a) Number of permutations for different compositions of group 2 and group 1 for P21 WT															
Group 2	**1**							**2**					**3**		
Group 1	1	2	3	4	5	6	7	2	3	4	5	6	3	4	5
Permutations	112	495	1320	2310	2772	2310	1320	1980	4620	6930	6930	4620	9240	11550	9240

b) Number of permutations for different compositions of group 2 and group 1 groups for P21 MT															
Group 2	**1**							**2**					**3**		
Group 1	1	2	3	4	5	6	7	2	3	4	5	6	3	4	5
Permutations	74	252	504	630	504	252	74	756	1260	1260	756	252	1680	1260	504

In addition to the effect of treatment group and baseline group sizes, a different method for separating the litters into group 2 and group 1 was investigated. Here, a litter was separated randomly in half into two groups (group 2 and group 1). The two were either directly compared for statistical significance or combined from 2, 3, or 4 halved litters, where a half of each litter was assigned to the group 2, and a half to the group 1. This analysis includes computationally intractable numbers of potential permutations as each litter can be split differently and then combined with another litter. Thus, a random sample of the permutations was chosen and included in the analysis. For 1 litter only 18 permutations were possible in the mutant data as at least 4 animals were required for the analysis when only 1 litter was investigated, only 3 litters in the mutant data satisfied this condition, thus the results for 1 litter split are significantly less reliable than the others. For 2 litter combinations, 960 permutations were included. For 3 litter combinations, 5134 permutations were included and for 4 litter combinations, 11020 permutations were included. The results of this analysis is included in each section individually accompanied by explanatory graphics of the group 2 and group 1 compositions.

5-2-6 Suture patency and craniofacial morphology correlation analysis

Correlation analysis was carried out by producing a correlation matrix which included the suture patency, linear measurements, and PC scores. This analysis was conducted for both P21 and P42 MT animals.

For P21, linear and quadratic regression analyses were carried out to understand the interplay between different suture fusion effects on the skull shape. Metopic, coronal, sagittal, interparietal sutures, and the ISS were investigated as predictors for the first 14 PC scores (95% of shape variation). Additionally, just metopic, coronal, and interparietal sutures were investigated as predictors as these showed the highest correlation levels with overall shape.

For P21, MT animals animated visualisations of the individual PCs contribution to the skull shape were produced. The corresponding correlations to the different suture patency scores were included to help qualitatively highlight the effect of patency on skull shape.

5-2-7 Statistical analysis

Statistical analyses was performed in SPSS (IBM SPSS, NY, USA), R, and Python for the various analyses. One-way analysis of variance (ANOVA), with Levene's test was used to test for equal variances. MANOVA was used in comparisons of PC scores including the first PC scores to account for 95% of the variation. The significance level was set at $p < 0.05$. Correlation ranges: $-0.8 > c$, very strong negative correlation,

$-0.6 > c > -0.8$, strong negative correlation $-0.4 > c > -0.6$, moderate negative correlation,

$-0.2 > c > -0.4$, weak negative correlation, $0.2 > c > -0.2$, no correlation, $0.4 > c > 0.2$, weak positive correlation, $0.6 > c > 0.4$ moderate positive correlation, $0.8 > c > 0.6$, strong positive correlation, $c > 0.8$, very strong positive correlation.

5-3 Results

5-3-1 Linear measurements

Figure 5.7 summarises the linear measurements for each litter. The averages for each group (P21 MT, P21 WT, P42 MT and P42 WT) are available in Table 5.3. The grouping analysis is available in Figure 5.12 for P21 animals. The full analysis for the P42 could not be carried out due to an insufficient number of litters available, but partial P42 MT analysis is available in Figure 5.13. These data highlighted that:

1) The length of the skull increased from P21 to P42 for both MT and WT animals, with MT showing an 8.4% increase compared to WT's 13.0% increase. All other measurements remained consistent between age groups for both MT and WT animals. (Table 5.3)

2) High variation between litters was observed in both WT and MT animals at P21, with individual variation being higher in MT animals. The length measurements in WT animals showed particularly tight distributions within litters (0.24mm standard deviation) compared to across-group variation (0.47mm standard deviation) (Figure 5.7 and Figure 5.8).

3) The incidence of statistically significantly different groups between the possible groupings of the litters ranged from 10-30% in MT animals and 15-56% in WT animals with four litters used as the "baseline". When separating each litter into "treated" and

“baseline” groups in half, the statistical significance was reduced to around 5% in all cases except 1 litter MT skull length measurement (11%) (Figure 5.12).

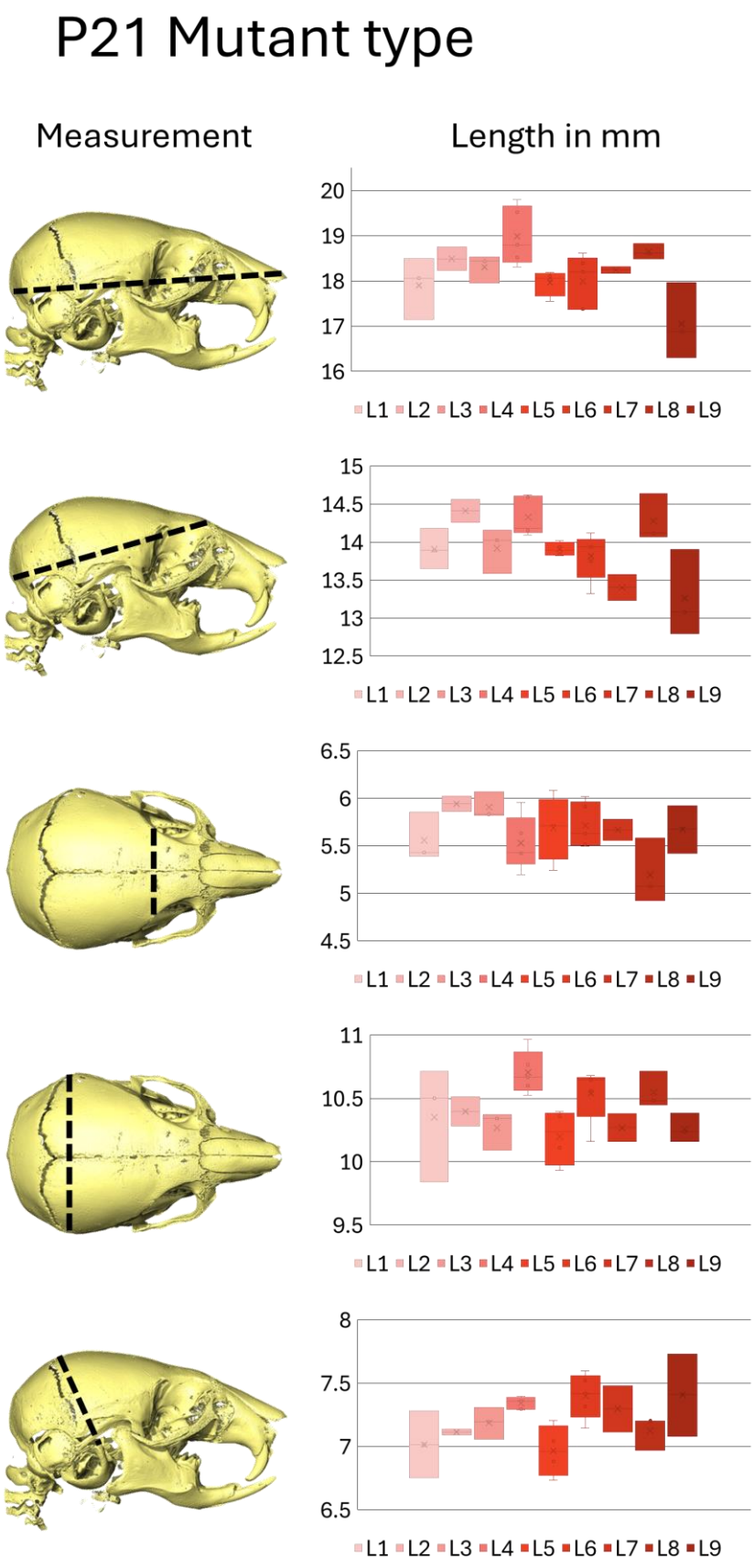

Figure 5.7 Linear measurements across the skull, including skull length, braincase length, frontal bone width, braincase width, and braincase height for each litter in P21 MT.

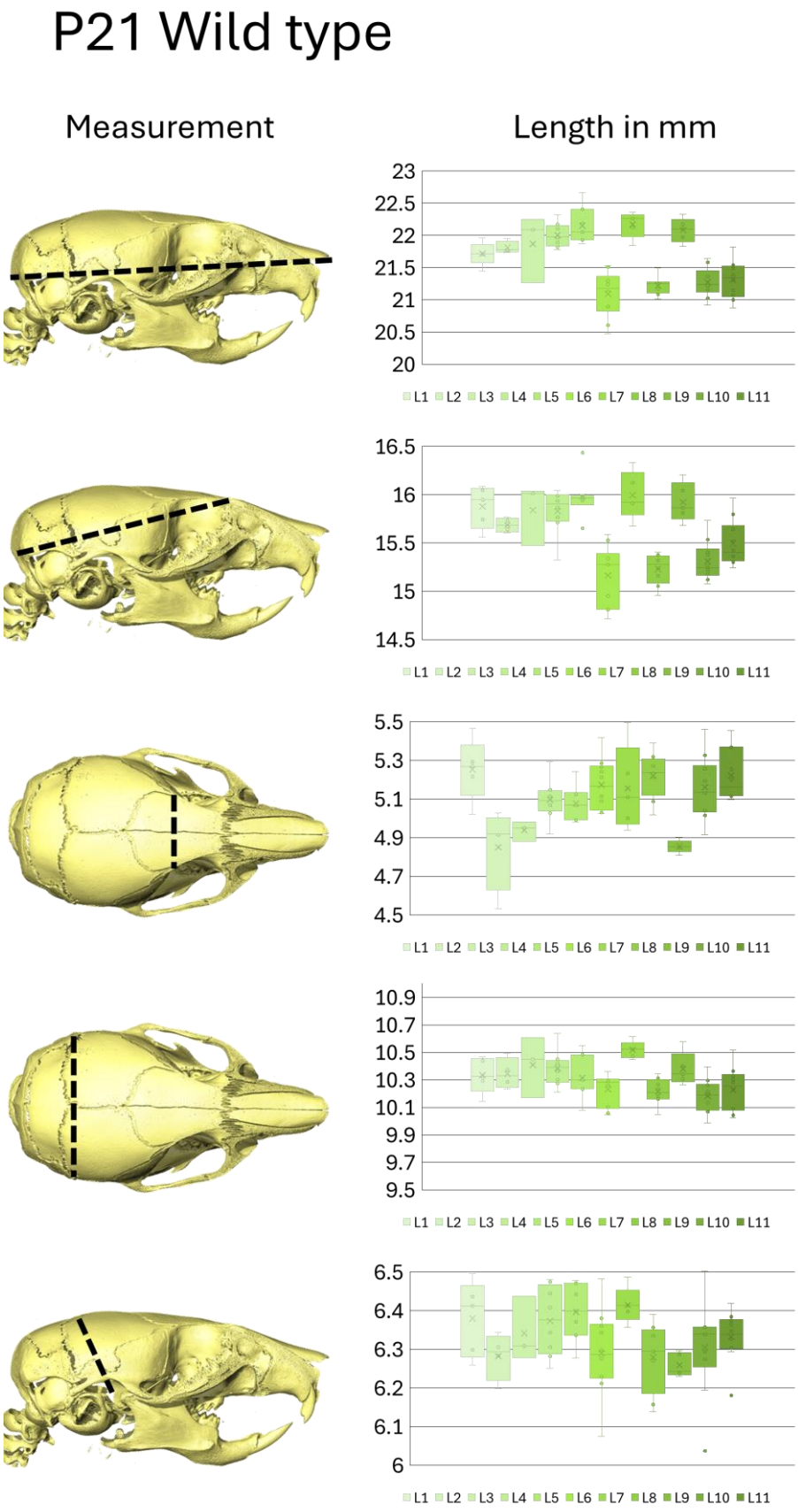

Figure 5.8 Linear measurements across the skull, including skull length, braincase length, frontal bone width, braincase width, and braincase height for each litter in P21 WT.

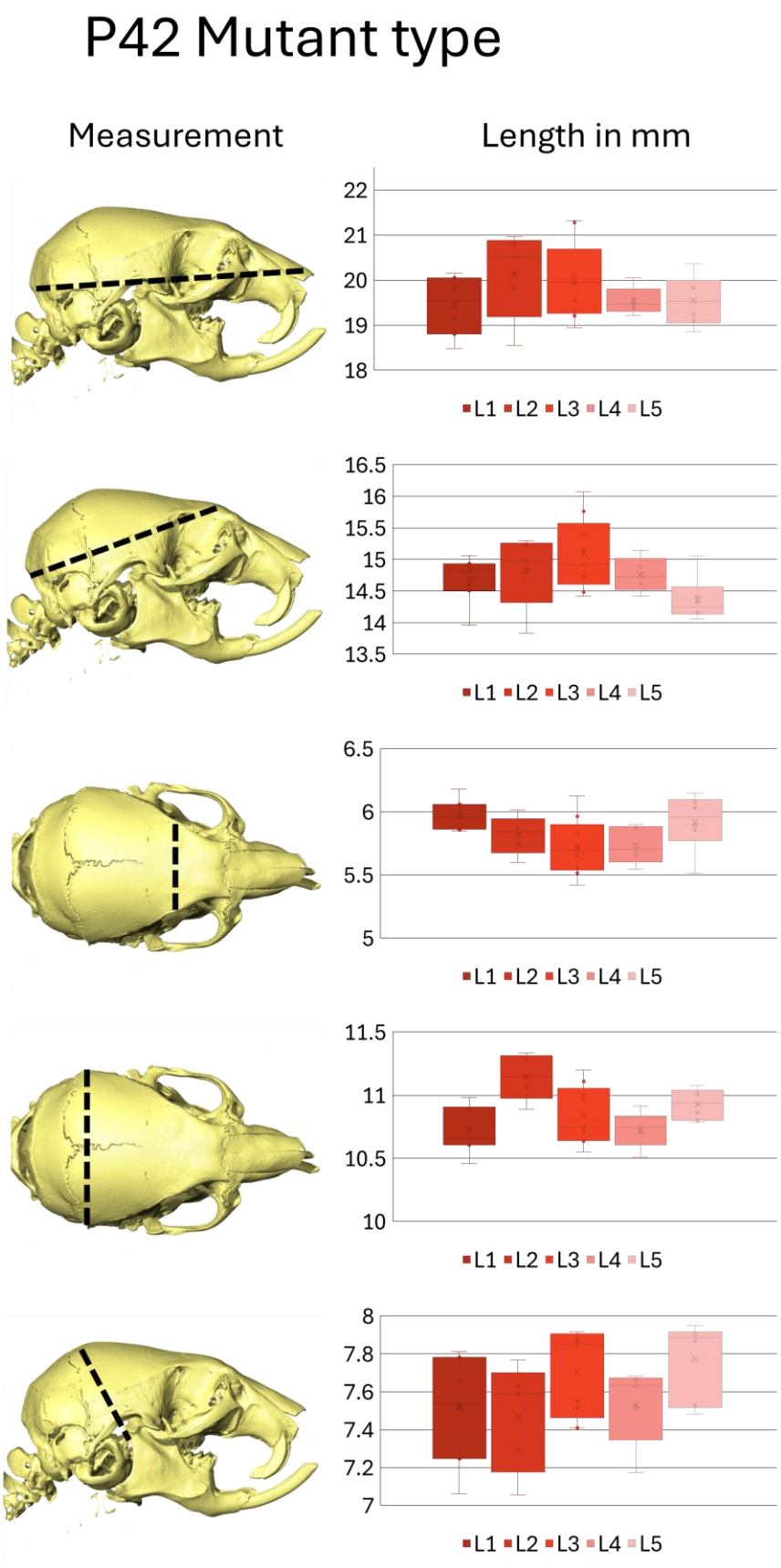

Figure 5.9 Linear measurements across the skull, including skull length, braincase length, frontal bone width, braincase width, and braincase height for each litter in P42 MT.

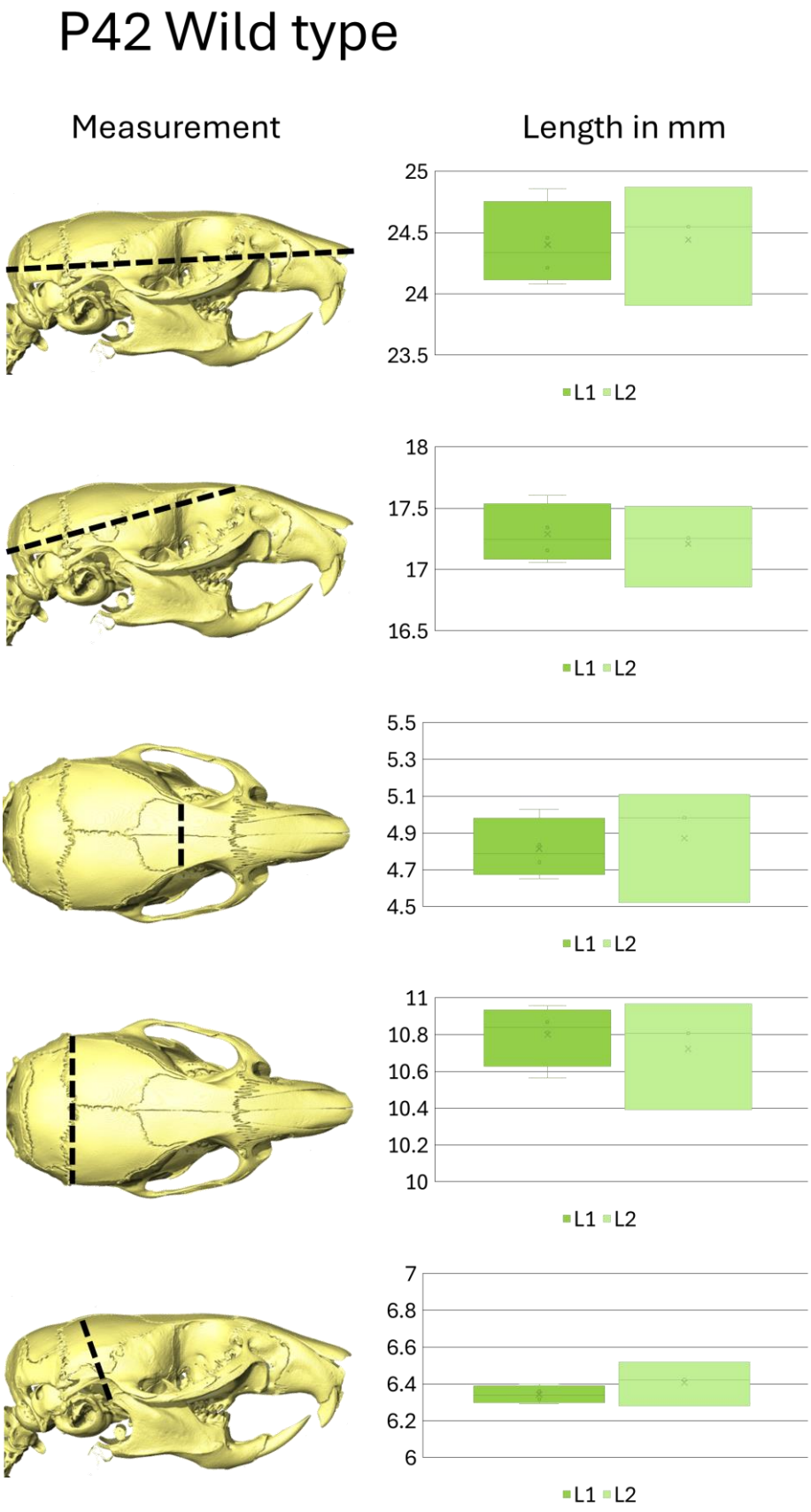

Figure 5.10 Linear measurements across the skull, including skull length, braincase length, frontal bone width, braincase width, and braincase height for each litter in P42 WT.

Table 5.3 Average linear measurements and standard deviations in each group (P21 MT, P21 WT, P42 MT, and P42 WT).

Linear measurement averages across all the litters in the age/type group						
Group	**Results**	**Skull length (mm)**	**Braincase length (mm)**	**Frontal width (mm)**	**Braincase width (mm)**	**Braincase height (mm)**
P21 MT	Average	**18.20**	**13.94**	**5.64**	**10.42**	**7.22**
	Standard deviation	0.71	0.44	0.30	0.26	0.23
P21 WT	Average	**21.61**	**15.59**	**5.12**	**10.30**	**6.33**
	Standard deviation	0.47	0.38	0.18	0.15	0.10
P42 MT	Average	**19.73**	**14.77**	**5.83**	**10.86**	**7.61**
	Standard deviation	0.73	0.50	0.20	0.23	0.26
P42 WT	Average	**24.42**	**17.26**	**4.84**	**10.77**	**6.37**
	Standard deviation	0.37	0.26	0.21	0.21	0.08

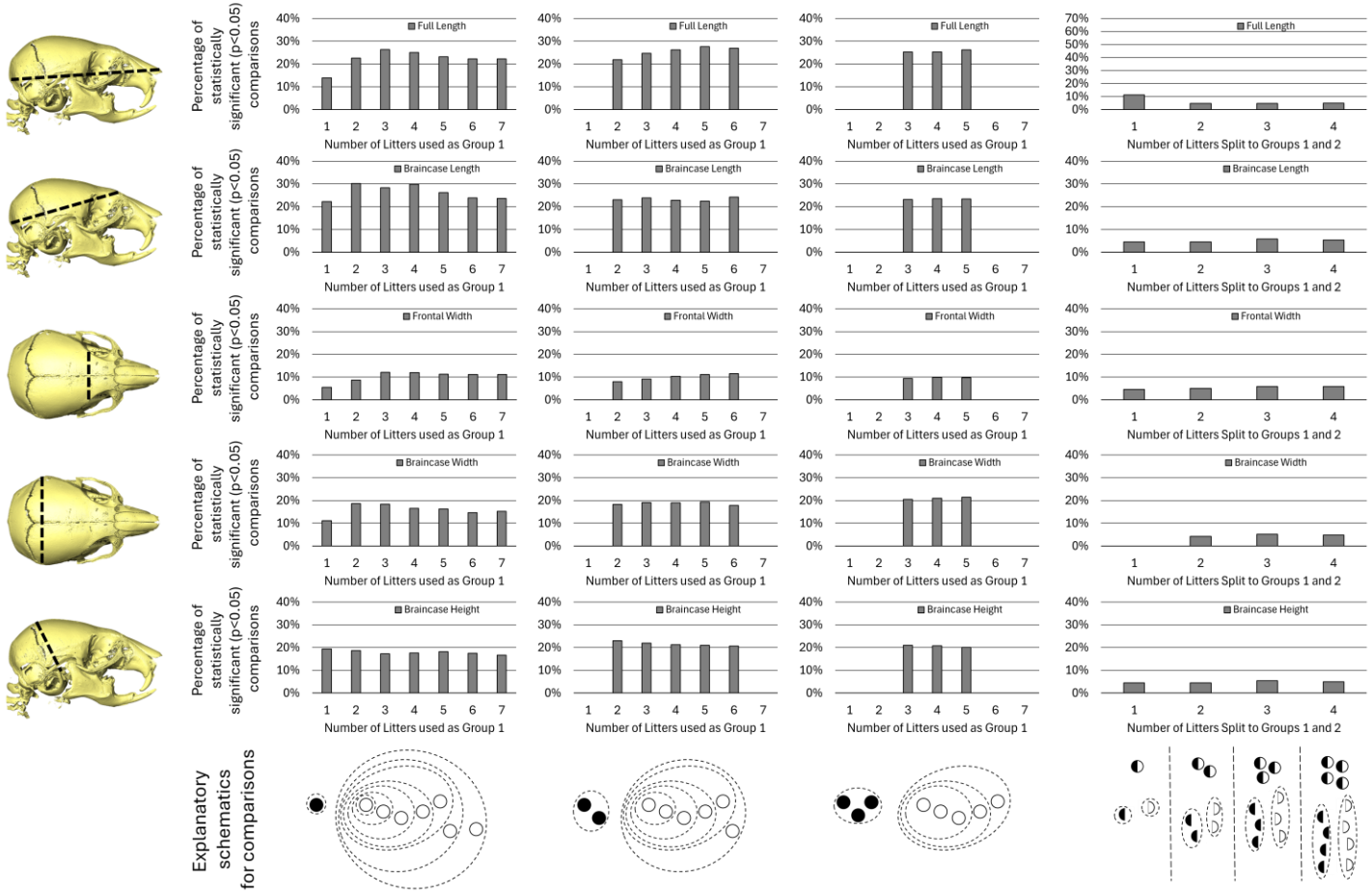

Figure 5.11 Grouping analysis results of the 5 investigated linear measurements for P21 MT animals. One, two, and three litters were used as the group 2 with one, two, three, four, five, six, and seven litters as the group 1. As well as one to four litters were split in half where one half was the group 2 and one was group 1. Explanatory illustrations for the separation are included.

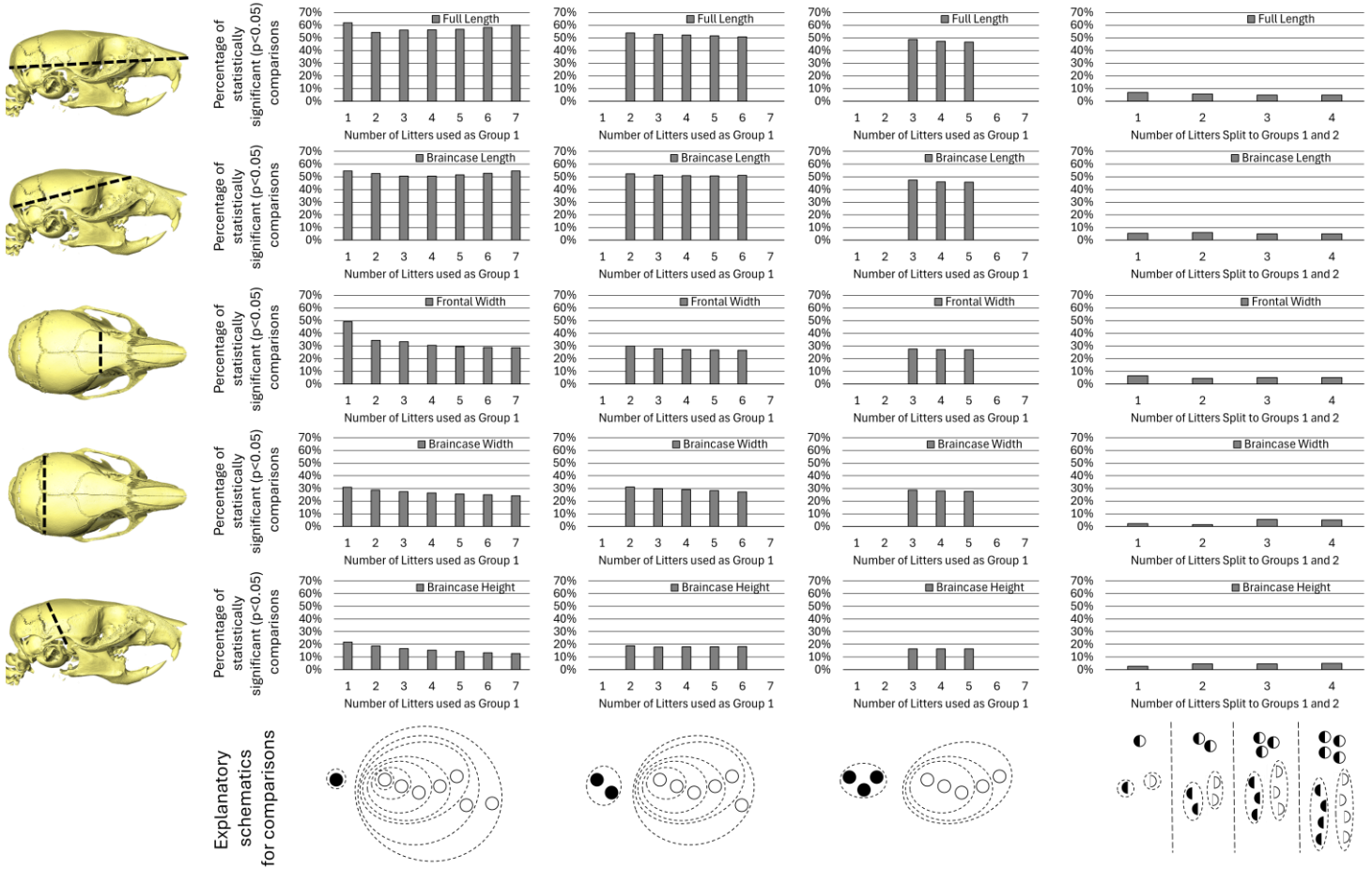

Figure 5.12 Grouping analysis results of the 5 investigated linear measurements for P21 WT animals. One, two, and three litters were used as the group 2 with one, two, three, four, five, six, and seven litters as the group 1. As well as one to four litters were split in half where one half was the group 2 and one was group 1. Explanatory illustrations for the separation are included.

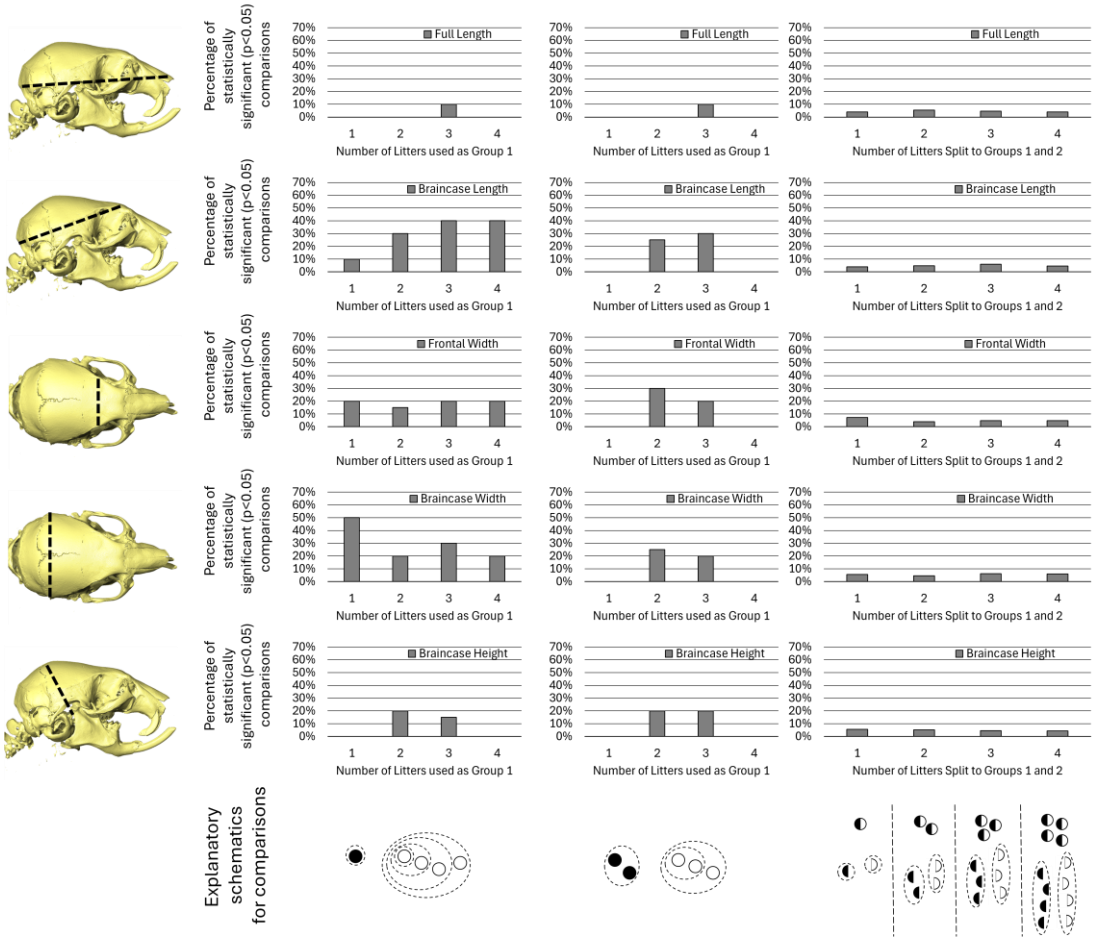

Figure 5.13 Partial grouping analysis results of the 5 investigated linear measurements for P42 MT. One and two three litters were used as the group 2 with one, two, three, and four litters as the group 1. As well as one to four litters were split in half where one half was the group 2 and one was the group 1. Explanatory illustrations for the separation are included.

5-3-2 Principal component analysis (PCA)

PCA was carried out for all animals and for each group individually. Both size and shape and shape only (see Figure 5.14Figure 5.15Figure 5.16Figure 5.17 Figure 5.18) analyses were conducted. Grouping analysis analogous to the linear measurements was carried out for the PC scores, the landmark data was grouped as described in the methodology and PCA was conducted for each grouping individually to best simulate the conditions in regular experiments where the other animals would not be available (Figure 5.19). The data highlighted:

1) PC1 in both form and shape analysis for all animals combined largely captured the severity of the phenotype, with MT and WT animals separated clearly in the component. The MT and WT animals were not clearly separated in PC2, but P21 and P42 in both the MT and WT groups were separated in PC2. For both PC1 and PC2 for all animals, strong correlations were observed with the individual group's (P21 MT, P21 WT, P42 MT and P42 WT) PC1 and PC2 scores.

2) The P42 MT animals grouped closer to the WT animals in PC1, which largely described the differences between MT and WT animals, for form (see Figure 5.14), however, this was not the case in the shape analysis. Thus, while the overall size of the P42 MT animals was more like the WT animals, the shape of the skull remained close to that of the P21 MT animals.

3) Litter clustering was present in all investigated groups for both form and shape (Figure 5.14c-j). All groups showed statistically significant differences ($p < 0.05$) between the litters across the top PC scores (top 14 for MT and top 17 for WT) accounting for 95% of the variation, with a singular exception of P42 WT Form ($p=0.071$).

4) For the MT animals, the incidence of statistically significant separation of litters ranged from 13-15% for form and 13-16% for shape with 4 litters as group 1. For the WT animals, it ranged from 12-16%, and 12-14% for form and shape respectively. Separation of litters into two groups reduced this to around 5% in all cases.

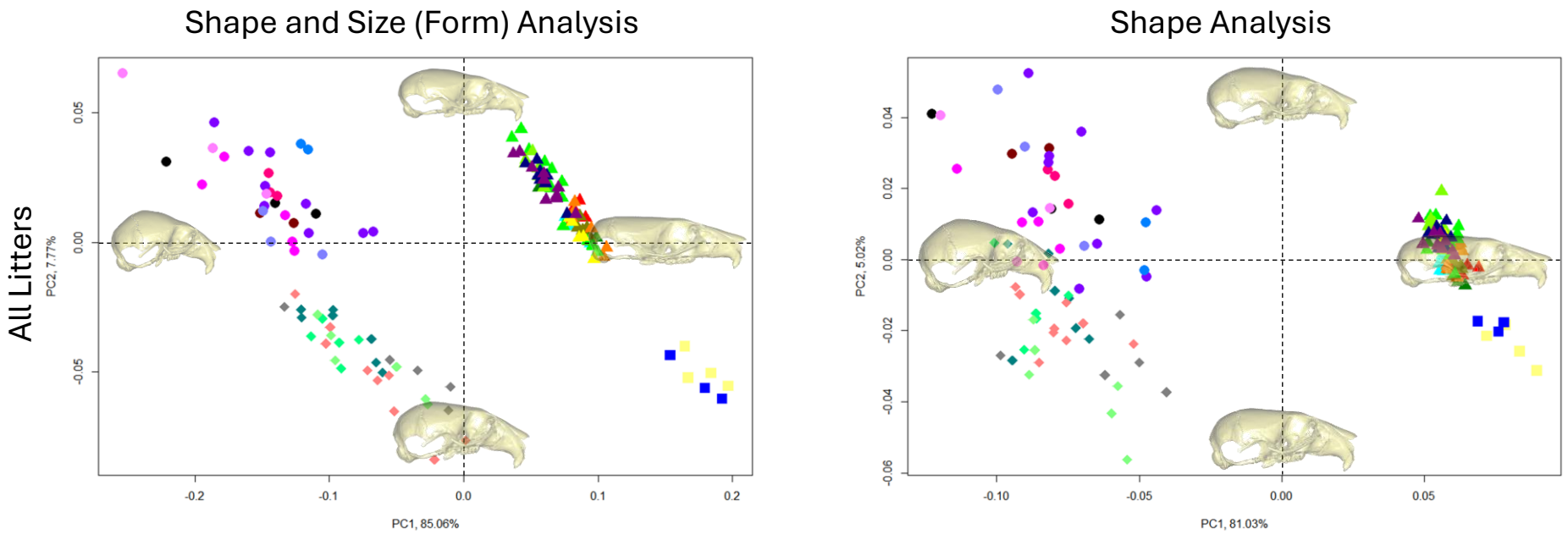

Figure 5.14 PC1 against PC2 plot from the PCA analysis for both shape and size, and shape. With different litters highlighted by different coloured markers. All litters shape and size and shape – circle: P21 MT, rhombus: P42 MT, triangle: P21 WT and square: P42 WT.

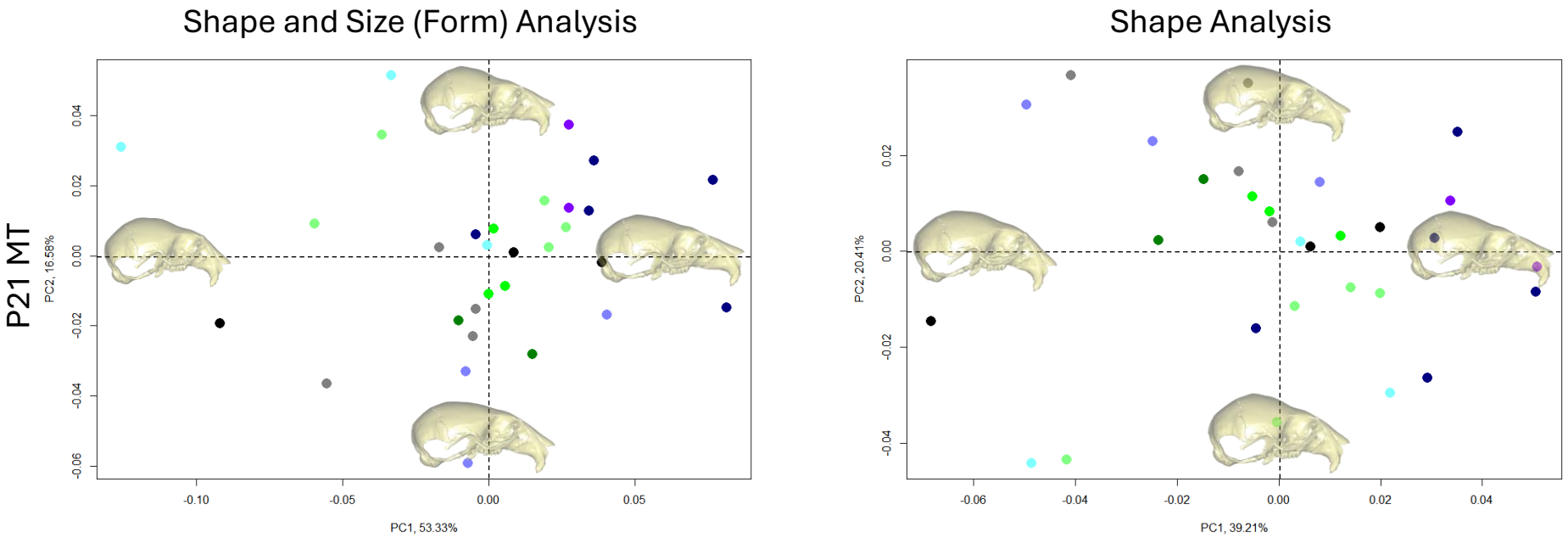

Figure 5.15 PC1 against PC2 plot from the PCA analysis for both shape and size, and shape. With different litters highlighted by different coloured markers. P21 MT shape and size and shape.

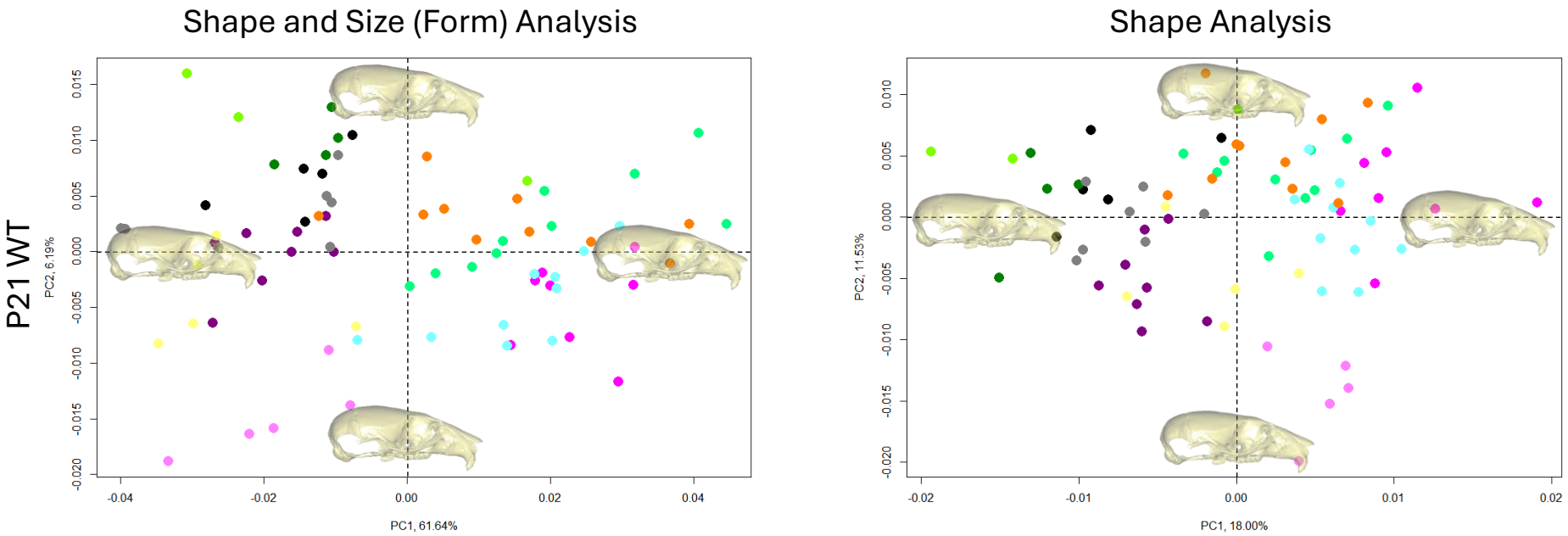

Figure 5.16 PC1 against PC2 plot from the PCA analysis for both shape and size, and shape. With different litters highlighted by different coloured markers. P21 WT shape and size and P21 WT shape.

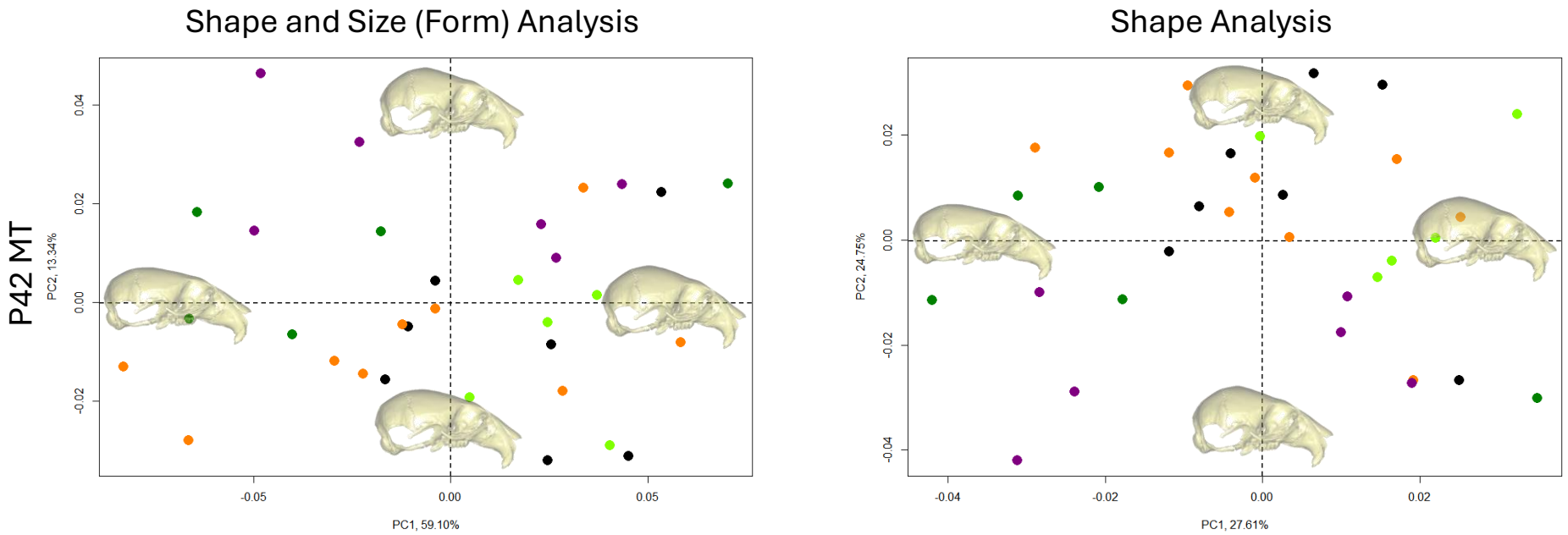

Figure 5.17 PC1 against PC2 plot from the PCA analysis for both shape and size, and shape. With different litters highlighted by different coloured markers. P42 MT shape and size and shape.

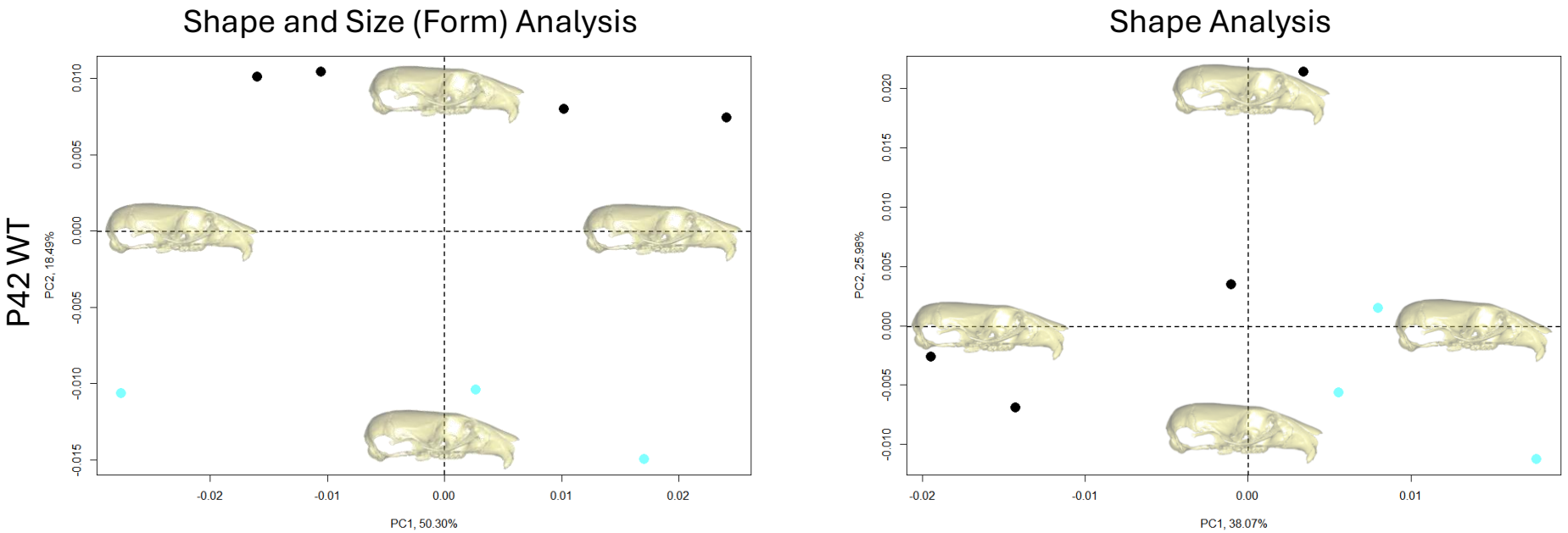

Figure 5.18 PC1 against PC2 plot from the PCA analysis for both shape and size, and shape. With different litters highlighted by different coloured markers. P42 WT shape and size and shape.

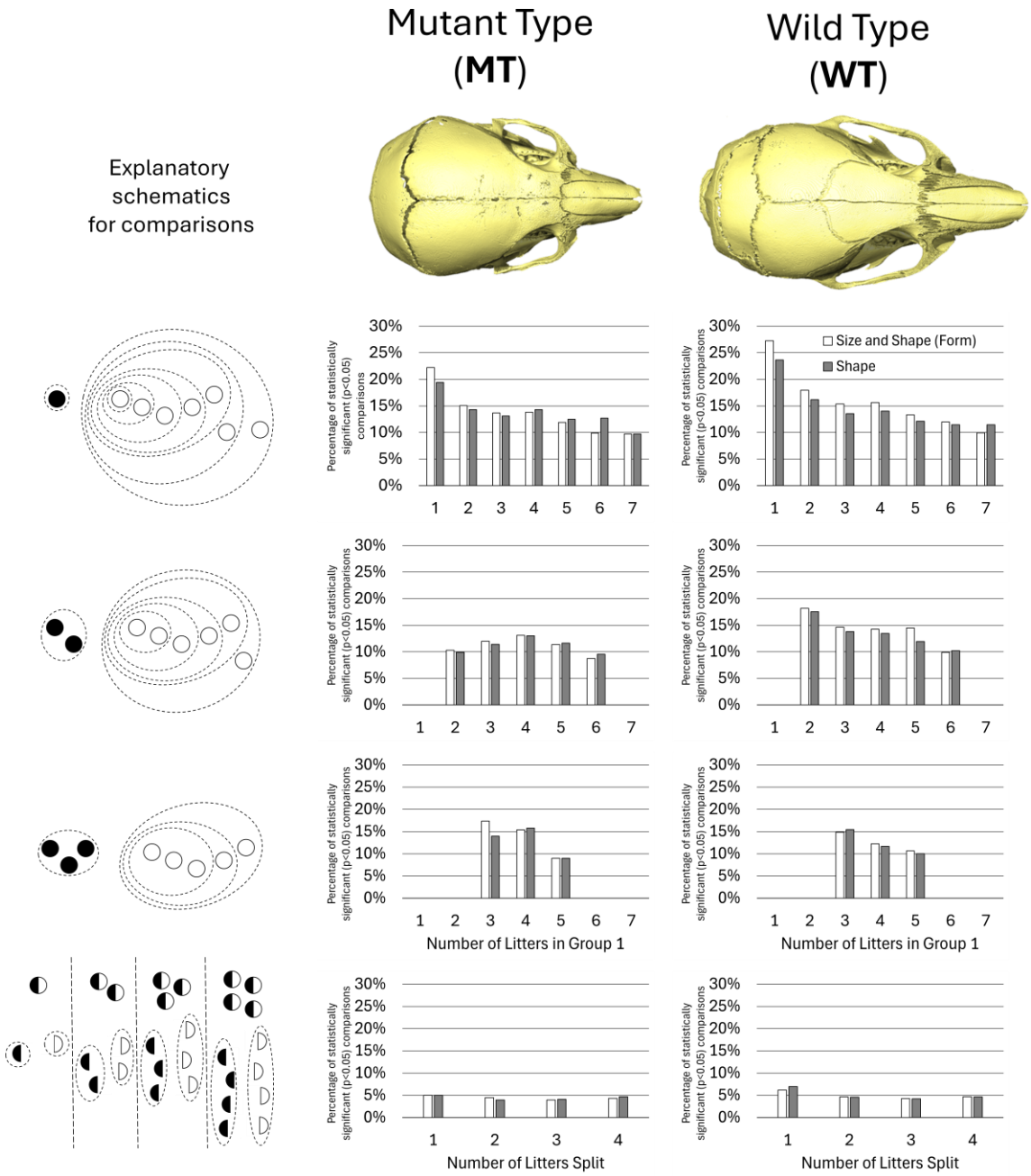

Figure 5.19 Grouping analysis carried out for the PC scores (first n PC scores to account for 95% of the variation) in P21 MT and WT animals. The PCA was conducted for each grouping permutation individually.

5-3-3 Suture patency

The patency of the metopic, coronal, sagittal, and interparietal sutures as well as the ISS was investigated quantitatively in the P21 MT and P42 MT animals. The patency percentages, where 100% is fully patent and 0% is fully fused, and the grouping analysis are available in Figure 5.20. The average patency across each suture is available in Table 5.4. The data highlighted:

1) At P21, suture fusion was observed in all the investigated sutures. The coronal suture was most affected at 18% patency while the sagittal suture remained the most patent at 89% average patency across the whole group. The largest variation was present in the coronal suture patency, with standard deviation of 26%, and the lowest variation was for the interparietal suture at 12% (Table 5.4).

2) Individuals with entirely patent sutures were observed for the coronal, sagittal, and interparietal sutures. No fully patent metopic sutures were observed (Figure 5.20). The litter appeared to have significantly less effect on suture patency compared to the previously observed shape variation, with notable exceptions of interparietal suture (average standard deviation within litters – 8%, standard deviation within group – 12%) and the ISS (average standard deviation within litters – 9%, standard deviation within group – 15%).

3) The grouping analysis largely reflected the litter effect on patency variation with relatively small incidence of statistical significance in metopic, coronal, and sagittal sutures ranging from 2% to 11%, where 4 litters are used as the baseline. This is significantly lower than the range between 25% and 31% for the interparietal and ISS patency. Once again, the separation of each litter into “treated” and baseline groups individually if at least two litters are included and reduced the incidence to around 5% (Figure 5.20).

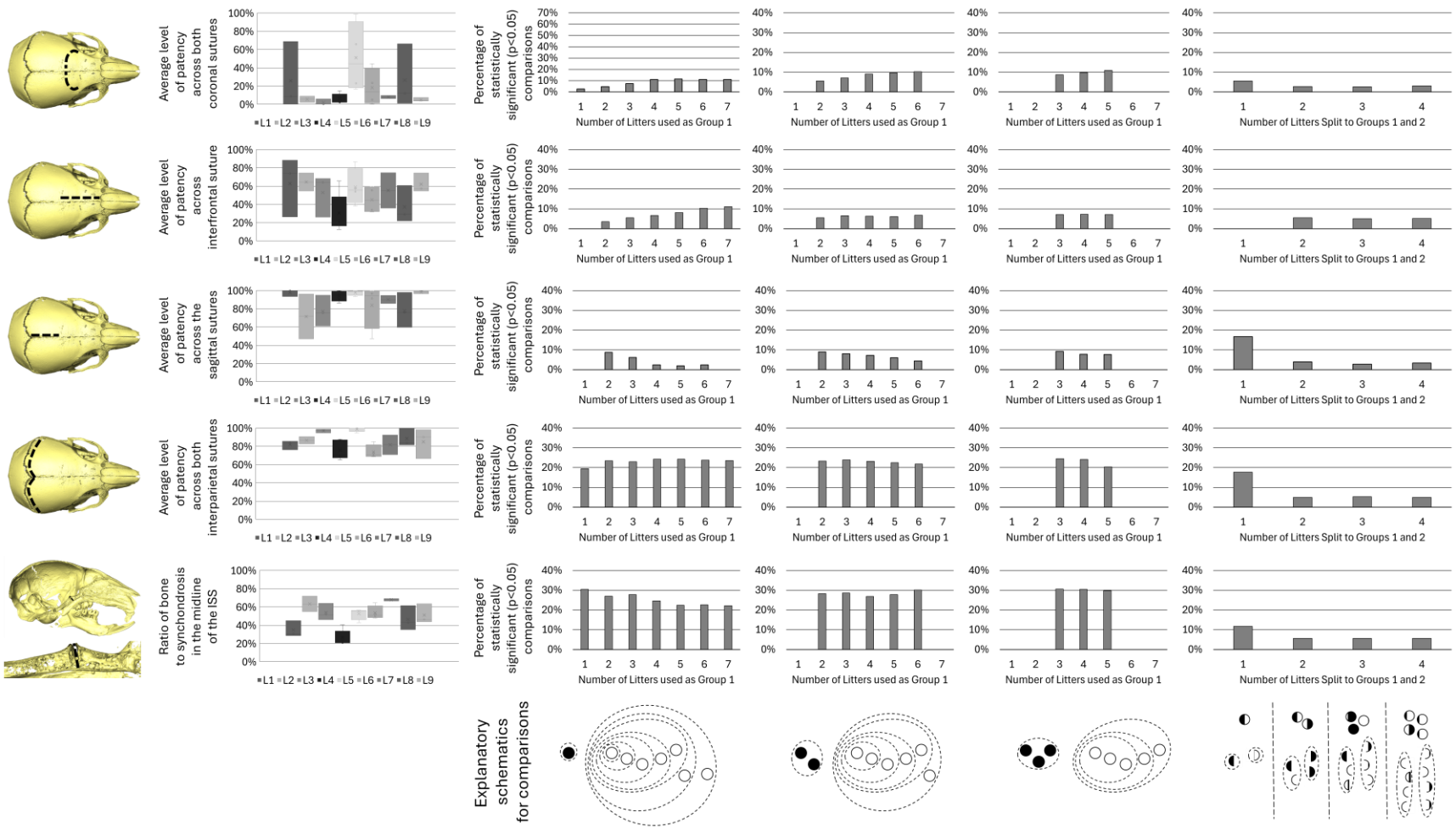

Figure 5.20 Suture and synchondrosis patency measurements and grouping analysis. Included joints in the order they appear in were coronal sutures, metopic suture, sagittal suture, lambdoid suture, and the inter-sphenoid synchondrosis. The grouping analysis carried out and presented the same as for the linear measurements.

Table 5.4 Average patency and standard deviations in each group (P21 MT and P42 MT). *Not available – the patency across the suture was not quantified as the sutures were fully fused in all the considered specimens.

Patency across the sutures and the ISS at P21 and P42 in the MT animals						
Group	**Results**	**Metopic**	**Coronal**	**Sagittal**	**Interparietal**	**ISS**
P21 MT	Average	**50%**	**18%**	**89%**	**85%**	**47%**
	Standard deviation	22%	26%	16%	12%	15%
P42 MT	Average	**0%**	**0%**	**20%**	**43%**	**0%**
	Standard deviation	N/A*	N/A*	20%	23%	N/A*

5-3-4 Intra vs inter litter variation

The results of the grouping analysis are largely presented in the preceding sections. The analysis largely focuses on study design and the effect of inter-litter variation on statistical significance between groups 2 and 1. The litter effects were investigated directly on the suture patency, linear measurements, and shape PC scores for the individual groups by intraclass correlation coefficients. P21 MT animals and P21 WT animals were investigated (Table 5.5). The results highlighted:

1) The ICC values for the suture patency in P21 MT animals largely reflect previous observations made with metopic, coronal, and sagittal suture patency levels suggesting weak correlation with the litters ranging from 0.26 to 0.32, while moderate correlation is observed for the interparietal suture patency at 0.46 and strong correlation for the ISS at 0.68.

2) The linear measurements in the WT animals correlated differently with litter. Centroid size, skull length, and braincase length all correlated strongly with the litters at 0.69, 0.72, and 0.65, respectively, with the frontal width correlating moderately at 0.54 and braincase width, and height correlating weakly at 0.39 and 0.26, respectively. The overall correlation in the MT animals is not as strong with the only strong correlation of braincase length at 0.65. All other measurements correlate moderately ranging from 0.41 to 0.52.

3) A similar trend is observed in the PC scores, with PC1 correlating very strongly at 0.82 in the WT animals, while the correlation is not as strong, however, was still present in the MT animals. Many of the PCs for both WT and MT animals suggest moderate to strong correlation with litter.

Table 5.5 Intraclass correlation coefficients, in P21 MT (patency, linear measurements, and shape PC scores) and P21 WT (linear measurements and shape PC scores). The PC scores are independent and unrelated between the WT and MT with the PCA carried out individually for each group.

Intraclass correlation coefficients			
Type	**Measurement**	**P21 WT**	**P21 MT**
Patency	Metopic	N/A	0.26
	Coronal	N/A	0.32
	Sagittal	N/A	0.32
	Interparietal	N/A	0.46
	ISS	N/A	0.68
Linear Measurements	Centroid Size	0.69	0.41
	Skull length	0.72	0.52
	Braincase length	0.65	0.65
	Frontal width	0.54	0.41
	Braincase width	0.39	0.45
	Braincase height	0.26	0.42
Shape PC scores (unrelated between WT and MT)	PC1	0.82	0.41
	PC2	0.74	0.53
	PC3	0.54	0.58
	PC4	0.66	0.60
	PC5	0.32	0.61
	PC6	0.41	0.41
	PC7	0.16	0.40
	PC8	0.38	0.17
	PC9	0.39	0.41
	PC10	0.26	0.34
	PC11	0.21	0.24
	PC12	0.48	0.49
	PC13	0.25	0.24
	PC14	0.12	0.16

5-3-5 Suture patency and craniofacial shape correlation

To understand the effects of suture patency on craniofacial shape, a correlation matrix was produced for both P21 MT (Figure 5.21a) and P42 MT (Figure 5.21b) animals. However, due to full obliteration of the other sutures, only the sagittal and interparietal sutures retained quantifiable patency at P42, thus only those sutures were considered in the P42 MT animals. For P21 MT animals, key PC score min and max shapes were visualised with the corresponding suture correlation coefficients included (see Figure 5.22, Figure 5.23Figure 5.24Figure 5.25). Animated morphs are included for all the PCs and their accompanying suture patency correlation coefficients (Appendix III – electronic version only). Static images of all the PCs are available for both P21 MT animals and P42 MT animals (Appendix III).

Linear and quadratic regression was carried out at P21 with metopic, coronal, sagittal, interparietal sutures, and the ISS as predictors for the PC scores; 3 animals were excluded from the data set to test for overfitting. The linear and quadratic regression was then repeated with only the metopic, coronal, and interparietal sutures as predictors (see Figure 5.26 and Figure 5.27). The results from the two investigations highlighted:

1) Suture patency showed positive correlations between different sutures, ranging from no correlation (sagittal-interparietal, c = 0.15) to moderate correlation (metopic-interparietal, c = 0.43). The ISS demonstrated negative correlation with sagittal suture patency, while metopic, coronal, and interparietal sutures showed a strong correlation with overall patency sum.

2) Negative correlations emerged between patency and skull dimensions, with metopic patency showing a moderate negative correlation with centroid size and skull length. The interparietal suture demonstrated the strongest correlation (c = -0.70) with braincase dimensions, while overall patency positively correlated with increased calvarial curvature.

3) PC1 captured overall phenotypic severity, with moderate negative correlations to metopic, coronal, and interparietal patency at P21. PC2 reflected calvarial bulge variations, showing moderate positive correlation with interparietal patency and weak positive correlations with coronal and ISS patency. PC3 and PC4 demonstrated weak

correlations with various suture patency levels, primarily related to calvarial bulge characteristics.

4) Quadratic regression model showed superior correlation compared to linear models when using metopic, coronal, and interparietal sutures as predictors. The reduced predictor set prevented overfitting, while maintaining enhanced predictive power.

a)

P21	Coronal	ISS	Saggital	Metopic	Patency Sum	Centroid Size	Full Length	Braincase Length	Frontal Width	Braincase Width	Braincase Height	Braincase Curve Length	Braincase Curve to Length Ratio	PC1	PC2	PC3	PC4	PC5	PC6	PC7	PC8	PC9	PC10	PC11	PC12	PC13	PC14
Interparietal	0.35	0.34	0.15	0.43	0.74	-0.38	-0.23	0.01	0.18	-0.51	-0.70	0.25	0.41	-0.55	0.41	0.05	-0.23	0.22	0.16	0.21	-0.31	0.44	-0.03	-0.09	0.04	-0.03	-0.02
Coronal		0.11	0.31	0.35	0.69	-0.35	-0.26	0.01	-0.14	-0.40	-0.51	0.33	0.56	-0.60	0.34	0.21	-0.11	-0.09	0.09	0.01	0.09	-0.26	0.01	-0.20	0.04	0.00	0.21
ISS			-0.34	0.18	0.42	-0.19	-0.20	-0.20	0.19	-0.35	-0.13	0.08	0.45	-0.17	0.22	0.32	0.12	0.03	0.30	0.16	-0.03	0.48	-0.05	-0.03	-0.03	0.26	0.11
Saggital				0.32	0.47	-0.30	-0.28	-0.18	0.20	0.00	-0.14	-0.14	0.06	-0.12	-0.21	0.01	-0.12	0.37	0.08	0.18	-0.01	-0.13	0.15	-0.15	-0.12	-0.06	-0.16
Metopic					0.75	-0.58	-0.56	-0.33	0.59	-0.44	-0.51	-0.16	0.28	-0.47	-0.11	0.19	0.15	0.49	-0.03	0.13	0.09	0.19	0.06	-0.11	-0.01	0.28	0.35
Patency Sum						-0.59	-0.50	-0.23	0.33	-0.55	-0.65	0.12	0.58	-0.62	0.21	0.25	-0.06	0.33	0.20	0.22	-0.05	0.24	0.04	-0.19	-0.03	0.15	0.16
Centroid Size							0.96	0.74	-0.25	0.63	0.34	0.44	-0.48	0.65	0.38	-0.42	0.02	-0.27	-0.19	-0.26	0.02	0.01	0.00	0.05	-0.05	-0.08	0.03
Full Length								0.82	-0.26	0.54	0.20	0.54	-0.46	0.54	0.50	-0.42	-0.13	-0.21	-0.15	-0.31	0.08	0.03	-0.01	0.04	-0.04	-0.17	-0.02
Braincase Length									-0.18	0.45	-0.13	0.83	-0.26	0.05	0.48	-0.55	-0.15	-0.13	-0.28	-0.40	-0.02	-0.06	0.04	0.04	0.02	-0.10	-0.03
Frontal Width										0.01	-0.04	-0.14	0.06	-0.04	-0.31	0.11	-0.06	0.57	-0.32	0.36	0.05	0.30	-0.25	0.12	0.01	0.14	0.19
Braincase Width											0.43	0.16	-0.49	0.45	-0.23	-0.37	-0.08	-0.17	-0.33	-0.09	-0.11	-0.09	0.26	0.32	-0.29	-0.16	0.05
Braincase Height												-0.19	-0.09	0.63	-0.35	0.26	0.15	-0.20	-0.22	-0.05	0.11	-0.12	-0.12	0.01	-0.05	0.01	-0.31
Braincase Curve Length													0.33	-0.28	0.62	-0.21	-0.05	-0.20	-0.34	-0.32	-0.03	0.02	-0.09	0.06	0.02	0.01	-0.12
Braincase Curve to Length Ratio														-0.56	0.26	0.57	0.17	-0.11	-0.12	0.12	0.00	0.12	-0.21	0.03	0.01	0.17	-0.17
PC1															0.00	0.00	0.00	0.00	0.00	0.00	0.00	0.00	0.00	0.00	0.00	0.00	0.00
PC2																0.04	0.02	-0.08	0.12	-0.15	-0.06	0.07	-0.12	0.03	-0.02	-0.04	0.00
PC3																	-0.01	0.03	-0.04	0.06	0.02	-0.02	0.05	-0.01	0.01	0.02	0.00
PC4																		0.01	-0.02	0.03	0.01	-0.01	0.02	0.00	0.00	0.01	0.00
PC5																			0.09	-0.11	-0.05	0.05	-0.09	0.02	-0.02	-0.03	0.00
PC6																				0.17	0.07	-0.07	0.14	-0.03	0.02	0.05	0.00
PC7																					-0.09	0.09	-0.17	0.04	-0.03	-0.06	0.00
PC8																						0.04	-0.07	0.02	-0.01	-0.02	0.00
PC9																							0.07	-0.02	0.01	0.02	0.00
PC10																								0.03	-0.03	-0.05	0.00
PC11																									0.01	0.01	0.00
PC12																										-0.01	0.00
PC13																											0.00

continued on the next page…

b)

P42	Sagittal	Patency Sum	Centroid	Full Length	Braincase Length	Frontal Width	Braincase Width	Braincase Height	Braincase Curve Length	Braincase Curve to Length Ratio	PC1	PC2	PC3	PC4	PC5	PC6	PC7	PC8	PC9	PC10	PC11	PC12	PC13	PC14	PC15	PC16	PC17
Interparietal	0.08	0.73	0.51	0.58	0.58	0.07	0.16	-0.77	0.39	-0.36	-0.55	0.54	0.02	0.33	0.04	-0.01	0.23	-0.04	-0.14	0.07	0.11	0.16	-0.13	0.12	0.09	-0.10	0.10
Sagittal		0.73	0.15	0.15	0.17	-0.08	0.32	-0.04	0.13	-0.05	0.01	0.08	0.02	-0.21	-0.35	0.35	0.01	-0.26	0.11	0.36	0.30	-0.20	-0.06	0.30	0.08	-0.01	-0.10
Patency Sum			0.45	0.50	0.51	-0.01	0.32	-0.55	0.36	-0.28	-0.36	0.42	0.03	0.08	-0.21	0.23	0.16	-0.20	-0.02	0.30	0.28	-0.02	-0.13	0.29	0.12	-0.07	0.00
Centroid				0.95	0.77	-0.01	0.54	-0.06	0.54	-0.44	-0.88	0.16	-0.01	-0.11	-0.30	-0.10	0.02	0.05	0.14	0.01	0.08	-0.01	-0.11	0.02	0.00	-0.01	-0.02
Full Length					0.87	-0.15	0.45	-0.19	0.66	-0.37	-0.82	0.35	-0.04	0.02	-0.34	-0.07	-0.14	0.00	0.15	-0.02	0.01	-0.04	-0.12	0.05	0.05	-0.03	-0.03
Braincase Length						-0.29	0.19	-0.30	0.91	-0.05	-0.54	0.69	-0.15	-0.10	-0.30	-0.14	-0.02	0.01	0.15	-0.05	0.08	-0.08	-0.07	-0.02	0.06	-0.05	-0.06
Frontal Width							-0.13	-0.04	-0.31	-0.10	-0.20	-0.22	0.31	-0.12	0.30	0.27	0.30	-0.13	-0.51	-0.08	-0.13	-0.06	-0.22	0.03	-0.26	0.26	0.00
Braincase Width								-0.02	-0.07	-0.60	-0.42	-0.29	0.08	0.22	-0.38	0.22	0.05	0.25	0.20	0.25	0.23	-0.12	-0.12	0.01	0.11	-0.22	-0.06
Braincase Height									-0.17	0.25	0.15	-0.57	0.05	-0.53	-0.10	-0.17	-0.21	-0.04	0.26	-0.31	-0.01	-0.16	0.02	-0.03	-0.12	-0.01	-0.05
Braincase Curve Length										0.36	-0.27	0.80	-0.14	-0.25	-0.20	-0.20	-0.12	0.00	0.14	-0.11	0.04	-0.08	-0.03	0.04	-0.06	0.00	-0.10
Braincase Curve to Length Ratio											0.58	0.38	-0.01	-0.38	0.20	-0.18	-0.23	-0.02	0.01	-0.15	-0.08	-0.01	0.09	0.14	-0.30	0.13	-0.10
PC1												0.00	0.00	0.00	0.00	0.00	0.00	0.00	0.00	0.00	0.00	0.00	0.00	0.00	0.00	0.00	0.00
PC2													0.00	0.00	0.00	0.00	0.00	0.00	0.00	0.00	0.00	0.00	0.00	0.00	0.00	0.00	0.00
PC3														0.00	0.00	0.00	0.00	0.00	0.00	0.00	0.00	0.00	0.00	0.00	0.00	0.00	0.00
PC4															0.00	0.00	0.00	0.00	0.00	0.00	0.00	0.00	0.00	0.00	0.00	0.00	0.00
PC5																0.00	0.00	0.00	0.00	0.00	0.00	0.00	0.00	0.00	0.00	0.00	0.00
PC6																	0.00	0.00	0.00	0.00	0.00	0.00	0.00	0.00	0.00	0.00	0.00
PC7																		0.00	0.00	0.00	0.00	0.00	0.00	0.00	0.00	0.00	0.00
PC8																			0.00	0.00	0.00	0.00	0.00	0.00	0.00	0.00	0.00
PC9																				0.00	0.00	0.00	0.00	0.00	0.00	0.00	0.00
PC10																					0.00	0.00	0.00	0.00	0.00	0.00	0.00
PC11																						0.00	0.00	0.00	0.00	0.00	0.00
PC12																							0.00	0.00	0.00	0.00	0.00
PC13																								0.00	0.00	0.00	0.00
PC14																									0.00	0.00	0.00
PC15																										0.00	0.00
PC16																											0.00

Figure 5.21 Correlation matrix between suture patency, linear measurements, and the PC scores for a)) P21 MT and b) P42 MT.

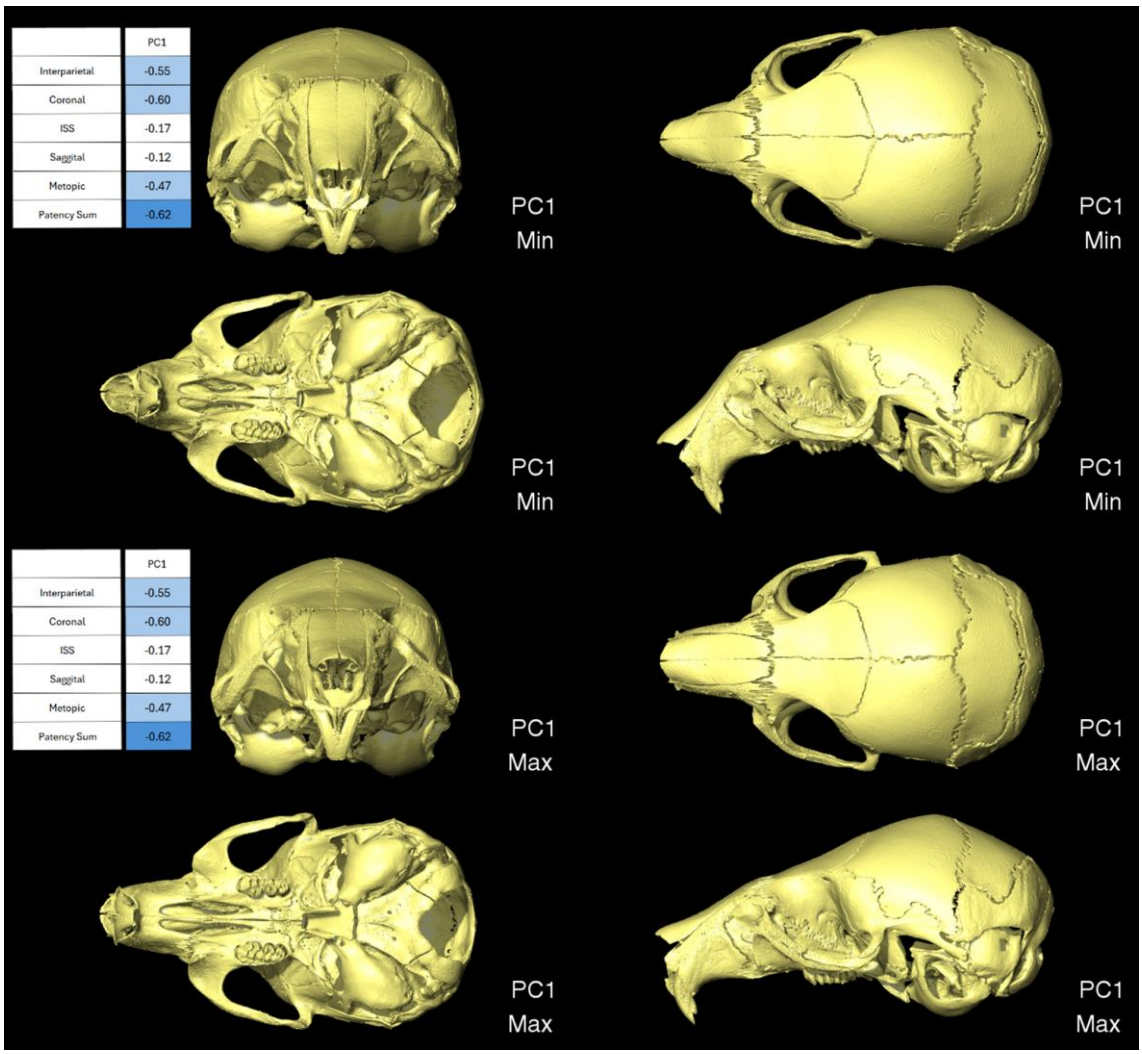

Figure 5.22 P21 MT PC1 visualised for max and min shapes with corresponding suture patency correlation coefficients. Visualisations for all PCs are available in Appendix III for P21 MT, P42 MT and for animated interpolations of the min and max shape for P21 MT.

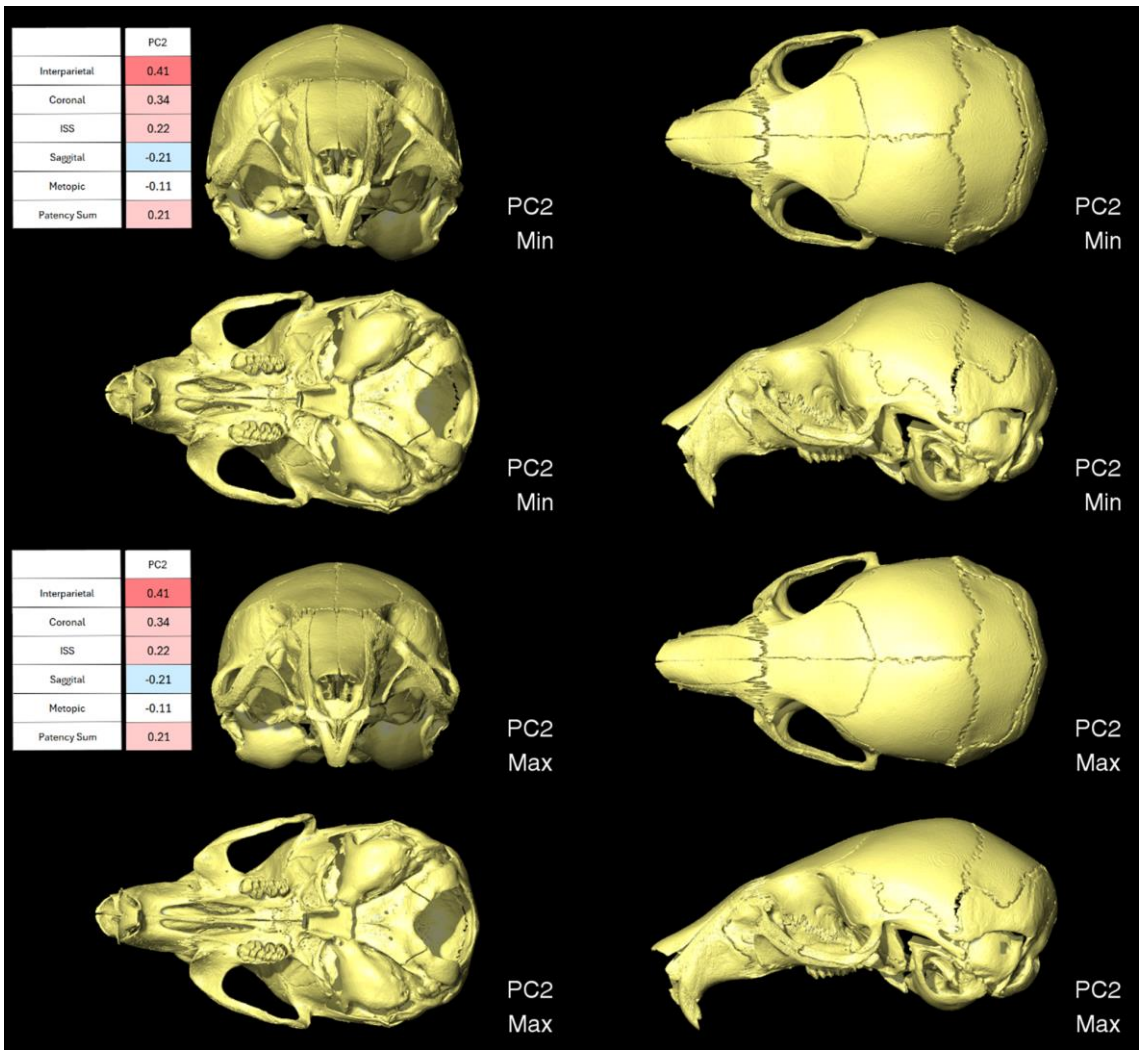

Figure 5.23 P21 MT PC2 visualised for max and min shapes with corresponding suture patency correlation coefficients. Visualisations for all PCs are available in Appendix III for P21 MT, P42 MT and for animated interpolations of the min and max shape for P21 MT.

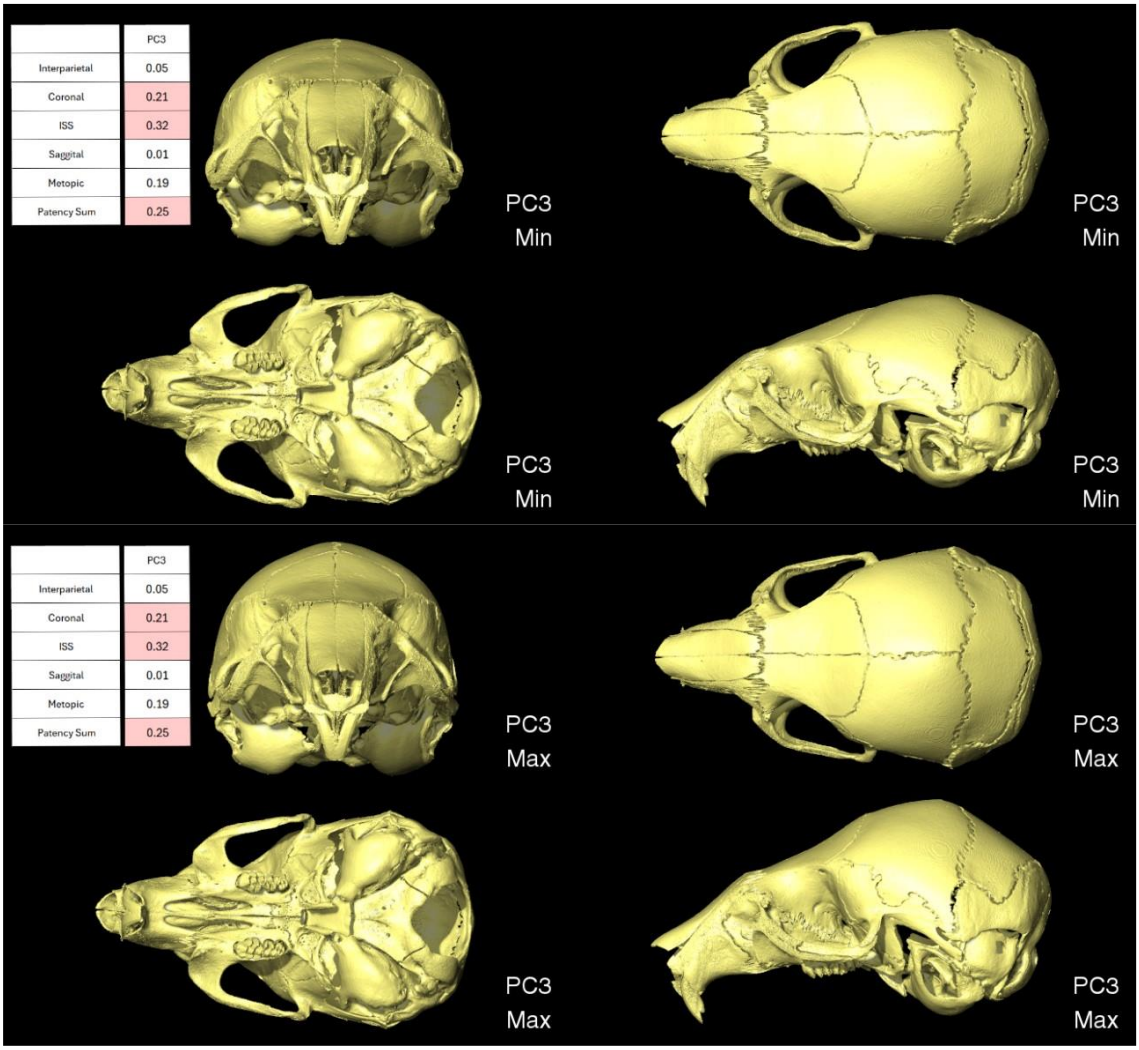

Figure 5.24 P21 MT PC3 visualised for max and min shapes with corresponding suture patency correlation coefficients. Visualisations for all PCs are available in Appendix III for P21 MT, P42 MT and for animated interpolations of the min and max shape for P21 MT.

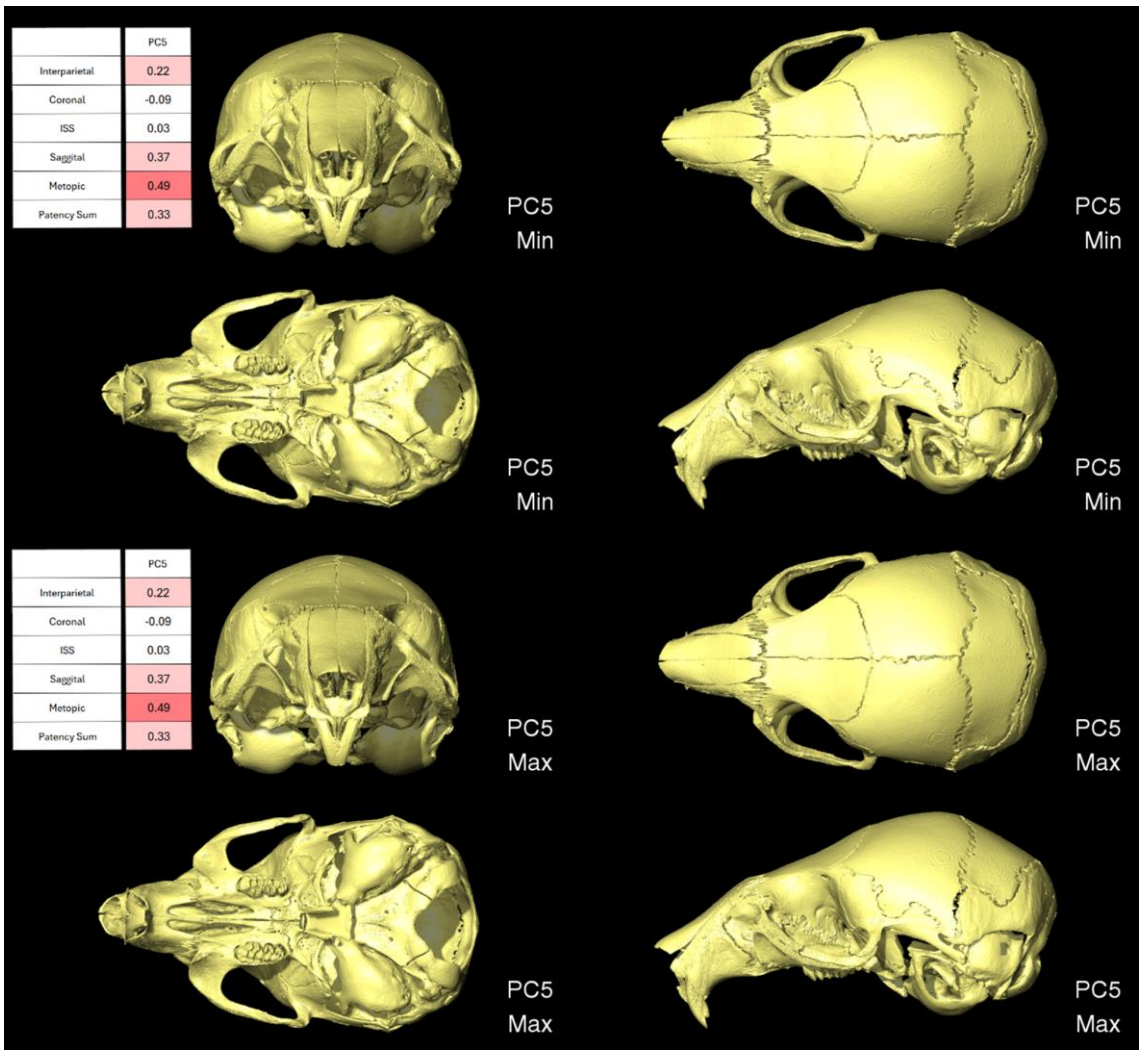

Figure 5.25 P21 MT PC5 visualised for max and min shapes with corresponding suture patency correlation coefficients. Visualisations for all PCs are available in Appendix III for P21 MT, P42 MT and for animated interpolations of the min and max shape for P21 MT.

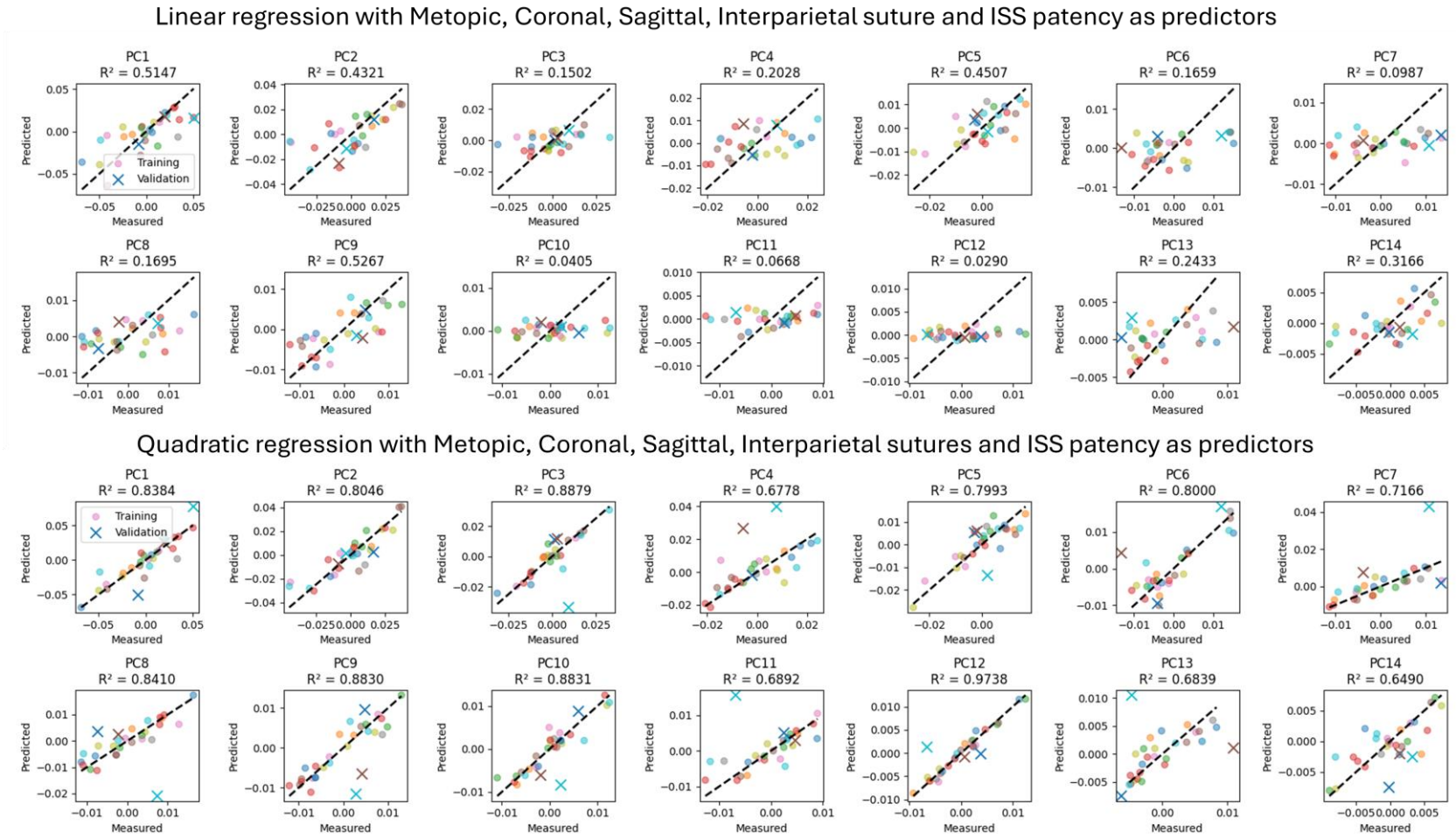

Figure 5.26 Linear and quadratic regression models with metopic, coronal, sagittal interparietal sutures, and the ISS patency as predictors for shape.

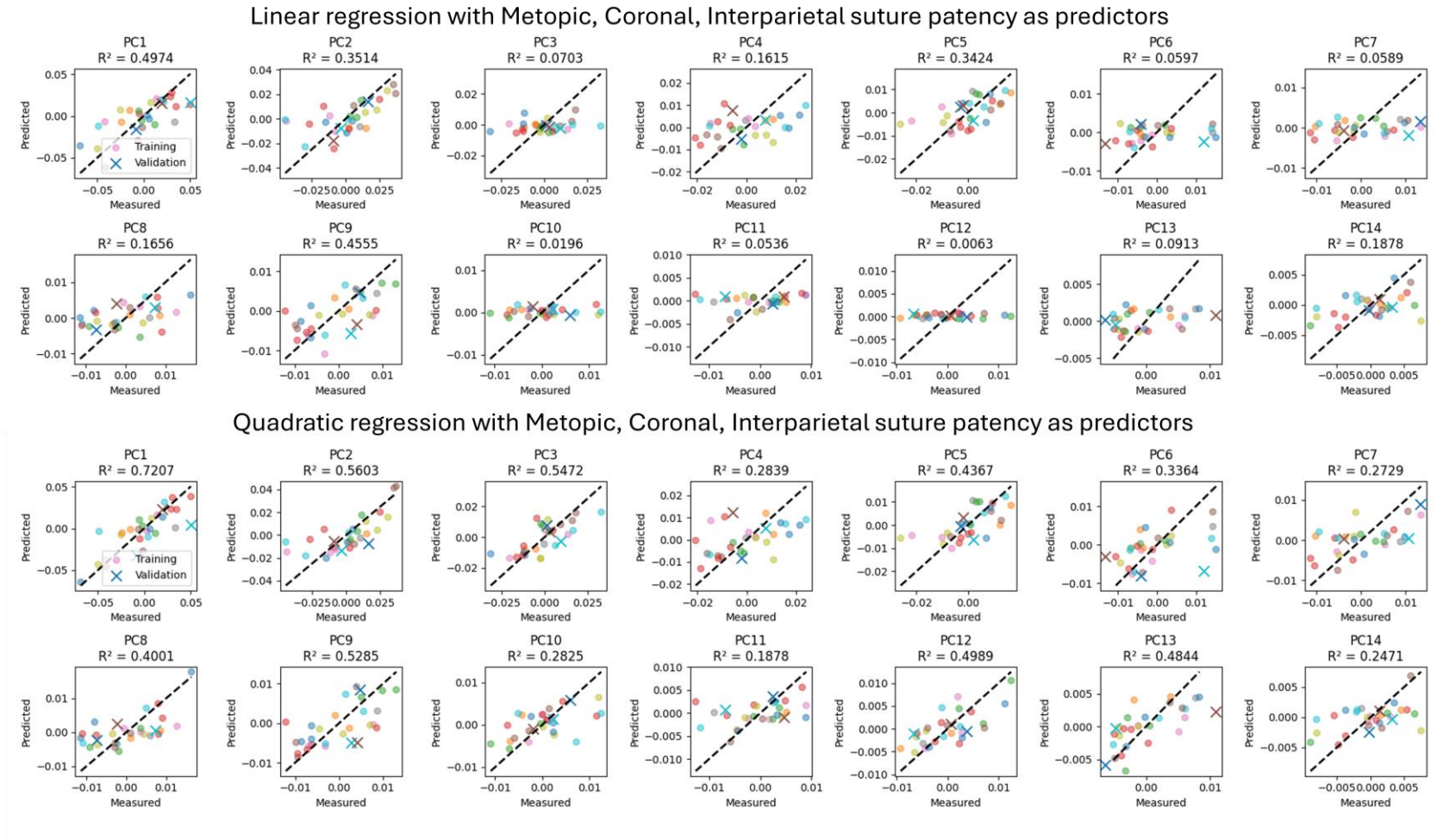

Figure 5.27 Linear and quadratic regression models with metopic, coronal, and interparietal sutures as predictors for shape.

5-4 Discussion

The inherent variability of the phenotype of the craniofacial system in terms of shape in the WT animals and shape and suture patency in the MT animals play a significant role in the reproducibility of results in craniofacial studies. Equally, the unclear relation between suture patency and phenotypic severity in the Crouzon mice complicates the development of novel treatment approaches and their investigation in the animal model for craniosynostosis research. This Chapter aimed to address these two significant challenges. Firstly, to understand and address the litter effects on the craniofacial phenotype and secondly, to unravel the effect the suture patency has on the craniofacial morphology.

Linear measurements effectively capture critical skull morphology information, with MT animals showing characteristic brachycephalic shape through shortened skull and increased height (see also Eswarakumar et al. 2004; Liu et al. 2013). Growth trajectories differed significantly between MT and WT animals, with MT showing reduced length increase from P21 to P42, while width and height remain stable in both groups. These measurements showed strong inter-litter variation, particularly in WT animals, where intra-litter variation was significantly lower than the across-group variation.

The principle component analyses largely complemented the linear measurements and provided a more nuanced view of the skull shape variation later used to understand the relation between skull shape and suture patency. The analysis additionally allowed the investigation of the shape without including the size differences included in the linear measurements. The data highlighted that while the MT skulls still increased in size at P42 their phenotypic severity largely remained the same as it was at P21, as indicated by the similar placement of the two groups in PC1(largely captured phenotypic severity) in the shape analyses. P21 and P42 MT groups were separated in PC2 suggesting other shape differences between the groups exist. The litter effects observed in the linear measurements are reflected and amplified in the PCA with statistically significant differences between the litter in all investigated cases except for one (P42 WT Form), which is likely related to the insufficient number of litters included. As P42, WT only included two litters, and further analysis was not carried out on these animals.

For PC1 in all of the included analyses strong correlation with the centroid size and full skull length was observed, which includes both form and shape analysis. Suggesting that

even with the size differences removed, the shape variations are largely related to the shape variations. PC1 captured the differences between MT and WT animals. The strong correlation with size suggests that size is a significant and related part of the phenotype. PC2 correlated with the braincase curve length the most amongst a different pattern of moderate correlations compared to PC1, and appeared to largely capture the age shape differences.

Suture patency analysis was only included for P21 MT animals (metopic, coronal, sagittal, interparietal, and the ISS) and for P42 MT animals (sagittal and interparietal). Commonly, suture patency is determined qualitatively either through the visual inspection of stained specimens or surface reconstructions of CT data in binary (either patent or fused, for example, Bradley et al. 1997; Perlyn et al. 2006). Dorsally apparently patent sutures can include sutures that are fully fused at the ventral side of the suture, as shown in the coronal suture at P21 in Crouzon mice in Steacy et al. (in review). The methodology devised in this work combats both issues by quantifying the number of slices fused compared to the number of slices across the full suture; the proportion of patent slices is then considered as the patency percentage. A different approach was used to determine the level of patency of the ISS. The depth of the bone and the depth of the synchondroses was measured at the midline of the ISS. The ratio of the ISS depth to the full depth of both bone and the ISS was used as the patency percentage. It is possible that this measurement may not be directly comparable to the suture patency percentage as based on the methodology for the sutures the ISS would be considered fully fused.

The patency results highlighted that different sutures were affected differently in the considered MT mouse model in this study at P21 and P42. While the coronal suture showed the lowest patency across all the investigated sutures, it also showed the highest variability. Additionally, a single animal out of the included MT animals in the study showed full patency of both coronal sutures. Sagittal and interparietal sutures showed the highest levels of patency, with the lowest levels of variation between animals. For both sutures specimens, 100% patent sutures were observed. The metopic suture was the only suture with no animals showing full patency, likely linked to the fact that the suture is also partially fused at P21 in the WT animals. Similarly, the ISS showed some level of fusion across all the investigated animals. The litter effects appeared to be the strongest in the ISS followed by the interparietal suture. At P42, full fusion of the metopic and coronal sutures as well as the ISS had occurred, and significant progression of the interparietal (from 85% at P21 to 43% at P42) and sagittal (from 89% at P21 to 20% P42)

suture fusion had taken place. Highlighting that the fate of all the investigated sutures is fusion, however, they undergo fusion at different developmental time points.

The grouping analysis conducted for each of the previously discussed measurements highlighted a clear effect of the selection of treated and baseline groups on experimental results. Additionally, it appears that larger numbers of animals can have little to no effect on specific measurements. The simple action of using a litter for treatment and a litter for control appeared to have significant implications on the reliability of statistical significance for gross linear measurements, overall skull shape from PCA, or more granular investigations into suture patency. The data presented in this chapter clearly suggests that while this is a significant consideration in the Crouzon mouse model it is equally important in the WT mice that in turn suggests that similar effects could be taking place in other mouse models.

Similar litter effects have been observed and quantified for neurodevelopmental studies in mice (Valiquette et al. 2023). The comparable findings support the generalisability of the findings in this study outside the variation of the craniofacial phenotype. However, the proposed solution in the aforementioned study largely focused on the increased number of litter, while decreasing the number of animals in the litter. The data presented in our work suggests that the increased number of litters has a limited effect on controlling the incidence of statistical significance between control and "treated" groups for the measurements of the craniofacial phenotype considered. "Between-litter design" and "within-litter design" for animal studies have been previously investigated more broadly with "within-litter design" shown as the more powerful approach (Festing 2006).

The "within-litter design" is strongly suggested from these investigations as it fully accounts for the observed differences in full for both MT and WT animals at P21. Separation of litters into two groups randomly for control/"treated", when two or more litters are included reduces to around 5% with $p<0.05$ as the significance level. The presented approach has the potential to not only improve the reproducibility and confidence of craniofacial research results but could also be used to reduce the required number of animals. The P42 MT animals did not have a sufficient number of litters to run the full grouping analysis. Partial one has been included in Figure 5.13, similarly highlighting the effectiveness of this litter division approach at later developmental time points. The grouping analysis assumed that the distribution and variation of the litters observed in this work were a good representation of the natural variation of these animals. The animals used in this study are largely control animals from other experiments, thus

the MT animal distribution is not ideal with the relatively small litter sizes obtained. However, the WT animals with more animals per litter and more litters overall show the effects more than the MT animals. This suggests that more and larger litters for the MT may enhance the effect further rather than diminish it.

The intraclass correlation coefficient analysis supports the findings from the grouping analysis with the most problematic measurements in the grouping analysis showing the highest ICC values. Particularly high levels of correlation are observed for the WT animals in the linear measurements especially the length of the skull echoed in the particularly high incidences of statistical significance between different compositions of groups in the grouping analysis. Similarly, low values of ICC such as for the metopic suture patency in the MT animals correspond to low incidences of statistical significance in the grouping analysis. The results suggest that the level of patency of the ISS is strongly linked with the litter. The suture patency, however, is in general less strongly correlated with litter than the shape as observed in both the linear measurements and PC scores. This may suggest that the two are not as interconnected as previously thought in the Crouzon mouse model.

The suture patency and craniofacial shape relations were primarily investigated at P21 in the mutant animals. Weak to moderate positive correlation was observed between pairwise comparisons of different sutures with strong correlation between the individual suture patency and the patency sum. This suggests that although the patency of one suture in not strongly correlated with the patency of another, the overall patency is correlated. In turn, patency is somewhat conserved between individuals. Crucially, higher levels of interparietal, coronal, and metopic suture patency show moderate negative correlation. The patency sum shows strong negative correlation with PC1 which largely captures the phenotypic differences between WT and MT with lower numbers indicating more severe overall phenotype. It is unlikely that more patent sutures would produce a more abnormal shape, perhaps indicating that the higher patency is the result of the abnormal skull shape, equally, they might both be controlled by an unknown underlying factor. What is certain from this analysis is that suture patency does not lead to more overall WT like skull shape in the Crouzon mice. The one animal with complete coronal suture patency also followed this trend of higher patency correlating with a more severe phenotype.

Moderate positive correlation is observed between interparietal suture patency and PC2 which largely captured the calvarial bulge and skull base shape with larger numbers indicating a more normal shape. Thus, while overall phenotype is worse as the patency

increases, finer shape variations can be positively correlated with suture patency. Weak positive correlation of the ISS and the coronal suture indicated a significantly more pronounced calvarial bulge (related to the parietal bone) with the increased patency of the two joints. Weak negative correlation of the interparietal suture patency with PC4 indicated reduced calvarial bulge (related to the interparietal bone shape) from increased patency. Metopic suture patency showed moderate positive correlation with the PC5 which primarily captured the frontal bone width with higher numbers showing higher width. Overall, the correlations of the suture patency levels and the PC scores are not strong, with the only exception of patency sum to PC1. This suggests that the link between suture patency and specific shape variation is relatively weak. Interestingly, however, at P42, the correlation between interparietal suture patency and PC1 was negative and moderate. This showed the opposite correlation as it did at P21 because the PC1 for the P42 MT animals was related to a more normal shape with decreased values. This suggests that the relation between suture patency and shape is not consistent across all developmental timepoints.

To further understand the relationship between suture patency and craniofacial shape, linear and quadratic regression was carried out. Using all the investigated sutures and the ISS as predictors led to overfitting the model due to the limited amount of available data. Therefore, instead, the strongest correlating sutures (metopic, coronal, and interparietal) were used, which caused a marginal decrease in R^2 values for each PC score in the linear regression model. The quadratic regression model showed a significantly better correlation between the predictors and shape without significant overfitting. This suggests the presence of non-linear effects between suture patency and shape, however, the dataset is likely too small to place any confidence even in the adjusted model. More data could enable further analysis of the relation between all the suture patency levels and the skull shape, without overfitting the model, and providing sufficient dataset for proper validation.

Limitations

Three key limitations are included in this Chapter. 1) the grouping analysis assumes that the distribution of the investigate values across the groups and litters observed in the investigated cohorts are representative of normal variation. While large numbers of animals were considered in this investigation, the independent investigations are required to establish the generalisability of the results. 2) only CD-1 background animals were

investigated. Similarly, questioning the generalisability of the results. 3) No investigations into earlier developmental time points were carried out, thus both the study design implications and the suture patency correlations remain unclear for studies in early neonatal mice.

5-5 Summary

This chapter produced a detailed investigation into the skull shape of the WT animals and the suture patency and skull shape of the MT animals. While investigating the litter effects, a clear problem of using entire litters and combining them as control or treated groups was established for all the different measurements when considering animal study design. This litter effect problem was established for both MT and WT animals and a solution was identified by dividing litters into two equal halves, where one half is used for the control and the other for treatment (the "within-litter design" approach). The "within-litter design" was shown to entirely counteract the litter effects in the variation of linear measurements, PCA, and suture patency. At the same time, the correlation of suture patency and skull shape investigations have shown that suture fusion is not driving the phenotype of the Crouzon mice. While some correlation is observed at P21, primarily the phenotype is more severe with more patent sutures. The effect of suture patency remains unclear at earlier development time points and requires further investigation. Similarly, further analysis of the litter effects for earlier and later developmental time points, and other mouse models could validate the generalisability of the study design findings presented in this work.

The animals used in this chapter act as control animals in the following chapter. The investigations in the two chapters were conducted in parallel meaning the study design implications were not fully considered during the experimental design of Chapter 6. Where possible, littermate controls were used in the investigations of the varied *in vivo* treatment regimes.

Chapter 6 Characterising the effects of *in vivo* loading on the mouse craniofacial phenotype

6-1 Introduction

The overall aim of this chapter was to assess the effects of the various treatment regimes on the linear measurements of the skull, overall morphology, and suture patency through a series of *in vivo* experiments largely based or exactly following the loading regime set out in Moazen et al. (2022). The methodology of this chapter was developed outside the considerations established in **Chapter 5**. However, the findings of this chapter were considered in the context of the study design implications from the previous chapter. The efficacy of external cyclical loading of the frontal bone as such and with varied parameters as a treatment avenue for craniosynostosis was evaluated.

Aim: Quantify the effects of external cyclic loading of the frontal bone on the gross morphology and suture patency in Crouzon mice.

Objectives: Establish the loading effects on the linear measurement, gross morphological changes, qualitative coronal suture patency and quantitative patency of interfrontal, coronal, sagittal and interparietal sutures. Test whether the effects are still observed with littermate controls where available.

6-2 Materials and methods

The overall workflow for this chapter is available in Figure 6.1 detailing the number of animals, the investigated loading regimes, and the analysis carried out. The latter is largely derived from the analysis conducted in **Chapter 5**. The control animals in this investigation were the same as those considered in the previous chapter.

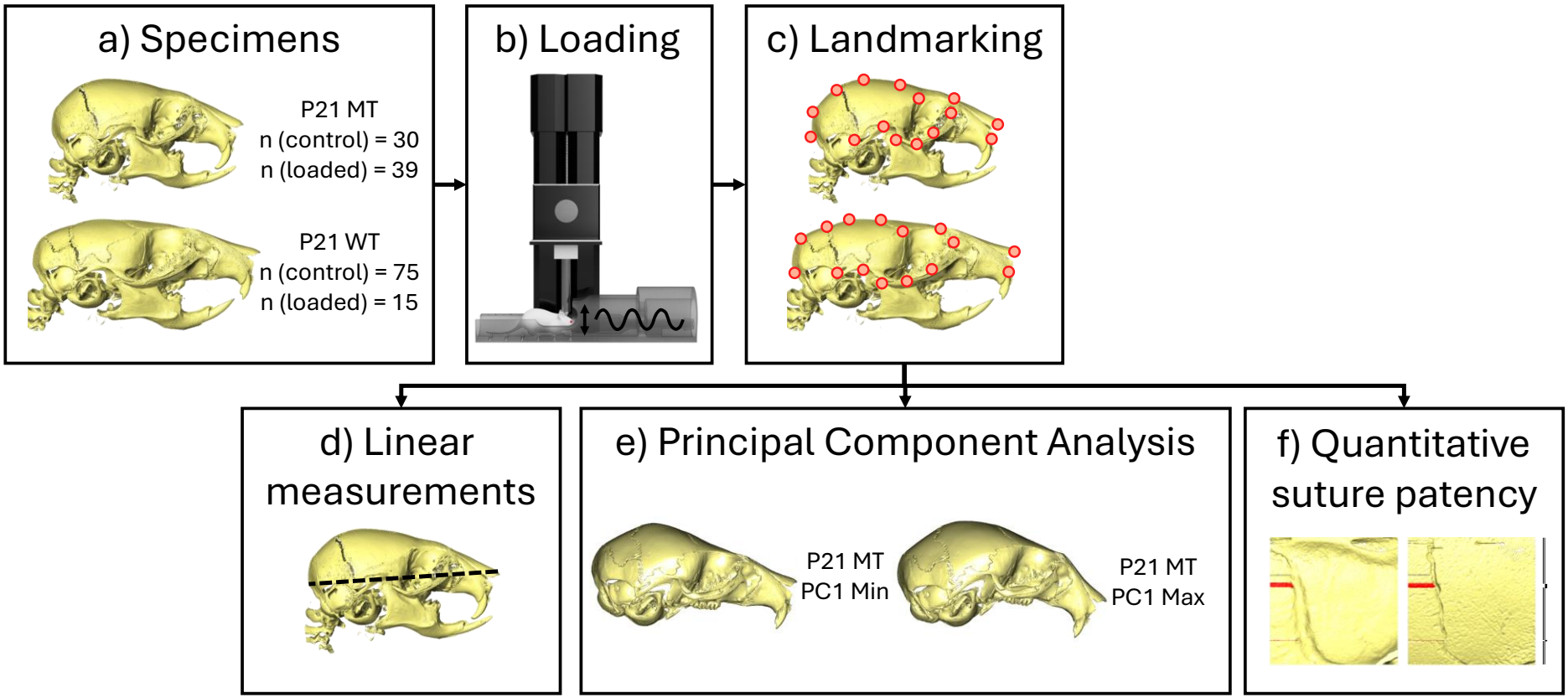

Figure 6.1 The overall workflow of the chapter. a) Specimens included in the study, b) loading, c) landmarking, d) linear measurement, e) PCA and f) quantitative suture patency.

6-2-1 Specimens

In total, 159 animals were considered in this chapter (69 P21 MT – with 39 animals treated and 90 P21 WT – with 15 animals treated). Control (not treated) animals are described in detail in section 5-2-1. The distribution of the treated animals across the different loading protocols is available in Figure 6.2. All the animals investigated were collected at P21.

Note: all animal experiments were approved by the UK Home Office and performed as part of a Project License (number: PP8161503) under the UK Animals (Scientific Procedures) Act 1986. Animal procedures complied with the ARRIVE guidelines and were performed under the supervision of UCL Biological Services.

6-2-2 Loading setup

The same custom-built dynamic loading setup was used as described in the materials and methods of section 3-2-2. To reiterate, the setup (mock-up available in Figure 6.1b) was comprised of an actuator (Newmark Systems, Inc: res. 0.04 μm with Maximum velocity of 25 mm/sec), a force sensor (GSO Series, Transducer Techniques: res. 0.01 N with 1.5 N capacity), and controlled by a custom LabVIEW programme (National Instruments Corp, Austin, TX, USA). The control program enabled the easy manipulation of loading parameters such as frequency and duration.

6-2-3 Loading regimes

The original treatment by Moazen et al. (2022) was again investigated in this work with further cellular response investigations on the same animals are available in Steacy et al. (in prep). The loading consisted of 10-minute sessions of frontal bone loading (a tip diameter way from the midline on the left side) with a force-controlled loading at 1N with a sine profile at 1Hz per day from P7 to P18 (P7, P8, P9, P10, P11, P14, P15, P16, P17, and P18) with two days break in the middle. This baseline loading is then referred to as weekend interrupted asymmetric loading. 10 MT and 11 WT animals were investigated under this regime.

All the following loading regimes act as variations of this initial regime. Weekend interrupted symmetric loading (6 MT and 4 WT animals) was changed by applying the

treatment on both sides (left and right) for 5 minutes on each side for a total of 10 minutes of loading per session. Preliminary investigations highlighted little effect on WT animals, thus these were not further investigated in the other loading regimes primarily due to experimental time constraints and animal welfare considerations. Weekend interrupted asymmetric 2Hz loading was achieved by adjusting the frequency of the original loading from 1Hz to 2Hz with everything else remaining the same.

Three of the loading regimes retained the loading parameters and location of the original treatment, which focused on the comparison of the number of sessions and their timing. 1st week only asymmetric loading (5 MT) consisted of animals loaded from P7 to P13 without interruption. 2nd week only asymmetric loading (4 MT) consisted of animals loaded from P14 to P20 without interruption. Lastly, uninterrupted asymmetric loading (5 MT) consisted of animals loaded from P7 to P20 without interruption (Figure 6.2b).

Partially, the variety of loading regimes were investigated to establish general effects of external cyclic loading of the frontal bone on gross craniofacial morphology, however individual loading regimes were chosen to answer individual questions if more significant changes were detected. Weekend interrupted asymmetric – was to investigate the reproducibility of results from Moazen et al. (2022), weekend interrupted symmetric - was to investigate whether more symmetrical results would be observed, weekend interrupted asymmetric 2Hz – was to investigate whether a higher frequency would affect the results (there was some indications that the original 1Hz - Moazen et al. (2022) may have been misreported and was closer to 1.5Hz), 1st week only and 2nd week only asymmetric loadings – were to investigate whether the initial start date would significantly affect the results, the specific hypothesis was that the 2nd week only asymmetric loading would have a larger effect (if the mechanism was mechanical disarticulation of the fusion points in the coronal suture, the porous frontal bone at P7 would prevent meaningful transfer of the load to the suture), and lastly, the uninterrupted asymmetric loading – was to test the effects of the 2 day break in the middle of the treatment.

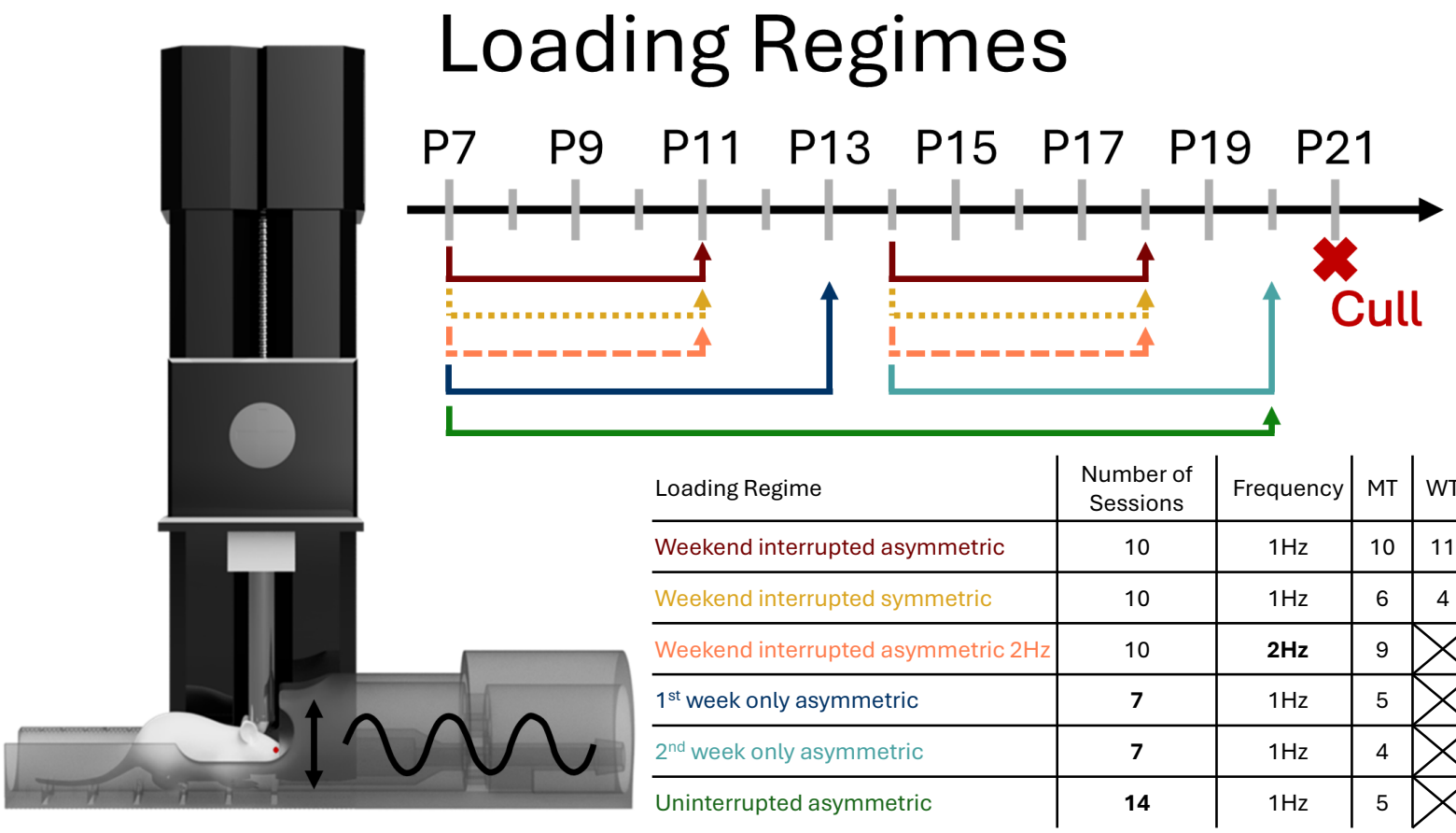

Loading Regime	Number of Sessions	Frequency	MT	WT
Weekend interrupted asymmetric	10	1Hz	10	11
Weekend interrupted symmetric	10	1Hz	6	4
Weekend interrupted asymmetric 2Hz	10	**2Hz**	9	
1st week only asymmetric	**7**	1Hz	5	
2nd week only asymmetric	**7**	1Hz	4	
Uninterrupted asymmetric	**14**	1Hz	5	

Figure 6.2 Loading regimes investigated with explanatory timeline, numbers of animals included, and loading set-up mock-up. Differences to the original treatment highlighted in bold.

6-2-4 Imaging and analysis

The skulls were immediately fixed in 10% formalin at 4°C for 7 days. The fixed skulls were scanned in the micro-CT scanner (XT H 225ST, Nikon, Herts., UK) with the following parameters: 9.6 μm × 9.6 μm × 9.6 μm, 90 kV, 90 μA, 1 s exposure. CT images were imported into an image processing software (Avizo 2022.1, ThermoFisher Scientific, Mass, USA), where the data was converted to 16-bit, the skulls were aligned using the image registration tool, and reconstructed using a consistent threshold of 19000.

The same imaging and analysis as carried out in Chapter 5 was used in this investigation. The same 56 landmark layout was employed as described in section 5-2-3 and the same linear measurements included in Chapter 5 were investigated in this work including the braincase curve length and braincase curve to curve length ratio. PCA was carried out following the methodology set out **in Chapter 5**.

Qualitative apparent coronal suture patency was investigated as described in Steacy et al. (in review). Left and right coronal sutures were investigated individually. The suture for each animal was categorised as patent if a clear suture gap was visible across most of the suture from a dorsal view; sutures with small bone bridges across the suture were still categorised as patent. If no clear suture gap was present in the reconstruction, the suture was categorised as fused. It should be noted here that the patency categorised in this way is only a dorsally apparent patency and as shown in Steacy et al. (in review) can include actually fused sutures.

The same sutures studied in **Chapter 5** were investigated for quantitative patency here. However, the investigation did not average the patency scores across laterally symmetrical sutures due to the one sided loading included in the treatments. Thus, the scores for each suture are presented individually for left and right sides. Additionally, the metopic suture was investigated both separately for anterior and posterior metopic suture and across the full suture as in **Chapter 5**.

The analysis also included results for all loading regimes considered as one group to understand whether loading, in general, had any significant impact on any of the investigated metrics. Additionally, the loading experiments undertaken in this work have been undertaken largely in parallel with the other investigations carried out in the thesis. Thus, the significant study design implications of **Chapter 5** were not known during the

experimental design of the loading treatment experiments. However, litter mate controls were available for the 1st week only loading (3 MT) and uninterrupted loading (2 MT). The comparisons between the treated animals and their littermate controls were included for linear measurements and for both qualitative and quantitative suture patency analyses. The low numbers in the littermate controls represent a significant limitation and the results require scrutiny when discussed.

6-2-5 Statistical analysis

For linear measurement, morphometric analysis and quantitative suture patency analysis unpaired t-test with Welch's correction and Levene's test were performed. Additionally, MANOVA was used in PC score comparison and ANOVA with Fisher's LSD was used for pairwise comparisons. A p-value of <0.05 was considered significant.

6-3 Results

6-3-1 Linear measurements

Linear measurements across the skull were taken for the full length of the skull, braincase length, frontal bone width, braincase width, braincase height and across the braincase following the landmarks in the curvature path. Figure 6.3 presents the measurements for each loading regime, control, and all loading regimes combined. Statistically significant pairwise comparisons are summarised in Table 6.1. 1st week only asymmetric loading and uninterrupted loaded comparisons against their control littermates are available in Figure 6.4. The same animals are included in Figure 6.3 with the control littermates contained in the full control group. These data highlighted that:

1) The treated animals with all regimes as one group did not show any statistically significant effect when compared to the control animals in any of the measurements in either the WT or MT animals. In MT animals, a pattern of limited decrease ranging from 0.03% (decrease in skull length) to 1.35% (decrease in braincase height) of the control averages was observed in the treated averages (Figure 6.3 comparing dark green – combined regimes, to grey - control).

2) Considering the loading groups individually, statistically significant decreases compared to the control were observed for the braincase height and curvature to length ratio (4.7% and 1.2% respectively) in WT animals for the weekend interrupted symmetric loading (Figure 6.3 fifth and seventh rows). In MT animals, statistically significant decreases in skull length, braincase length, and braincase curvature (4.12%, 5.56%, and 5.90%, respectively) were observed when comparing uninterrupted asymmetric loading treated animals with control animals (Figure 6.3 first, second and sixth rows). Statistically significant comparisons between differently treated MT animals were present largely compared to the uninterrupted asymmetric loading (see Table 6.1).

3) The statistically significant differences in the MT animals disappeared when littermates were compared as controls for the treated animals (Figure 6.4 - previously statistically significant measurements in first, second, and sixths rows) With p values (decrease of average) reducing from 0.042 (4.12%), 0.002 (5.56%), and 0.002 (5.90%) to 0.192 (4.38%), 0.658 (1.52%), and 0.888703 (2.98%) for skull length, braincase length, and braincase curvature, respectively in the uninterrupted asymmetric loading comparison.

4) Considering therapeutic effects, no changes that could be considered beneficial were statistically significant. Still, a slight increase in skull length (~1.5% of control length) was observed for the weekend interrupted and weekend interrupted 2Hz loading regimes. The difference between control WT and MT was an increase of 18.7% of MT length in WT animals. This was coupled with a slight (~1.8% increase) in frontal bone width in the two groups, which is less WT like as WT frontal bone width is 9.2% lower than in MT.

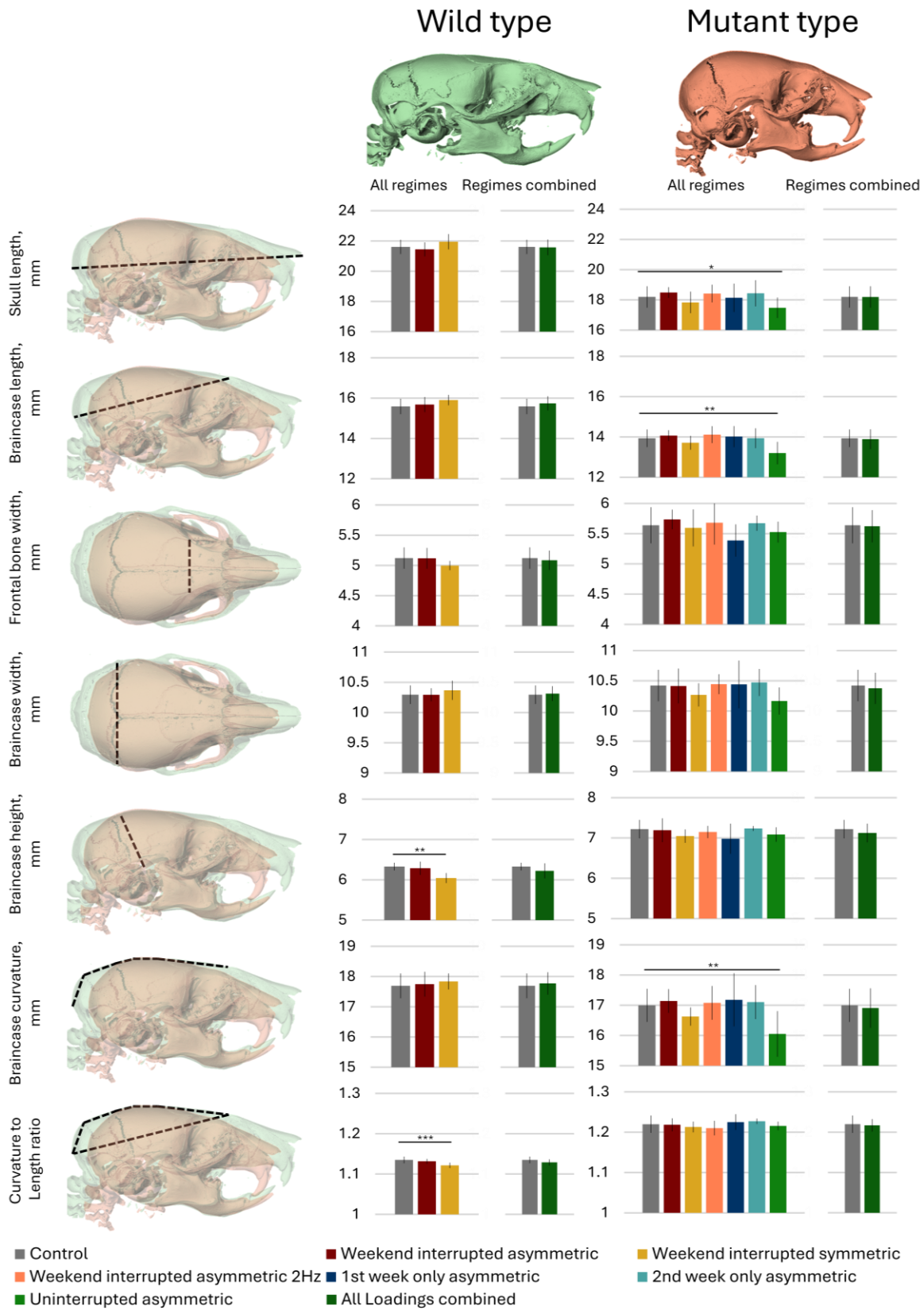

Figure 6.3 Linear measurement results for MT and WT animals. Including individual loading regime groups and all loading regimes combined. Statistically significant differences highlighted when compared to the control only.

Table 6.1 Statistically significant differences with P values across all pair-wise comparisons for the linear measurements including the control comparisons.

Skull Length			
Group 1	Group 2	P-Value	Percent Change
Control	Uninterrupted Asymmetric	0.0423	-4%
Weekend Interrupted Asymmetric	Weekend Interrupted Symmetric	0.0266	-4%
Weekend Interrupted Asymmetric	Uninterrupted Asymmetric	0.0019	-5%
Weekend Interrupted Asymmetric 2Hz	Uninterrupted Asymmetric	0.0183	-5%

Braincase Length			
Group 1	Group 2	P-Value	Percent Change
Control	Uninterrupted Asymmetric	0.002	-5%
Weekend Interrupted Asymmetric	Weekend Interrupted Symmetric	0.0346	-3%
Weekend Interrupted Asymmetric	Uninterrupted Asymmetric	0.0011	-6%
Weekend Interrupted Asymmetric 2Hz	Uninterrupted Asymmetric	0.0046	-6%
1st Week Only Asymmetric	Uninterrupted Asymmetric	0.0445	-6%

Frontal Bone Width			
Group 1	Group 2	P-Value	Percent Change
Weekend Interrupted Asymmetric	Uninterrupted Asymmetric	0.002	-4%
Weekend Interrupted Asymmetric	1st Week Only Asymmetric	0.0074	-6%

Braincase Curvature			
Group 1	Group 2	P-Value	Percent Change
Control	Uninterrupted Asymmetric	0.0018	-6%
Weekend Interrupted Asymmetric	Weekend Interrupted Symmetric	0.016	-3%
Weekend Interrupted Asymmetric	Uninterrupted Asymmetric	0.0024	-6%
Weekend Interrupted Asymmetric 2Hz	Uninterrupted Asymmetric	0.0128	-6%

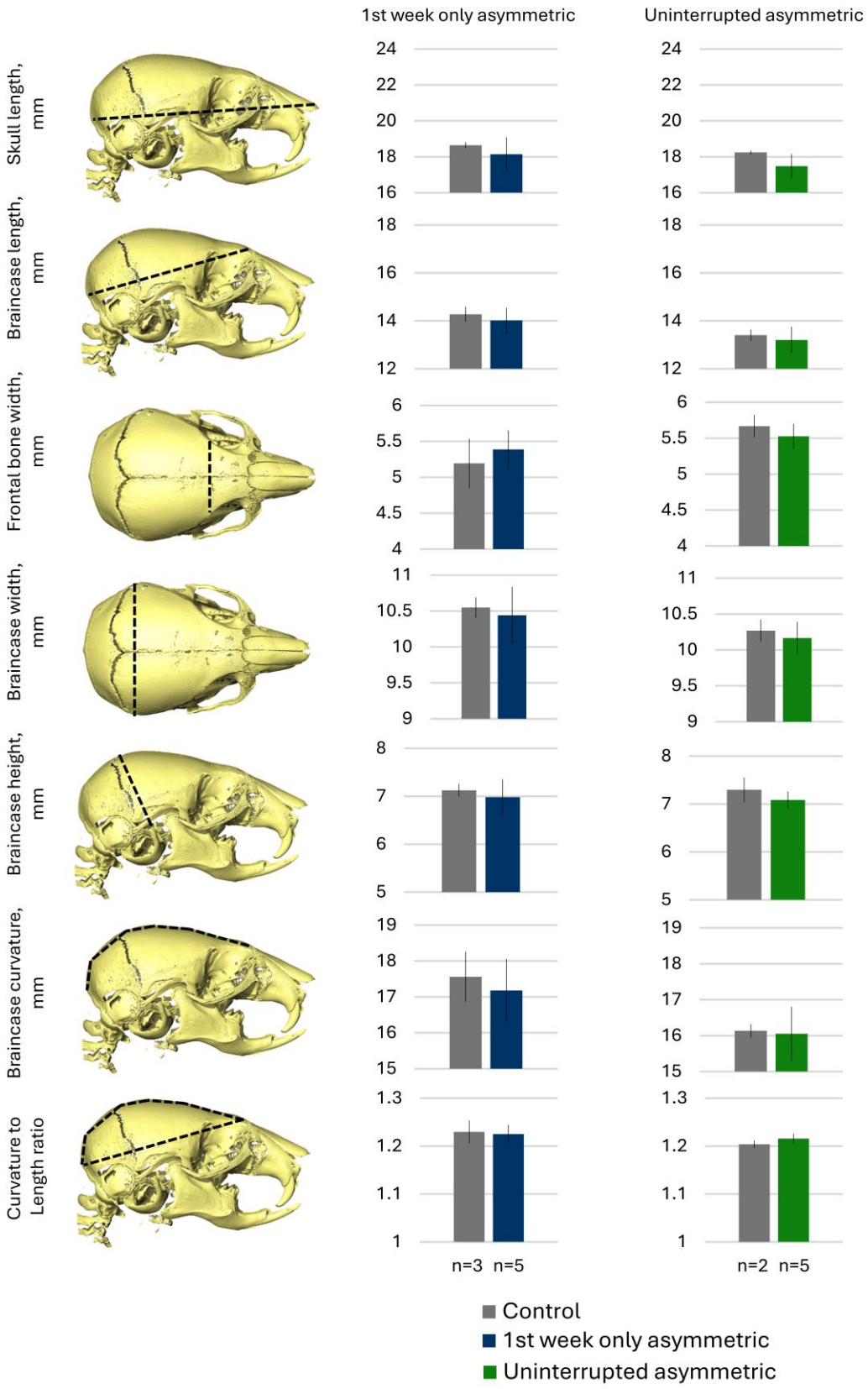

Figure 6.4 Linear measurement results MT animals for 1st week only asymmetric and uninterrupted asymmetric loading groups with comparisons to their control littermates.

6-3-2 Principal component analysis

PCA was carried out for all animals together and for mutant and wildtype animals individually. Both size and shape (form) and shape analyses were conducted (see Figure 6.5 – for PC1 and PC2 and Figure 6.7 – for PC3, PC4, PC5 and PC6). Statistical analysis by MANOVA was carried out including first PCs to account for 95% of variation with the Wilks' lambda p values available in Table 6.2. The data highlighted:

1) When considering the PCA for both WT and MT together, it is clear that the differences between mutant and wildtype skull morphological phenotypes are largely captured in PC1. No apparent shift of the treated mutant animals when considering the loading regimes individually or combined was observed towards a more WT like shape (Figure 6.5 regimes combined comparison – grey to green, first row).

2) WT animals showed statistically significant differences both when comparing individual treatment regimes and all regimes combined both for form and shape. The highest difference compared to the control animals was across PC3 (Table 6.2 and Figure 6.7 – first row).

3) Statistically significant differences in terms of form and shape across the skull comparing control and treated animals varied by treatment. With weekend interrupted asymmetric, weekend interrupted symmetric, and weekend interrupted asymmetric 2Hz showing statistically significant differences in both form and shape. With all regimes combined, these differences were not statistically significant (Table 6.2).

4) Similar to the WT animals, the largest differences occurred in PC3. The weekend interrupted asymmetric and symmetric loading treated animals have shifted towards a more pronounced calvarial bulge, generally associated with more severe phenotype. The weekend interrupted asymmetric 2Hz loaded animals, however, shifted towards a less pronounced bulge (Figure 6.7 – second row).

5) Considering therapeutic effects, only the aforementioned weekend interrupted asymmetric 2Hz showed a statistically significant and potentially beneficial result. However, the effects appeared to be limited to PC3, with no effects in PC1, that largely captured the overall MT/WT differences.

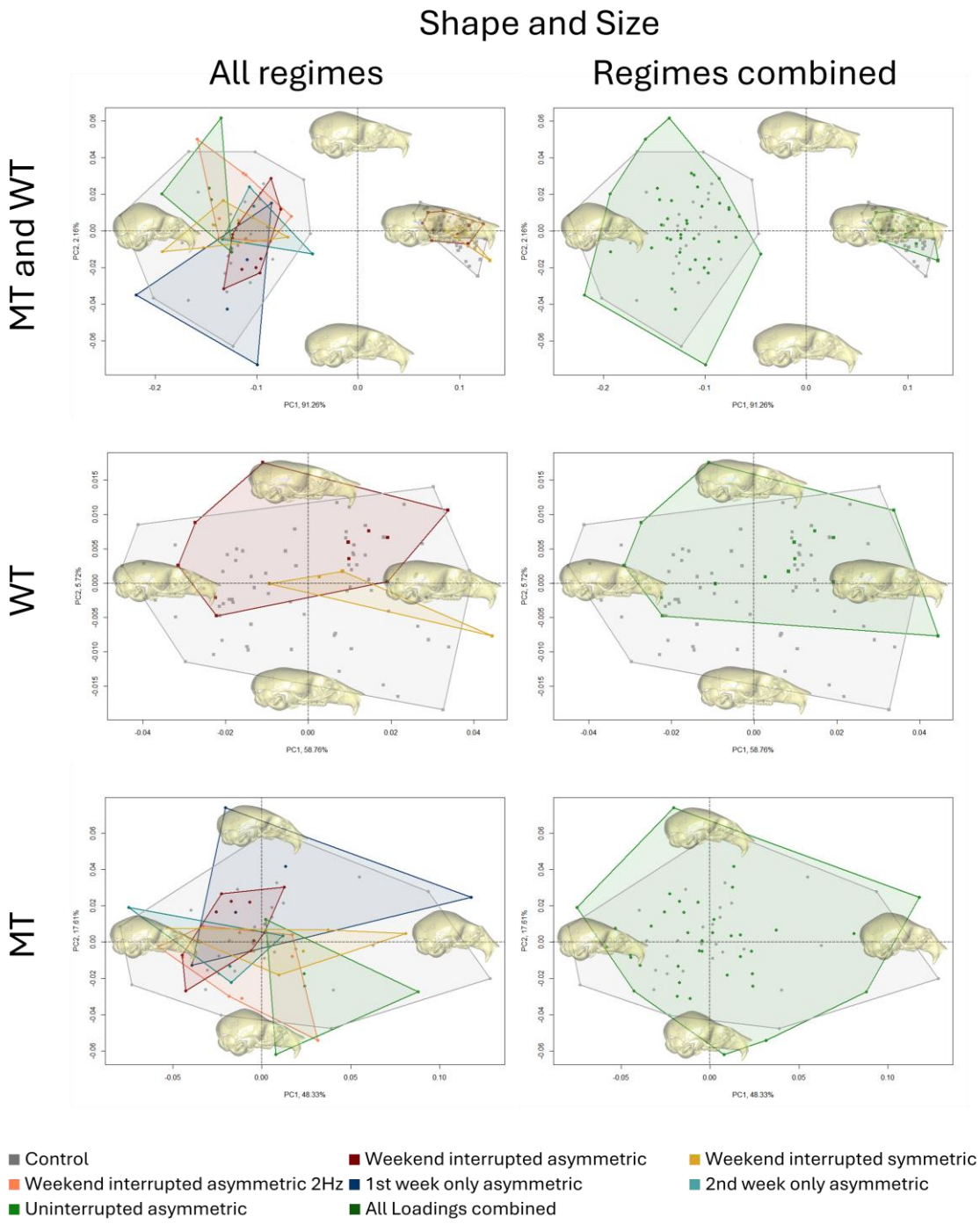

Figure 6.5 PC1 vs PC2 graphs from the shape and size analysis. Carried out for MT and WT together and MT and WT separately, with individual loading regime groups highlighted and all loading regimes combined.

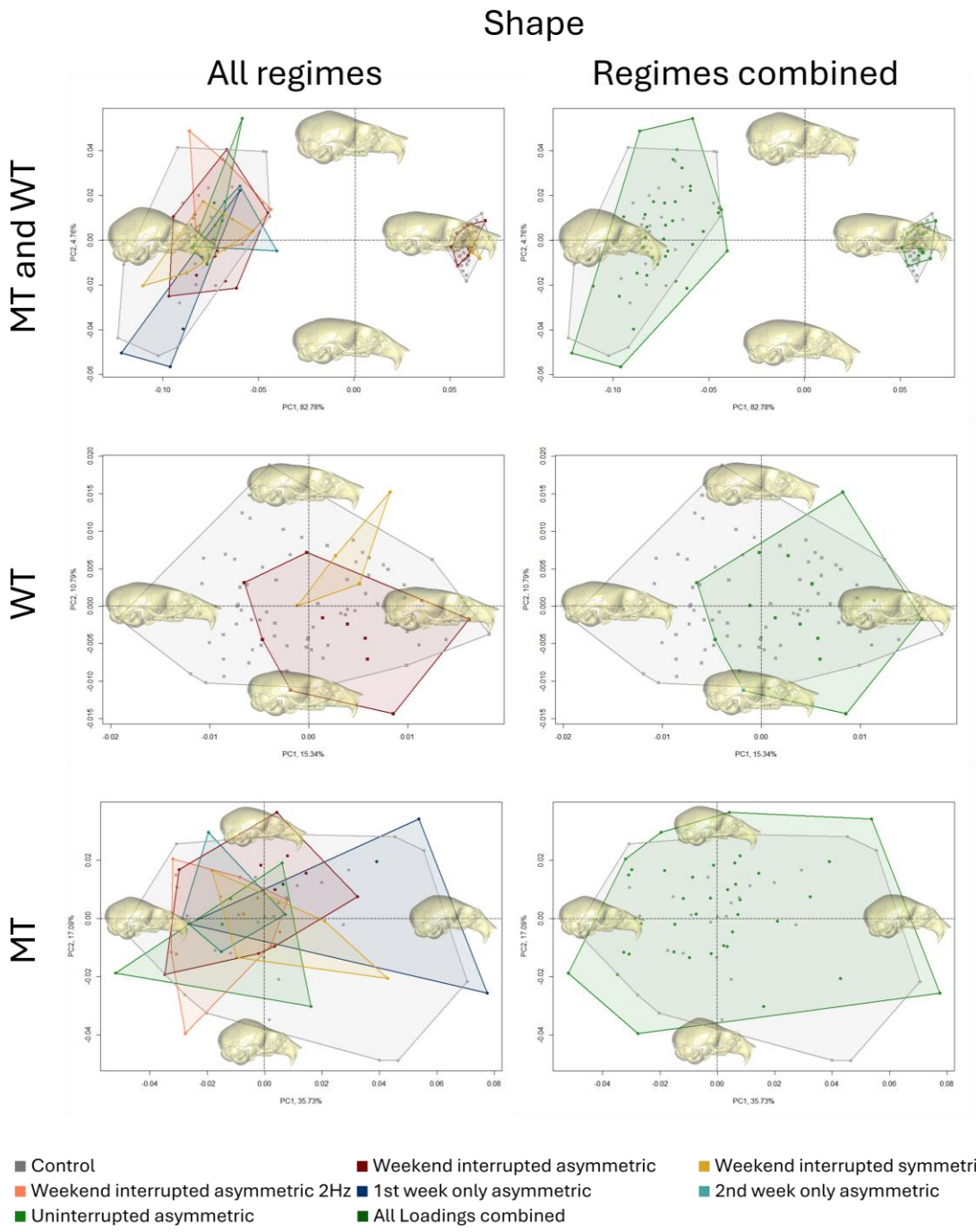

Figure 6.6 PC1 vs PC2 graphs from the shape analysis. Carried out for MT and WT together and MT and WT separately, with individual loading regime groups highlighted and all loading regimes combined.

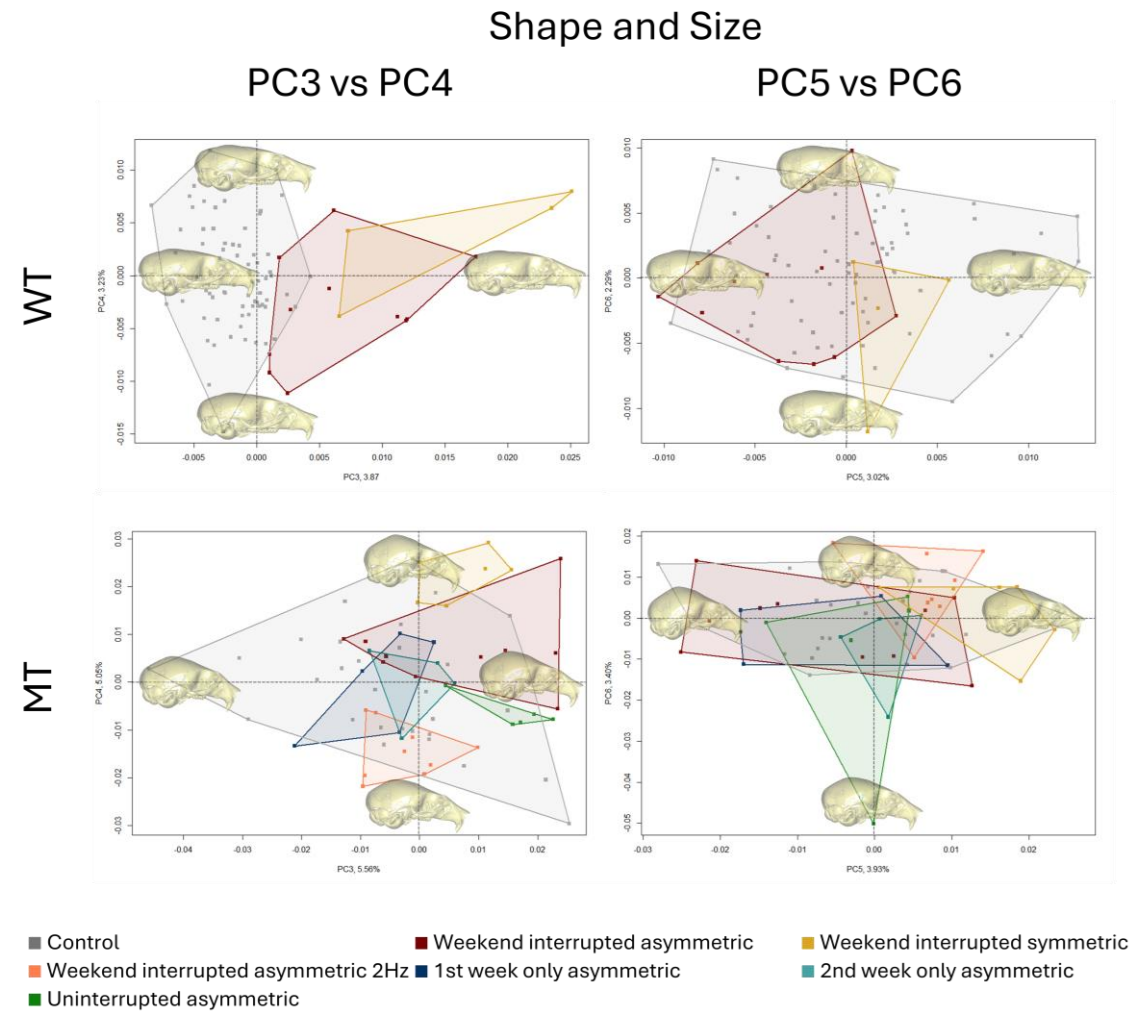

Figure 6.7 PC3 vs PC4 and PC5 vs PC6 graphs from the shape and size analysis. Carried out for MT and WT separately, with individual loading regime groups highlighted.

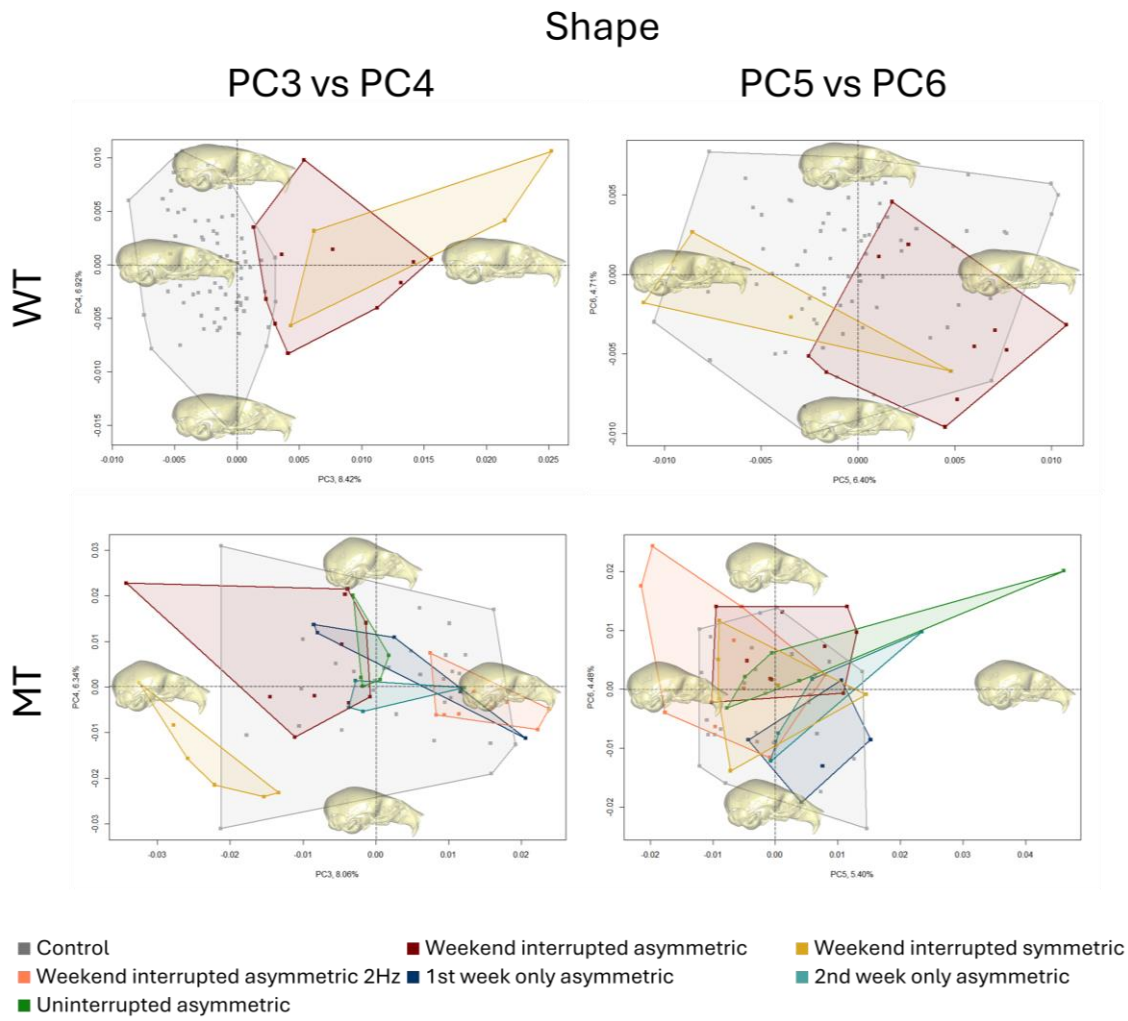

Figure 6.8 PC3 vs PC4 and PC5 vs PC6 graphs from the shape analysis. Carried out for MT and WT separately, with individual loading regime groups highlighted.

Table 6.2 Wilks' lambda P values across control comparisons for the PC scores, including the first PCs to account for 95% of the shape variation.

WT Shape		
Group 1	Group 2	P-Value
Control	Weekend interrupted asymmetric	<0.001***
Control	Weekend interrupted symmetric	<0.001***
Control	Regimes Combined	<0.001***

WT Shape and Size		
Group 1	Group 2	P-Value
Control	Weekend interrupted asymmetric	<0.001***
Control	Weekend interrupted symmetric	<0.001***
Control	Regimes Combined	<0.001***

MT Shape		
Group 1	Group 2	P-Value
Control	Weekend interrupted asymmetric	<0.001***
Control	Weekend interrupted symmetric	0.030*
Control	Weekend interrupted asymmetric 2Hz	0.006**
Control	1st week only asymmetric	0.254
Control	2nd week only asymmetric	0.225
Control	Uninterrupted asymmetric	0.728
Control	Regimes Combined	0.091

MT Shape and Size		
Group 1	Group 2	P-Value
Control	Weekend interrupted asymmetric	<0.001***
Control	Weekend interrupted symmetric	0.048*
Control	Weekend interrupted asymmetric 2Hz	0.005**
Control	1st week only asymmetric	0.354
Control	2nd week only asymmetric	0.235
Control	Uninterrupted asymmetric	0.377
Control	Regimes Combined	0.068

6-3-3 Qualitatively apparent suture patency

Coronal suture patency was investigated qualitatively. This was carried out by observing the reconstructed skull from the dorsal view and categorising the apparently patent sutures and apparently fused sutures on both left (loaded side in asymmetric loadings) and right sides (Figure 6.9). This is similar to the linear measurements comparison to littermate control highlighted in Figure 6.9b. Statistically significant differences between groups are presented in Table 6.3. The results highlighted:

1) The only statistically significant difference compared to the control was the right (not loaded) side coronal suture patency increase from 30% of control animals to 80% of 1st week only asymmetric loading treated animals. Additionally, increases on the left (loaded) side from 27% to 60% for the weekend interrupted asymmetric loading and 1st week only asymmetric loading were observed, however, these were not statistically significant (Table 6.3 and Figure 6.9a – burgundy and navy blue).

2) Neither left nor right coronal suture showed statistically significant differences when comparing control with all loading regimes combined. However, on the left side the percentage of animals with apparently patent sutures were 27% of the control and 38% of treated animals. For the right side, these values were 30% and 33%, respectively. Highlighting some differences and perhaps limited therapeutic benefit of the treatment. (Figure 6.9a – comparing dark green - regimes combined to grey - control)

3) 1st week only asymmetric and uninterrupted asymmetric loading showed the most extreme results with the highest and lowest numbers of animals with suture patency observed, respectively. Their littermate controls replicated their distribution closely, with 3 out of 3 animals showing patency for 1st week only asymmetric loading littermates showing patency and 2 out of 2 uninterrupted loading littermates showing fusion (Figure 6.9b).

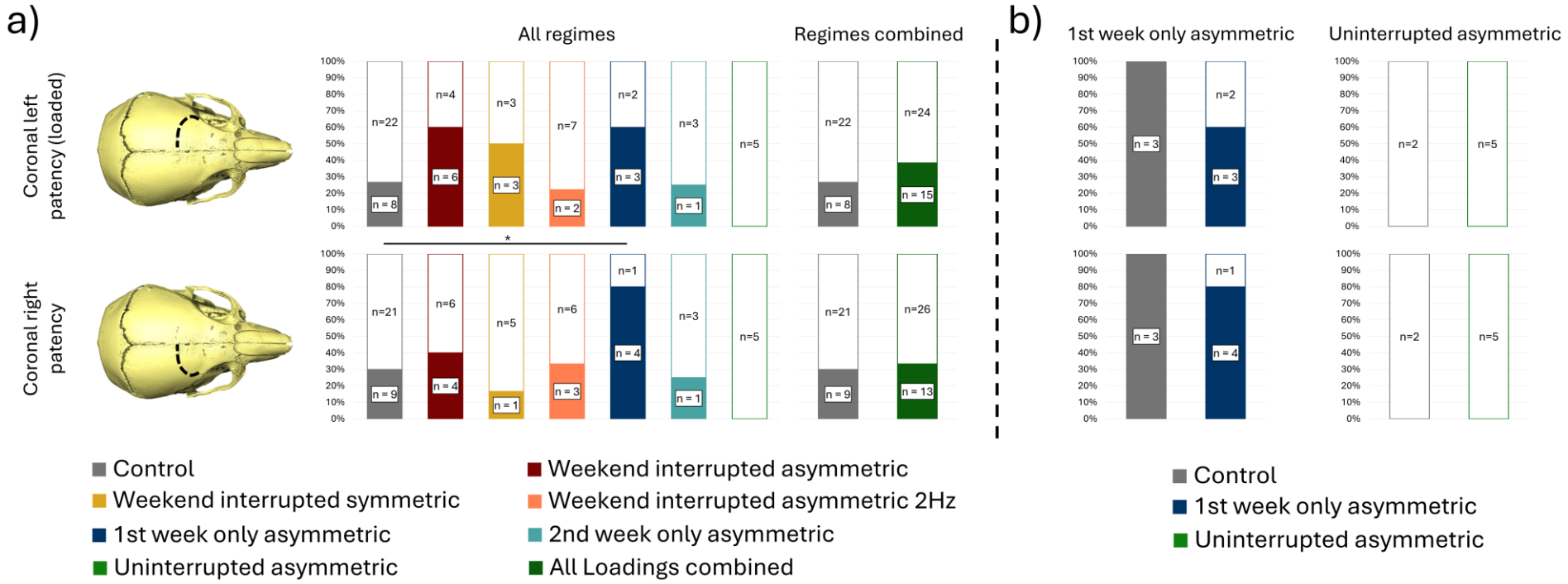

Figure 6.9 Dorsally qualitatively apparent coronal suture patency results a) across all the loading groups individually and all loading regimes combined and b) comparing 1st week only asymmetric and uninterrupted asymmetric with their littermate controls. Statistically significant differences only highlighted in comparisons to the control.

Table 6.3 Statistically significant differences with P values across all pair-wise comparisons for the apparent coronal suture patency.

Left Coronal		
Group 1	Group 2	P-Value
1st week only asymmetric	Uninterrupted asymmetric	0.0400
Weekend interrupted asymmetric	Uninterrupted asymmetric	0.0242

Right Coronal		
Group 1	Group 2	P-Value
Control	1st week only asymmetric	0.0383
1st week only asymmetric	Weekend interrupted symmetric	0.0364
1st week only asymmetric	Uninterrupted asymmetric	0.0040

6-3-4 Qualitatively apparent suture patency

Quantitative suture patency was measured across the metopic, coronal, sagittal, and interparietal sutures as well as a measure of level of fusion was investigated for the ISS (Figure 6.10). The results demonstrate the effects across the major calvarial sutures, which produced a more nuanced investigation of the coronal suture as the apparent patency is binary and fails to capture fusion in suture that show the suture gap dorsally but are ventrally fused. Statistically significant differences are summarised in Table 6.4. Following the previous analyses, littermate control comparisons are included where available in Figure 6.10b. In all analysis, 100% correspond to fully patent suture and 0% to fully fused sutures. The data highlighted:

1) Statistically significant differences compared to control suture patency existed for 1st week only asymmetric loading for the left coronal suture (16.4% ± 27.7% for control and 57.1% ± 50.7% for treated). Representing a statistically significant increase in both the average and the variance. Additionally, a statistically significant decrease in interparietal right suture patency was observed for the weekend interrupted symmetric loading from 85.8% ± 12.0% (control) to 63.9% ± 21.9%. A statistically significant increase in patency was also observed for 1st week asymmetric and uninterrupted asymmetric loadings, from 47.5% ± 14.7% (control) to 66.9% ± 9.5% (1st week only), and 65.5% ± 20.0% (uninterrupted) for the ISS (Figure 6.10a fourth, eighth, and ninth rows).

2) Similar to the other measurement, no statistically significant differences were observed when comparing control against all treated animals as one group. Left (loaded) coronal suture did not show any differences between the two groups (16.4% ± 27.7% for control and 16.2% ± 27.9% for all loading regimes combined). While the right coronal suture patency was slightly decreased (not statistically significant) in the treated group from 18.9% ± 26.9% to 12.0% ± 23.7%, for controls and treated, respectively (Figure 6.10a – comparing dark green - regimes combined to grey - control).

3) The only statistically significant increase in the littermate control comparison was in the ISS patency for the 1st week only asymmetric loading (66.9% ± 9.5%) compared to their littermate controls (46.4% ± 13.5%). However, while the increase observed in left coronal suture patency was no longer statistically significant in the littermate comparison, it still represented a large increase in the average coronal suture patency from 23.3% ± 38.5% (control) to 57.1% ± 50.7% (treated) (Figure 6.10b ninth row).

4) Considering therapeutic effects, all regimes combined did not show any significant improvement, contrary to qualitative suture patency results. The aforementioned 1st week only asymmetric loading showed statistically significant improvements across both right coronal suture (and not statistically significant but large improvement across the left coronal suture. The only other treatment highlighting any level of coronal suture patency improvement was weekend interrupted symmetric loading on the right side (from 16.4% ± 27.7% patency in the control to 20.4% ± 23.3% patency in the treated group). All loadings except for the 1st week only asymmetric loading showed a decrease in coronal suture patency on the left side.

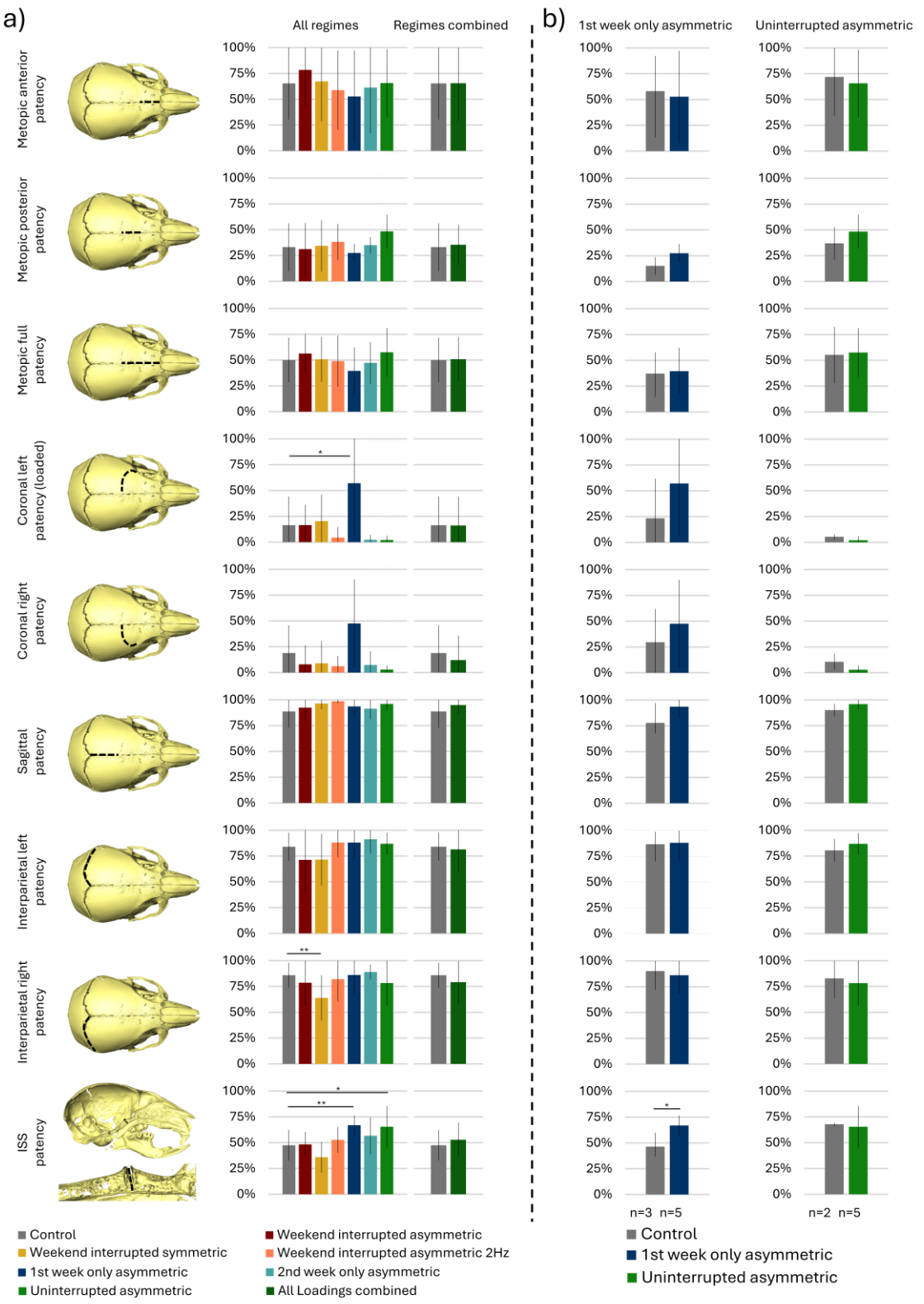

Figure 6.10 Quantitative suture (metopic, coronal, sagittal, and interparietal) and ISS patency results a) across all the loading groups individually and all loading regimes combined and b) comparing 1st week only asymmetric and uninterrupted asymmetric with their littermate controls. Statistically significant differences only highlighted in comparisons to the control.

Table 6.1 Statistically significant differences with P values across all pair-wise comparisons for the suture and ISS patency.

Metopic Posterior		
Group 1	Group 2	P-Value
1st week only asymmetric	Uninterrupted asymmetric	0.0369

Coronal Left		
Group 1	Group 2	P-Value
Control	1st week only asymmetric	0.0120
1st week only asymmetric	Weekend interrupted asymmetric	0.0405
1st week only asymmetric	Weekend interrupted asymmetric 2Hz	0.0092
1st week only asymmetric	Uninterrupted asymmetric	0.0419

Coronal Right		
Group 1	Group 2	P-Value
1st week only asymmetric	Weekend interrupted asymmetric	0.0233
1st week only asymmetric	Weekend interrupted asymmetric 2Hz	0.0141
1st week only asymmetric	Weekend interrupted symmetric	0.0479

Interparietal Right		
Group 1	Group 2	P-Value
Control	Weekend interrupted symmetric	0.0015

Intersphenoid Synchondrosis		
Group 1	Group 2	P-Value
Control	1st week only asymmetric	0.0080
Control	Uninterrupted asymmetric	0.0228
1st week only asymmetric	Weekend interrupted asymmetric	0.0095
1st week only asymmetric	Weekend interrupted asymmetric 2Hz	0.0485
1st week only asymmetric	Weekend interrupted symmetric	0.0031
Weekend interrupted asymmetric 2Hz	Weekend interrupted symmetric	0.0342
Uninterrupted asymmetric	Weekend interrupted symmetric	0.0205

6-4 Discussion

The effects of external cyclic loading as a potential treatment for craniosynostosis was investigated in this chapter using a series of *in vivo* experiments. Following the experiments, animals were CT scanned and a series of morphological analysis were performed based on linear measurements across the skull, PCA, qualitatively apparent coronal suture patency and quantitative suture patency across the major calvarial sutures and the ISS. Six different loading regimes were investigated including weekend interrupted asymmetric following the parameters established in Moazen et al. (2022). The other loading regimes represented small changes from the original regime including weekend interrupted symmetric, weekend interrupted asymmetric 2Hz, 1st week only asymmetric, 2nd week only asymmetric, and uninterrupted asymmetric loadings. The results were investigated for individual treated groups against the control. All treated animals as one group were measured against the control as well as for individual treated groups against their littermate controls when available. These comparisons allowed nuanced interpretation of the results.

Linear measurements highlighted similar variability of the treated groups to litter groups in **Chapter 5**. For the mutants, only one treatment group (uninterrupted asymmetric) was significantly different across full skull length, braincase length, and braincase curvature. All three of these measurements were interdependent and showed an overall shorter skull of this treated group. All measured parameters were reduced in the treated group highlighting overall smaller skulls in this treated group. A number of possible explanations for the decrease can be considered.

Firstly, both full skull length and the braincase length were found to be the most litter-dependent linear measurements. False positive rates (incidence of artefactual statistical significance from **Chapter 5**) for a similar comparison were found to be 22% for the skull length and 24% for the braincase length. Coincidentally, 2 animals in the control were littermates of the uninterrupted asymmetric loading cohort. This enabled some comparison between littermates. While statistically significant differences were no longer present in these comparisons and the control littermates were smaller than the general control population, a non-statistically significant decrease in the linear measurement values was still present for the treated group. This highlights that the treatment may have an influence, but the effect size could be significantly lower than previously thought.

Equally, the differences may be the same individual variation observed throughout this work.

One possible driver of the differences is direct loading effects. However, the loading parameters in this group are consistent with the other treatments, with the only change of duration. This loading group did not have the rest days at P12, P13, P19, and P20, as did the weekend interrupted loading regimes. It is possible that the rest day could play a biological role in suture retention. However, if suture retention is mechanical by disrupting the formation of bone bridges across the coronal suture better results would be expected of this group. Here, all the other treated groups did not show improved shape across the linear measurements compared to the WT animals. However, the uninterrupted group showed adverse effects, suggesting that the decreased values are not necessarily loading related.

The uninterrupted loading showed deformation across the frontal bone in some of the treated animals. As the loading location on the frontal bone happens to correspond to the most porous part of the MT skulls, it appears that the loading has had a significant effect in the immediate loading area (see Figure 6.11b). This was not observed as clearly for the other loading regimes. The damage was observed directly in animals loaded from P7 to P11 and culled at P11 with the standard loading parameters of asymmetric loading (see Figure 6.10a). Potentially indicating that the rest days are important to allow ossification of the frontal bone and healing from the loading. However, the weekend interrupted asymmetric 2Hz loaded animals showed qualitatively similar if not larger damage to the frontal bone (see Figure 6.10c). This was likely related to an increase in locally transferred energy due to the higher loading frequency, which occurred regardless of the rest days included in the treatment regime. These animals, however, did not show any comparable decrease in the linear measurements observed in the uninterrupted asymmetric loading group. This suggests that the damage might not be the key contributing factor.

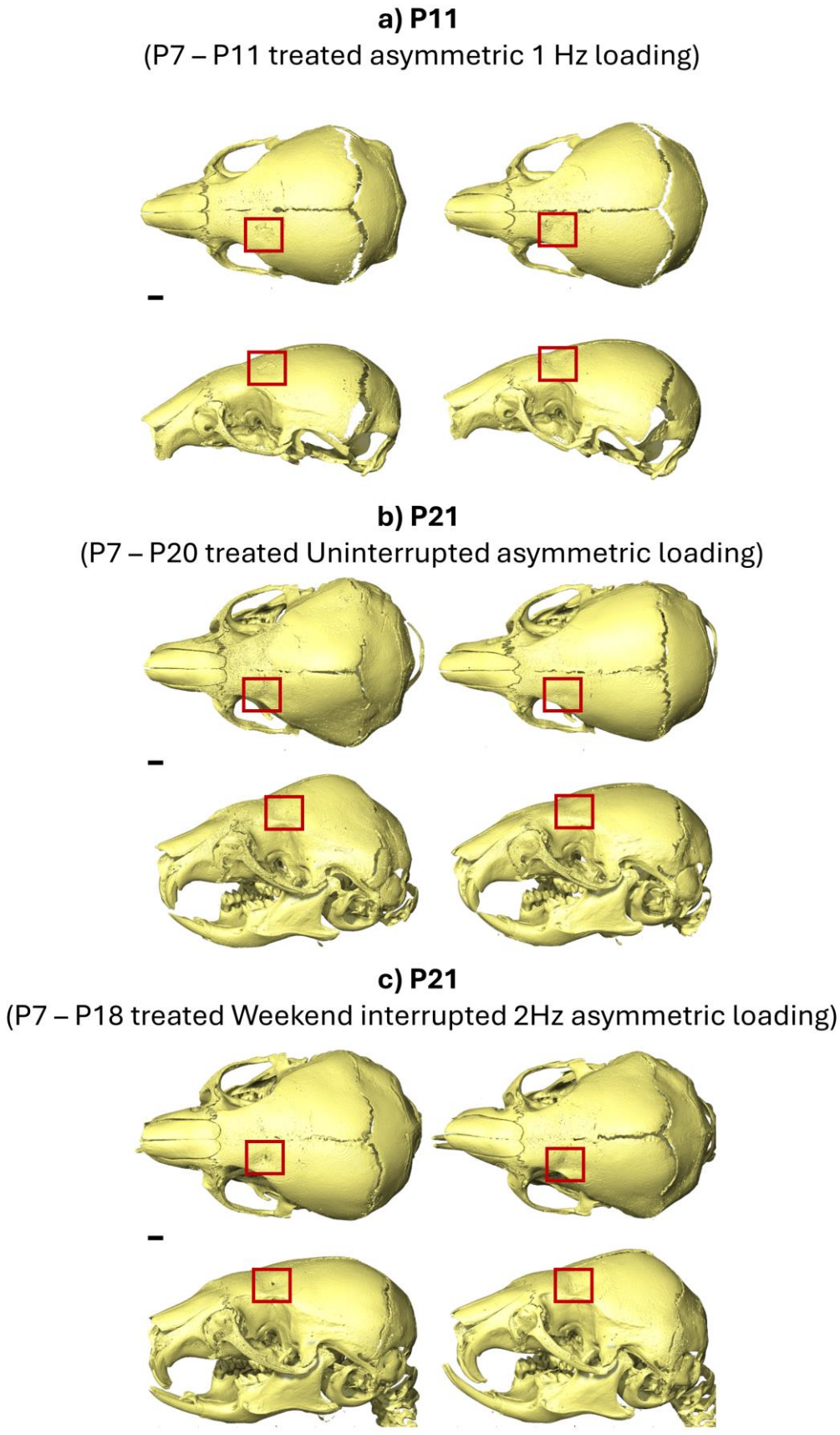

Figure 6.11 Qualitative comparison of the frontal bone damage for two distinct individuals per group in a) P11 treated from P7 to P11, b) P21 treated from P7 to P20 and c) P21 treated from P7 to P18 with weekend interruption at 2Hz. Boxes highlight damaged areas and 1mm scale bar is included.

A possible explanation for the observed differences remains. The total isoflurane (anaesthetic) dose is higher in these animals compared to the other treatment regimes. This is because they have been loaded for more days; additionally, the lack of rest days may further hinder normal growth compared to both the general control population and more specifically their littermate controls. As sham loading was not included in the control cohort, the effects of isoflurane exposure remain unaccounted for. The exposure can have direct negative effects on cell behaviour (Istaphanous et al. 2013; Zhao et al. 2020) and effects of cognitive impairment (Liu et al. 2017) in neonatal mice and has been shown to contribute to weight loss in adult mice (Spencer et al. 2023). The daily exposure to isoflurane in this group may account for the observed effects, however, further investigations are required to validate the speculation here, as no literature exists on direct morphological effects of early postnatal isoflurane administration.

While investigation of the individual treatment groups can help better understand the potential effects of various loading parameters, the study design implications laid out in Chapter 5 make the results hard to interpret. To partially account for this, in addition to the direct littermate control comparisons investigated where available, all treatment regimes were considered as one group allowing for similar N numbers between the treated (n = 39) and control (n = 30) groups. This was included in the hopes to understand whether the loading has an effect across all the investigated dimensions. As the loading regimes are largely similar to each other with minor changes to the number of sessions, symmetricity, and frequency, the combined treated group should allow for a good overview of the general effects of loading. Considering linear measurements, no statistically significant effects were observed between the control and treated groups in terms of both average values and variance. Such distinct agreement between the control and treated group may indicate that the variation between different loading regimes is the same variation between different litters observed in the control animals.

Lastly, concerning the linear measurements, the results of the weekend interrupted asymmetric loading were directly compared to the results of Moazen et al. (2022). The same landmarks were placed on the treated and untreated animals from the Moazen et al. (2022) study; the linear measurements are presented in Figure 6.12. Generally, greater morphological improvement was observed in the previous study compared to this work. Additionally, significant differences are observed in the control group. It is unclear why the improvements, specifically, in skull length were not replicated in the current study.

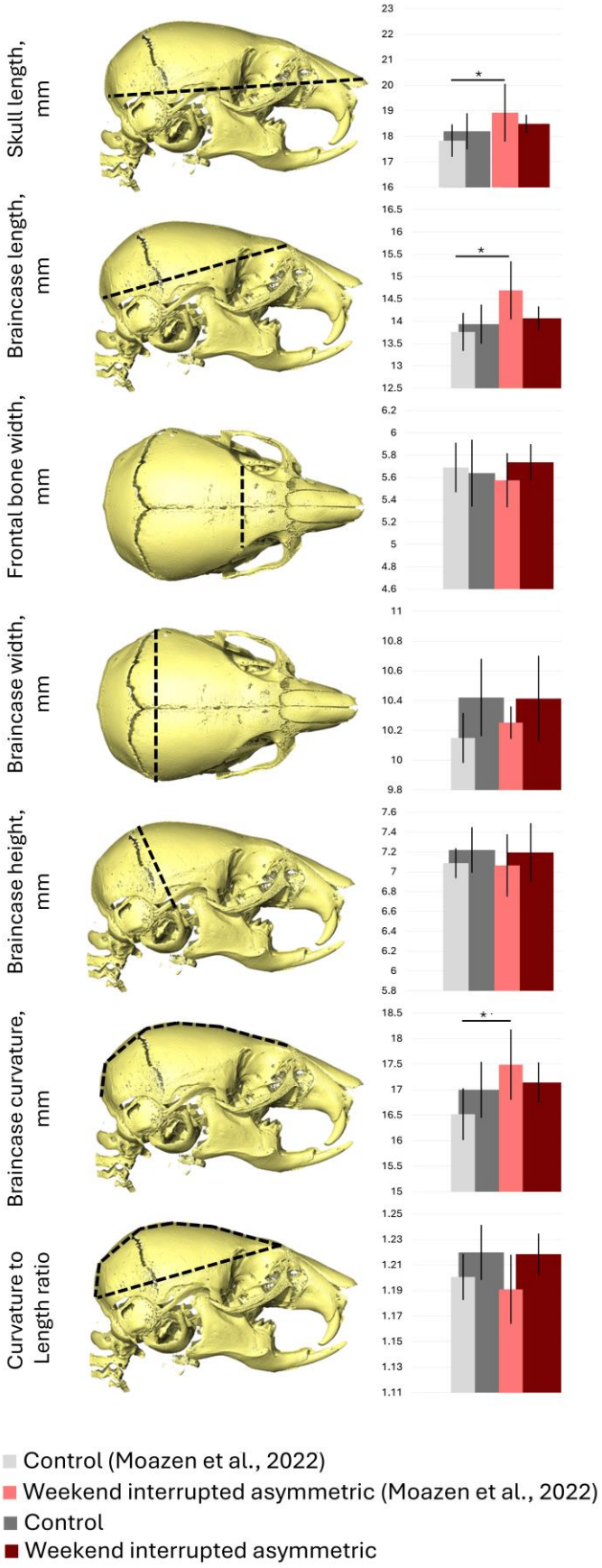

Figure 6.12 Linear measurement results for MT animals. Control and weekend interrupted asymmetric loading in this work and in Moazen et al. (2022).

One possible explanation could be genetic drift and thus phenotypic drift, explaining both the observed differences in control animals and potentially the treatment effects. For example, Moazen et al. (2022) reported entirely patent ISS in both control and treated animals (in total 4 of 31 mutant animals). Of the 69 MT animals investigated in this study, none of the animals showed ISS patency. Potentially indicating significant phenotypic differences between the control animals. Which, in turn, potentially permitted more prominent treatment effects. The possibility of this is strengthened by observed variability in phenotypic severity across different mice backgrounds, highlighting how the interplay between the background genetics and the specific mutation can alter phenotypic presentation (Dudakovic et al. 2020). This is further discussed in Section 2-3. Additionally, the fixation protocol was entirely different in the original study, resulting in severe shrinkage during the CT scan. It is unclear what effects this has had on morphology and suture patency. The available data simply did not have sufficient resolution to accurately investigate suture patency. Thus, the Moazen et al. (2022) animals were generally omitted from treatment comparisons.

The PCA largely supports the linear measurement findings, especially highlighting limited effects of loading in general in the mutant animals, with no significant shift towards the more wildtype shape across PC1. However, some individual loading groups exhibit overall statistically significant forms and shapes. In the WT group, the investigated treatment regimes highlighted statistically significant differences to the control animals, primarily related to PC3, which in the WT only PCA largely captured braincase height and braincase curvature to length ratio, capturing reduced bulge. The linear measurements for these also highlighted statistically significant differences for the weekend interrupted symmetric loading group. The same loading groups also showed statistically significant differences in form and shape compared to the control animals in the MT analysis. Similarly, the differences largely hinged on PC3 for shape and PC4 for form, however, the weekend interrupted asymmetric and symmetric loading groups showed increased bulge and reduced length (generally considered a more severe phenotype) compared to the control animals. Weekend interrupted asymmetric 2Hz loaded group was also statistically significantly different from the control and showed opposite clustering in PC3 with a slightly reduced bulge and increased length.

Neither linear measurements nor the PCA highlighted any strong effects linked to loading in general or individual loading regimes to significantly normalise the overall skull shape of the treated mutant animals to more wild-type like skull shapes. In Moazen et al. (2022),

the proposed mechanism for skull phenotype rescue is the rescue of the coronal suture patency and potentially the ISS. The coronal patency was investigated through qualitative dorsal observation of the coronal suture. Quantitative patency measurements were carried out across the metopic, coronal, sagittal, and interparietal sutures and the ISS to further uncover the effects of the treatment on the major calvarial sutures.

The qualitative coronal suture investigation highlighted a statistically significant increase in the right (not loaded) side patency for the 1st week only asymmetric loading group. Due to the low number of observations, large differences in distribution is required for statistical significance. Thus, the increases on the left (loaded) side patency for both 1st week only asymmetric and weekend interrupted asymmetric loading regimes were not statistically significant. 1st week only asymmetric loading and uninterrupted asymmetric loading groups both happened to have littermate controls and were the most extreme cases with the most and the least patent sutures, respectively. Comparison with their littermate controls highlights that these extremes are likely linked to littermate effects rather than the treatment. Considering the regimes combined, the incidence of patent sutures appears to be consistent between the control and treated animals. With these considerations in mind, it is unclear whether the non-significant increase for the weekend interrupted asymmetric group is linked to treatment effects or the normal litter-specific variation in the mouse model.

The gross qualitative coronal suture patency analysis is significantly limited. As shown in Steacy et al. (in review), some dorsally apparently patent sutures will be entirely fused on the ventral side of the suture. As sutures play a mechanical role in skull growth, bony bridges across the suture or, in some cases, entire ventral suture fusion would significantly impair or effectively eliminate the deformation permitting function of the sutures, that allows for normal skull development (seen as no deformation across the partially fused sutures in **Chapter 4**). Thus, the qualitative analysis is largely inappropriate for suture fusion estimation and potentially entirely irrelevant in considerations of suture mechanical function rescue. These limitations are addressed by the qualitative suture patency analysis introduced in **Chapter 5** and repeated in this chapter.

Across the targeted coronal sutures again, the only statistically significant increase in quantitative suture patency is observed for the coronal suture in 1st week only asymmetric loading compared to the control on the left side. While not statistically significant, a large increase in quantitative suture patency was observed for the group on the right side as well. The statistically not significant increase for the qualitative suture patency was not

replicated by the quantitative suture patency in the weekend interrupted asymmetric loading, with no change observed on the left side and a decrease in patency observed on the right side. Like the other measurements, the coronal suture patency when comparing all loaded groups to the control showed no change. The loading regimes that showed statistically significant differences in shape and form (weekend interrupted asymmetric, symmetric, and asymmetric 2Hz) did not show any statistically significant differences in coronal suture patency and the differences observed were largely a decreased patency compared to the control animals.

Across all other sutures, only the right interparietal suture for the weekend interrupted symmetric loading, was statistically significantly affected when compared to the control, with a decrease in suture patency. However, both weekend interrupted asymmetric and symmetric treated groups showed a decrease in left and right interparietal suture. While not statistically significant, this may partially account for the observed statistically significant differences in shape, as some correlation between the interparietal suture patency and the calvarial bulge was observed in **Chapter 5**. Akin to all observed values in this work, the comparison between all treated animals against the control animals did not show any statistically significant differences.

1st week only asymmetric group and uninterrupted asymmetric group showed statistically significant differences in ISS patency when compared to the control. In the only instance, littermate comparison failed to reduce the difference in patency of the ISS to a statistically nonsignificant one for the 1st week only asymmetric group. However, the difference was eliminated for the uninterrupted asymmetric loading group. While this may suggest that the loading influenced the ISS patency in only the 1st week loaded group, the numbers of animals included are too small to confidently assert this. Especially as the ISS patency showed the strongest link with litter across all investigated patency scores in **Chapter 5** (ICC = 0.68). Additionally, it is unclear why this loading regime would be the only one to produce positive results, considering that the only difference compared to the weekend asymmetric loading is the reduced number of sessions. **Chapter 5** highlighted that patency is somewhat correlated across different sutures in individuals. The statistically nonsignificant increase observed in the other suture patency may indicate natural variation.

The ISS patency here investigated is the level of partial patency for the ISS as opposed to actual patency for the other sutures, due to the fusion of the ISS in all investigated animals. The role of the potential rescue observed is unclear, as no strong correlations were

observed in **Chapter 5** and equally the other group (uninterrupted asymmetric loading), with significantly more patent ISS showed significantly worse skull shape compared to control animals, contradicting the potential skull shape rescue locus.

Limitations

Several limitations are considered in this chapter. 1) The treatment study was not designed with littermate control for comparison, which was shown to be critical in **Chapter 5** for meaningful statistical interpretation of treatment effects in these animals. Where control littermates were available, they largely captured the same effects. This further highlighted the potential effects of littermate variation and the difficulty in interpreting the results without the littermate controls. 2) While a comparison of all treatment regimes combined showed a very high level of agreement with the control animals, it is critical to note that the investigation does not indicate that no loading regime can have an effect on the investigated values, but rather that the loading regimes investigated in this work, as a group, did not show any effects. 3) While the chapter investigated various loading regimes, the loading parameter space remains largely uninvestigated. The effects of increased or decreased force, duration per session, and frequency remain unknown.

6-5 Summary

In summary, this chapter investigated the effects of external cyclic loading *in vivo* on craniofacial morphology in MT and WT mice and MT mice suture patency. The original treatment regime proposed by Moazen et al. (2022) was repeated, and five other regimes were investigated with minor changes to the symmetry, number of sessions, and loading frequency. This investigation failed to reproduce the phenotypic rescue effects for both skull shape and suture patency of the external cyclic loading, following the same loading parameters laid out in Moazen et al. (2022) – weekend interrupted asymmetric loading or in any of the adjusted loading regimes investigated. It highlighted no effects of loading in general across all investigated variables, with limited and apparently unconnected effects for individual loading regimes. Where differences between the control and individual treated groups existed, they were largely explained by litter variation (in the comparison between littermate controls) and following the findings of **Chapter 5**.

Chapter 7 Discussion, conclusions and future work

This project aimed to understand the response of the craniofacial system to external loading. In summary, this was achieved by following the methodology set out in **Chapter 1**. First, the response of the skull was investigated *ex vivo* in terms of mechanical strain induced across the sutures during frontal loading and compared to *in vivo* results to establish comparability between the two loading types. Then, additional loading locations were investigated *ex vivo* and *in silico*. The variability of the WT and MT skull shape was characterised specifically as it relates to littermate groups, and the correlation of suture patency to shape was investigated in MT animals. A set of *in vivo* treatment experiments were carried out to further investigate the effects of external loading on craniofacial suture patency and shape. These investigations are crucial in translating the treatment regime proposed by Moazen et al. (2022) and in understanding its efficacy and the underlying mechanisms by which it impacts the craniofacial system. This chapter summarises the key findings, limitations of the works conducted in this thesis and future work.

7-1 Synthesis of key findings

7-1-1 *Ex vivo* static loading suture strains provide baseline values for translation of the treatment and development of *in silico* models

The first body of work carried out in this thesis (**Chapter 3**) examined the response of the craniofacial sutures to external loading of the frontal bone in the dorsoventral direction. It focused on the comparison between the craniofacial deformations across *in vivo* and *ex vivo* dynamic loading and *ex vivo* static loading. These comparisons highlighted the suitability of *ex vivo* static loading as a proxy for *in vivo* dynamic loading in terms of apparent deformation across the sutures. While largely focusing on the WT animals, this chapter established the level of mechanical strain induced across the coronal suture during external loading. These data are already in use by other researchers for the translation of the treatment approach to larger animal models. The data also established a validation data set for *in silico* investigations.

Large strains across the coronal sutures were observed in this work. ~0.6 to ~0.8 for the loaded side suture and ~0.5 to ~0.7 for the unloaded side suture, suggesting significant load transfer. Additionally, in both *in vivo* and *ex vivo* investigations, a permanent deformation across the suture thickness was observed, highlighting that it was plastically deformed.

Sagittal suture strain quantifications, highlighted that significant deformations of the skull were present even across other sutures. The strains were the highest in the P7 animals and reduced in P14 and P21. These findings suggest age-related differences in skull morphology and most likely the metopic suture patency plays a key role in the deformation patterns across the skull during loading.

7-1-2 The response of the craniofacial system to loading is significantly varied with loading location suggesting location dependent stiffness and insufficiency of linear elastic models in capturing the effects

The second body of work carried out in this thesis (**Chapter 4**) largely augmented the findings of **Chapter 3**. The introduction of BounTI (Appendix II) enabled the investigation of all the major calvarial sutures as opposed to only the coronal and sagittal sutures in **Chapter 3**. Additionally, the automated segmentation tool enabled rapid development of *in silico* models, that enabled the development of WT models at 3 different ages (P7, P14, and P21).

Highly variable strain patterns were demonstrated for the different loading locations investigated. For both MT and WT animals, P7 frontal bone loading produced significantly less deformation than any of the other investigated locations. The qualitative results highlighted that at P14 this remained true in WT animals but not in MT animals where the level of deformation at both P14 and P21 appeared relatively consistent between the loading locations, highlighting the role suture fusion plays in permitting deformation across the skull. At P21, WT animals no longer showed the large differences between loading regimes.

In silico models failed to accurately predict suture strain, even considering adjusted material models. Two conclusions can be taken away from this finding: First, linear elastic isotropic material models are likely inappropriate for capturing the deformation patterns across the skull, especially at different locations (at least in early postnatal mice). Secondly, significantly different deformation responses are observed across the different loading locations, highlighting the physical effects not reducible to simple linear models even when optimised for this purpose.

The work highlighted significantly higher strains for “targeted” sutures (closest to the loading location) in the more posterior loading scenarios compared to frontal bone loading. At P7 and P14, this increase ranged from 2 to 5 times the strain, implying that for similar therapeutic effects observed in Moazen et al. (2022) critical consideration of the loading parameters is required for translation of the loading regime to other models of craniosynostosis and specifically targeting other sutures.

7-1-3 The inherent variability of the Crouzon mouse craniofacial phenotype shows significant inter-litter effects and little suture patency to morphology correlation

The third body of work carried out in this thesis (**Chapter 5**) investigated the intra vs inter-litter phenotypic variation in WT and MT animals and the effect of suture fusion on morphology in MT animals. Linear measurements, overall skull morphology, and local suture patency was investigated. Key take home messeges from this chapter are:

Firstly, intra vs inter-litter analysis highlighted that litter-based separation into treated and untreated groups produced statistically significantly different results across all investigated measures more frequently than the 5% set out by $p < 0.05$. In the extreme case of skull length in the WT, as high as 50% of comparison permutations showed statistically significant differences. In this chapter, an alternative study design is proposed, with the litter split in half (one half is used as control and one as treated). This approach appeared to eliminate the litter-specific effects with an average 5% of permutations showing statistical significance.

Secondly, there is limited correlation between the various sutures' patencies and the skull morphology in the Crouzon mouse model. Surprisingly, showing that where correlations existed increased suture patency also showed increased phenotypic severity. This challenges the common assumption of suture fusion, namely the fusion of the coronal suture as the locus of craniofacial dysmorphology in the Crouzon mouse model.

However, the fusion level of other sutures or the severity of the ISS fusion did not show any stronger or positive correlations with more WT-like skull shapes in the mutants, thus, no alternative driver of the phenotype was found in these investigations.

7-1-4 External cyclical *in vivo* loading of the frontal bone (across varied loading regimes) failed to reproduce the previously observed therapeutic effects for both overall morphology and suture patency

The fourth body of work carried out in this thesis (**Chapter 6**) repeated the *in vivo* treatment experiments set out by Moazen et al. (2022). The investigations were augmented by including other loading protocols (six in total) and more detailed morphological and suture patency analyses, largely following the analyses set out in **Chapter 5**.

The morphological improvements from the cyclic loading treatment originally reported in Moazen et al. (2022) were not replicated in this work. Where statistically different skull shapes were observed for mutant control to individual treatment comparisons, they were largely associated with increased phenotypic severity. When all loading regimes were combined, no meaningful differences were present. In these investigations, external cyclic loading did not treat the dysmorphology of the mouse model.

Only one treatment regime (P7-P13 loaded animals – 1Hz, 10g, 10min/day) showed statistically significant improvements in coronal suture patency. These improvements were observed in both qualitative and quantitative suture patency. However, these were largely explained by the litter-specific variation because their littermate controls showed similar levels of suture patency.

In general, where statistically significant differences were observed between individual treatment regimes and control animals, they were largely captured by litter variation, as discussed in **Chapter 5**. The effect of *in vivo* external cyclic loading remains unclear; however, the failure of this work to reproduce the therapeutic effects originally established in Moazen et al. (2022) questions the efficacy of external cyclic loading as a tool for the treatment of craniosynostosis.

7-2 Limitations of the present study

More broad limitations to the ones presented in each chapter are discussed here, specifically highlighting the scope of this study and equally introducing potential avenues for future research to investigate.

(1) A significant limitation of the *ex vivo* part of this work (**Chapter 3** and **Chapter 4**) is the lack of direct investigation of MT suture strain during external loading. While efforts were made to characterise the deformation in the MT suture in **Chapter 4**. The analysis is limited.

(2) Similarly, while efforts were made (**Chapter 3**) to establish the suitability of *ex vivo* static loading as a proxy for *in vivo* dynamic loading. True response during the *in vivo* dynamic loading remains unknown. This is particularly problematic in the MT case as the suitability of the static/dynamic loading strain equivalency was established by investigating the WT response.

(3) **Chapter 4** established the limitations of linear elastic properties in predicting the deformation patterns during static loading. These limitations stem directly from a lack of direct material investigations into the suture, bone, and brain materials during early postnatal development. Further material testing is critical to establish physically relevant material models and improve the current FE models.

(4) While the study design implications are discussed in detail in both **Chapter 5** and **Chapter 6**. These were not already established during the experimental design of any of the investigations in this work, as the analysis was carried out on the control animals from **Chapter 6**. The solution proposed by **Chapter 5** does not allow for post hoc reinterpretation of results. These limitations establish a need for the investigations of **Chapter 6** to be repeated with the statistical implications established in this work kept in mind.

(5) Finally, the overall loading parameter space (force, frequency, and duration) has been largely left unexplored. **Chapter 3** and **4** followed the loading parameters established by Moazen et al. (2022), with investigations across different loading locations included in **Chapter 4**. While **Chapter 6** investigated different loading regimes *in vivo* only, one investigation included a change to the original loading parameters themselves (frequency: from 1Hz to 2Hz). The possibility remains that the investigated loading parameters are suboptimal for the desired effect, suggesting a need for further exploration.

7-3 Future work

One potential avenue for future work is addressing the limitations of the presented investigations available throughout this work and generalised in the previous section. Equally, the thesis focuses on establishing the fundamental response of the craniofacial system to external loading. Thus, establishing a foundation for future *in silico* work and translation to both other mouse models of craniosynostosis and larger animal models.

From the limitations, a significant opportunity for further investigations remains the direct measurement of the coronal and other suture strain during loading (*in/ex vivo*). Further methodological advancements may enable future research to investigate the mutant sutures directly, quantifying strain in partially fused sutures. While regular μCT does not have sufficient resolution and contrast to use DVC tools to directly investigate bone strain during *in situ* loading in neonatal mice, phase contrast μCT enabled by synchrotrons may allow for both sufficient resolution and feature-rich bone contrast to directly investigate strains in the bone and suture during *in situ* loading.

Similarly, the thesis highlighted a need for further material characterisations for the sutures, bones, and brain. The data on suture strain across the different loading locations available in this work can be leveraged for FE model validation. Further material characterisations may enable highly predictive FE models, validated with the available data. If predictive FE models can be developed, a new avenue would be available for the characterisation of MT suture strain during external loading.

As this research was a part of a larger CranioMech project at the MoazenLab, a number of investigations are currently underway which could be considered as natural extensions of this work. Namely, Ms Steady and Dr Qiu are investigating the loading effects through the lens of molecular biology, working on immunohistochemistry and gene expression in the sutures. The first of these investigations is currently formulated in a manuscript by Steacy et al (in review) on the same animals as presented in **Chapter 6**. Similarly, translation to larger animals (pig) investigations are currently underway by Dr Vithanage and Dr Liang. The translation to other mouse models of craniosynostosis is in the planning stages.

Chapter 5 and **Chapter 6** highlight significant limitations in the previous investigation of *in vivo* loading effects (Moazen et al. 2022) and also in the ones presented in this work. As the investigations failed to reproduce the significant therapeutic loading treatment effects originally observed, a critical future consideration should be further investigations into the original loading regime, following the study design considerations laid out in **Chapter 5**. This should be focused directly on establishing the efficacy of the original treatment regime in treating craniosynostosis. Equally, to establish optimal loading parameters, the parameter space warrants further investigation. Currently, the suitability of the force and its frequency and duration are largely assumed, but more direct investigation into these parameters may reveal optimal values.

Lastly, the development of BounTI has already enabled the investigations presented in **Chapter 4**. Similarly, researchers across MoazenLab, UCL's Centre for Integrative Anatomy and other research institutions around the world (such as Leipzig University, Stanford University and University of California, San Francisco) have used the tool to enable detailed research in some cases previously considered prohibitively time-consuming. The methodology developed for BounTI has led to the development of new tools such as SPROUT (He et al. 2024) in collaboration with the Natural History Museum. With an ever-increasing user base producing disarticulated segmentations across the skull and other skeletal regions, the data available may be leveraged in the future to develop deep learning models. The developed models could possibly address BounTI's shortcomings, namely segmentation inaccuracies in poor-quality CT data, particularly applicable in clinical CT.

References

Aggarwal M, Zhang J, Miller MI, et al (2009) Magnetic resonance imaging and micro-computed tomography combined atlas of developing and adult mouse brains for stereotaxic surgery. Neuroscience 162:1339–50. https://doi.org/10.1016/j.neuroscience.2009.05.070

Ajami S, Van den Dam Z, Hut J, et al (2024) Cranial bone microarchitecture in a mouse model for syndromic craniosynostosis. J Anat. https://doi.org/10.1111/joa.14121

Alden TD, Lin KY, Jane JA (1999) Mechanisms of premature closure of cranial sutures. Child's Nervous System 15:670–675. https://doi.org/10.1007/s003810050456

Bailon-Zambrano R, Sucharov J, Mumme-Monheit A, et al (2022) Variable paralog expression underlies phenotype variation. Elife 11:. https://doi.org/10.7554/eLife.79247

Banstola A, Reynolds JNJ (2022) The sheep as a large animal model for the investigation and treatment of human disorders. Biology (Basel) 11:1251. https://doi.org/10.3390/biology11091251

Bar-Kochba E, Toyjanova J, Andrews E, et al (2015) A fast iterative digital volume correlation algorithm for large deformations. Exp Mech 55:261–274. https://doi.org/10.1007/s11340-014-9874-2

Barrell WB, Adel Al-Lami H, Goos JAC, et al (2022) Identification of a novel variant of the ciliopathic gene FUZZY associated with craniosynostosis. European Journal of Human Genetics 30:282–290. https://doi.org/10.1038/s41431-021-00988-6

Bay BK, Smith TS, Fyhrie DP, Saad M (1999) Digital volume correlation: Three-dimensional strain mapping using X-ray tomography. Exp Mech 39:217–226. https://doi.org/10.1007/BF02323555

Beck JA, Lloyd S, Hafezparast M, et al (2000) Genealogies of mouse inbred strains. Nat Genet 24:23–25. https://doi.org/10.1038/71641

Behr B, Longaker MT, Quarto N (2011) Craniosynostosis of coronal suture in Twist1+/− mice occurs through endochondral ossification recapitulating the

physiological closure of posterior frontal suture. Front Physiol 2:. https://doi.org/10.3389/fphys.2011.00037

Bilston L (1997) Linear viscoelastic properties of bovine brain tissue in shear. Biorheology 34:377–385. https://doi.org/10.1016/S0006-355X(98)00022-5

Bradley JP, Levine JP, McCarthy JG, Longaker MT (1997) Studies in cranial suture biology: Regional dura mater determines in vitro cranial suture fusion. Plast Reconstr Surg 100:1091–1099. https://doi.org/10.1097/00006534-199710000-00001

Breakey RWF, van de Lande LS, Sidpra J, et al (2021) Spring-assisted posterior vault expansion-a single-centre experience of 200 cases. Childs Nerv Syst 37:3189–3197. https://doi.org/10.1007/s00381-021-05330-5

Buchanan E, Xue Y, Xue A, et al (2017) Multidisciplinary care of craniosynostosis. J Multidiscip Healthc Volume 10:263–270. https://doi.org/10.2147/JMDH.S100248

Budday S, Nay R, de Rooij R, et al (2015) Mechanical properties of gray and white matter brain tissue by indentation. J Mech Behav Biomed Mater 46:318–330. https://doi.org/10.1016/j.jmbbm.2015.02.024

Buljac A, Jailin C, Mendoza A, et al (2018) Digital Volume Correlation: Review of progress and challenges. Exp Mech 58:661–708. https://doi.org/10.1007/s11340-018-0390-7

Buzi C, Profico A, Liang C, et al (2023) Icex : Advances in the automatic extraction and volume calculation of cranial cavities. J Anat 242:1172–1183. https://doi.org/10.1111/joa.13843

Campos-Ordoñez T, Buriticá J (2024) Assessment of the inbred C57BL/6 and outbred CD1 mouse strains using a progressive ratio schedule during development. Physiol Behav 277:114485. https://doi.org/10.1016/j.physbeh.2024.114485

Carlton MBL, Colledge WH, Evans MJ (1998) Crouzon-like craniofacial dysmorphology in the mouse is caused by an insertional mutation at the Fgf3/Fgf4 locus. Developmental Dynamics 212:242–249. https://doi.org/10.1002/(SICI)1097-0177(199806)212:2<242::AID-AJA8>3.0.CO;2-H

Carver EA, Oram KF, Gridley T (2002) Craniosynostosis in Twist heterozygous mice: a model for Saethre-Chotzen syndrome. Anat Rec 268:90–2. https://doi.org/10.1002/ar.10124

Chebrolu N, Labe T, Stachniss C (2020) Spatio-temporal non-rigid registration of 3D point clouds of plants. In: 2020 IEEE International Conference on Robotics and Automation (ICRA). IEEE, pp 3112–3118

Chen L, Li D, Li C, et al (2003) A Ser250Trp substitution in mouse fibroblast growth factor receptor 2 (Fgfr2) results in craniosynostosis. Bone 33:169–178. https://doi.org/10.1016/S8756-3282(03)00222-9

Chen ZF, Behringer RR (1995) Twist is required in head mesenchyme for cranial neural tube morphogenesis. Genes Dev 9:686–699. https://doi.org/10.1101/gad.9.6.686

Chien CH, Wu YD, Chao YJ, et al (2008) The effects of different cranial modules on mechanical properties of cranial suture in Lewis rats and same-aged C57BL/6 mice. Strain 44:272–277. https://doi.org/10.1111/j.1475-1305.2007.00385.x

Claessens M, Sauren F, Wismans J (1997) Modeling of the human head under impact conditions: A parametric study. In: Journal of Passager Cars. pp 3829–3848

Cleall JF, Bayne DI, Posen JM, Subtelny JD (1965) Expansion of the midpalatal suture in the monkey. Angle Orthod 35:23–35. https://doi.org/10.1043/0003-3219(1965)035<0023:EOTMSI>2.0.CO;2

Coats B, Margulies SS (2006) Material properties of human infant skull and suture at high rates. J Neurotrauma 23:1222–1232. https://doi.org/10.1089/neu.2006.23.1222

Cornelissen M, Ottelander B den, Rizopoulos D, et al (2016) Increase of prevalence of craniosynostosis. Journal of Cranio-Maxillofacial Surgery 44:1273–1279. https://doi.org/10.1016/j.jcms.2016.07.007

Cross C, Khonsari RH, Patermoster G, et al (2022) A computational framework to predict calvarial growth: optimising management of sagittal craniosynostosis. Front Bioeng Biotechnol 10:913190. https://doi.org/10.3389/fbioe.2022.913190

Dall'Ara E, Tozzi G (2022) Digital volume correlation for the characterization of musculoskeletal tissues: Current challenges and future developments. Front Bioeng Biotechnol 10:. https://doi.org/10.3389/fbioe.2022.1010056

David DJ, Sheen R (1990) Surgical correction of Crouzon syndrome. Plast Reconstr Surg 85:344–54. https://doi.org/10.1097/00006534-199003000-00002

de Rooij R, Kuhl E (2016) Constitutive modeling of brain tissue: Current perspectives. Appl Mech Rev 68:. https://doi.org/10.1115/1.4032436

Deck C, Willinger R (2008) Improved head injury criteria based on head FE model. International Journal of Crashworthiness 13:667–678. https://doi.org/10.1080/13588260802411523

Delille R, Lesueur D, Potier P, et al (2007) Experimental study of the bone behaviour of the human skull bone for the development of a physical head model. International Journal of Crashworthiness 12:101–108. https://doi.org/10.1080/13588260701433081

Delye HK, Borstlap W, van Lindert E (2018) Endoscopy-assisted craniosynostosis surgery followed by helmet therapy. Surg Neurol Int 9:59. https://doi.org/10.4103/sni.sni_17_18

Devine J, Vidal-García M, Liu W, et al (2022) MusMorph, a database of standardized mouse morphology data for morphometric meta-analyses. Sci Data 9:230. https://doi.org/10.1038/s41597-022-01338-x

Dias IE, Viegas CA, Requicha JF, et al (2022) Mesenchymal stem cell studies in the goat model for biomedical research—A review of the scientific literature. Biology (Basel) 11:1276. https://doi.org/10.3390/biology11091276

Didziokas M, Pauws E, Kölby L, et al (2024) BounTI (boundary-preserving threshold iteration): A user-friendly tool for automatic hard tissue segmentation. J Anat. https://doi.org/10.1111/joa.14063

Dudakovic A, Nam HK, Wijnen AJ van, Hatch NE (2020) Genetic background dependent modifiers of craniosynostosis severity. J Struct Biol 212:107629. https://doi.org/10.1016/j.jsb.2020.107629

Dutta S, Sengupta P (2016) Men and mice: Relating their ages. Life Sci 152:244–248

Eswarakumar VP, Horowitz MC, Locklin R, et al (2004) A gain-of-function mutation of Fgfr2c demonstrates the roles of this receptor variant in osteogenesis. Proc Natl Acad Sci U S A 101:12555–60. https://doi.org/10.1073/pnas.0405031101

Ferguson JW, Atit RP (2019) A tale of two cities: The genetic mechanisms governing calvarial bone development. Genesis 57:e23248. https://doi.org/10.1002/dvg.23248

Fernandes FA, Sousa RJA de (2015) Head injury predictors in sports trauma – A state-of-the-art review. Proc Inst Mech Eng H 229:592–608. https://doi.org/10.1177/0954411915592906

Festing MFW (2006) Design and statistical methods in studies using animal models of development. ILAR J 47:5–14. https://doi.org/10.1093/ilar.47.1.5

Flaherty K, Singh N, Richtsmeier JT (2016) Understanding craniosynostosis as a growth disorder. Wiley Interdiscip Rev Dev Biol 5:429–59. https://doi.org/10.1002/wdev.227

Galiay L, Cornette R, Lalième L, et al (2022) Intentional craniofacial remodelling in Europe in the XIXth century: Quantitative evidence of soft tissue modifications from Toulouse, France. J Stomatol Oral Maxillofac Surg 123:e342–e348. https://doi.org/10.1016/j.jormas.2022.05.002

Gefen A, Gefen N, Zhu Q, et al (2003) Age-dependent changes in material properties of the brain and braincase of the rat. J Neurotrauma 20:1163–1177. https://doi.org/10.1089/089771503770802853

Gefen A, van Nierop B, Bader DL, Oomens CW (2008) Strain-time cell-death threshold for skeletal muscle in a tissue-engineered model system for deep tissue injury. J Biomech 41:2003–2012. https://doi.org/10.1016/j.jbiomech.2008.03.039

Gillard F, Boardman R, Mavrogordato M, et al (2014) The application of digital volume correlation (DVC) to study the microstructural behaviour of trabecular bone during compression. J Mech Behav Biomed Mater 29:480–499. https://doi.org/10.1016/j.jmbbm.2013.09.014

Godinho RM, Toro-Ibacache V, Fitton LC, O'Higgins P (2017) Finite element analysis of the cranium: Validity, sensitivity and future directions. C R Palevol 16:600–612. https://doi.org/10.1016/j.crpv.2016.11.002

Grau N, Daw JL, Patel R, et al (2006) Nanostructural and nanomechanical properties of synostosed postnatal human cranial sutures. J Craniofac Surg 17:91–8; discussion 98-9. https://doi.org/10.1097/01.scs.0000179754.52154.42

Grova M, Lo DD, Montoro D, et al (2012) Models of cranial suture biology. Journal of Craniofacial Surgery 23:S12–S16. https://doi.org/10.1097/SCS.0b013e318258ba53

Harada M, Murakami H, Okawa A, et al (2009) FGF9 monomer–dimer equilibrium regulates extracellular matrix affinity and tissue diffusion. Nat Genet 41:289–298. https://doi.org/10.1038/ng.316

He Y, Camaiti M, Roberts LE, et al (2024) Introducing SPROUT (Semi-automated Parcellation of Region Outputs Using Thresholding): An adaptable computer vision tool to generate 3D segmentations. Biorxiv preprint. https://doi.org/10.1101/2024.11.22.624847

Henderson JH, Chang LY, Song HM, et al (2005) Age-dependent properties and quasi-static strain in the rat sagittal suture. J Biomech 38:2294–301. https://doi.org/10.1016/j.jbiomech.2004.07.037

Herring SW (2008) Mechanical influences on suture development and patency. Front Oral Biol 12:41–56. https://doi.org/10.1159/0000115031

Herring SW, Rafferty KL, Shin DU, et al (2024) Cyclic loading failed to promote growth in a pig model of midfacial hypoplasia. J Anat. https://doi.org/10.1111/joa.14043

Holmes G (2012) The role of vertebrate models in understanding craniosynostosis. Child's Nervous System 28:1471–1481. https://doi.org/10.1007/s00381-012-1844-3

Hoshino Y, Takechi M, Moazen M, et al (2023) Synchondrosis fusion contributes to the progression of postnatal craniofacial dysmorphology in syndromic craniosynostosis. J Anat 242:387–401. https://doi.org/10.1111/joa.13790

Hosseini-Farid M, Amiri-Tehrani-Zadeh M, Ramzanpour M, et al (2020) The strain rates in the brain, brainstem, dura, and skull under dynamic loadings. Mathematical and Computational Applications 25:21. https://doi.org/10.3390/mca25020021

Hua Y, Lin S, Gu L (2015) Relevance of blood vessel networks in blast-induced traumatic brain injury. Comput Math Methods Med 2015:1–8. https://doi.org/10.1155/2015/928236

Huang J, Birdal T, Gojcic Z, et al (2023) Multiway non-rigid point cloud registration via learned functional map synchronization. IEEE Trans Pattern Anal Mach Intell 45:2038–2053. https://doi.org/10.1109/TPAMI.2022.3164653

Hui C, Joyner AL (1993) A mouse model of Greig cephalo–polysyndactyly syndrome: the extra–toesJ mutation contains an intragenic deletion of the Gli3 gene. Nat Genet 3:241–246. https://doi.org/10.1038/ng0393-241

Ishii M, Sun J, Ting M-C, Maxson RE (2015) The development of the calvarial bones and sutures and the pathophysiology of craniosynostosis. Curr Top Dev Biol 115:131–56. https://doi.org/10.1016/bs.ctdb.2015.07.004

Istaphanous GK, Ward CG, Nan X, et al (2013) Characterization and quantification of isoflurane-induced developmental apoptotic cell death in mouse cerebral cortex. Anesth Analg 116:845–854. https://doi.org/10.1213/ANE.0b013e318281e988

Iyer RR, Ye X, Jin Q, et al (2018) Optimal duration of postoperative helmet therapy following endoscopic strip craniectomy for sagittal craniosynostosis. J Neurosurg Pediatr 22:610–615. https://doi.org/10.3171/2018.5.PEDS184

Jackson GW, Kokich VG, Shapiro PA (1979) Experimental and postexperimental response to anteriorly directed extraoral force in young Macaca nemestrina. Am J Orthod 75:318–333. https://doi.org/10.1016/0002-9416(79)90278-1

Jasinoski SC, Reddy BD (2012) Mechanics of cranial sutures during simulated cyclic loading. J Biomech 45:2050–2054. https://doi.org/10.1016/j.jbiomech.2012.05.007

Jaslow CR (1990) Mechanical properties of cranial sutures. J Biomech 23:313–321. https://doi.org/10.1016/0021-9290(90)90059-C

Joffre T, Isaksson P, Procter P, Persson C (2017) Trabecular deformations during screw pull-out: a micro-CT study of lapine bone. Biomech Model Mechanobiol 16:1349–1359. https://doi.org/10.1007/s10237-017-0891-9

Johnson D, Wilkie AOM (2011) Craniosynostosis. European Journal of Human Genetics 19:369–376. https://doi.org/10.1038/ejhg.2010.235

Kaster T, Sack I, Samani A (2011) Measurement of the hyperelastic properties of ex vivo brain tissue slices. J Biomech 44:1158–1163. https://doi.org/10.1016/j.jbiomech.2011.01.019

Katouni K, Nikolaou A, Mariolis T, et al (2023) Syndromic craniosynostosis: A comprehensive review. Cureus 15:e50448. https://doi.org/10.7759/cureus.50448

Katsianou MA, Adamopoulos C, Vastardis H, Basdra EK (2016) Signaling mechanisms implicated in cranial sutures pathophysiology: Craniosynostosis. BBA Clin 6:165–176. https://doi.org/10.1016/j.bbacli.2016.04.006

Katz DC, Aponte JD, Liu W, et al (2020) Facial shape and allometry quantitative trait locus intervals in the Diversity Outbred mouse are enriched for known skeletal and facial development genes. PLoS One 15:e0233377. https://doi.org/10.1371/journal.pone.0233377

Khudaverdyan A (2011) Trepanation and artificial cranial deformations in ancient Armenia. Anthropological Review 74:39–55. https://doi.org/10.2478/v10044-010-0004-1

Kim H, Diaz MB, Kim JY, et al (2020) Stress estimation through deep rock core diametrical deformation and joint roughness assessment using X-ray CT imaging. Sensors 20:6802. https://doi.org/10.3390/s20236802

Kiriyama Y, Sato Y, Muramatsu Y, et al (2022) Analysis of relationship between loading condition and cranial cracking pattern using a three-dimensional finite element model. BMC Musculoskelet Disord 23:310. https://doi.org/10.1186/s12891-022-05215-x

Kleiven S, Hardy WN (2002) Correlation of an FE model of the human head with local brain motion-consequences for injury prediction. 2002 46:123-44. https://doi.org/10.4271/2002-22-0007

Ko JM (2016) Genetic syndromes associated with craniosynostosis. J Korean Neurosurg Soc 59:187. https://doi.org/10.3340/jkns.2016.59.3.187

Koser DE, Moeendarbary E, Hanne J, et al (2015) CNS cell distribution and axon orientation determine local spinal cord mechanical properties. Biophys J 108:2137–2147. https://doi.org/10.1016/j.bpj.2015.03.039

Koser DE, Moeendarbary E, Kuerten S, Franze K (2018) Predicting local tissue mechanics using immunohistochemistry

Le Cann S, Tudisco E, Tägil M, et al (2020) Bone damage evolution around integrated metal screws using X-ray tomography — in situ pullout and digital volume correlation. Front Bioeng Biotechnol 8:. https://doi.org/10.3389/fbioe.2020.00934

Lee KKL, Stanier P, Pauws E (2019) Mouse models of syndromic craniosynostosis. Mol Syndromol 10:58–73. https://doi.org/10.1159/000491004

Li X, Sandler H, Kleiven S (2019a) Infant skull fractures: Accident or abuse? Forensic Sci Int 294:173–182. https://doi.org/10.1016/j.forsciint.2018.11.008

Li Y, Harada T (2022) Non-rigid point cloud registration with neural deformation pyramid.

Li Z, Hu J, Reed MP, et al (2011) Development, validation, and application of a parametric pediatric head finite element model for impact simulations. Ann Biomed Eng 39:2984–2997. https://doi.org/10.1007/s10439-011-0409-z

Li Z, Wang G, Ji C, et al (2019b) Characterization of the mechanical properties for cranial bones of 8-week-old piglets: the effect of strain rate and region. Biomech Model Mechanobiol 18:1697–1707. https://doi.org/10.1007/s10237-019-01169-7

Liang C, Marghoub A, Profico A, et al (2024) A physico-mechanical model of postnatal craniofacial growth in human. iScience 27:110617. https://doi.org/10.1016/j.isci.2024.110617

Liang C, Profico A, Buzi C, et al (2023) Normal human craniofacial growth and development from 0 to 4 years. Sci Rep 13:9641. https://doi.org/10.1038/s41598-023-36646-8

Liu J, Nam HK, Wang E, Hatch NE (2013) Further analysis of the Crouzon mouse: Effects of the FGFR2(C342Y) mutation are cranial bone-dependent. Calcif Tissue Int 92:451–66. https://doi.org/10.1007/s00223-013-9701-2

Liu J, Zhao Y, Yang J, et al (2017) Neonatal Repeated Exposure to Isoflurane not Sevoflurane in Mice Reversibly Impaired Spatial Cognition at Juvenile-Age. Neurochem Res 42:595–605. https://doi.org/10.1007/s11064-016-2114-7

Liu YH, Kundu R, Wu L, et al (1995) Premature suture closure and ectopic cranial bone in mice expressing Msx2 transgenes in the developing skull. Proceedings of the National Academy of Sciences 92:6137–6141. https://doi.org/10.1073/pnas.92.13.6137

Losken HW, Mooney MP, Zoldos J, et al (1999) Coronal suture response to distraction osteogenesis in rabbits with delayed-onset craniosynostosis. J Craniofac Surg 10:27–37. https://doi.org/10.1097/00001665-199901000-00007

Lyu D, Zhou R, Lin C, et al (2022) Development and validation of a new anisotropic visco-hyperelastic human head finite element model capable of predicting multiple brain injuries. Front Bioeng Biotechnol 10:. https://doi.org/10.3389/fbioe.2022.831595

MacManus DB, Pierrat B, Murphy JG, Gilchrist MD (2016) Mechanical characterization of the P56 mouse brain under large-deformation dynamic indentation. Sci Rep 6:21569. https://doi.org/10.1038/srep21569

Madden JC, Enoch SJ, Paini A, Cronin MTD (2020) A review of in silico tools as alternatives to animal testing: Principles, resources and applications. ATLA Alternatives to Laboratory Animals 48:146–172

Maga AM (2016) Postnatal development of the craniofacial skeleton in male C57BL/6J Mice. J Am Assoc Lab Anim Sci 55:131–6

Maloul A, Fialkov J, Whyne CM (2013) Characterization of the bending strength of craniofacial sutures. J Biomech 46:912–917. https://doi.org/10.1016/j.jbiomech.2012.12.016

Managuli V, Bothra YS, S SK, et al (2023) Overview of mechanical characterization of bone using nanoindentation technique and its applications. Engineered Science. https://doi.org/10.30919/es8d820

Mao JJ (2003) Strain induced osteogenesis of the craniofacial suture upon controlled delivery of low-frequency cyclic forces. Frontiers in Bioscience 8:917. https://doi.org/10.2741/917

Marghoub A, Libby J, Babbs C, et al (2019a) Characterizing and modeling bone formation during mouse calvarial development. Phys Rev Lett 122:048103. https://doi.org/10.1103/PhysRevLett.122.048103

Margulies SS, Thibault KL (2000) Infant skull and suture properties: measurements and implications for mechanisms of pediatric brain injury. J Biomech Eng 122:364–71. https://doi.org/10.1115/1.1287160

Martínez-Abadías N, Motch SM, Pankratz TL, et al (2013) Tissue-specific responses to aberrant FGF signaling in complex head phenotypes. Dev Dyn 242:80–94. https://doi.org/10.1002/dvdy.23903

Martínez-Abadías N, Percival C, Aldridge K, et al (2010) Beyond the closed suture in apert syndrome mouse models: evidence of primary effects of FGFR2 signaling on facial shape at birth. Dev Dyn 239:3058–71. https://doi.org/10.1002/dvdy.22414

Marupudi NI, Sood S, Rozzelle A, Ham SD (2016) Effect of molding helmets on intracranial pressure and head shape in nonsurgically treated sagittal craniosynostosis patients. J Neurosurg Pediatr 18:207–212. https://doi.org/10.3171/2016.1.PEDS15569

Mathijssen IMJ (2015) Guideline for care of patients with the diagnoses of craniosynostosis. Journal of Craniofacial Surgery 26:1735–1807. https://doi.org/10.1097/SCS.0000000000002016

McElhaney JH, Fogle JL, Melvin JW, et al (1970) Mechanical properties of cranial bone. J Biomech 3:495–511. https://doi.org/10.1016/0021-9290(70)90059-X

McLaughlin E, Zhang Y, Pashley D, et al (2000) The load-displacement characteristics of neonatal rat cranial sutures. Cleft Palate Craniofac J 37:590–5. https://doi.org/10.1597/1545-1569_2000_037_0590_tldcon_2.0.co_2

Meikle MC, Reynolds JJ, Sellers A, Dingle JT (1979) Rabbit cranial sutures in vitro: A new experimental model for studying the response of fibrous joints to mechanical stress. Calcif Tissue Int 28:137–144. https://doi.org/10.1007/BF02441232

Meiklejohn C, Agelarakis A, Akkermans PA, et al (1992) Artificial cranial deformation in the Proto-neolithic and Neolithic Near East and its possible origin : Evidence from four sites. Paléorient 18:83–97. https://doi.org/10.3406/paleo.1992.4574

Menon S, Salhotra A, Shailendra S, et al (2021) Skeletal stem and progenitor cells maintain cranial suture patency and prevent craniosynostosis. Nat Commun 12:4640. https://doi.org/10.1038/s41467-021-24801-6

Merkuri F, Fish JL (2019) Developmental processes regulate craniofacial variation in disease and evolution. Genesis 57:e23249. https://doi.org/10.1002/dvg.23249

Mihai LA, Chin L, Janmey PA, Goriely A (2015) A comparison of hyperelastic constitutive models applicable to brain and fat tissues. J R Soc Interface 12:20150486. https://doi.org/10.1098/rsif.2015.0486

Miller K, Chinzei K (2002) Mechanical properties of brain tissue in tension. J Biomech 35:483–90. https://doi.org/10.1016/s0021-9290(01)00234-2

Miller K, Chinzei K, Orssengo G, Bednarz P (2000) Mechanical properties of brain tissue in-vivo: experiment and computer simulation. J Biomech 33:1369–1376. https://doi.org/10.1016/S0021-9290(00)00120-2

Ming Tse K, Lee H, Piang Lim S, et al (2014) A review of head injury and finite element head models. American Journal of Engineering 1:28–52

Moazen M, Hejazi M, Savery D, et al (2022a) Mechanical loading of cranial joints minimizes the craniofacial phenotype in Crouzon syndrome. Sci Rep 12:9693. https://doi.org/10.1038/s41598-022-13807-9

Moazen M, Peskett E, Babbs C, et al (2015a) Mechanical properties of calvarial bones in a mouse model for craniosynostosis. PLoS One 10:e0125757. https://doi.org/10.1371/journal.pone.0125757

Monaco G, van Dam S, Casal Novo Ribeiro JL, et al (2015) A comparison of human and mouse gene co-expression networks reveals conservation and divergence at the tissue, pathway and disease levels. BMC Evol Biol 15:259. https://doi.org/10.1186/s12862-015-0534-7

Moran CJ, Ramesh A, Brama PAJ, et al (2016) The benefits and limitations of animal models for translational research in cartilage repair. J Exp Orthop 3:1. https://doi.org/10.1186/s40634-015-0037-x

Motch Perrine SM, Cole TM, Martínez-Abadías N, et al (2014) Craniofacial divergence by distinct prenatal growth patterns in Fgfr2 mutant mice. BMC Dev Biol 14:8. https://doi.org/10.1186/1471-213X-14-8

Motch Perrine SM, Pitirri MK, Durham EL, et al (2022) A dysmorphic mouse model reveals developmental interactions of chondrocranium and dermatocranium. Elife 11:. https://doi.org/10.7554/eLife.76653

Motherway JA, Verschueren P, Van der Perre G, et al (2009) The mechanical properties of cranial bone: the effect of loading rate and cranial sampling position. J Biomech 42:2129–35. https://doi.org/10.1016/j.jbiomech.2009.05.030

Myronenko A, Xubo Song (2010) Point set registration: Coherent point drift. IEEE Trans Pattern Anal Mach Intell 32:2262–2275. https://doi.org/10.1109/TPAMI.2010.46

Nogatz T, Redenbach C, Schladitz K (2022) 3D optical flow for large CT data of materials microstructures. Strain 58:. https://doi.org/10.1111/str.12412

Nuri T, Ota M, Ueda K, Iseki S (2022) Quantitative morphologic analysis of cranial vault in Twist1 +/− mice: Implications in craniosynostosis. Plast Reconstr Surg 149:28e–37e. https://doi.org/10.1097/PRS.0000000000008665

Oefner C, Herrmann S, Kebbach M, et al (2021) Reporting checklist for verification and validation of finite element analysis in orthopedic and trauma biomechanics. Med Eng Phys 92:25–32. https://doi.org/10.1016/j.medengphy.2021.03.011

Olson E, Graham D (2014) Animal models in pharmacogenomics. Handbook of Pharmacogenomics and Stratified Medicine. Elsevier, pp 73–87

Olufsen SN, Tekseth KR, Breiby DW, et al (2020) A technique for in situ X-ray computed tomography of deformation-induced cavitation in thermoplastics. Polym Test 91:106834. https://doi.org/10.1016/j.polymertesting.2020.106834

Oppenheimer AJ, Rhee ST, Goldstein SA, Buchman SR (2012) Force-induced craniosynostosis via paracrine signaling in the murine sagittal suture. J Craniofac Surg 23:573–7. https://doi.org/10.1097/SCS.0b013e318241db3e

Opperman LA (2000) Cranial sutures as intramembranous bone growth sites. Dev Dyn 219:472–85. https://doi.org/10.1002/1097-0177

Palomo JM, Inomata T, Triadan D (2017) Mortuary rituals and cranial modifications at ceibal: From the early middle preclassic to the terminal classic period. Ancient Mesoamerica 28:305–327. https://doi.org/10.1017/S0956536117000062

Pan B, Wang B (2020) Some recent advances in digital volume correlation. Opt Lasers Eng 135:106189. https://doi.org/10.1016/j.optlaseng.2020.106189

Parsons TE, Weinberg SM, Khaksarfard K, et al (2014) Craniofacial shape variation in Twist1+/- mutant mice. Anat Rec (Hoboken) 297:826–33. https://doi.org/10.1002/ar.22899

Peña Fernández M, Barber AH, Blunn GW, Tozzi G (2018) Optimization of digital volume correlation computation in SR-microCT images of trabecular bone and bone-biomaterial systems. J Microsc 272:213–228. https://doi.org/10.1111/jmi.12745

Peptan AI, Lopez A, Kopher RA, Mao JJ (2008) Responses of intramembranous bone and sutures upon in vivo cyclic tensile and compressive loading. Bone 42:432–8. https://doi.org/10.1016/j.bone.2007.05.014

Percival CJ, Huang Y, Jabs EW, et al (2014) Embryonic craniofacial bone volume and bone mineral density in Fgfr2(+/P253R) and nonmutant mice. Dev Dyn 243:541–51. https://doi.org/10.1002/dvdy.24095

Percival CJ, Liberton DK, Pardo-Manuel de Villena F, et al (2016) Genetics of murine craniofacial morphology: diallel analysis of the eight founders of the Collaborative Cross. J Anat 228:96–112. https://doi.org/10.1111/joa.12382

Percival CJ, Marangoni P, Tapaltsyan V, et al (2017) The interaction of genetic background and mutational effects in regulation of mouse craniofacial shape. G3 Genes|Genomes|Genetics 7:1439–1450. https://doi.org/10.1534/g3.117.040659

Perlyn CA, DeLeon VB, Babbs C, et al (2006) The craniofacial phenotype of the crouzon mouse: Analysis of a model for syndromic craniosynostosis using three-dimensional MicroCT. The Cleft Palate Craniofacial Journal 43:740–747. https://doi.org/10.1597/05-212

Peskett E, Kumar S, Baird W, et al (2017) Analysis of the Fgfr2C342Y mouse model shows condensation defects due to misregulation of Sox9 expression in prechondrocytic mesenchyme. Biol Open 6:223–231. https://doi.org/10.1242/bio.022178

Pomerleau F, Colas F, Siegwart R (2015) A review of point cloud registration algorithms for mobile robotics. Foundations and Trends in Robotics 4:1–104. https://doi.org/10.1561/2300000035

Popowics TE, Herring SW (2007) Load transmission in the nasofrontal suture of the pig, Sus scrofa. J Biomech 40:837–844. https://doi.org/10.1016/j.jbiomech.2006.03.011

Powierza B, Gollwitzer C, Wolgast D, et al (2019) Fully experiment-based evaluation of few digital volume correlation techniques. Review of Scientific Instruments 90:. https://doi.org/10.1063/1.5099572

Rafferty KL, Herring SW (1999) Craniofacial sutures: morphology, growth, and in vivo masticatory strains. J Morphol 242:167–79. https://doi.org/10.1002/(SICI)1097-4687

Rahimov C, Asadov R, Hajiyeva G, et al (2016) Crouzon syndrome: Virtual planning of surgical treatment by application of internal distractors. Ann Maxillofac Surg 6:135–40. https://doi.org/10.4103/2231-0746.186144

Rahmoun J, Auperrin A, Delille R, et al (2014) Characterization and micromechanical modeling of the human cranial bone elastic properties. Mech Res Commun 60:7–14. https://doi.org/10.1016/j.mechrescom.2014.04.001

Rayfield EJ (2007) Finite element analysis and understanding the biomechanics and evolution of living and fossil organisms. Annu Rev Earth Planet Sci 35:541–576. https://doi.org/10.1146/annurev.earth.35.031306.140104

Ribitsch I, Baptista PM, Lange-Consiglio A, et al (2020) Large animal models in regenerative medicine and tissue engineering: To do or not to do. Front Bioeng Biotechnol 8:. https://doi.org/10.3389/fbioe.2020.00972

Rice DPC (2003) Molecular mechanisms in calvarial bone and suture development, and their relation to craniosynostosis. The European Journal of Orthodontics 25:139–148. https://doi.org/10.1093/ejo/25.2.139

Rice DPC, Connor EC, Veltmaat JM, et al (2010) Gli3Xt-J/Xt-J mice exhibit lambdoid suture craniosynostosis which results from altered osteoprogenitor proliferation and differentiation. Hum Mol Genet 19:3457–3467. https://doi.org/10.1093/hmg/ddq258

Richtsmeier JT, Baxter LL, Reeves RH (2000) Parallels of craniofacial maldevelopment in down syndrome and Ts65Dn mice. Developmental Dynamics 217:137–145. https://doi.org/10.1002/(SICI)1097-0177

Roberts BC, Perilli E, Reynolds KJ (2014) Application of the digital volume correlation technique for the measurement of displacement and strain fields in bone: A literature review. J Biomech 47:923–934. https://doi.org/10.1016/j.jbiomech.2014.01.001

Rodriguez-Florez N, Oyen ML, Shefelbine SJ (2013) Insight into differences in nanoindentation properties of bone. J Mech Behav Biomed Mater 18:90–99. https://doi.org/10.1016/j.jmbbm.2012.11.005

Schijman E (2005) Artificial cranial deformation in the Pre-Columbian Andes. Child's Nervous System 21:939–939. https://doi.org/10.1007/s00381-005-1264-8

Seymour-Dempsey K, Baumgartner JE, Teichgraeber JF, et al (2002) Molding helmet therapy in the management of sagittal synostosis. Journal of Craniofacial Surgery 13:631–635. https://doi.org/10.1097/00001665-200209000-00007

Sharir A, Barak MM, Shahar R (2008) Whole bone mechanics and mechanical testing. The Veterinary Journal 177:8–17. https://doi.org/10.1016/j.tvjl.2007.09.012

Sharma VP, Fenwick AL, Brockop MS, et al (2013) Mutations in TCF12, encoding a basic helix-loop-helix partner of TWIST1, are a frequent cause of coronal craniosynostosis. Nat Genet 45:304–307. https://doi.org/10.1038/ng.2531

Shen W, Cui J, Chen J, et al (2015) Correction of craniosynostosis using modified spring-assisted surgery. J Craniofac Surg 26:522–5. https://doi.org/10.1097/SCS.0000000000001547

Shim VB, Handsfield GG, Fernandez JW, et al (2018) Combining in silico and in vitro experiments to characterize the role of fascicle twist in the Achilles tendon. Sci Rep 8:13856. https://doi.org/10.1038/s41598-018-31587-z

Skolnick GB, Yu JL, Patel KB, et al (2021) Comparison of 2 sagittal craniosynostosis repair techniques: spring-assisted surgery versus endoscope-assisted craniectomy with helmet molding therapy. Cleft Palate-Craniofacial Journal 58:678–686. https://doi.org/10.1177/1055665620966521

Soh SH, Rafferty K, Herring S (2018) Cyclic loading effects on craniofacial strain and sutural growth in pigs. American Journal of Orthodontics and Dentofacial Orthopedics 154:270–282. https://doi.org/10.1016/j.ajodo.2017.11.036

Sood S, Rozzelle A, Shaqiri B, et al (2011) Effect of molding helmet on head shape in nonsurgically treated sagittal craniosynostosis. J Neurosurg Pediatr 7:627–32. https://doi.org/10.3171/2011.4.PEDS116

Southard KA, Forbes DP (1988) The effects of force magnitude on a sutural model: A quantitative approach. American Journal of Orthodontics and Dentofacial Orthopedics 93:460–466. https://doi.org/10.1016/0889-5406(88)90074-1

Spencer KA, Mulholland M, Snell J, et al (2023) Volatile anaesthetic toxicity in the genetic mitochondrial disease Leigh syndrome. Br J Anaesth 131:832–846. https://doi.org/10.1016/j.bja.2023.08.009

Takeshita N, Hasegawa M, Sasaki K, et al (2017) In vivo expression and regulation of genes associated with vascularization during early response of sutures to tensile force. J Bone Miner Metab 35:40–51. https://doi.org/10.1007/s00774-016-0737-z

Tanaka E, Miyawaki Y, del Pozo R, Tanne K (2000) Changes in the biomechanical properties of the rat interparietal suture incident to continuous tensile force application. Arch Oral Biol 45:1059–64. https://doi.org/10.1016/s0003-9969(00)00082-0

Ten Cate AR, Freeman E, Dickinson JB (1977) Sutural development: Structure and its response to rapid expansion. Am J Orthod 71:622–636. https://doi.org/10.1016/0002-9416(77)90279-2

Teng CS, Cavin L, Maxson RE, et al (2019) Resolving homology in the face of shifting germ layer origins: Lessons from a major skull vault boundary. Elife 8:. https://doi.org/10.7554/eLife.52814

Tholpady SS, Freyman TF, Chachra D, Ogle RC (2007) Tensional forces influence gene expression and sutural state of rat calvariae in vitro. Plast Reconstr Surg 120:601–611. https://doi.org/10.1097/01.prs.0000270284.69632.6b

Tuenge RH, Elder JR (1974) Posttreatment changes following extraoral high-pull traction to the maxilla of Macaca mulatta. Am J Orthod 66:618–644. https://doi.org/10.1016/S0002-9416(74)90307-8

Turunen MJ, Le Cann S, Tudisco E, et al (2020) Sub-trabecular strain evolution in human trabecular bone. Sci Rep 10:13788. https://doi.org/10.1038/s41598-020-69850-x

Tuttle AH, Philip VM, Chesler EJ, Mogil JS (2018) Comparing phenotypic variation between inbred and outbred mice. Nat Methods 15:994–996. https://doi.org/10.1038/s41592-018-0224-7

Twigg SRF, Healy C, Babbs C, et al (2009) Skeletal analysis of the *Fgfr3* ^{P244R} mouse, a genetic model for the Muenke craniosynostosis syndrome. Developmental Dynamics 238:331–342. https://doi.org/10.1002/dvdy.21790

Valiquette V, Guma E, Cupo L, et al (2023) Examining litter specific variability in mice and its impact on neurodevelopmental studies. Neuroimage 269:119888. https://doi.org/10.1016/j.neuroimage.2023.119888

Valverde-Franco G, Liu H, Davidson D, et al (2004) Defective bone mineralization and osteopenia in young adult FGFR3-/- mice. Hum Mol Genet 13:271–84. https://doi.org/10.1093/hmg/ddh034

van der Meulen J, van der Hulst R, van Adrichem L, et al (2009) The increase of metopic synostosis: a pan-European observation. J Craniofac Surg 20:283–6. https://doi.org/10.1097/scs.0b013e31818436be

Vega RB, Matsuda K, Oh J, et al (2004) Histone deacetylase 4 controls chondrocyte hypertrophy during skeletogenesis. Cell 119:555–566. https://doi.org/10.1016/j.cell.2004.10.024

Vij K, Mao JJ (2006) Geometry and cell density of rat craniofacial sutures during early postnatal development and upon in vivo cyclic loading. Bone 38:722–30. https://doi.org/10.1016/j.bone.2005.10.028

Vora SR, Camci ED, Cox TC (2016) Postnatal ontogeny of the cranial base and craniofacial skeleton in male C57BL/6J mice: A reference standard for quantitative analysis. Front Physiol 6:. https://doi.org/10.3389/fphys.2015.00417

Voyiadjis GZ, Samadi-Dooki A (2018) Hyperelastic modeling of the human brain tissue: Effects of no-slip boundary condition and compressibility on the uniaxial deformation. J Mech Behav Biomed Mater 83:63–78. https://doi.org/10.1016/j.jmbbm.2018.04.011

Wang J, Zou D, Li Z, et al (2014) Mechanical properties of cranial bones and sutures in 1-2-year-old infants. Med Sci Monit 20:1808–13. https://doi.org/10.12659/MSM.892278

Wang Y, Hou ZQ, Hu YZ (2019) In situ X-ray computed tomography experiment on mesodamage evolution of subgrade bimsoil during cycle loading. Journal of Materials in Civil Engineering 31:. https://doi.org/10.1061/(ASCE)MT.1943-5533.0002796

Wang Y, Xiao R, Yang F, et al (2005) Abnormalities in cartilage and bone development in the Apert syndrome FGFR2+/S252W mouse. Development 132:3537–3548. https://doi.org/10.1242/dev.01914

Wang Y, Zhou X, Oberoi K, et al (2012) p38 Inhibition ameliorates skin and skull abnormalities in Fgfr2 Beare-Stevenson mice. Journal of Clinical Investigation 122:2153–2164. https://doi.org/10.1172/JCI62644

Watson PJ, Sharp AC, Choudhary T, et al (2021) Computational biomechanical modelling of the rabbit cranium during mastication. Sci Rep 11:13196. https://doi.org/10.1038/s41598-021-92558-5

Wei X, Thomas N, Hatch NE, et al (2017) Postnatal Craniofacial Skeletal Development of Female C57BL/6NCrl Mice. Front Physiol 8:. https://doi.org/10.3389/fphys.2017.00697

Wilkinson CC, Stence N V., Serrano CA, et al (2020) Fusion patterns of major calvarial sutures on volume-rendered CT reconstructions. J Neurosurg Pediatr 25:519–528. https://doi.org/10.3171/2019.11.PEDS1953

Yamashita Y, Uematsu H, Tanoue S (2023) Calculation of strain energy density function using ogden model and mooney–rivlin model based on biaxial elongation experiments of silicone rubber. Polymers (Basel) 15:2266. https://doi.org/10.3390/polym15102266

Yan Y, Bacos JT, DiPatri AJ, Gosain AK (2020) Spring-assisted distraction osteogenesis for the treatment of shunt-induced craniosynostosis. Cleft Palate-Craniofacial Journal 57:1336–1339. https://doi.org/10.1177/1055665620947617

Yen H-Y, Ting M-C, Maxson RE (2010) Jagged1 functions downstream of Twist1 in the specification of the coronal suture and the formation of a boundary between osteogenic and non-osteogenic cells. Dev Biol 347:258–270. https://doi.org/10.1016/j.ydbio.2010.08.010

Yu JC, Lucas JH, Fryberg K, Borke JL (2001) Extrinsic tension results in fgf-2 release, membrane permeability change, and intracellular ca ++ increase in immature cranial sutures. Journal of Craniofacial Surgery 12:391–398. https://doi.org/10.1097/00001665-200107000-00018

Yuan Y, Ge Z, Lai B, et al (2023) Three dimensional deformation measurement method based on image guided point cloud registration. Opt Lasers Eng 161:107399. https://doi.org/10.1016/j.optlaseng.2022.107399

Yue YY, Lai C-Z, Guo X-S, et al (2024) New CRISPR/Cas9-based Fgfr2C361Y/+ mouse model of Crouzon syndrome exhibits skull and behavioral abnormalities. J Mol Med (Berl) 102:1255–1266. https://doi.org/10.1007/s00109-024-02476-y

Zampogiannis K, Fermuller C, Aloimonos Y (2021) Topology-aware non-rigid point cloud registration. IEEE Trans Pattern Anal Mach Intell 43:1056–1069. https://doi.org/10.1109/TPAMI.2019.2940655

Zhang ZQ, Yang JL (2015) Biomechanical dynamics of cranial sutures during simulated impulsive loading. Appl Bionics Biomech 2015:1–11. https://doi.org/10.1155/2015/596843

Zhao S, Fan Z, Hu J, et al (2020) The differential effects of isoflurane and sevoflurane on neonatal mice. Sci Rep 10:19345. https://doi.org/10.1038/s41598-020-76147-6

Zhou C, Khalil TB, King AI (1995) A new model comparing impact responses of the homogeneous and inhomogeneous human brain. Stapp Car Crash Conference Proceedings 299. https://doi.org/10.4271/952714

Zhou R, Li Y, Cavanaugh JM, Zhang L (2020) Investigate the variations of the head and brain response in a rodent head impact acceleration model by finite element modeling. Front Bioeng Biotechnol 8:. https://doi.org/10.3389/fbioe.2020.00172

Zhou Y-X (2000) A Pro250Arg substitution in mouse Fgfr1 causes increased expression of Cbfa1 and premature fusion of calvarial sutures. Hum Mol Genet 9:2001–2008. https://doi.org/10.1093/hmg/9.13.2001

Zwirner J, Scholze M, Waddell JN, et al (2019) mechanical properties of human dura mater in tension – An analysis at an age range of 2 to 94 years. Sci Rep 9:16655. https://doi.org/10.1038/s41598-019-52836-9

Appendix I

A1-1 Relaxation

During CT scanning, the specimen should move as little as possible. However, a constant static load applied to the skull led to significant soft tissue relaxation. Figure A1.1 shows the effect of soft tissue relaxation. Here, the loading tip displacement was quantified while applying a constant force of 0.1N to a P7 skull over 180min.

The P7 WT animals were found to show the highest soft tissue relaxation among the considered mice in this study. Hence, the scanning protocol for all specimens was based on these results. The movement can be seen to be mostly stabilised after 120min. Following these findings, all the animals were scanned after 120mins of the static loading.

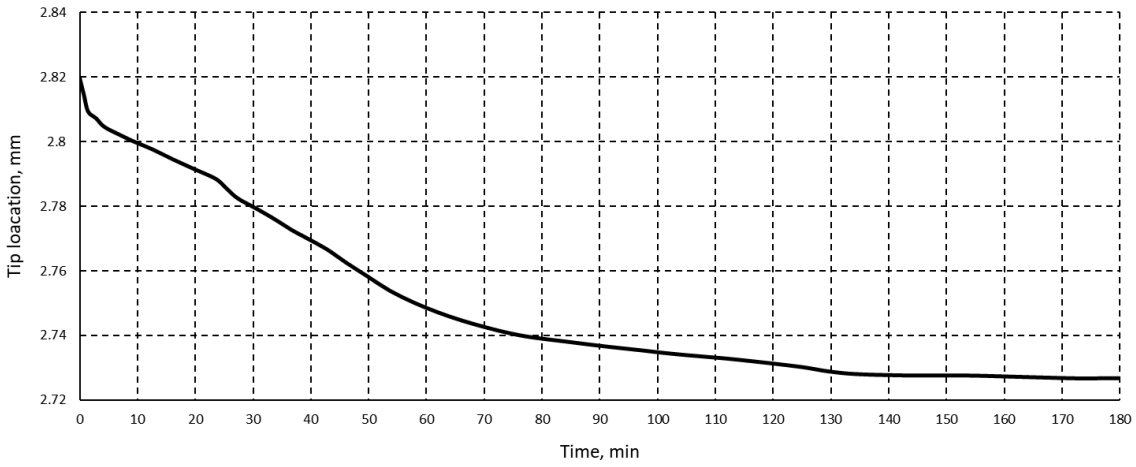

Figure A1.1. Relaxation as measured by the position of the loading tip for a P7 WT specimen during static loading.

A1-2 Validation

To build confidence in the strain estimation produced by the developed code, two simplified geometries shown in Figure A1.2a and b were modelled using commercial finite element software (ANSYS, Pennsylvania, USA) and the code developed here. Mesh independence was carried out on both models in both tools. In brief, mesh independence was examined for both geometries quantitatively and a qualitative analysis of the strain contours in the specimen-specific geometry was produced.

The material properties for the FE analysis were adjusted so the 0.1N load would produce an average von Mises strain of 1 in the suture. This was chosen to capture roughly the same level of displacement observed in the real system during static loading.

When comparing the mesh dependence in Figure A1.2c for the idealised geometry. It was clear that the FE results were affected by the number of elements in terms of the maximum von Mises strain; however, the difference between the estimated (DSC) and calculated values remained stable, indicating that this had little effect on the approaches ability to capture the deformation patterns.

A comparable pattern was observed in the specimen-specific geometry in Figure A1.2d. Additionally, it was noted that the average remained stable for both FE and DSC in the simplified geometry. In contrast, a slight decrease in average strain was observed for both FE and DSC results in the animal-specific geometry.

Figure A1.2d shows the approach's capabilities in capturing strain patterns in the calvarial sutures for the specimen-specific geometries. Namely, it can be seen that the two strain contours were extremely similar, with slight underestimation in the DSC results. The average von Mises strain across the coronal sutures was underestimated by 3.8% for the 72, 132 and 274 thousand element cases, with the underestimation decreasing to 1.8% for the 1729 thousand element case.

A case with no strain was considered. Here the undeformed surfaces were remeshed to obtain an imaginary "deformed" surface. This surface was compared to the original surface where in fact both surfaces were undeformed surfaces with different surface meshes. The code developed here estimated an average von Mises strain of 0.0117 (that should have been zero). Nonetheless, this represented 1-4% of the measured strains in the sutures of WT animals.

The bone strains, however could not be investigated with this approach as the relative displacement within the bone is small and the large elements used to align the undeformed surface to the deformed surface do not allow for the required level of accuracy. As the focus of this work was on the mechanical response of the sutures further refinement to the algorithm used was deemed unnecessary in light of the level of under/overestimation of strain results for the sutures presented in Figure A1.2d. The method used at best could only estimate the surface strains of the bones.

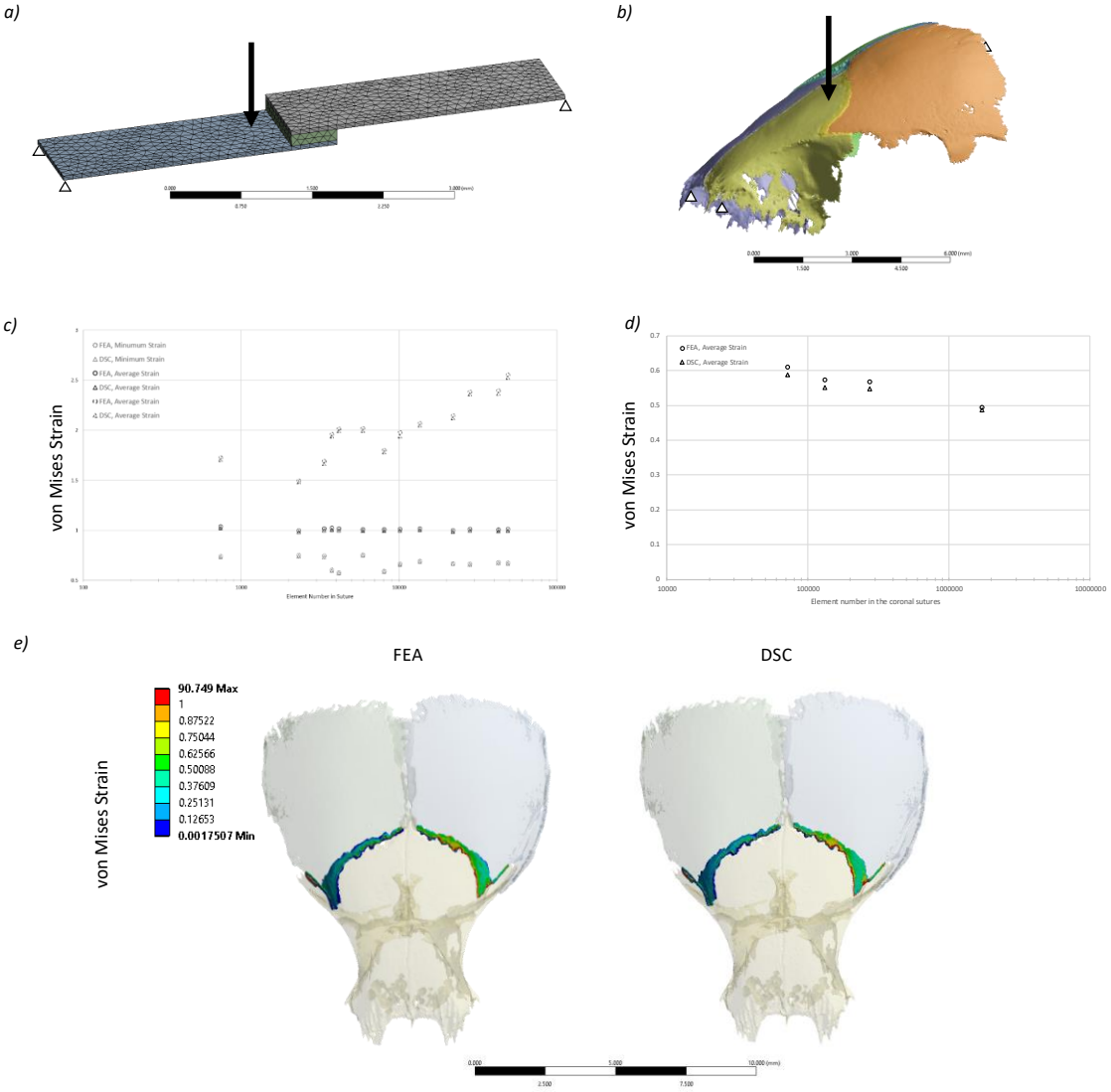

Figure A1.2. Strain estimation approach sensitivity summary. a) Idealised suture geometry, b) specimen-specific cranial geometry, c) mesh dependence results for the idealised geometry, d) mesh dependence results for the specimen-specific geometry, e)comparison of FEA and DSC strain contours for the coronal sutures.

A1-3 Loading tip displacement

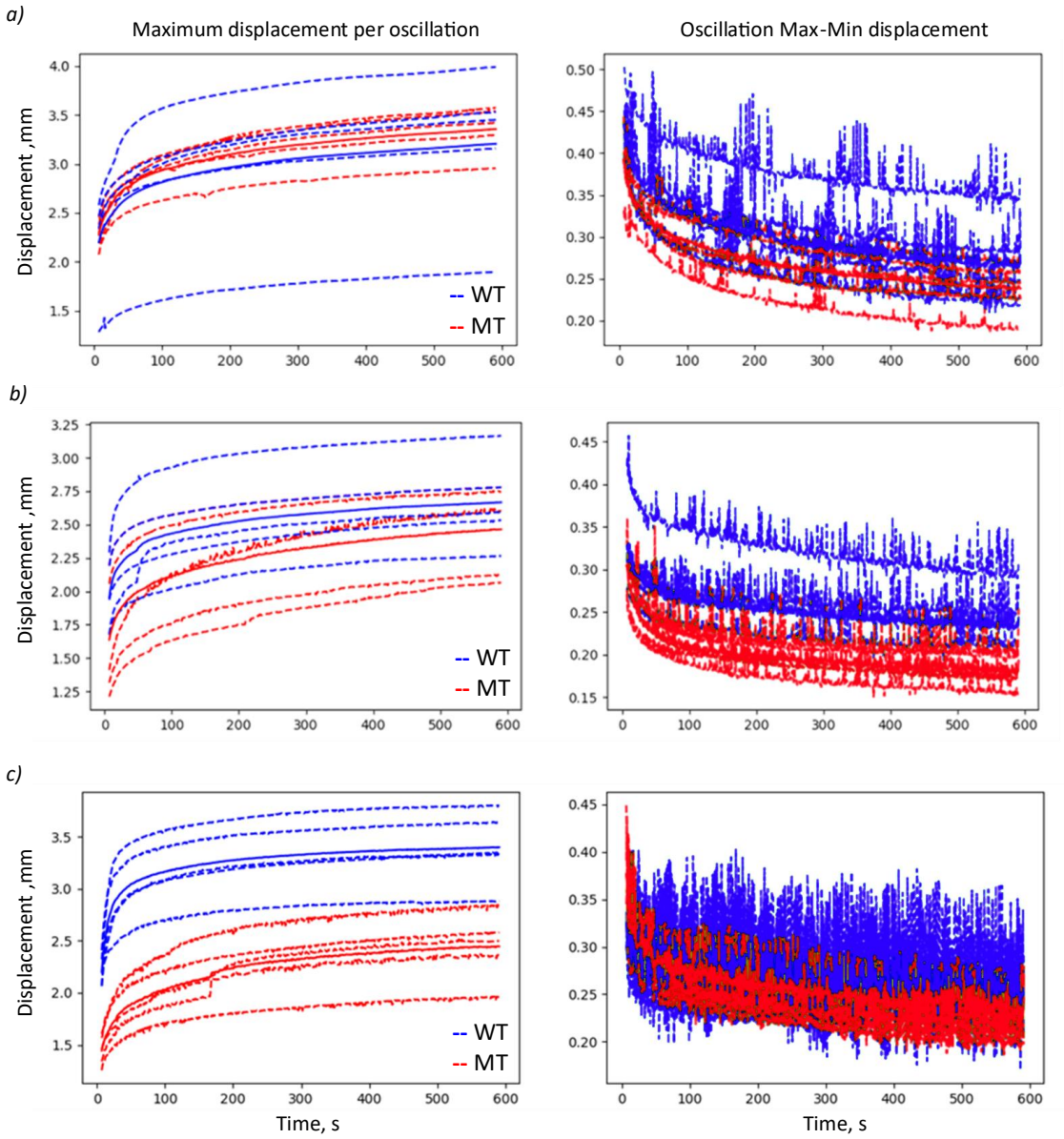

Figure A1.3. Maximum displacement per oscillation and oscillation Max-Min displacement throughout the 10 minutes of loading at 1Hz and 0.1N. The position was sampled every millisecond. a) P7, b) P14 and c) P21. Dashed lines indicate each specimen, while the solid line indicates the average.

A1-4 1st and 3rd principal strain value distribution

The strain results indicated a slightly higher absolute value of the first principle strain compared to the third principle strain on the left side coronal suture and the opposite on the pattern on the right side. This may suggest that the left coronal suture experiences more tension than compression, while the opposite is true for the right coronal suture.

To further investigate this, a deeper look into the first and third principal strains is presented in Figure A1.4 for the WT specimens. The higher third principal strain is evident in the P7 right-side results. While two specimens show this pattern, one shows the opposite pattern. Thus, making it hard to unravel the strain polarity patterns. Further investigation with a larger number of animals should be conducted to confirm the observations made here regarding whether the sutures are in tension or compression.

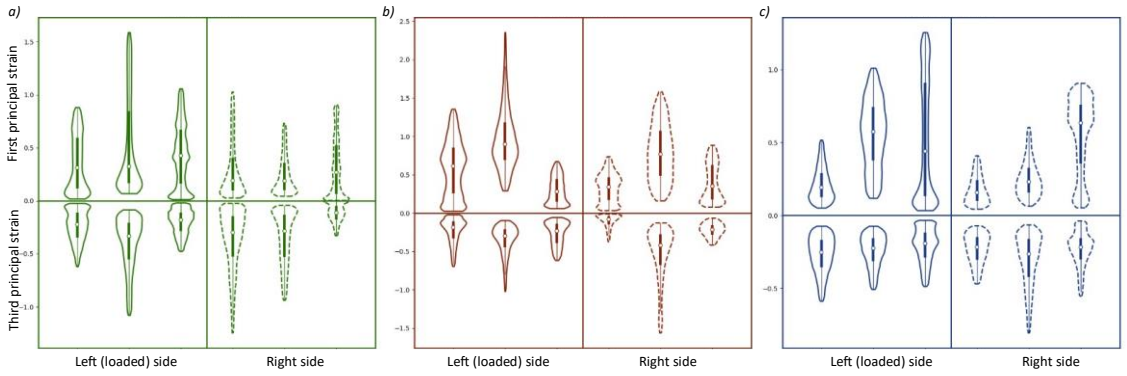

Figure A1.4. First and third principal strains across both coronal sutures for wild-type specimens at P7, P14, and P21 during ex vivo static loading. This plot presents the distribution of element strains in each specimen individually. A circle indicates the average, bar indicates the quartiles and a line indicates the distribution. A solid line is used for the left side (loaded), and a dashed line is used for the right side. a) P7, b) P14 and c) P21.

Appendix II BounTI (boundary-preserving threshold iteration): A user-friendly tool for automatic hard tissue segmentation

A2-1 Introduction

This Appendix focuses on the development and validation of BounTI a user-friendly tool for automatic segmentation of CT data. For this thesis, in particular, BounTI has enabled the increased scope of investigated sutures and rapid development of *in silico* models in

Chapter 4. Additionally, the tool has inspired the development of spinoff methodologies (He et al. 2024), and has been used both at UCL and across institutions globally to enhance research.

A2-2 Materials and methods

BounTI iterates through thresholds and slowly builds segments onto the seed generated from the initial threshold (Figure A2.1). It is specifically designed to be accessible to as wide an audience as possible and, thus is available as an add-on for the Avizo/Amira suite, a Python package and a stand-alone Windows application. The tool and full user guides, including tutorials and further segmentation examples and visualisations, are available in the online repository. All the visualisations in this work were produced through Avizo 2022.1 (Thermo Fisher Scientific, MA, USA). Neither the stand-alone executable nor the Python library contain built-in visualisation modules, thus, visualising the segmentation results and introducing further manual segmentation for non-Avizo/-Amira users will require third-party software.

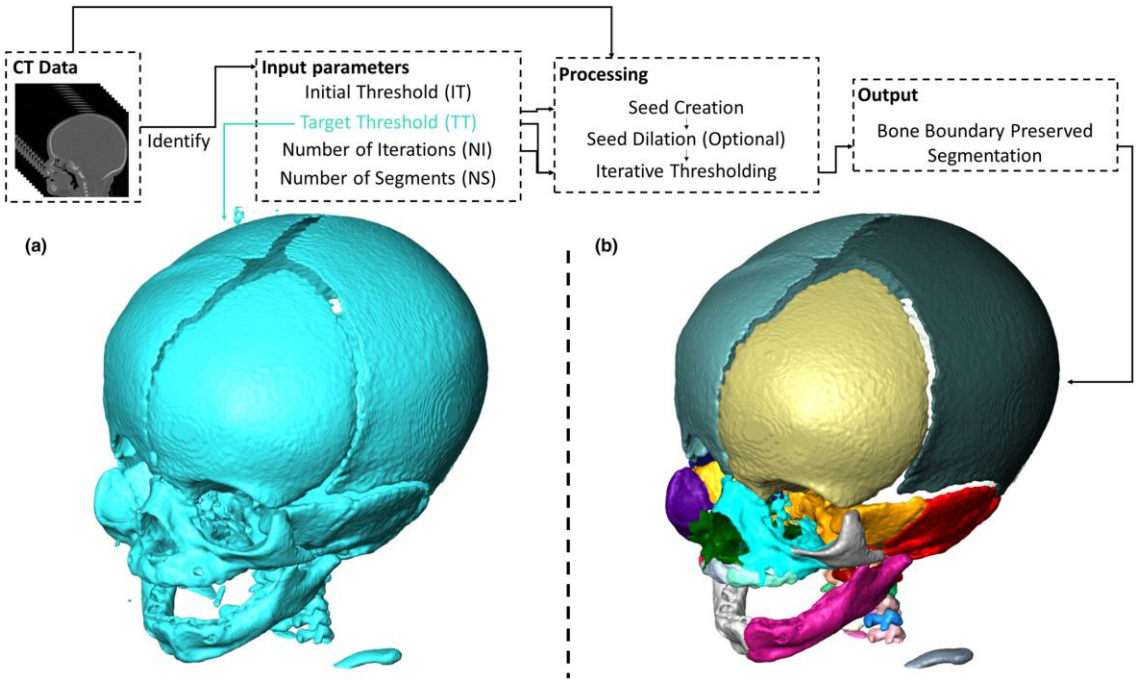

Figure A2.1 An overview of the technique developed, and threshold-based versus BounTI segmentation. (a) segmentation using the target threshold (27,000) and (b) segmentation using BounTI (IT – 35,000, TT – 27,000, NI – 150 and NS – 40).

A2-2-1 BounTI algorithm

A2-2-1-1 Input parameters

The algorithm takes volume data and four numerical variables defined by the operator as input. These include:

- The initial threshold (IT) – a high grey scale value above which the segmentation results in the desired separation of anatomical elements.
- The target threshold (TT) – a low grey scale value above which the segmentation results in the desired bone definition.
- The number of iterations (NI) – a number of threshold steps from the initial threshold to the target threshold.
- The number of segments (NS) – a number of largest separate segments that will be retained for processing from the initial threshold.

The two parameters that are the most challenging to select are the initial threshold and the number of iterations. Thus, several sensitivity tests were performed on the choice of these parameters on a sample dataset to investigate the effect of the aforementioned parameters.

A1-2-1-2 Processing

BounTI first creates the seed from the initial threshold. The seed here is a segmentation of fully disarticulated components obtained using the initial threshold where the largest separate segments are extracted. The number of these segments in the seed is equal to the number of segments parameter. Each segment in the seed can be optionally expanded by one voxel to include surrounding voxels (dilated), which can produce cleaner results. This option was not employed in these investigations because it can also lead to less predictable results. The threshold step (TS) is the amount by which the threshold will be changed between iterations and is obtained using the following Equation A2.1.

$$TS = \frac{IT - TT}{NI} \tag{A2.1}$$

The volume data is thresholded using a current iteration threshold (CIT) given by the following Equation A2.2.

$$CIT = IT - TS \times CI \quad \text{(A2.2)}$$

Here, CI is the current iteration. The surrounding connected voxels are added to all the seed segments individually and the current iteration is increased by one starting from zero. This is repeated until the current iteration is equal to the number of iterations and the last threshold is completed at a threshold equal to the target threshold. This results in segmentation that can simultaneously keep the separation achieved by using a high threshold (that alone results in extremely poor definition) and the segment definition that can be obtained by using a low threshold (that alone results in erroneously connected segments).

A2-2-2 BounTI tool

The algorithm devised in this work has been implemented into an easy-to-use tool available in three distinct forms (Avizo/Amira add-on, Python library, and Stand-alone Windows executable). While in-depth user guides are available in the online repository, this section briefly introduces the input and output data types, common considerations, and highlights the differences between the three implementations of the algorithm.

The workflows for the three implementations are shown in Figure A2.2. Data preparation can be done in any preferred image processing software. Input CT data should be converted to 16-bit unsigned format. When converting from 32-bit data, the input range often requires adjustments to minimise bone grey value information loss. As 8-bit data is rarely used in research settings, the tool is not designed to take in such data. Thus, 8-bit data should be converted to 16-bit unsigned data with the output range set from 0 to 255. Additionally, it is often advisable to resample the data to at least be under 2Gb, this ensures timely segmentation, which can be particularly important when fine-tuning the input parameters.

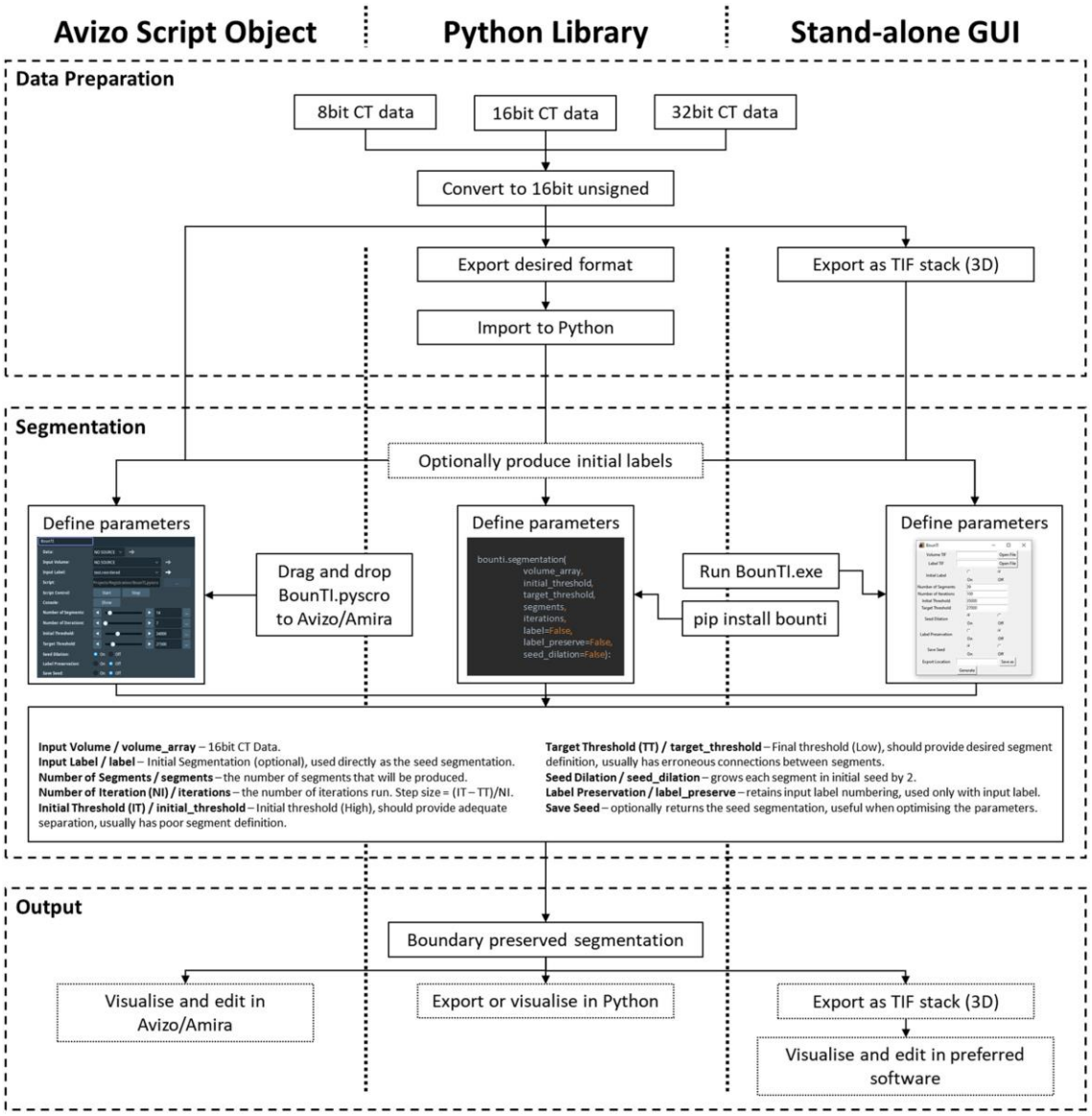

Figure A2.2 An overview of the three implementations of the algorithm. This highlights the data input and output types, and the different data import and export steps for the Avizo/Amira add-on, Python library, and the Stand-alone executable.

If the Avizo/Amira add-on is used, the data preparation can be conducted in Avizo/Amira. However, if it is conducted in other software packages, any data type that Avizo/Amira accepts can be used. The Python package uses 3D NumPy array (dtype - np.uint16) as input, thus the users can use any external library to convert the data from any data type to the array. A built-in method is available to import 3D tiff stacks. The stand-alone executable requires the 3D tiff stack as input data.

While the tool can significantly reduce the segmentation time, manual postprocessing is often a recommended final step. The Avizo/Amira add-on produces segmentation data that the users will be familiar with and will be able to manipulate as any other segmentation. Similar to the input data type, the Python function will output the same

data type. External libraries can be used to visualise or export the segmentation or a built-in method is available to export the segmentation as a 3D tiff stack. The stand-alone executable will export the output as a 3D tiff stack.

The manual in Supplement 1 includes a detailed step-by-step guide on how to achieve the best results from specific CT data, highlighting some possible use cases and how the tool can be used in conjunction with manual segmentation. While all the steps are laid out in Avizo, the same steps should apply to any other image segmentation tool.

A2-2-3 Volume data

The volume data used in this work were CT images of the craniofacial region. This was chosen as it is a complex system consisting of several bones joined together by cranial and facial sutures and synchondroses (e.g. Richtsmeier and Flaherty, 2013). Hence, it is ideal to test the functionality of BounTI.

First, a preoperative craniosynostosis patient skull (female right-sided coronal suture fusion, 92 days old) was used to highlight the sensitivity of the BounTI to the choice of its input parameters. Second, to establish the versatility of BounTI, five additional scans were used. These included: a snake (Lamprophis olivaceus, adult; Natural History Museum, UK), a lizard (Pseudopus apodus, adult; Evans Lab., UK), an amphibian (Andrias japonicus, adult; Kanagawa Prefectural Museum of Natural History, JP), a mouse (Mus musculus, 7 days old; Pauws Lab, UK), and a healthy anonymised human skull (female, 111 days old; Necker-Enfants Malades University Hospital, France).

A2-2-4 Sensitivity tests

Three sensitivity tests were performed on the preoperative craniosynostosis patient scan to investigate the effects of input parameters on the segmentation results:

Initial threshold sensitivity: the initial threshold for this scan was varied from 30,000 to 40,000 in increments of 1,000. These were set to capture the full range of the bone grey values from the scan. At threshold values lower than 30,000, the soft tissues and noise were included, while at values higher than 40,000 little to no bone would be selected. The number of segments was set to 28 as this was deemed sufficient to capture the 23 cranial bones (Dixon et al., 1997) as well as the mandible and vertebrae present in the scan. The number of iterations was adjusted to retain a threshold step of 50, which was done to remove the influence of step size on the outcome. Thus, the segmentations with higher

initial thresholds would require more iterations (see Equation A2.1); if the number of iterations was left unchanged it would result in different step sizes between iterations. Here, the target threshold of 27,000 was used for this scan given that it resulted in the desired bone definition.

Number of iterations sensitivity: the number of iterations defines how many times the algorithm should be repeated between the initial and target thresholds. Tested values were 10, 25, 50, 100, 150, and 200 resulting in threshold steps of 800, 320, 160, 80, 53, and 40, respectively. These were chosen to capture the full range of the CT contrast resolution, that is, the step size of 40 was finer than the actual spread of the grey values, meaning that further increasing the number of iterations would have had no effect on the segmentation results. An initial threshold of 35,000 (obtained from the initial threshold sensitivity test) was used and the target threshold set to 27,000. The number of segments was set to 28.

File size sensitivity: Resampling was used to obtain volumes ranging from 7 MB to 1.2 GB in file size by increasing or decreasing the voxel size of the original scan (Lanczos resampling in Avizo). Execution time was taken as the wall time (the amount of time that the program takes from start to finish) on a Windows machine with 128 GB RAM, Intel Xeon W-2265 CPU @ 3.50 GHz. Algorithm parameters were as follows: 35,000, 27,000, 10, and 28 for the initial threshold, target threshold, number of iterations, and number of segments, respectively (Table A2.1).

Table A2.1 BounTI parameters used for the different sensitivity tests carried out.

Test	Initial threshold	Target threshold	Number of iterations	Number of segments	File size, MB
Initial threshold sensitivity	30,000–40,000	27,000	60–260	28	181
Number of iterations sensitivity	35,000	27,000	10–200	28	181
File size sensitivity	35,000	27,000	10	28	7–1200

A2-2-5 Versatility analysis

BounTI segmentation was performed on all the specimens described in the volume data section. The scans were obtained from different CT machines with different resolutions and qualities. Figure A2.3 presents a sagittal slice of the aforementioned scans as well as the grey value distribution (left – 0, right – 65,535, range markers show the initial [higher – left] and target [lower – right] threshold used for each case study in the versatility analysis) and volume dimensions in voxels. The initial threshold was selected as the value at which the bones were sufficiently separated when using a direct threshold. The target threshold was the value at which the desired bone definition was reached. As the CT data was arbitrarily converted from 32-bit to 16-bit with the goal of preserving the greyscale value data for the bone, the numeric values are arbitrary and have little physical meaning beyond higher values signifying higher x-ray attenuation. Specific BounTI and scan parameters used for each specimen were as follows:

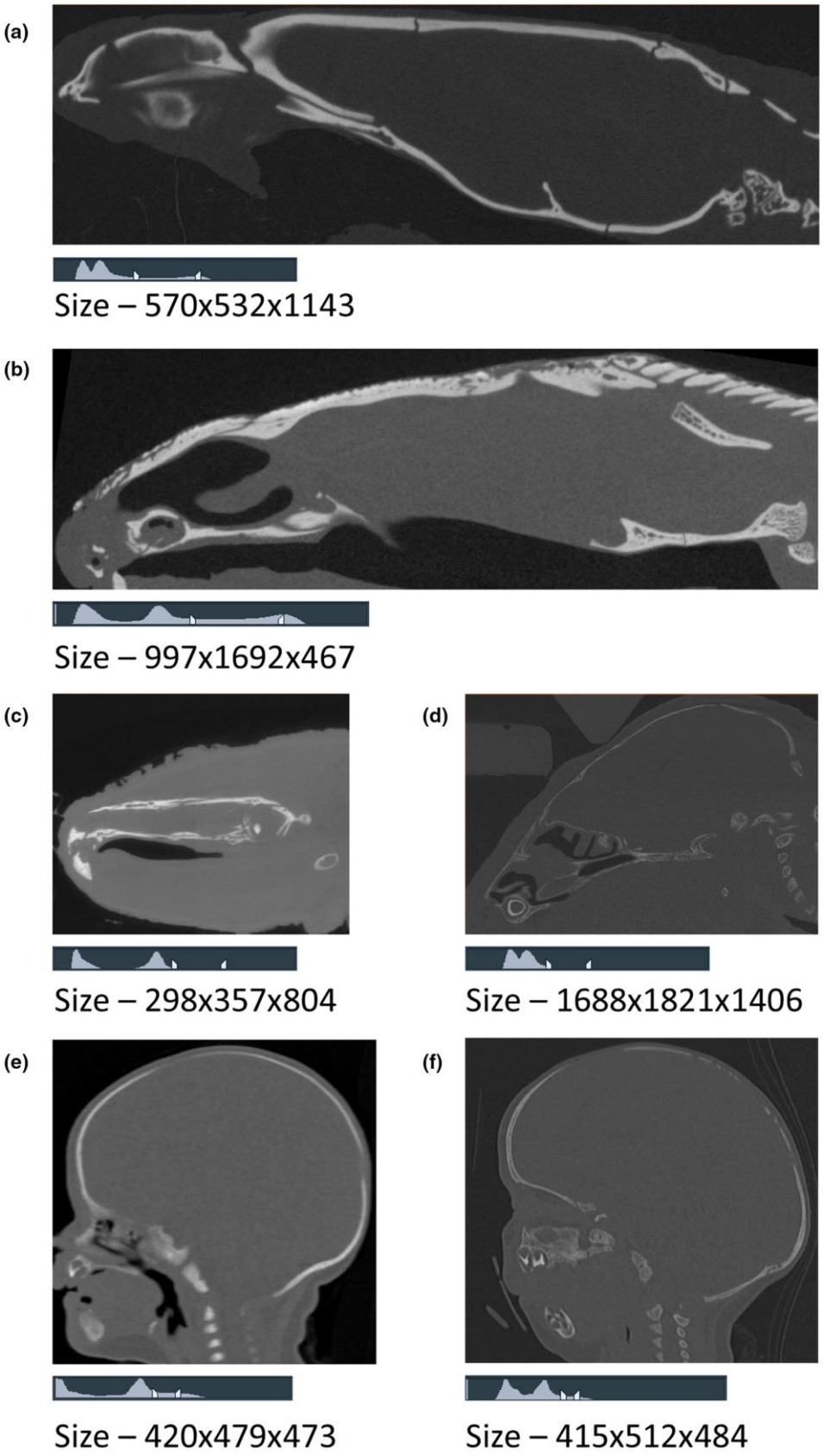

Figure A2.3 Sagittal slices and scan volume size in voxels for the segmented cases. The histogram range is from 0 (left) to 65,535 (right) and pointers initial (higher) and target (lower) thresholds used for example segmentations. (a) Snake – Lamprophis olivaceus adult, (b) Lizard – Pseudopus apodus adult, (c) Amphibian – Andrias japonicus adult, (d) Mouse – Mus Musculus 7 days old, (e) Human – Female right-side coronal suture fusion 92 days old, (f) Human – Female 111 days old. Note: visualisations in this figure were generated in Avizo image processing software.

Lamprophis olivaceus (Snake): BounTI – Initial threshold of 40,000, target threshold of 21,000, number of segments set to 40, and number of iterations set to 100; Scan – 13 μm × 13 μm × 13 μm, 90 kV, 111 μA, 0.354s exposure.

Pseudopus apodus (Lizard) (Marghoub et al., 2023): BounTI – Initial threshold of 48,000, target threshold of 28,000, number of segments set to 200, and number of iterations set to 200; Scan – 23 μm × 23 μm × 23 μm, not known to us.

Andrias japonicus (Amphibian) (Matsumoto et al., 2024): BounTI – Initial threshold of 47,000, target threshold of 32,000, number of segments set to 40, and number of iterations set to 100; Scan – 100 μm × 100 μm × 100 μm, not known to us.

Mus musculus (Mouse) (Didziokas et al., 2024): BounTI – Initial threshold of 34,000, target threshold of 21,000, number of segments set to 30, and number of iterations set to 100; Scan – 9.6 μm × 9.6 μm × 9.6 μm, 90 kV, 90 μA, 1 s exposure.

Homo Sapiens (Human), female right-sided coronal suture fusion, 92 days old (Mellgren et al., 2024): BounTI – Initial threshold of 35,000, target threshold of 27,000, number of segments set to 28, and number of iterations set to 100; Scan – 293 μm × 293 μm × 300 μm, not known to us.

Homo Sapiens (Human), female, 111 days old (Liang et al., 2023): BounTI – Initial threshold of 29,000, target threshold of 22,000, number of segments set to 28, and number of iterations set to 100; Scan – 304 μm × 304 μm × 296 μm, not known to us.

A2-3 Results

A2-3-1 Initial threshold sensitivity

The analysis showed that a lower initial threshold resulted in erroneously connected segments because the segments were connected in the seed (Figure A2.4). Conversely, an overly high initial threshold led to erroneous separation as seen on the parietal bone in the 40,000-threshold case. Additionally, in the latter case, some segments were also erroneously connected due to the seed lacking a segment to build onto (see parietal bone in Figure 4). For brevity, five out of the 11 cases tested are shown in Figure 4. The full set is available in supplement of the published version. Note, the colours of the segments in all figures were based on the volume of the segment in the seed. This resulted in different colours of the same bone in some of the BounTI segmentation. While this can

be easily changed manually or algorithmically to coincide between segmentations in this work, it was chosen to present the results exactly as generated.

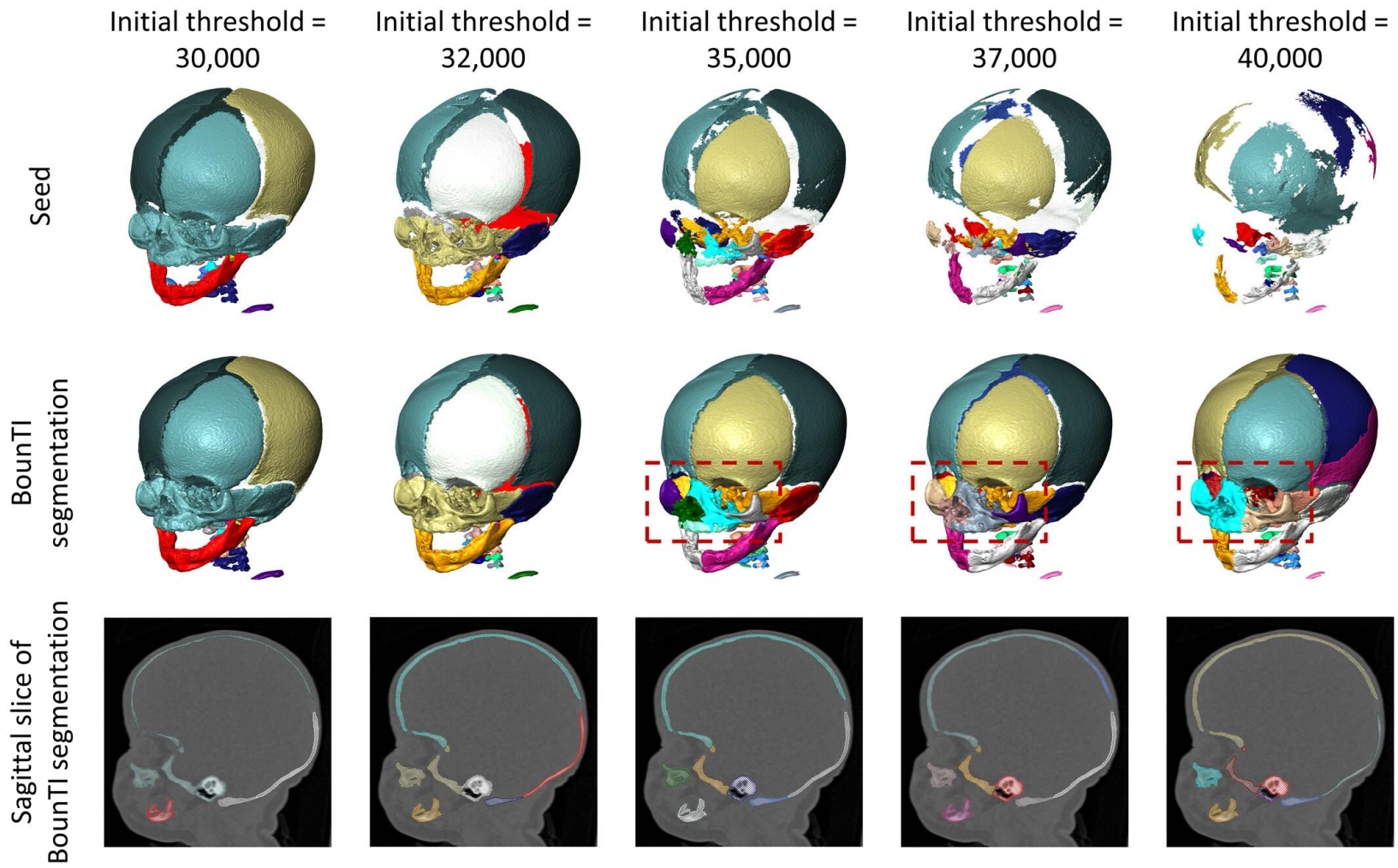

Figure A2.4 Effects of initial threshold value on the generated seed segments and the final segmentation. (Number of segments set to 28 and the number of iterations adjusted for each threshold to retain a step size of 50). Boxes outline the facial region (nasal, maxilla, and zygomatic bones).

A2-3-2 Number of iterations sensitivity

The effects of the number of iterations are shown in Figure A2.5a. The main effect was the definition of the boundary between two adjacent regions, with the higher number of iterations resulting in a cleaner, more anatomically accurate boundary. However, the differences in the boundary between the 100 and 200 iterations cases were hard to identify, suggesting a limit on the boundary-improving effect of the number of iterations used. For brevity, three out of the six cases tested are shown in Figure A2.5a. The full set is available in the supplement of the published version.

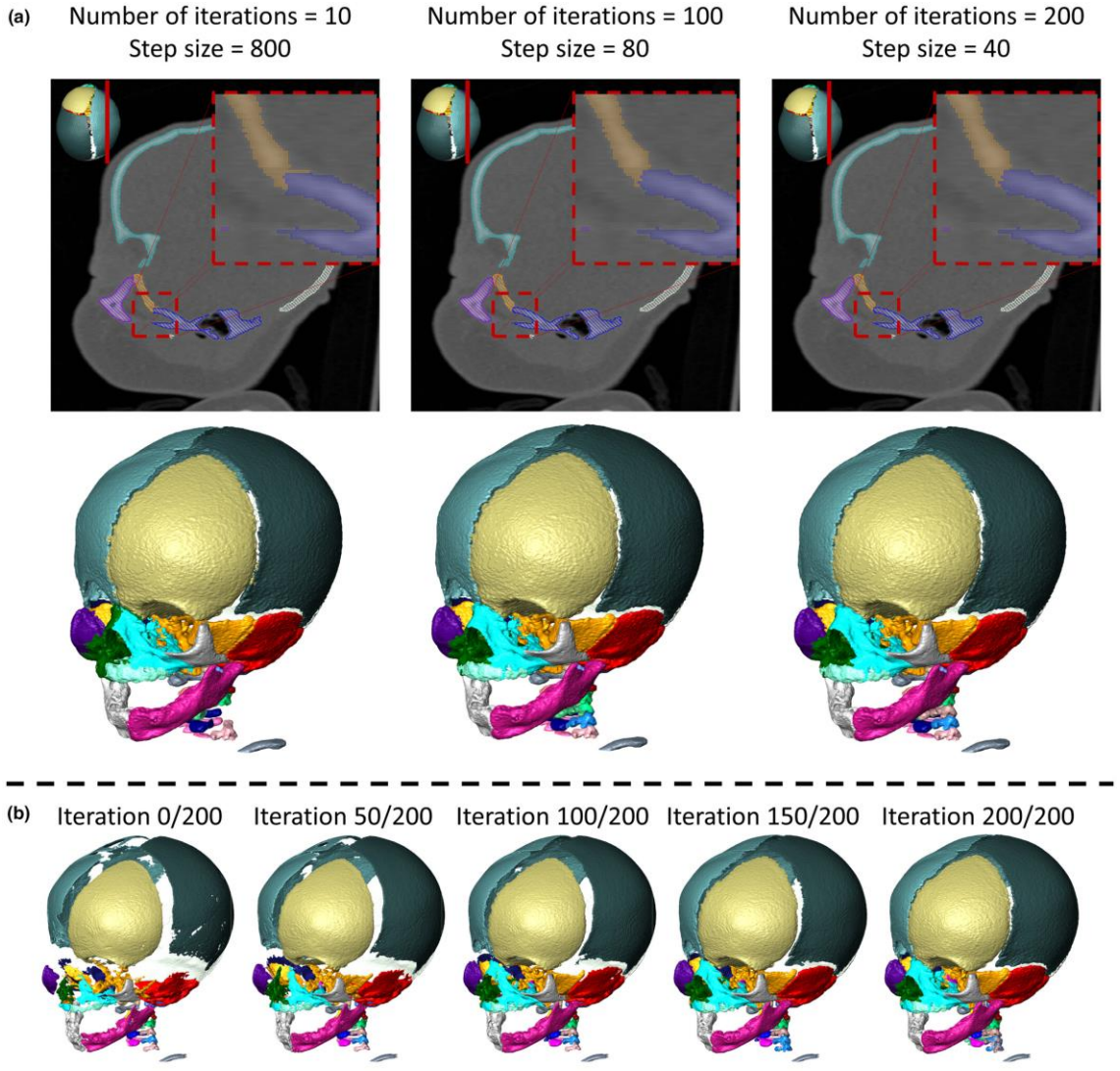

Figure A2.5 (a) Effect of the number of iterations on segment boundary quality. Boxes outline the interface of two segments and (b) change in the segmentation with iterations completed with an initial threshold of 35,000, target threshold of 27,000, number of segments set to 28, and number of iterations set to 200, resulting in a step size of 40.

Additionally, Figure A2.5b highlights the working principles of the algorithm showing the outcome of the segmentation at different iterations, where the number of iterations was set at 200 that is, at 0 (0%), 50 (25%), 100 (50%), 150 (75%), and 200 (100%). Animated visualisations for the iterations for both the craniosynostosis case and the normal skull scans is available in the supplement of the published work.

A2-3-3 Number of iterations sensitivity

Some loss of segmentation quality occurred when the volume data were down-sampled, namely the facial bones (nasal and maxilla), see Figure A2.6a. Overall, bone definition was also affected and can be observed as more apparent voxels in the down-sampled cases. Additionally, the execution time was directly proportional to the file size when the data was down-sampled (see Figure A2.6). While the specific relation shown here will not be true for all data sets and BounTI settings, the direct relation between computation time and file size is always present, meaning that as file size increases execution time will also increase.

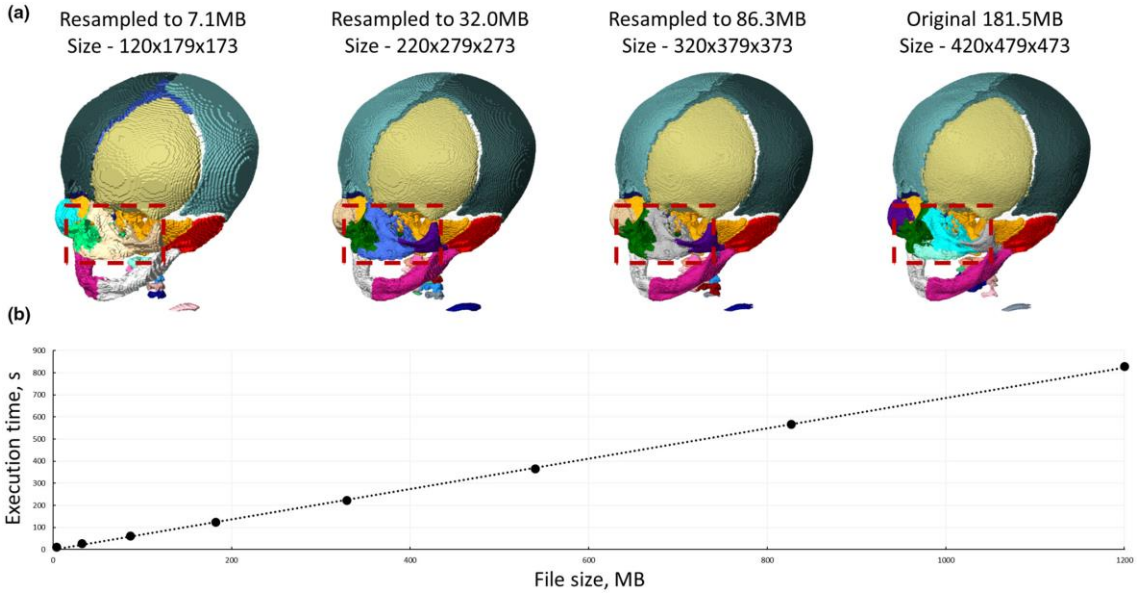

Figure A2.6 (a) Comparison of segmentation results for downsampled CT data and (b) Execution time in seconds against CT data set size in megabytes. All tests were segmented with an initial threshold of 35,000, target threshold of 27,000, number of segments at 28, and number of iterations set to 10, resulting in a step size of 800.

A2-3-4 Versatility analysis

The algorithm successfully segmented various bony parts of the craniofacial skeleton in all presented cases (Figure A2.7). Nonetheless, the results were still dependent on both the specimen type and scan quality and not all the bones were separated even if,

anatomically, the bony segments were distinct. This can be observed to some extent in all cases considered and may still require some manual segmentation. However, the results also highlight the versatility and capabilities of the approach with the majority of the bones segmented and, in the lizard case, including all the individual osteoderms (Figure 7b).

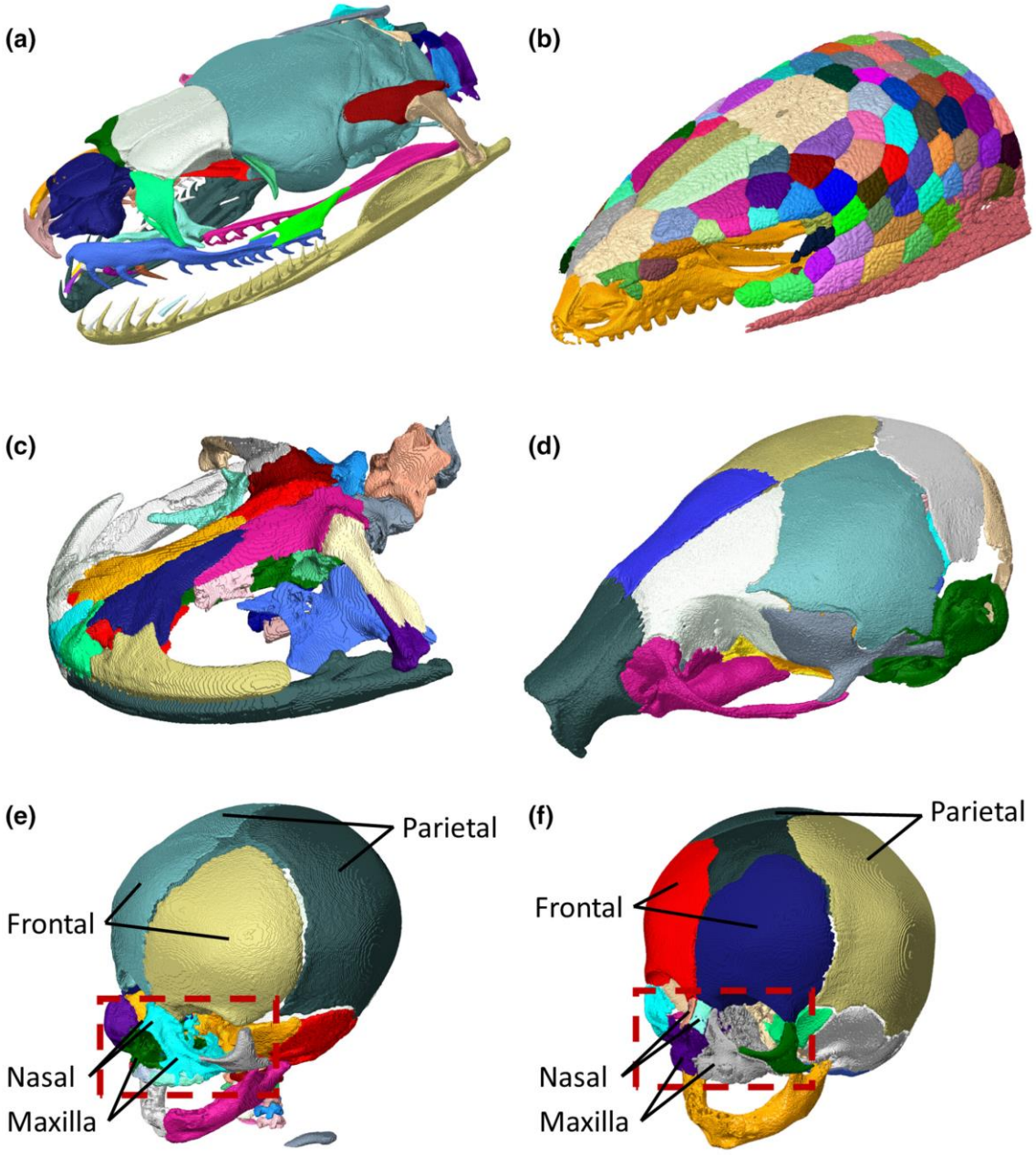

Figure A2.7 Segmentation results for different CT scans (a) Snake - Lamprophis olivaceus adult, (b) Lizard - Pseudopus apodus adult (c) Amphibian – Andrias japonicus adult, (d) Mouse – Mus musculus 7 days old, (e) Human – Female right-sided coronal suture fusion 92 days old, (f) Human – Female 111 days old. Boxes outline the facial region (nasal, maxilla, and zygomatic bones) in the human segmentations. Bones of interested are highlighted.

The comparison between the segmentation of the craniosynostosis infant and the normal infant skulls (i.e. Figure A2.7e vs A2.7f) highlights two key aspects of the algorithm.

Firstly, the fused frontal and parietal bones were not segmented in the former specimen. Additionally, the latter specimen showed better and more anatomical segmentation as seen in the nasal and maxillary bones (see highlight boxes in Figure A2.7e,f). The unclear boundaries in the craniosynostosis skull segmentation are known as overflow and are a direct result of the scan quality (contrast, resolution, and sharpness).

A2-4 Discussion

We have here presented a novel automated segmentation tool and highlighted its capabilities. BounTI was successfully developed and used to segment craniofacial bones of different species. The 'right' choice of input parameters for this algorithm will depend on a range of parameters including the quality of volume data, specifically resolution, and greyscale value distribution (contrast). The user manual available in the online repository can be a useful resource to identify the input parameters. Nonetheless, the sensitivity tests included in this study can act as a troubleshooting guide for users when selecting these parameters for their specific data sets.

The sensitivity tests demonstrated that the segmentation results are primarily affected by the choice of initial threshold. The initial threshold first identifies the seed, that is, produces the initial segmentation from which each segment is then grown. Thus, it had a profound effect on the separation (i.e. segmentation) obtained from the algorithm. A low threshold led to insufficient separation in the initial seed and therefore erroneous connections between the segments. On the other hand, an overly high threshold led to more disconnected segments in the initial seed and, thus, erroneous disconnections between the segments in the final segmentation. Additionally, the high threshold led to missing segments as the threshold was too high to obtain segments in the initial seed in certain regions. This is observed in Figure A2.4 (see highlight box) for the 40,000 threshold case, where nasal and maxilla bones lack the separation seen in the 35,000 and 38,000- threshold cases.

A direct segmentation from a high threshold could be used to obtain the initial threshold parameter. If the segmentation shows connected segments where they are expected to be anatomically separate, the initial threshold should be higher, and if some segments are missing, the initial threshold should be lower. Additionally, the tool developed here allows the direct extraction of the created and optionally dilated seed, which can then be investigated and used to adjust the initial threshold accordingly.

Some volume data may not have sufficient resolution, contrast, or sharpness to obtain a well-separated seed with enough definition to build the segments in the iteration process. In such cases, the initial seed can be put in manually, instead of using the generated seed from the initial threshold. If this approach is employed, the initial seed can either be preserved that is, the segment assignments retained, or disregarded by selecting the largest disconnected segments. For the latter method, all the desired segments should already be disconnected in the seed, while using the former will retain the segment separation even when the segments are in contact (connected). This option was not investigated in this work, more details on how to perform seed manipulation are available in the online repository.

The number of iterations sensitivity test did not display a large difference between the values considered due to the volume data used. The spread of the grey value range (across the bone voxels, see Figure A2.3e histogram) in the initial data was relatively small (Figure A2.5b). This significantly limits the effect of increasing the number of iterations. However, when comparing the 10 and 100 iterations cases a clear difference in the quality of the boundaries between the segments can be seen, with the higher iteration producing a more anatomical boundary definition. This was not further improved by increasing the number of iterations to 200 iterations (see highlight boxes in Figure A2.5b). This analysis suggests that the number of iterations that should be selected is affected by the spread of grey values across the bone. The spread is dependent on the resolution, contrast, and level of noise in the scan among other factors. An overly high number of iterations may not necessarily improve the quality of the final segmentation results, but it will impact the computational time. For example, in a lower file size volume (e.g. clinical CT), this may not be of concern. However, for larger volumes, it can considerably impact the computational time.

The file size sensitivity test showed that a larger file required more computational time (Figure A2.6b). Volume data file size can be reduced by three main methods. First, the grey values can be converted to use fewer bits. In the case of this algorithm, unsigned 16-bit data is required as input, thus 32-bit, signed 16-bit, and 8-bit data should be converted to unsigned 16-bit data. For the 8-bit case, the output should be from 0 to 255 when converting. Secondly, the volume of interest can be cropped to include only the desired parts for segmentation. Lastly, the data may be down-sampled, however, as shown in Figure A2.6a, this can impact the quality of the final segmentation. Down-sampling can

lead to the largest decrease in computational time and should be considered when using extremely large microCT volumes such as those presented in Figure A2.3d.

Lastly, the versatility is highlighted in Figure A2.7 as the approach can be used for a variety of species as well as a range of initial volume qualities, as seen in Figure A2.3. This suggests that BounTI can be an invaluable tool for a range of disciplines from anatomical research to surgical planning as segmentation has been a historically tedious and time-consuming manual process. As a manual target threshold is used in the algorithm for the final threshold, it can never yield any selection different to one segmented with the same threshold directly. Consequently, in the worst-case scenario, BounTI will have separated meaningless segments, but the overall definition will be exactly as it would have been using direct thresholding. However, in all cases shown here the majority of the segments separated are anatomically accurate and useful.

Nonetheless, BounTI has limitations. The comparison between craniosynostosis and normal human skull scans shows that the algorithm cannot separate physically fused bones. More crucially, the higher quality of the normal human scan highlights the importance of scan quality as the segmentation was more anatomically accurate for the normal skull. Namely, the more accurate separation of the nasal and maxillary bones in the normal skull compared to the craniosynostosis skull highlighted in Figure A.27e,f. A conceptually similar approach attempted to address the overflow issue that has led to these scan quality-based separation differences in BounTI (Huang et al., 2011). However, this method requires significantly more computational steps, and the overflow issue only occurs for low-resolution and low-contrast images. Direct threshold iteration was chosen for BounTI to retain the relative simplicity of the algorithm and to maximise the information obtained from the grey values of the volume data directly, but this resulted in lower-quality segmentation for some clinical CT scans that tend to yield lower resolution/lower contrast images compared to higher-quality images such as those produced with microCT. The required scan quality largely depended on the specimen investigated as specimens with smaller gaps between bones may require higher resolution or specimens with less difference in the x-ray attenuation between the bones and tissues connecting the bones may require longer scans to improve contrast.

The focus of this work was on the segmentation of the craniofacial system, however, the tool can be used to segment other skeletal regions. Segmentation of iodine-stained soft tissues may be possible using the tool, however, the slightly higher grey values observed surrounding the soft tissue boundaries in these scans contradict the core principle of the

algorithm that the grey value is lower at the boundary than other parts of the segment. Similar issues are present in fossil scans as well as MRI scans. While it may be possible to segment these scans either with or without additional processing steps using BounTI, this has not been tested.

Pilot validation has been included in the supplement of the published work. This includes a comparison of two extremely different manual segmentation cases, a normal human infant skull to later be used for FEA and a minimally segmented Yucatan 1-month-old mini pig where the goal of the segmentation was to separate the segments manually by removing the material in the sutures connecting bones. These validation examples are in no way comprehensive and BounTI users are highly advised to carry out case-specific sensitivity tests, especially when the segmentation is used directly for analysis as opposed to further manual corrections.

A commonly used score to evaluate segmentation accuracy is the Dice Similarity Coefficient. It captures the similarity between two arrays. In this case, Dice scores were calculated for each segment and the average of these scores presented as the overall similarity between the manual and BounTI segmentation. The average Dice scores for the human scan were 56% and 72% with the missing components in the BounTI segmentation included and not included in the average, respectively. For the pig segmentation, no components were missing in the BounTI segmentation, and the average accuracy was 99%. As FE models require increased suture thickness to be computationally viable, the majority of the difference between manual and BounTI segmentation is present across the sutures in the human segmentations (Supplement in the published paper). The sutures have been significantly idealised in the manual segmentation giving rise to the majority of discrepancies in dice scores between the human and pig segmentation accuracy (Liang et al., 2024). Additionally, some of the segments in the manual human segmentation were not separated in the BounTI segmentation due to insufficient grey value separation of these small facial bones further contributing to the differences in accuracy. This investigation highlights the variability of BounTI segmentation accuracy due to segmentation goals and data quality.

A2-5 Summary

Even with the limitations laid out in this work, BounTI was able to successfully segment the vast majority of the anatomically separate bones in all of the investigated specimens

in a matter of minutes compared to days, weeks, or, in the lizard cases, months of work that required the manual separation of the segments. The tool is available in three distinct forms – Avizo/Amira addon (Script Object), Python library, and a stand-alone executable. As the method is shown to be versatile, it is crucial to make it as accessible as possible to researchers and clinicians of all backgrounds (see also Davies et al., 2017). With the segmentations produced by BounTI, it is sometimes possible to automatically infer the soft tissue joints connecting the craniofacial bones (as shown in the online repository). Further investigations into the techniques described in this work may lead to the automation of not only the bone segmentation but also the segmentation of sutures and synchondroses.

Appendix III

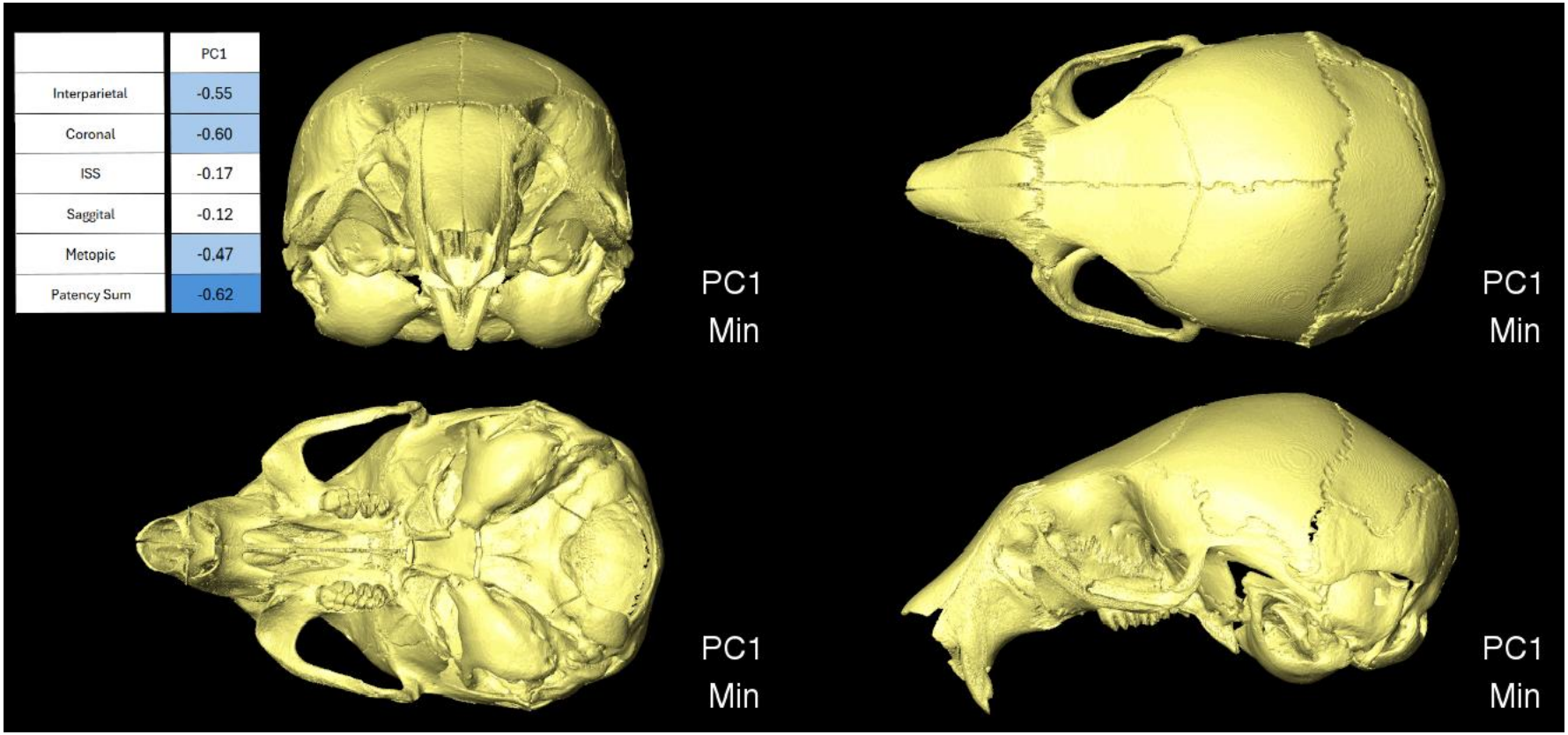

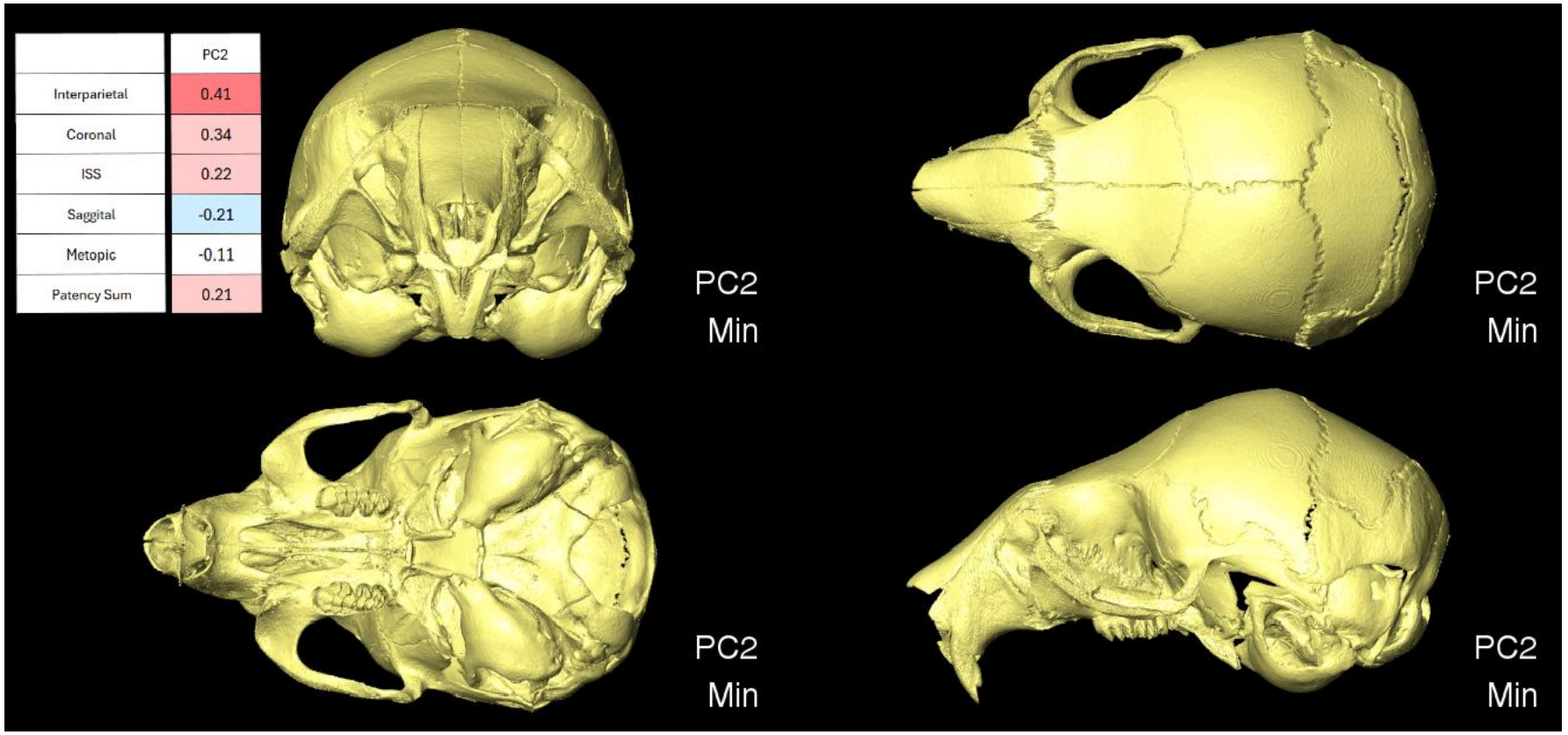
PC2
Interparietal 0.41
Coronal 0.34
ISS 0.22
Saggital -0.21
Metopic -0.11
Patency Sum 0.21
PC2 Min
PC2 Min
PC2 Min
PC2 Min

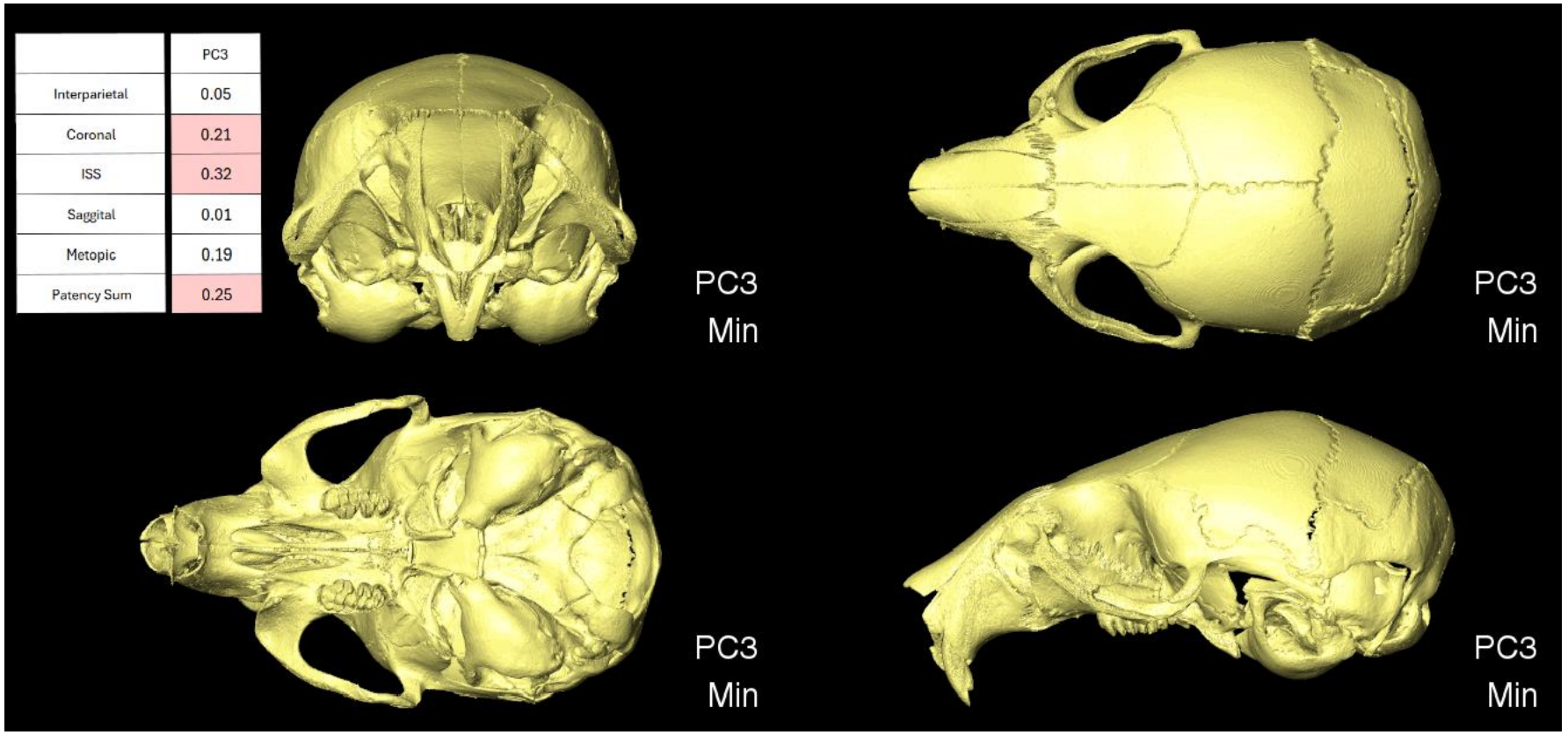
PC3
Interparietal 0.05
Coronal 0.21
ISS 0.32
Saggital 0.01
Metopic 0.19
Patency Sum 0.25
PC3 Min
PC3 Min
PC3 Min
PC3 Min

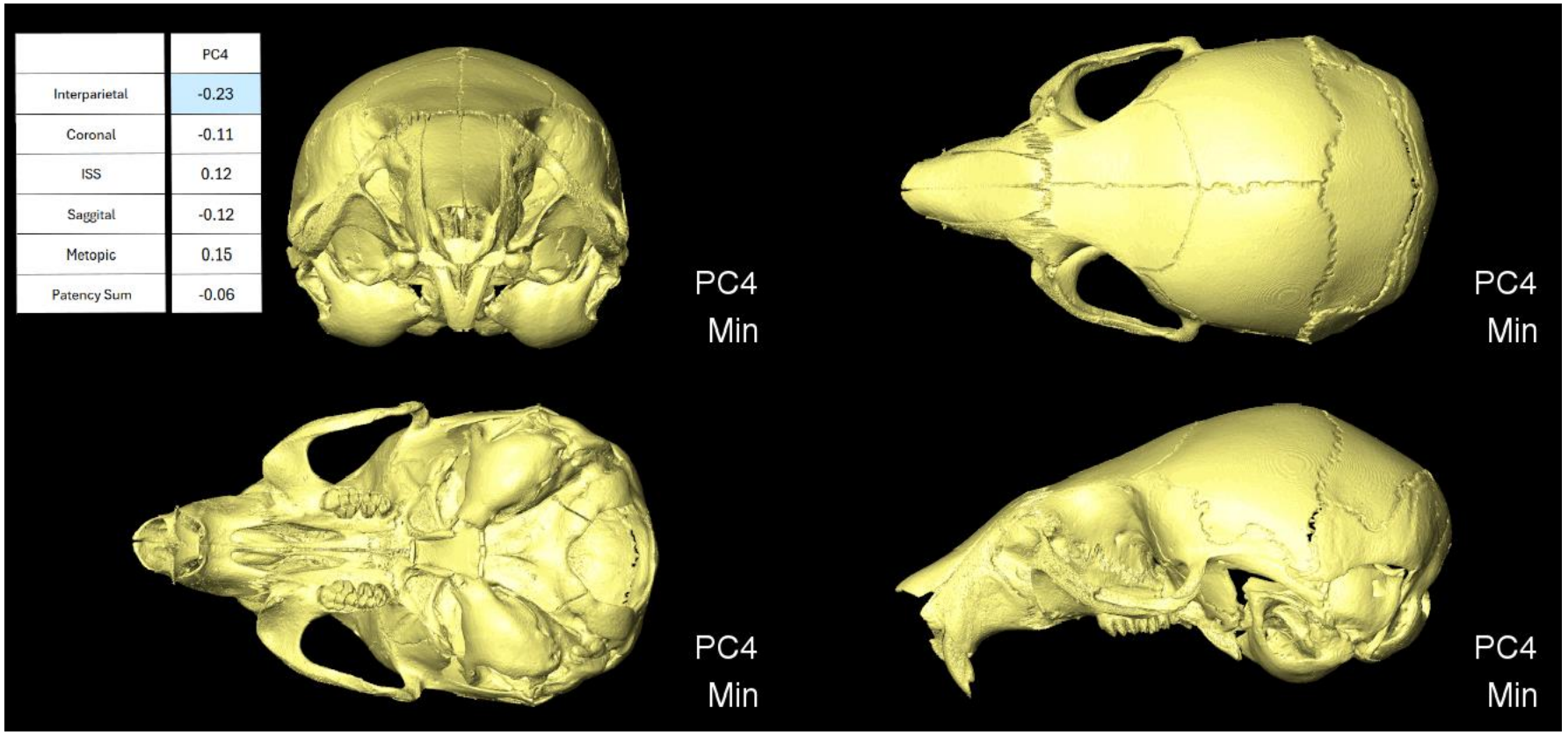
PC4
Interparietal -0.23
Coronal -0.11
ISS 0.12
Saggital -0.12
Metopic 0.15
Patency Sum -0.06
PC4 Min
PC4 Min
PC4 Min
PC4 Min

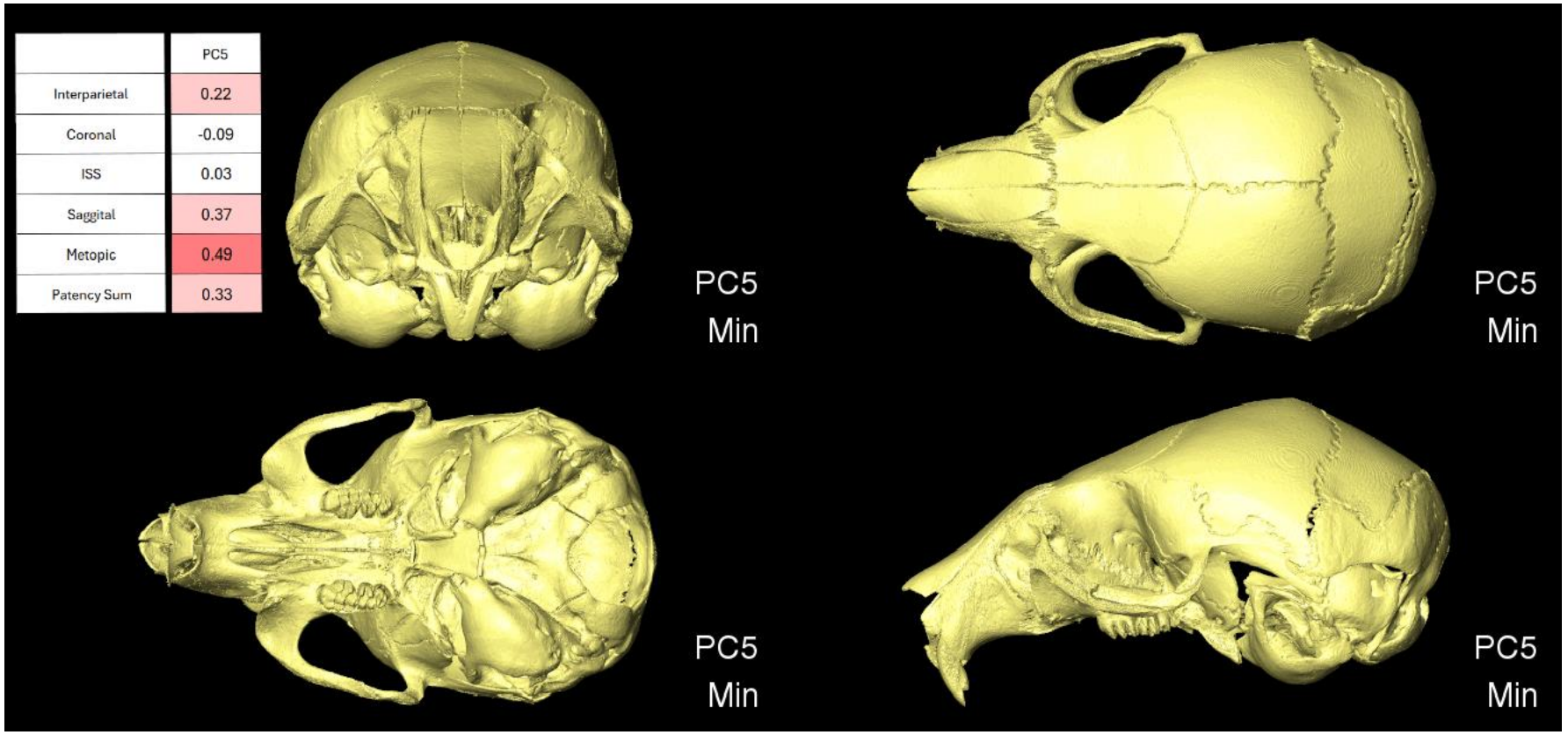
PC5
Interparietal 0.22
Coronal -0.09
ISS 0.03
Saggital 0.37
Metopic 0.49
Patency Sum 0.33
PC5 Min
PC5 Min
PC5 Min
PC5 Min

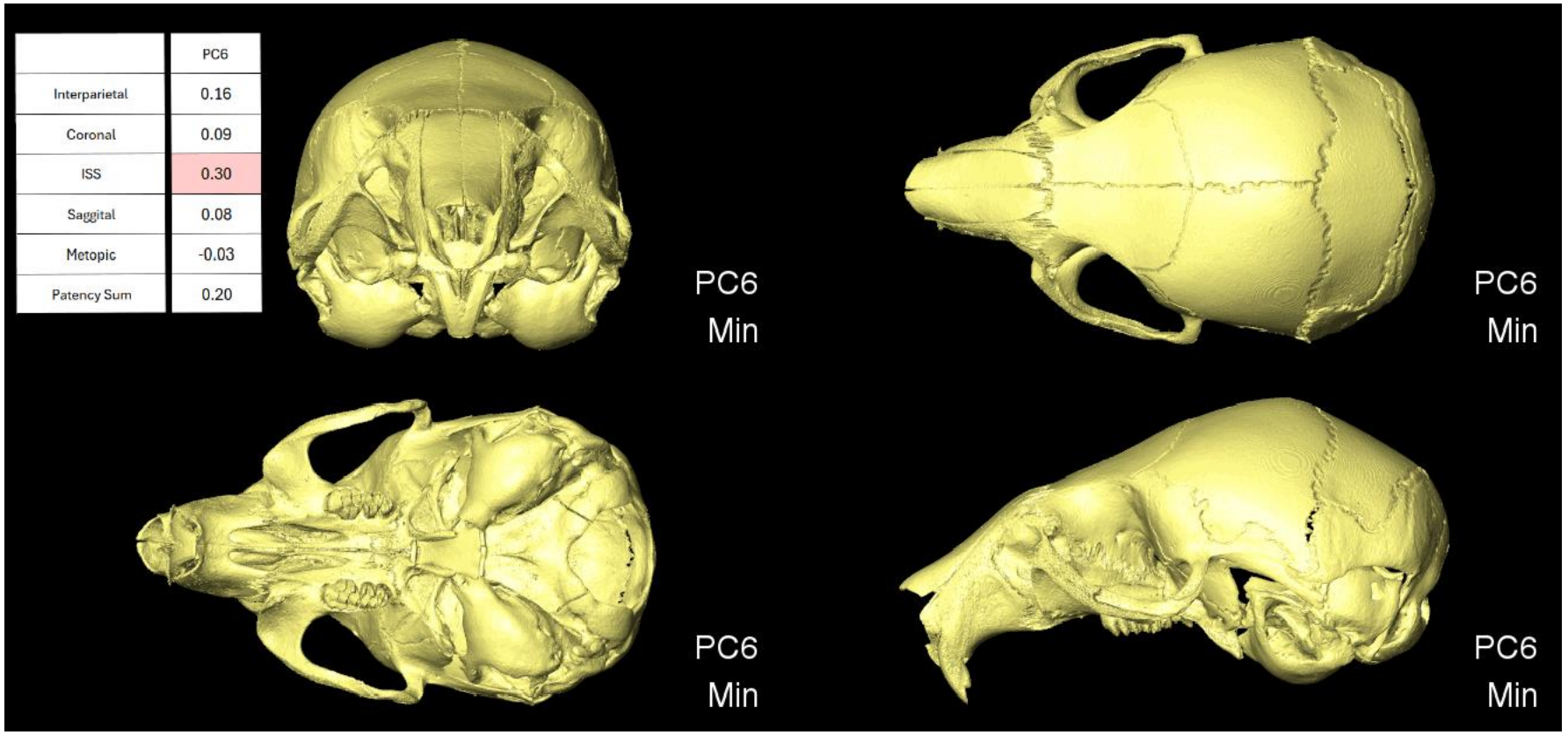
PC6
Interparietal 0.16
Coronal 0.09
ISS 0.30
Saggital 0.08
Metopic -0.03
Patency Sum 0.20
PC6 Min
PC6 Min
PC6 Min
PC6 Min

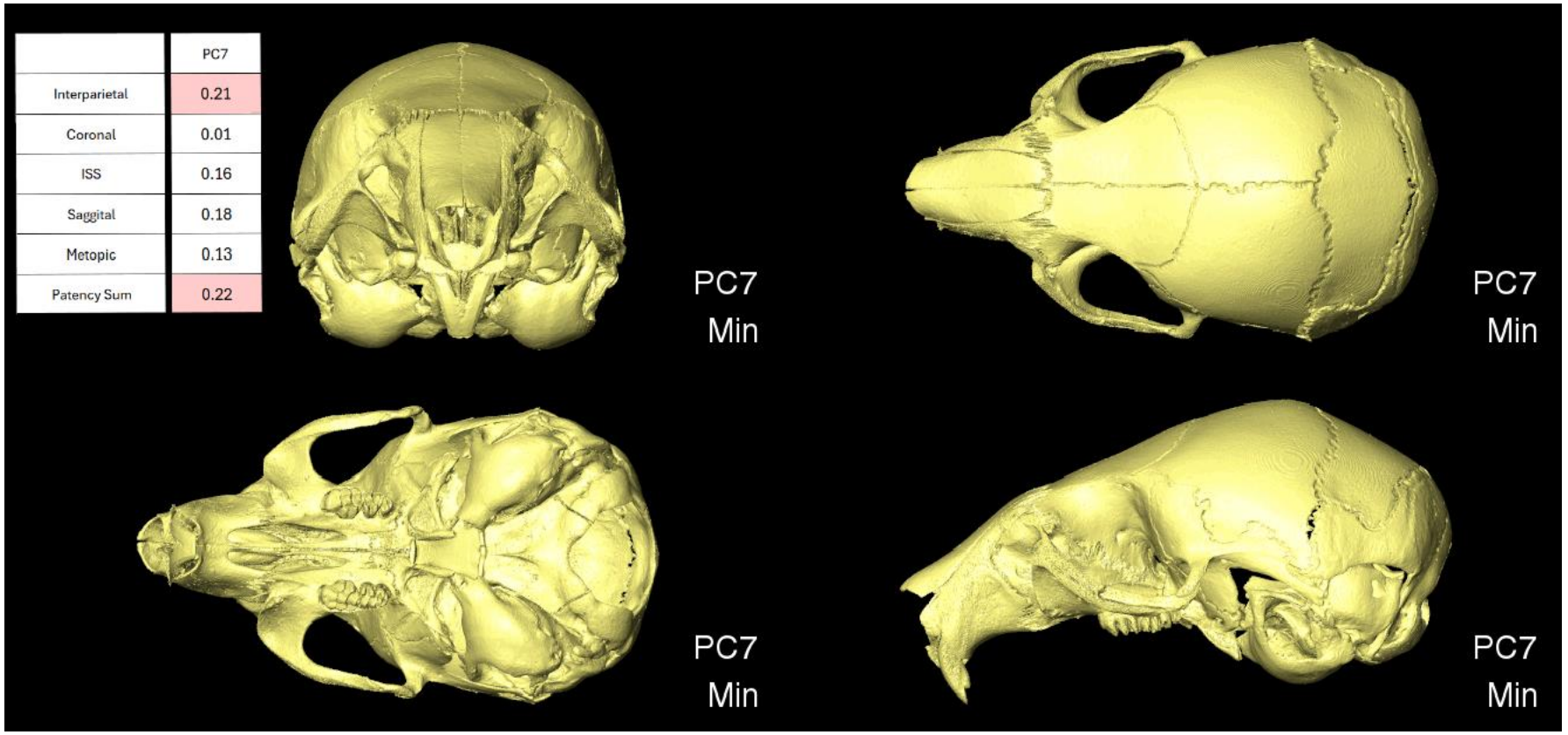
PC7
Interparietal 0.21
Coronal 0.01
ISS 0.16
Saggital 0.18
Metopic 0.13
Patency Sum 0.22
PC7 Min
PC7 Min
PC7 Min
PC7 Min

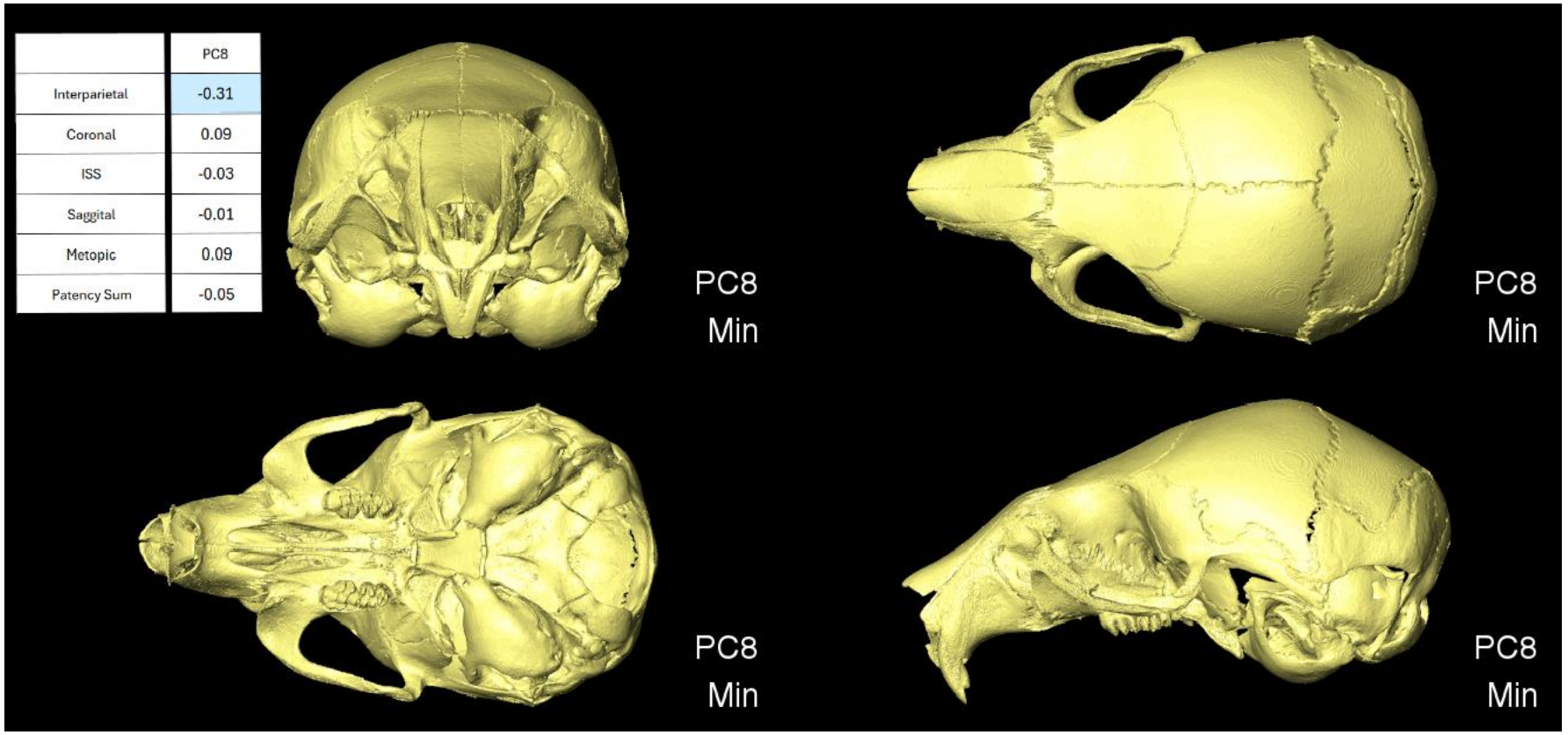
PC8
Interparietal -0.31
Coronal 0.09
ISS -0.03
Saggital -0.01
Metopic 0.09
Patency Sum -0.05
PC8 Min
PC8 Min
PC8 Min
PC8 Min

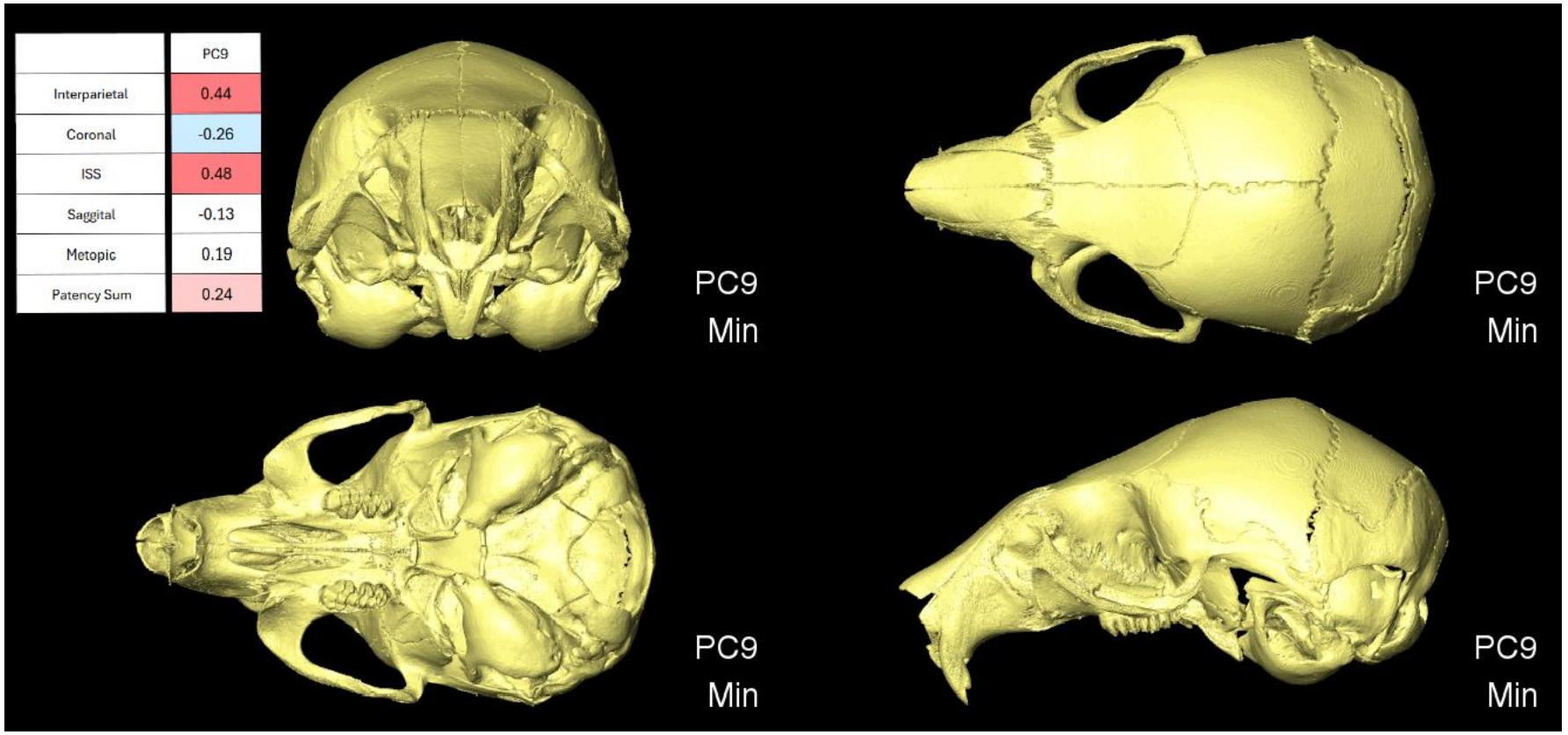
PC9
Interparietal 0.44
Coronal -0.26
ISS 0.48
Saggital -0.13
Metopic 0.19
Patency Sum 0.24
PC9 Min
PC9 Min
PC9 Min
PC9 Min

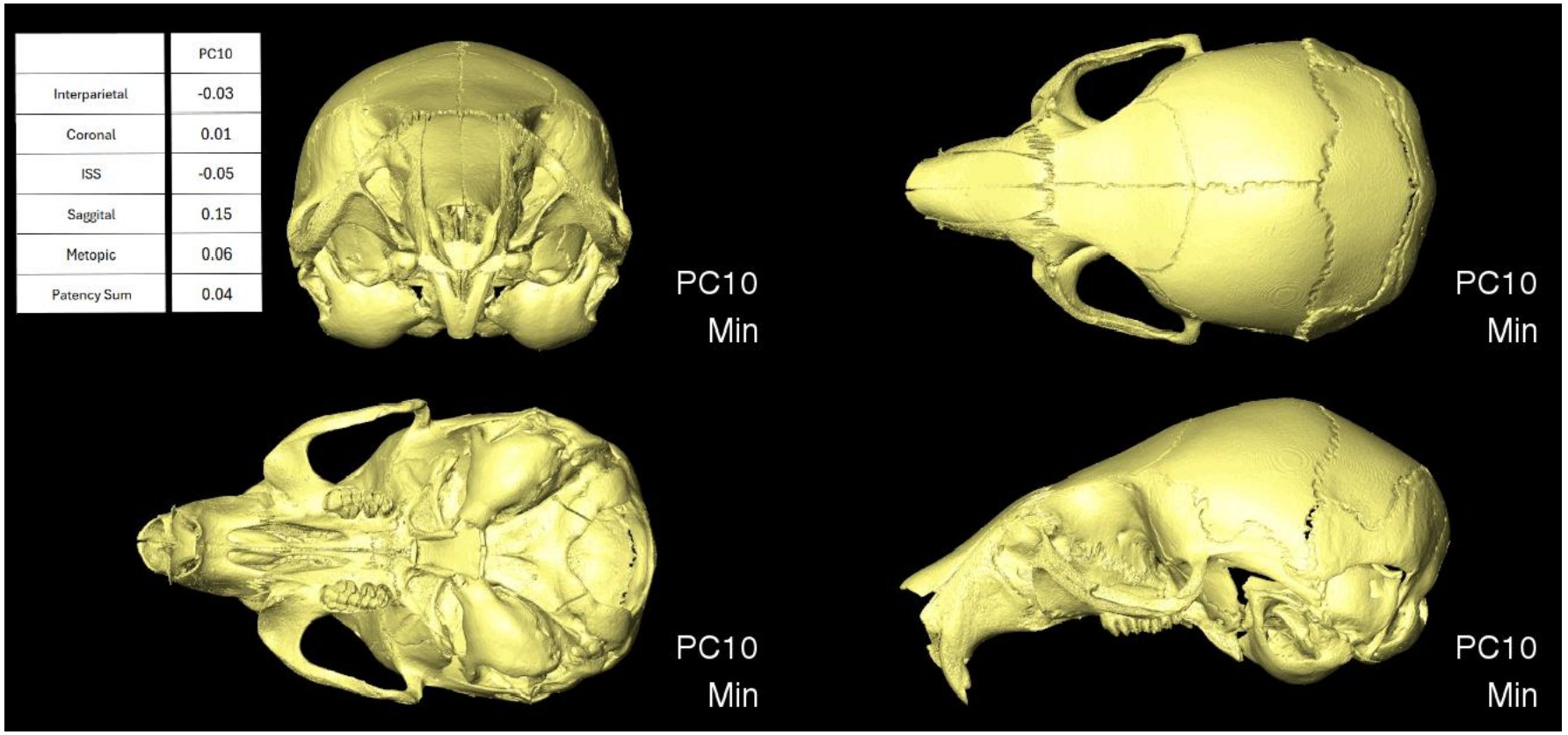
PC10
Interparietal -0.03
Coronal 0.01
ISS -0.05
Saggital 0.15
Metopic 0.06
Patency Sum 0.04
PC10 Min
PC10 Min
PC10 Min
PC10 Min

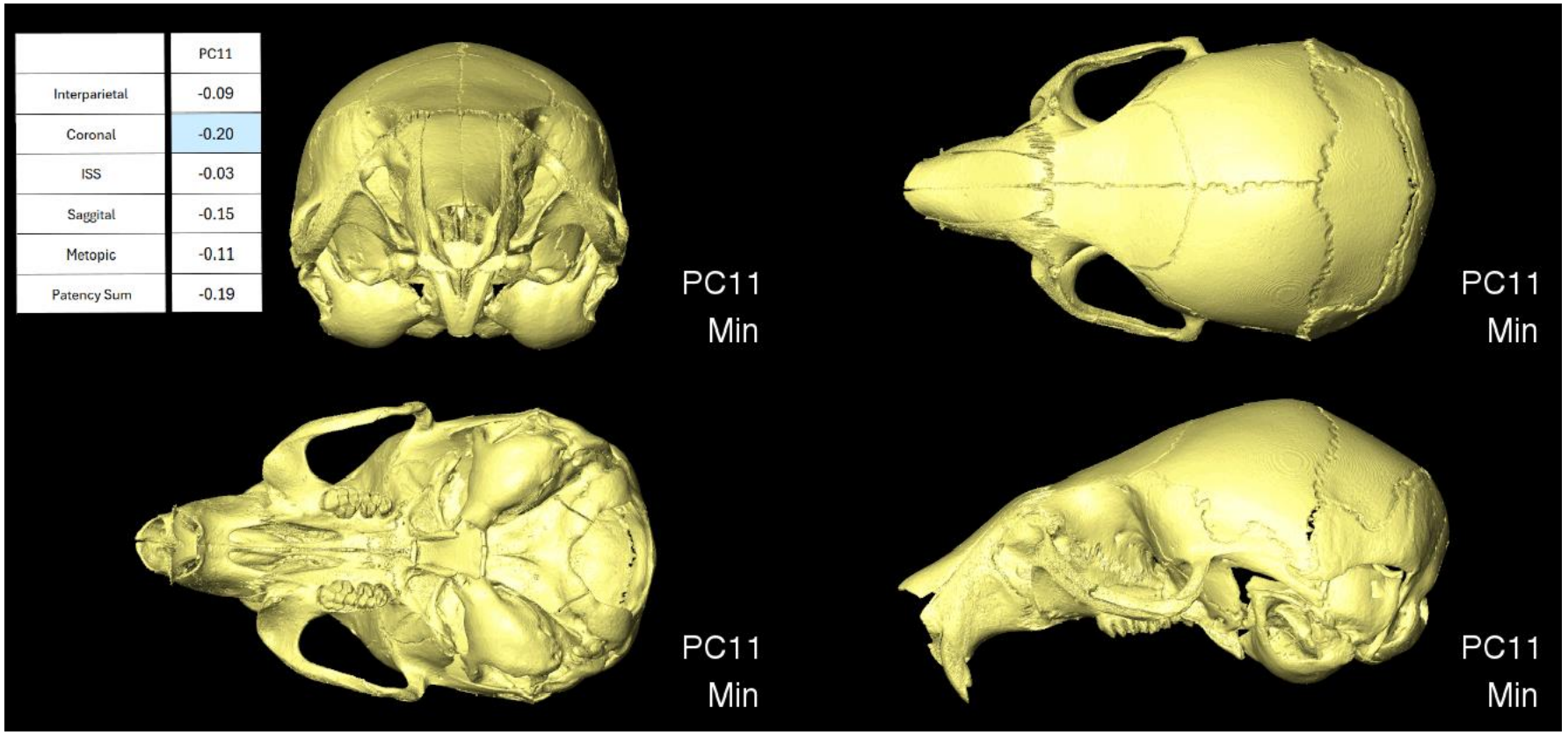
PC11
Interparietal -0.09
Coronal -0.20
ISS -0.03
Saggital -0.15
Metopic -0.11
Patency Sum -0.19
PC11 Min
PC11 Min
PC11 Min
PC11 Min

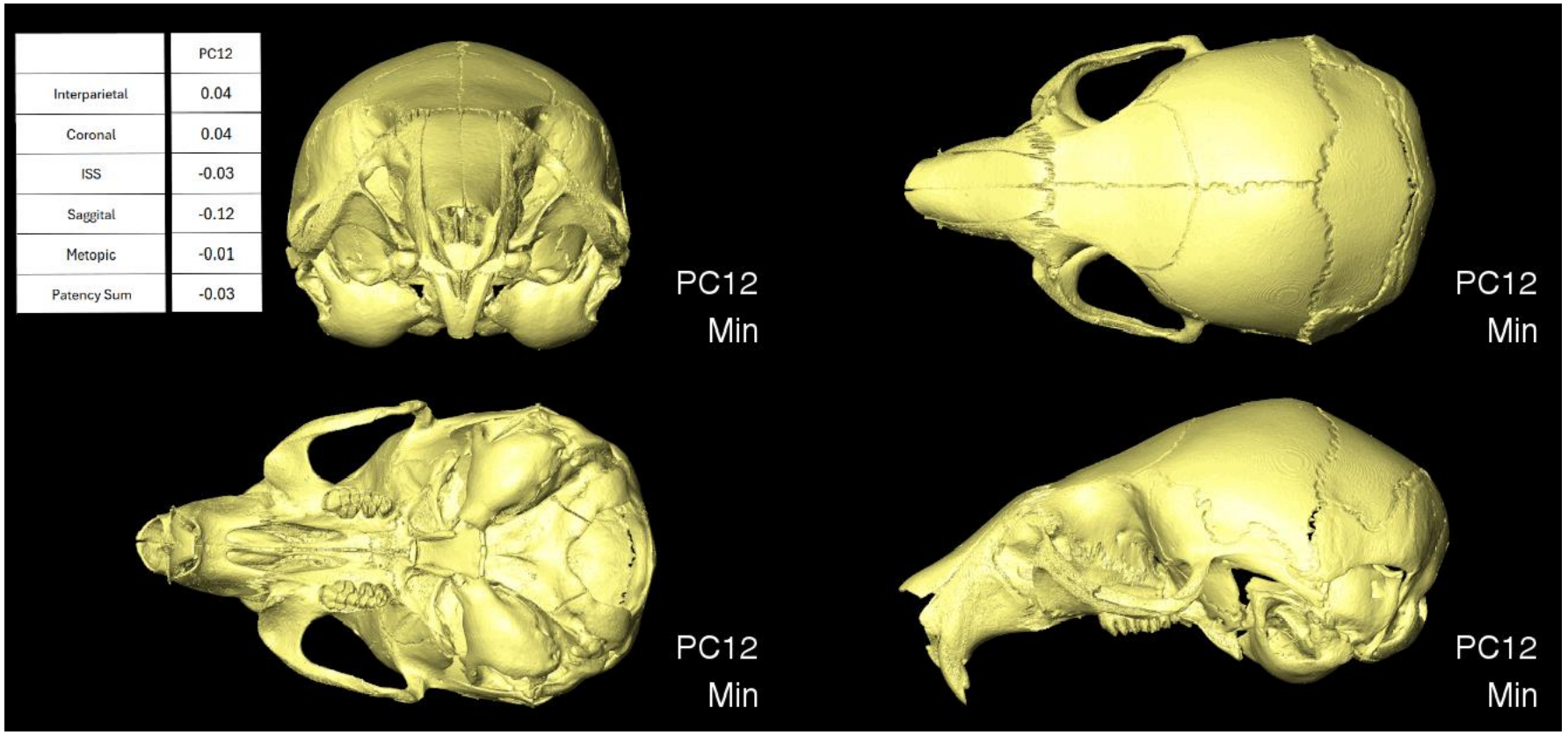
PC12
Interparietal 0.04
Coronal 0.04
ISS -0.03
Saggital -0.12
Metopic -0.01
Patency Sum -0.03
PC12 Min
PC12 Min
PC12 Min
PC12 Min

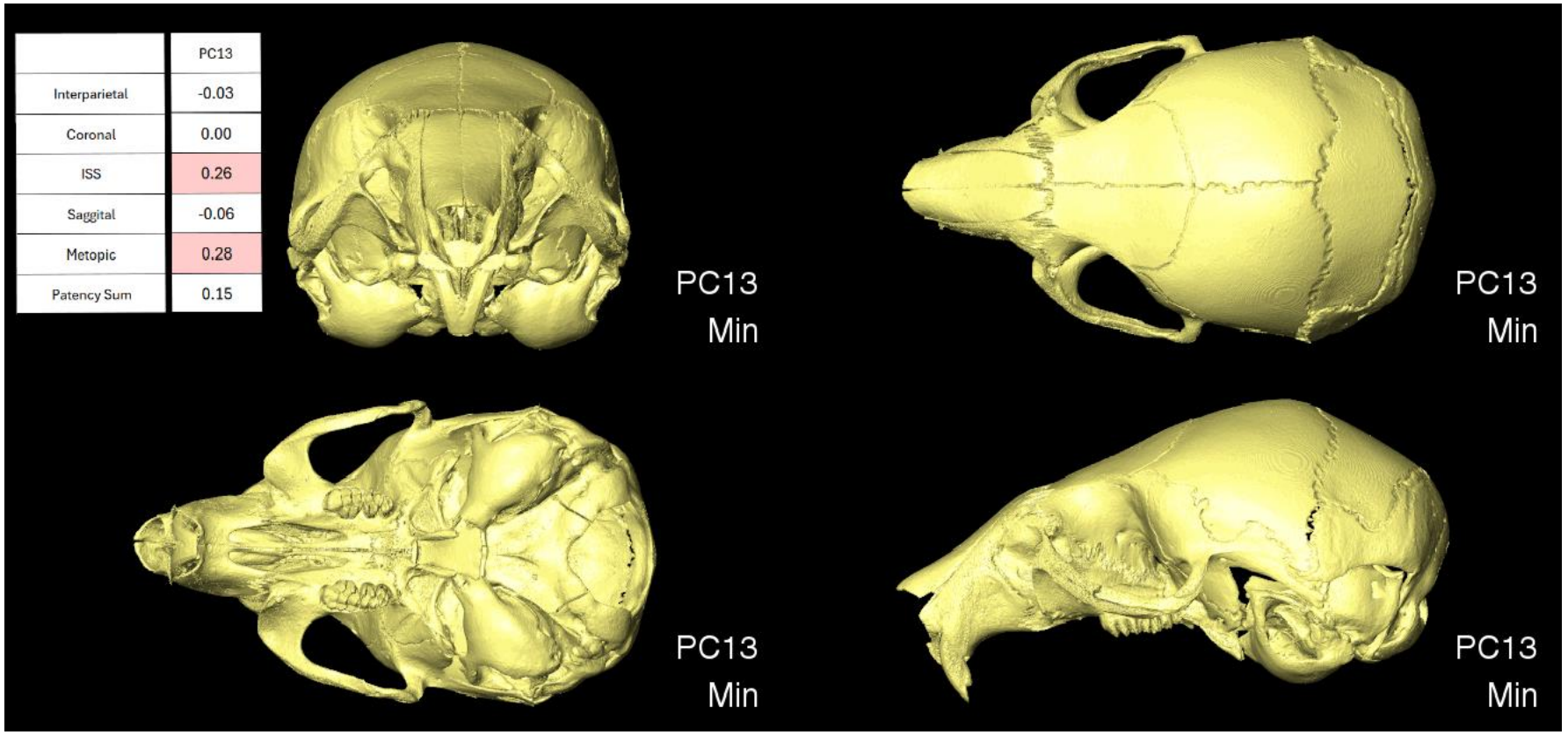
PC13
Interparietal -0.03
Coronal 0.00
ISS 0.26
Saggital -0.06
Metopic 0.28
Patency Sum 0.15
PC13
Min
PC13
Min
PC13
Min
PC13
Min

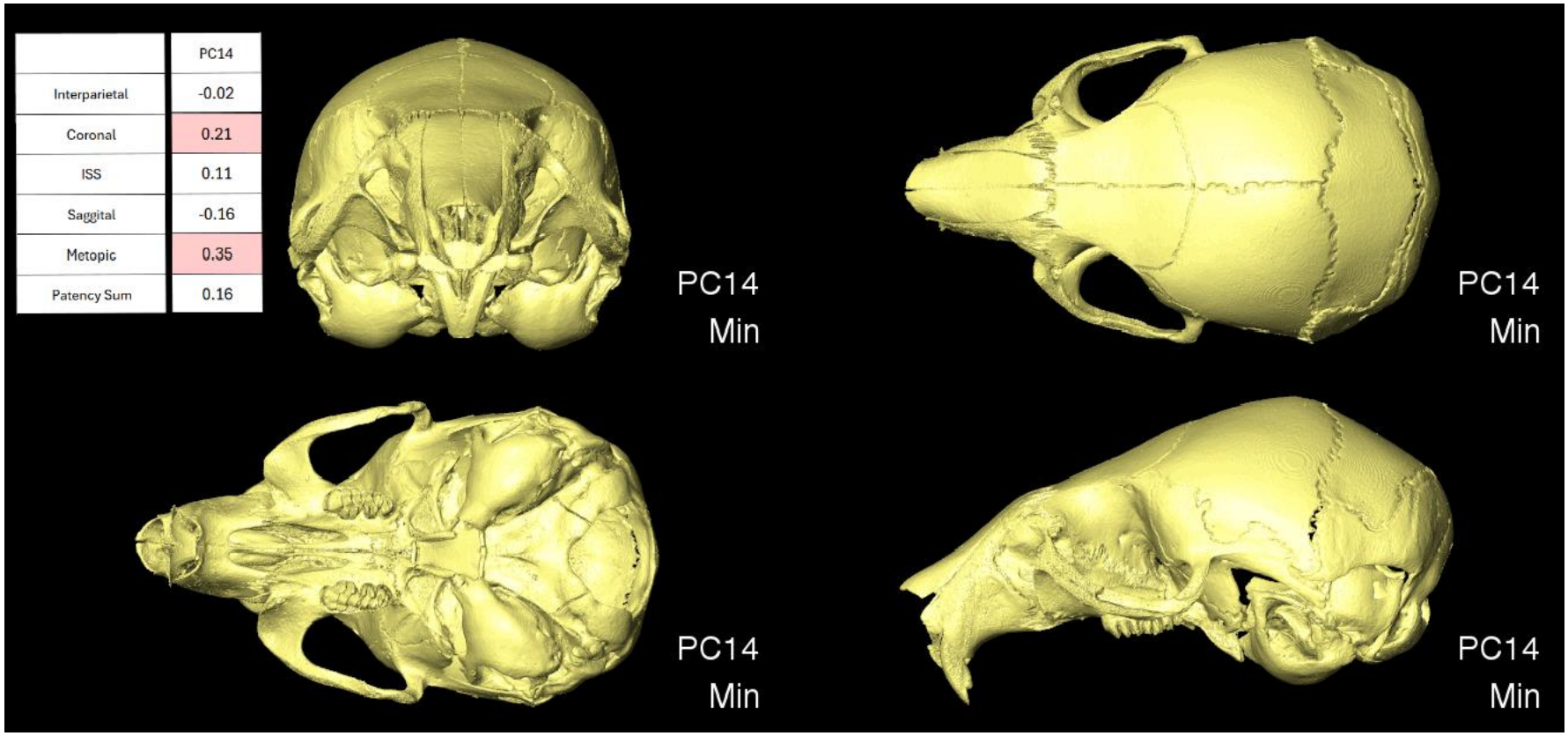

Figure A3.1. Animated morphs of the shapes from the min to the max PC shapes for the first 14 PCs (>95% of the shape variation) for P21 MT morphed from a WT skull, with corresponding correlation values from the correlation matrix.

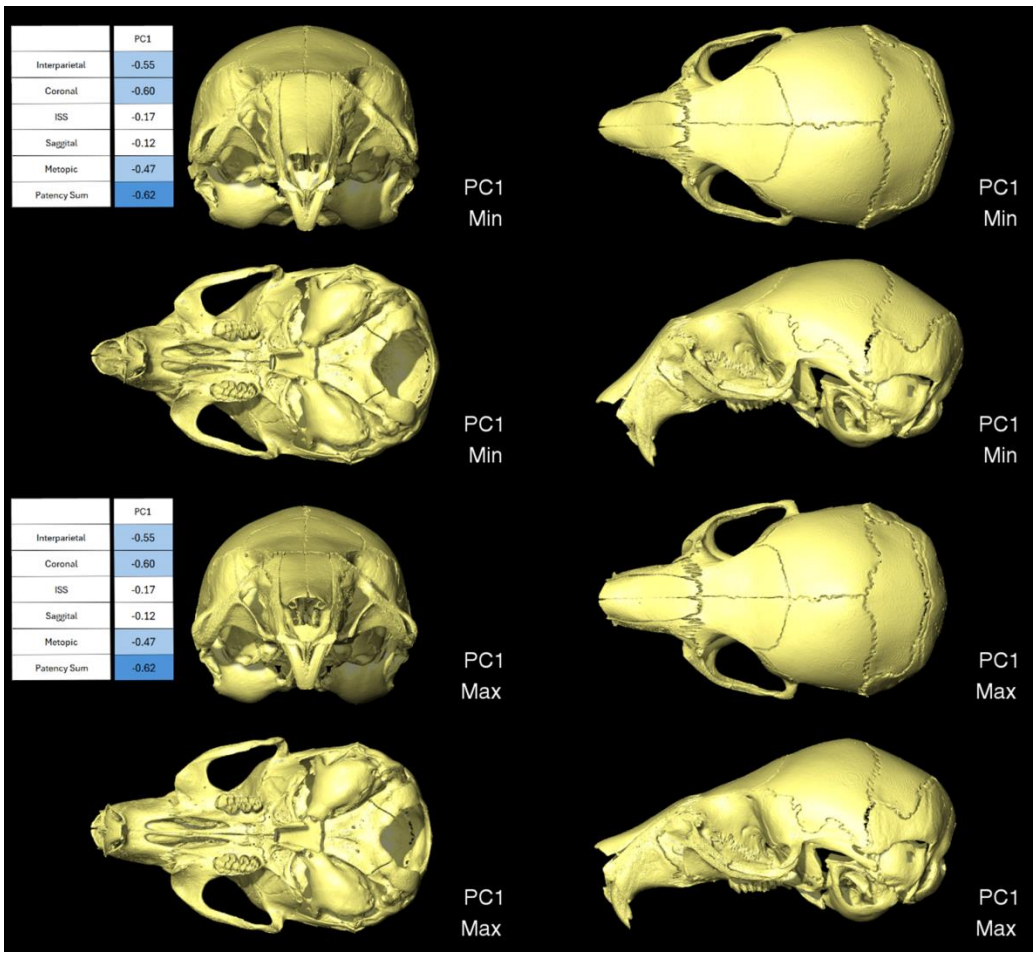
PC1
Interparietal -0.55
Coronal -0.60
ISS -0.17
Saggital -0.12
Metopic -0.47
Patency Sum -0.62
PC1 Min
PC1 Min
PC1 Min
PC1 Min
PC1
Interparietal -0.55
Coronal -0.60
ISS -0.17
Saggital -0.12
Metopic -0.47
Patency Sum -0.62
PC1 Max
PC1 Max
PC1 Max
PC1 Max

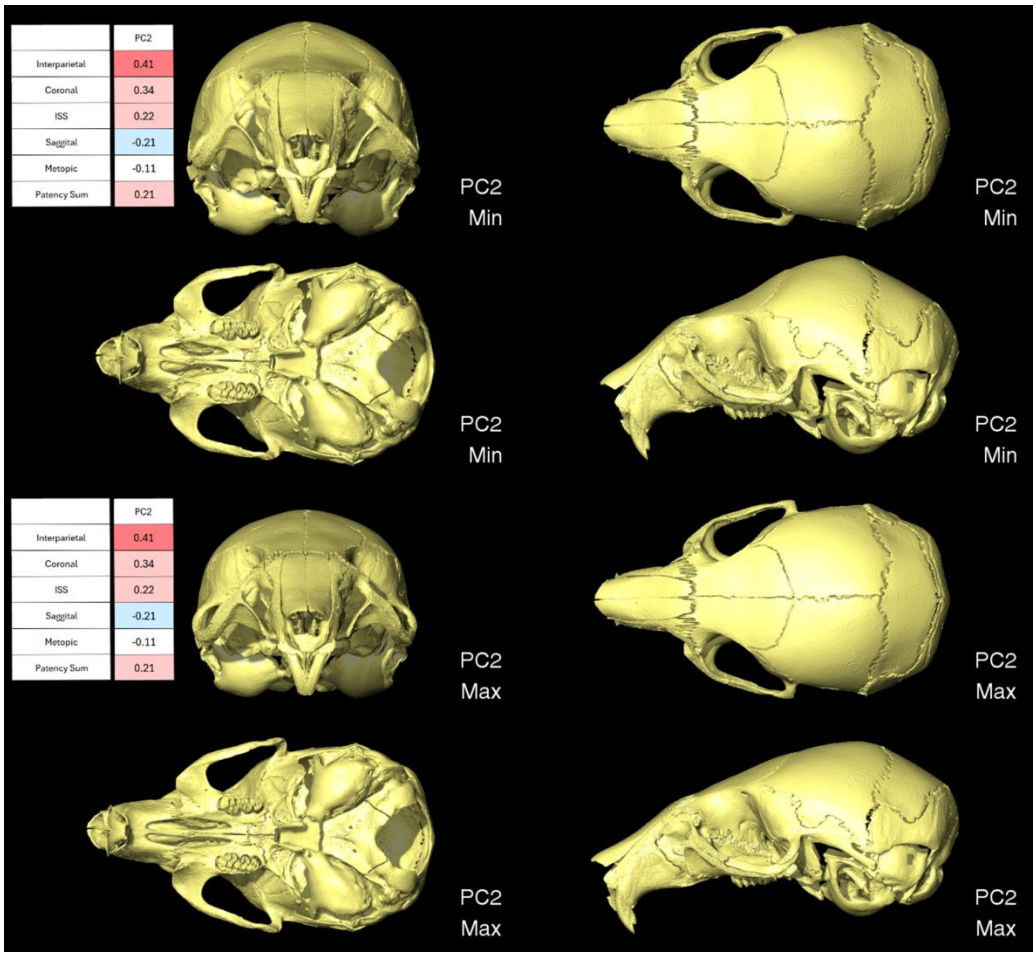
PC2
Interparietal 0.41
Coronal 0.34
ISS 0.22
Saggital -0.21
Metopic -0.11
Patency Sum 0.21
PC2 Min
PC2 Min
PC2 Min
PC2 Min
PC2
Interparietal 0.41
Coronal 0.34
ISS 0.22
Saggital -0.21
Metopic -0.11
Patency Sum 0.21
PC2 Max
PC2 Max
PC2 Max
PC2 Max

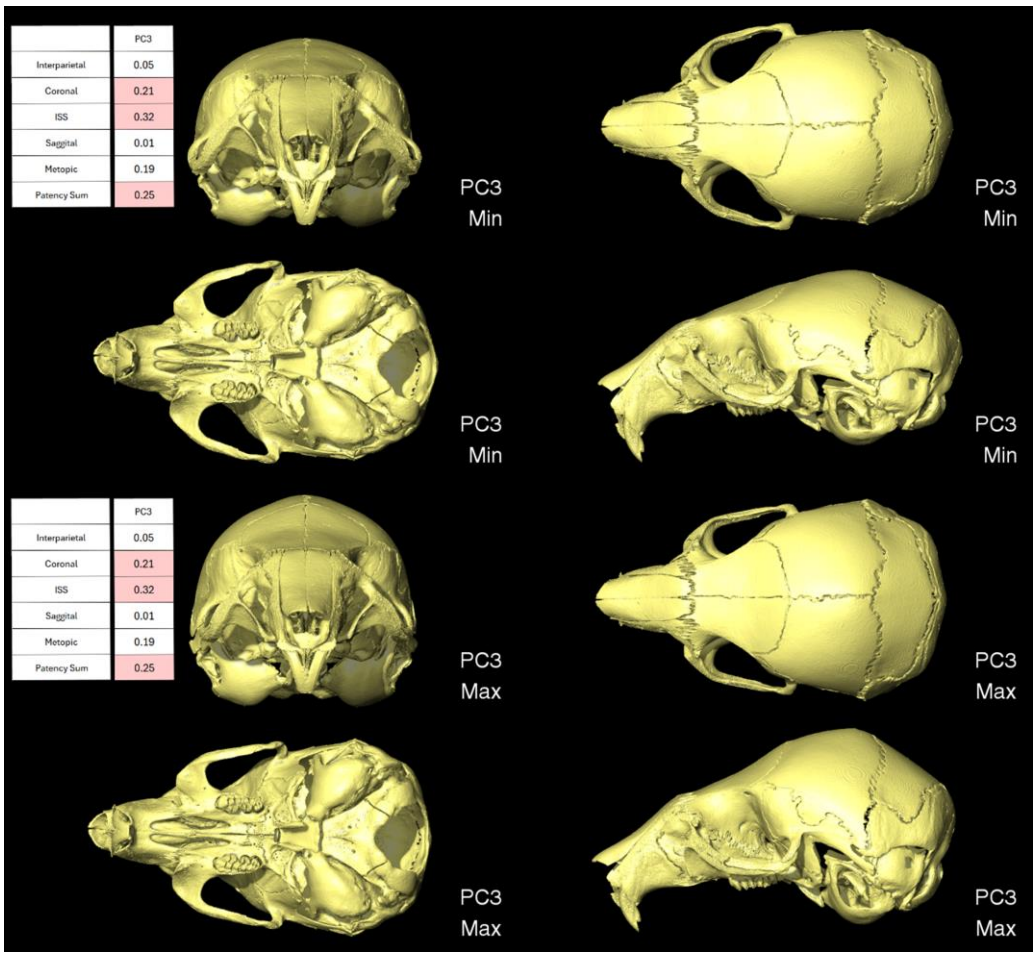
PC3
Interparietal 0.05
Coronal 0.21
ISS 0.32
Sagittal 0.01
Metopic 0.19
Patency Sum 0.25
PC3 Min
PC3 Min
PC3 Min
PC3 Min
PC3
Interparietal 0.05
Coronal 0.21
ISS 0.32
Sagittal 0.01
Metopic 0.19
Patency Sum 0.25
PC3 Max
PC3 Max
PC3 Max
PC3 Max

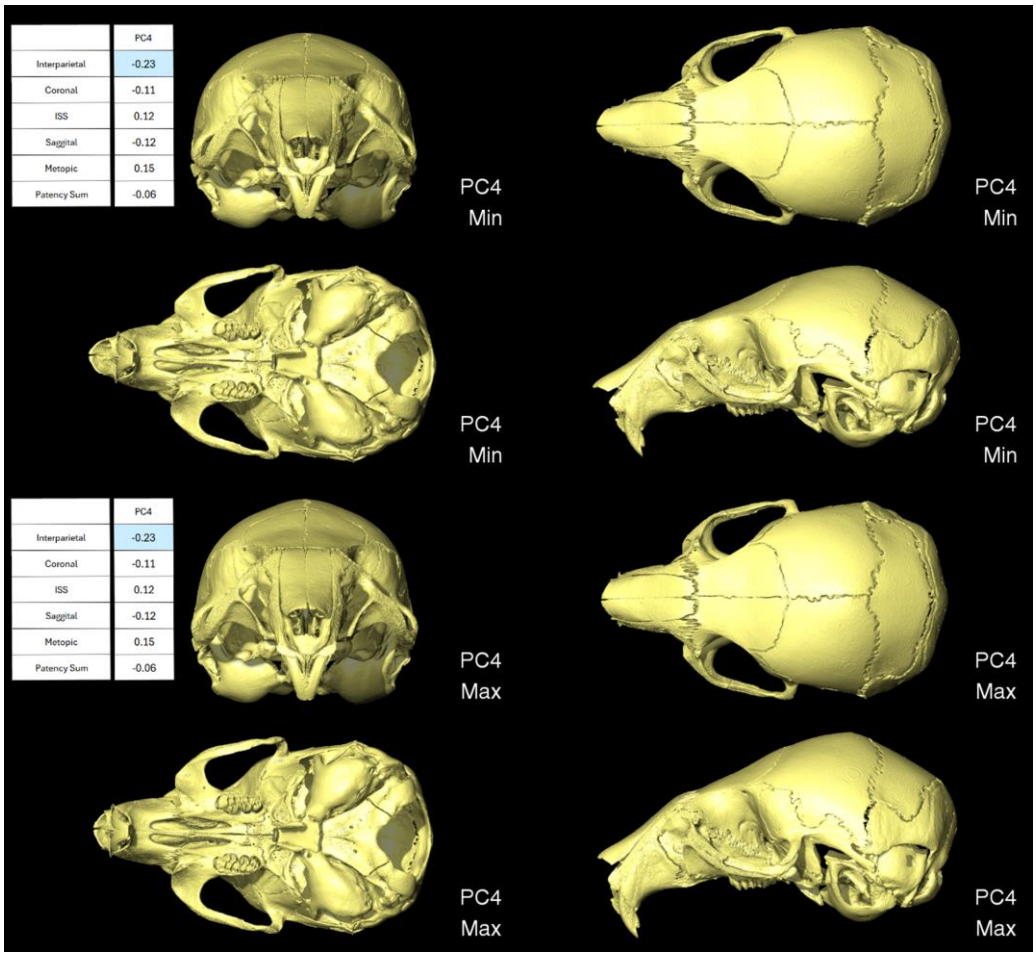
PC4
Interparietal -0.23
Coronal -0.11
ISS 0.12
Sagittal -0.12
Metopic 0.15
Patency Sum -0.06
PC4 Min
PC4 Min
PC4 Min
PC4 Min
PC4
Interparietal -0.23
Coronal -0.11
ISS 0.12
Sagittal -0.12
Metopic 0.15
Patency Sum -0.06
PC4 Max
PC4 Max
PC4 Max
PC4 Max

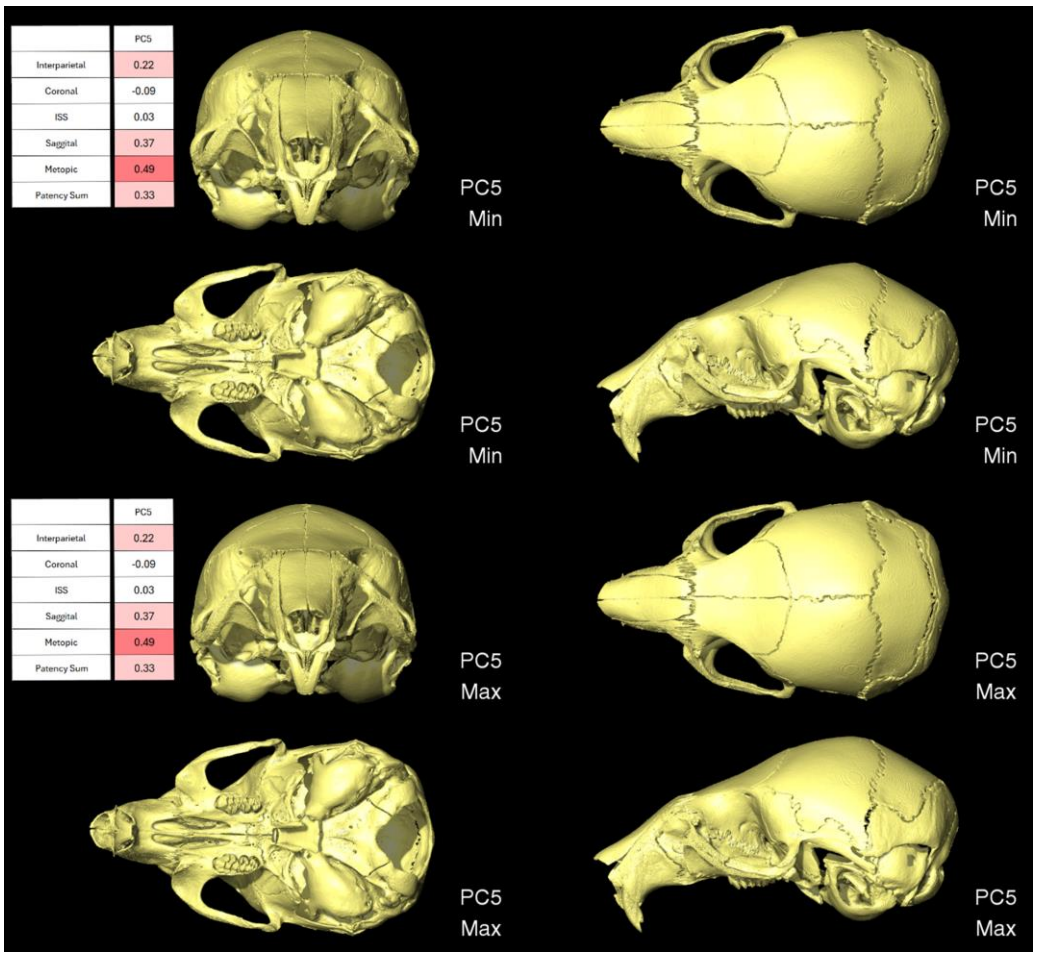
PC5
Interparietal 0.22
Coronal -0.09
ISS 0.03
Sagittal 0.37
Metopic 0.49
Patency Sum 0.33
PC5 Min
PC5 Min
PC5 Min
PC5 Min
PC5
Interparietal 0.22
Coronal -0.09
ISS 0.03
Sagittal 0.37
Metopic 0.49
Patency Sum 0.33
PC5 Max
PC5 Max
PC5 Max
PC5 Max

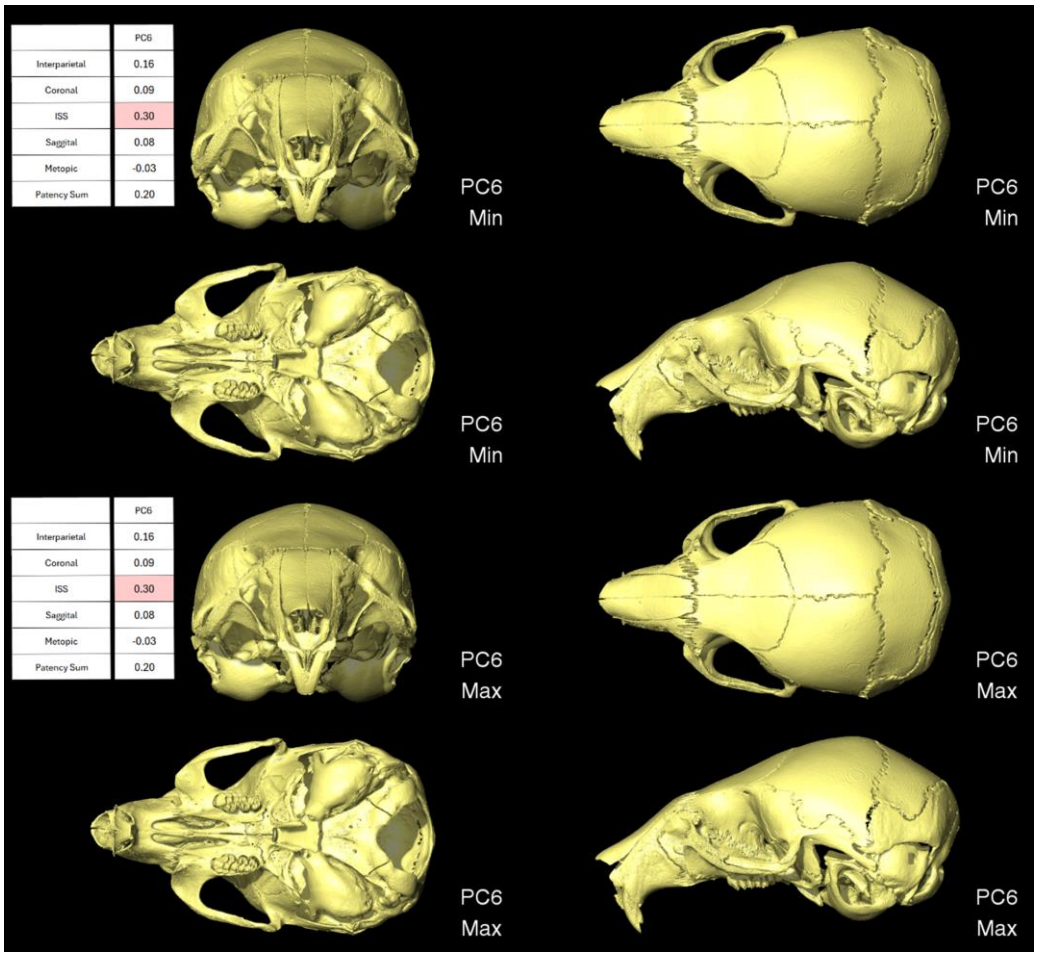
PC6
Interparietal 0.16
Coronal 0.09
ISS 0.30
Sagittal 0.08
Metopic -0.03
Patency Sum 0.20
PC6 Min
PC6 Min
PC6 Min
PC6 Min
PC6
Interparietal 0.16
Coronal 0.09
ISS 0.30
Sagittal 0.08
Metopic -0.03
Patency Sum 0.20
PC6 Max
PC6 Max
PC6 Max
PC6 Max

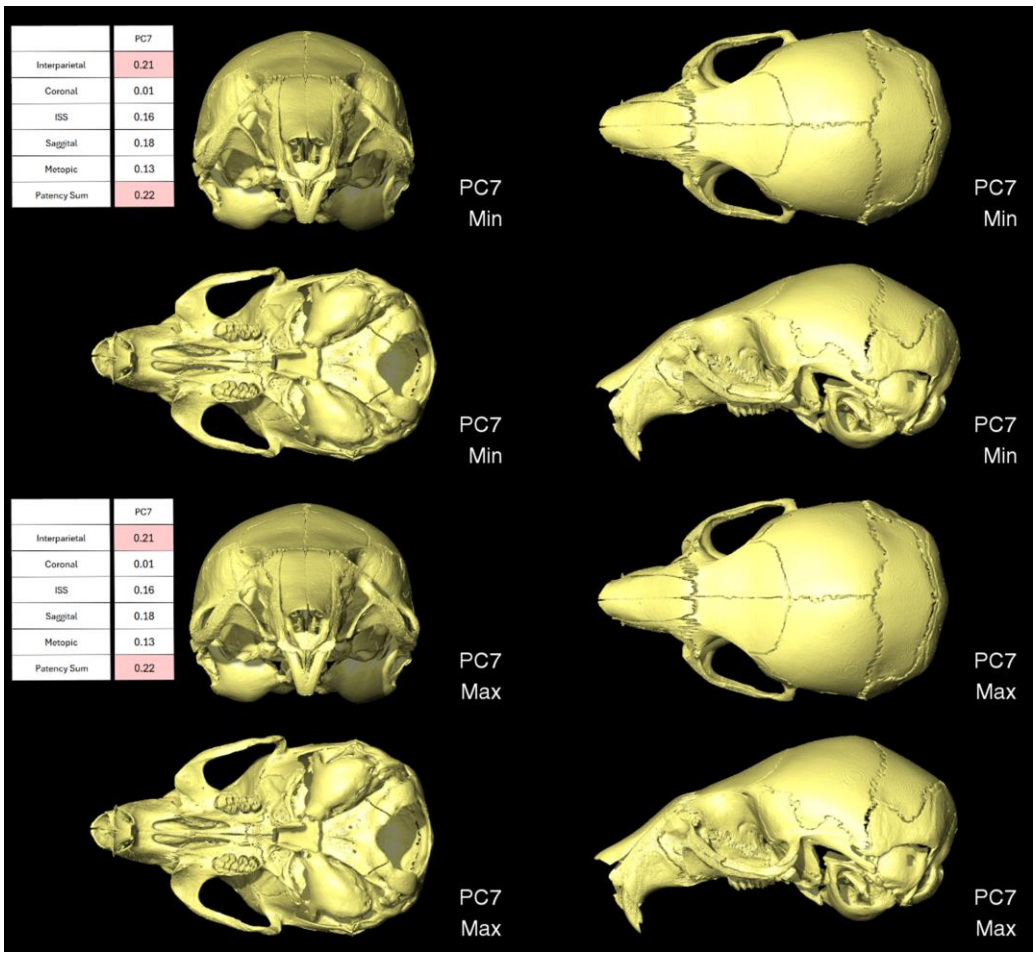
PC7
Interparietal 0.21
Coronal 0.01
ISS 0.16
Sagittal 0.18
Metopic 0.13
Patency Sum 0.22
PC7 Min
PC7 Min
PC7 Min
PC7 Min
PC7
Interparietal 0.21
Coronal 0.01
ISS 0.16
Sagittal 0.18
Metopic 0.13
Patency Sum 0.22
PC7 Max
PC7 Max
PC7 Max
PC7 Max

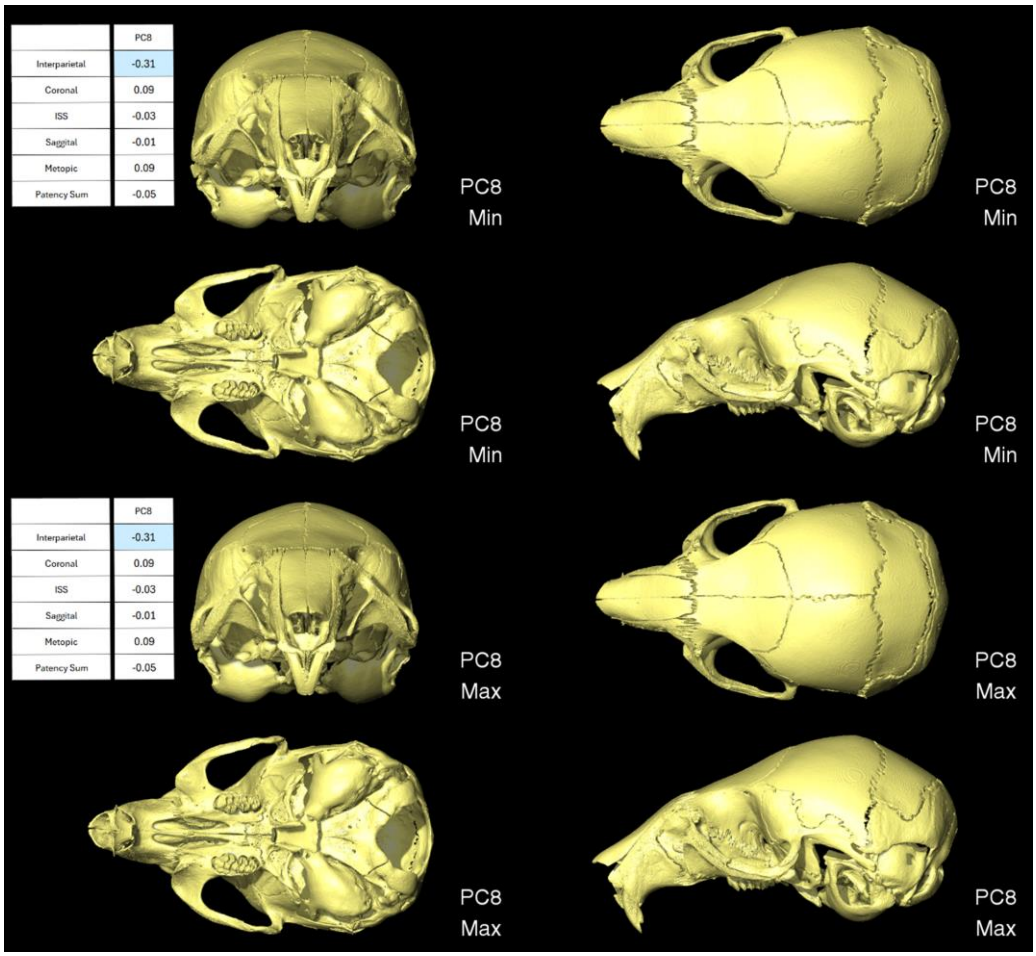
PC8
Interparietal -0.31
Coronal 0.09
ISS -0.03
Sagittal -0.01
Metopic 0.09
Patency Sum -0.05
PC8 Min
PC8 Min
PC8 Min
PC8 Min
PC8
Interparietal -0.31
Coronal 0.09
ISS -0.03
Sagittal -0.01
Metopic 0.09
Patency Sum -0.05
PC8 Max
PC8 Max
PC8 Max
PC8 Max

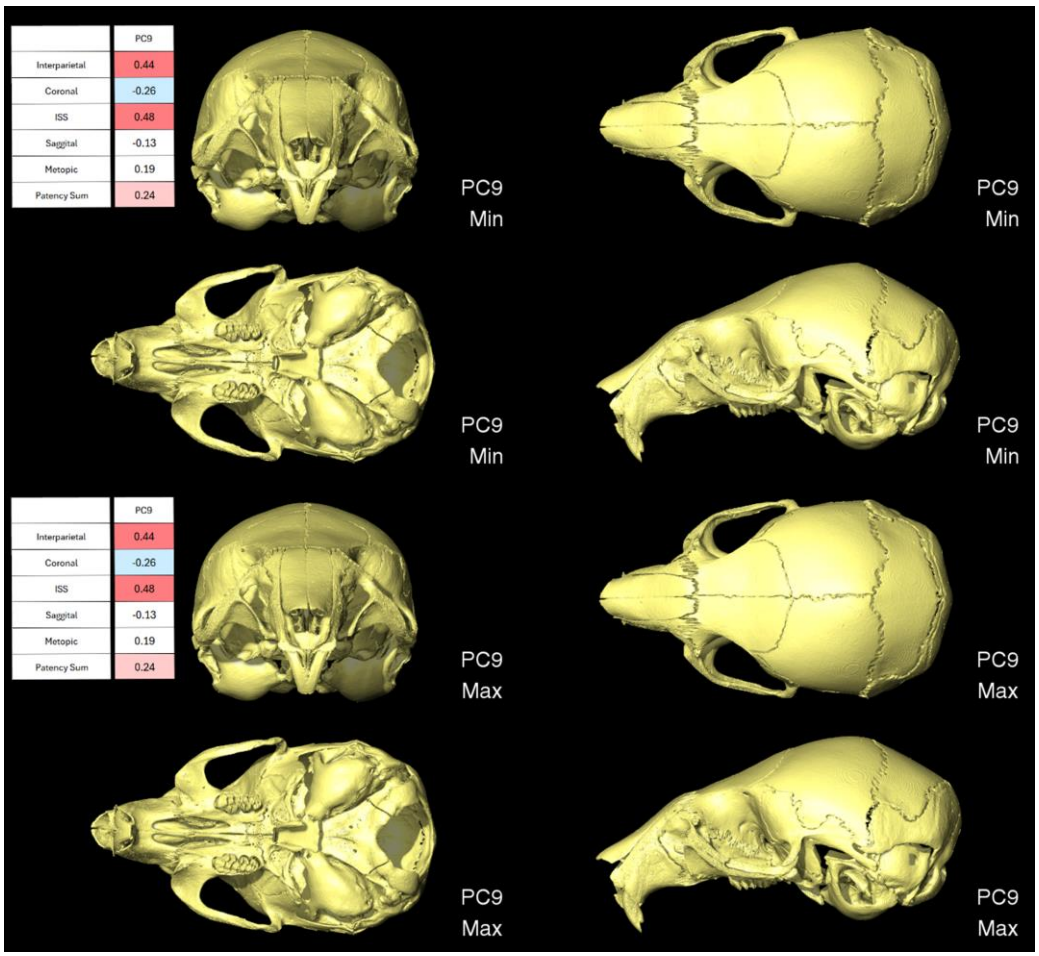
PC9
Interparietal 0.44
Coronal -0.26
ISS 0.48
Sagittal -0.13
Metopic 0.19
Patency Sum 0.24
PC9 Min
PC9 Min
PC9 Min
PC9 Min
PC9
Interparietal 0.44
Coronal -0.26
ISS 0.48
Sagittal -0.13
Metopic 0.19
Patency Sum 0.24
PC9 Max
PC9 Max
PC9 Max
PC9 Max

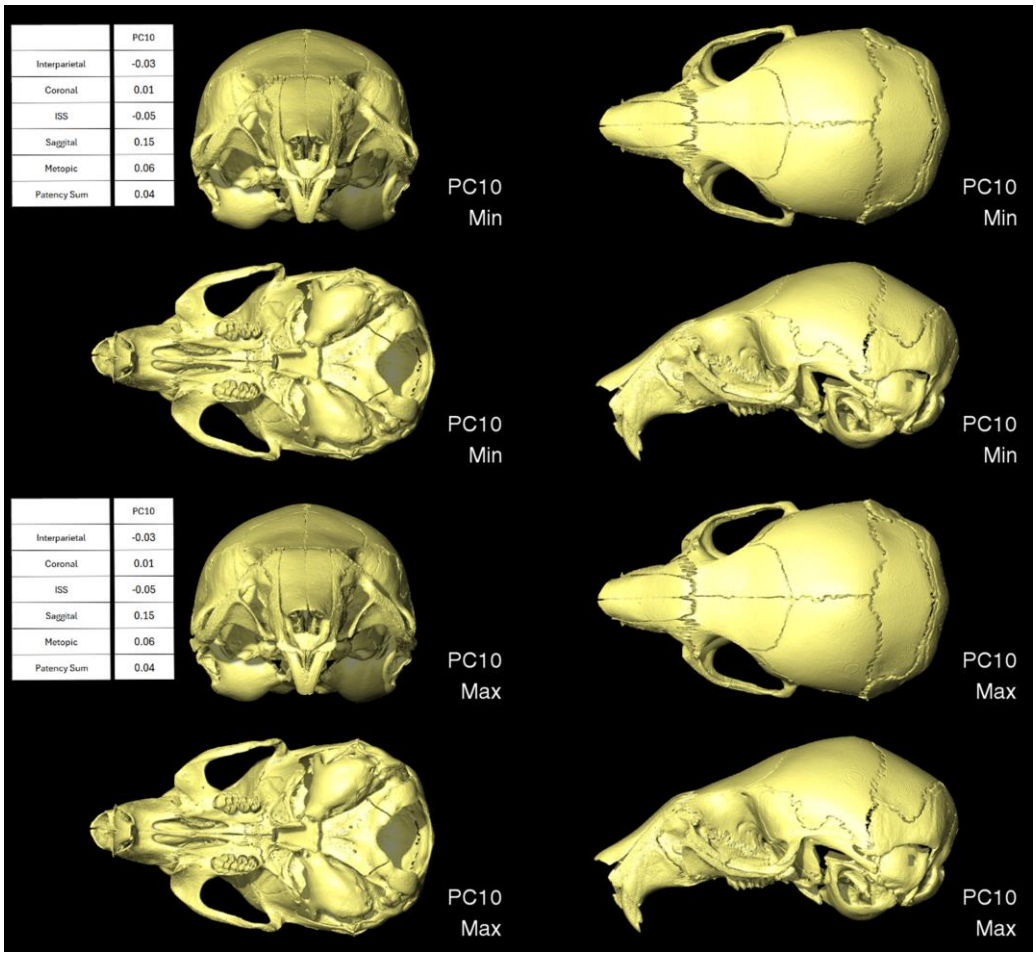
PC10
Interparietal -0.03
Coronal 0.01
ISS -0.05
Sagittal 0.15
Metopic 0.06
Patency Sum 0.04
PC10 Min
PC10 Min
PC10 Min
PC10 Min
PC10
Interparietal -0.03
Coronal 0.01
ISS -0.05
Sagittal 0.15
Metopic 0.06
Patency Sum 0.04
PC10 Max
PC10 Max
PC10 Max
PC10 Max

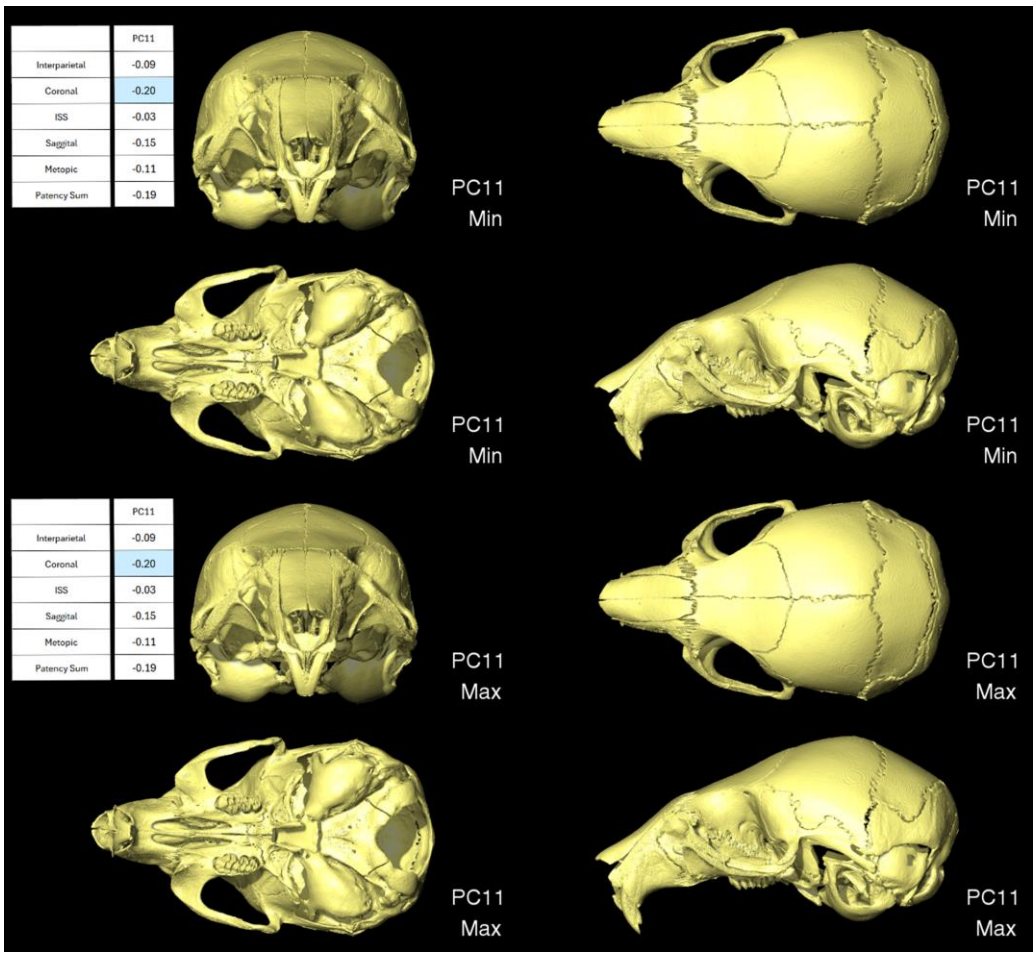
PC11
Interparietal -0.09
Coronal -0.20
ISS -0.03
Sagittal -0.15
Metopic -0.11
Patency Sum -0.19
PC11 Min
PC11 Min
PC11 Min
PC11 Min
PC11
Interparietal -0.09
Coronal -0.20
ISS -0.03
Sagittal -0.15
Metopic -0.11
Patency Sum -0.19
PC11 Max
PC11 Max
PC11 Max
PC11 Max

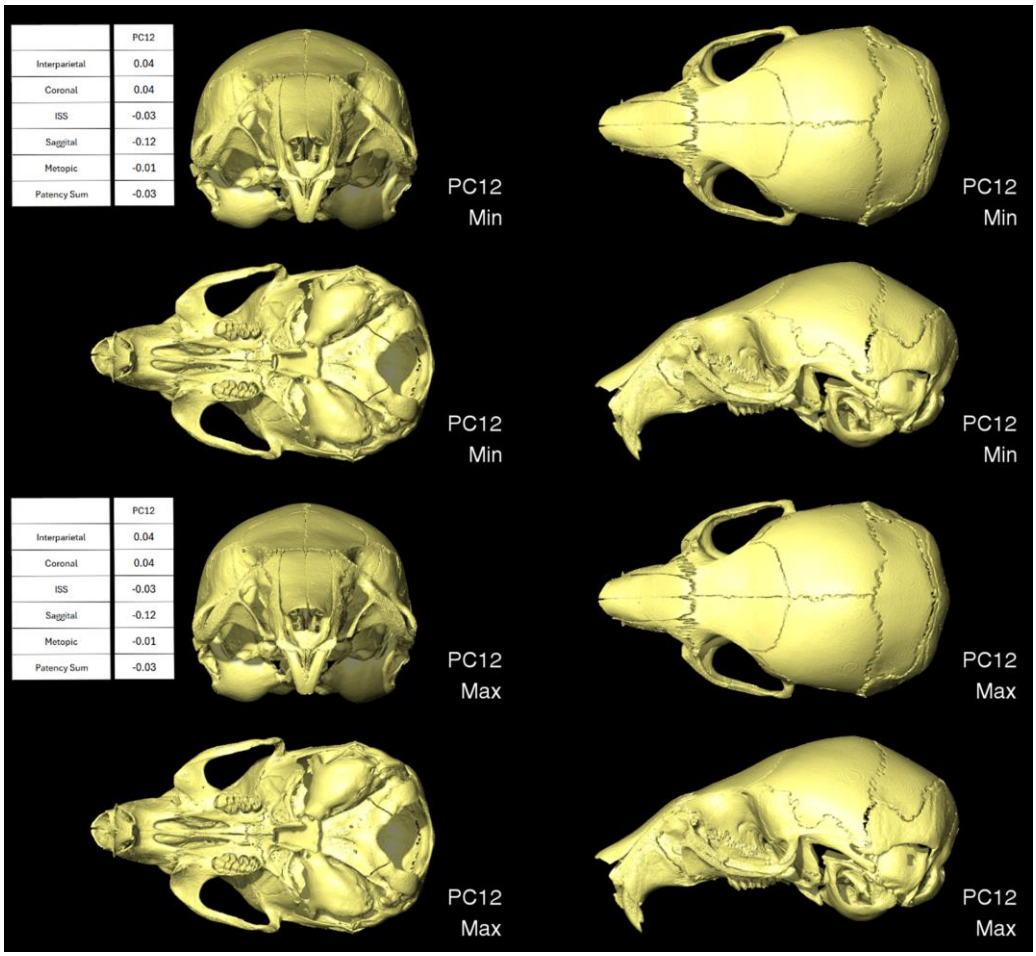
PC12
Interparietal 0.04
Coronal 0.04
ISS -0.03
Sagittal -0.12
Metopic -0.01
Patency Sum -0.03
PC12 Min
PC12 Min
PC12 Min
PC12 Min
PC12
Interparietal 0.04
Coronal 0.04
ISS -0.03
Sagittal -0.12
Metopic -0.01
Patency Sum -0.03
PC12 Max
PC12 Max
PC12 Max
PC12 Max

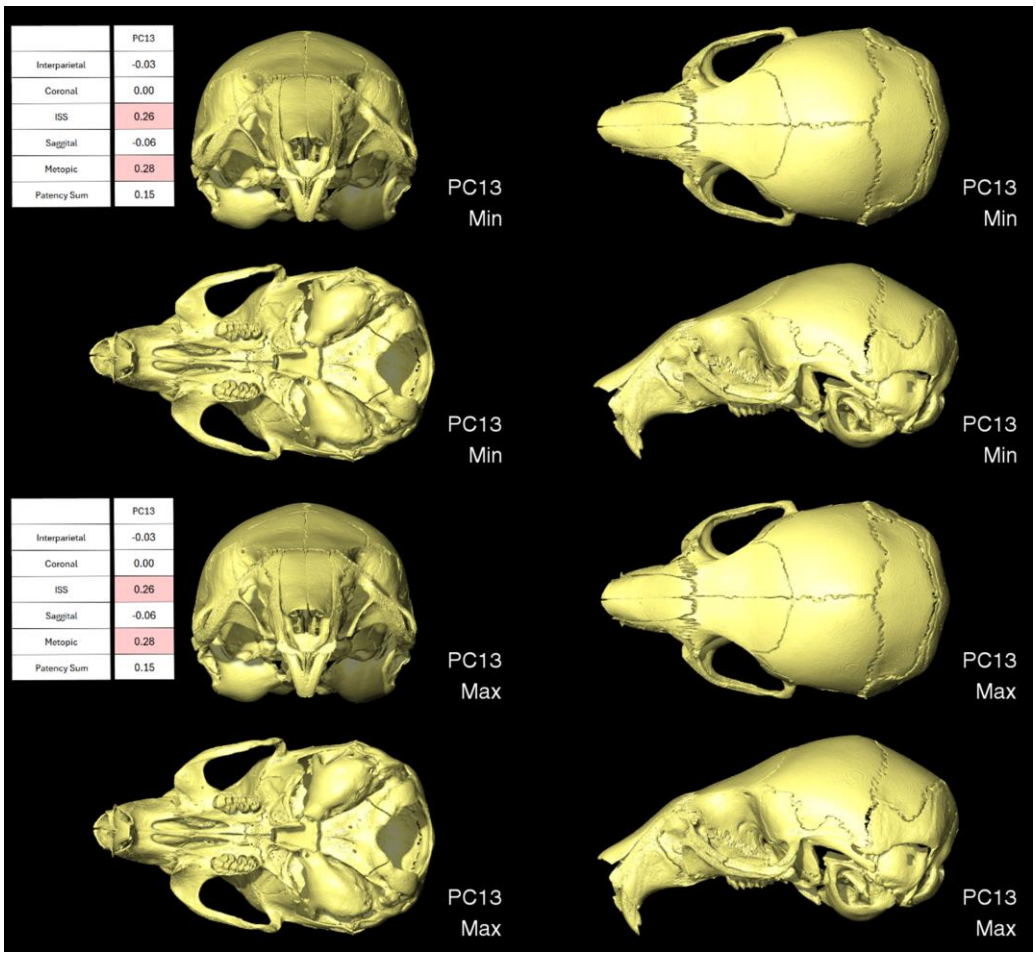
PC13
Interparietal -0.03
Coronal 0.00
ISS 0.26
Sagittal -0.06
Metopic 0.28
Patency Sum 0.15
PC13 Min
PC13 Min
PC13 Min
PC13 Min
PC13
Interparietal -0.03
Coronal 0.00
ISS 0.26
Sagittal -0.06
Metopic 0.28
Patency Sum 0.15
PC13 Max
PC13 Max
PC13 Max
PC13 Max

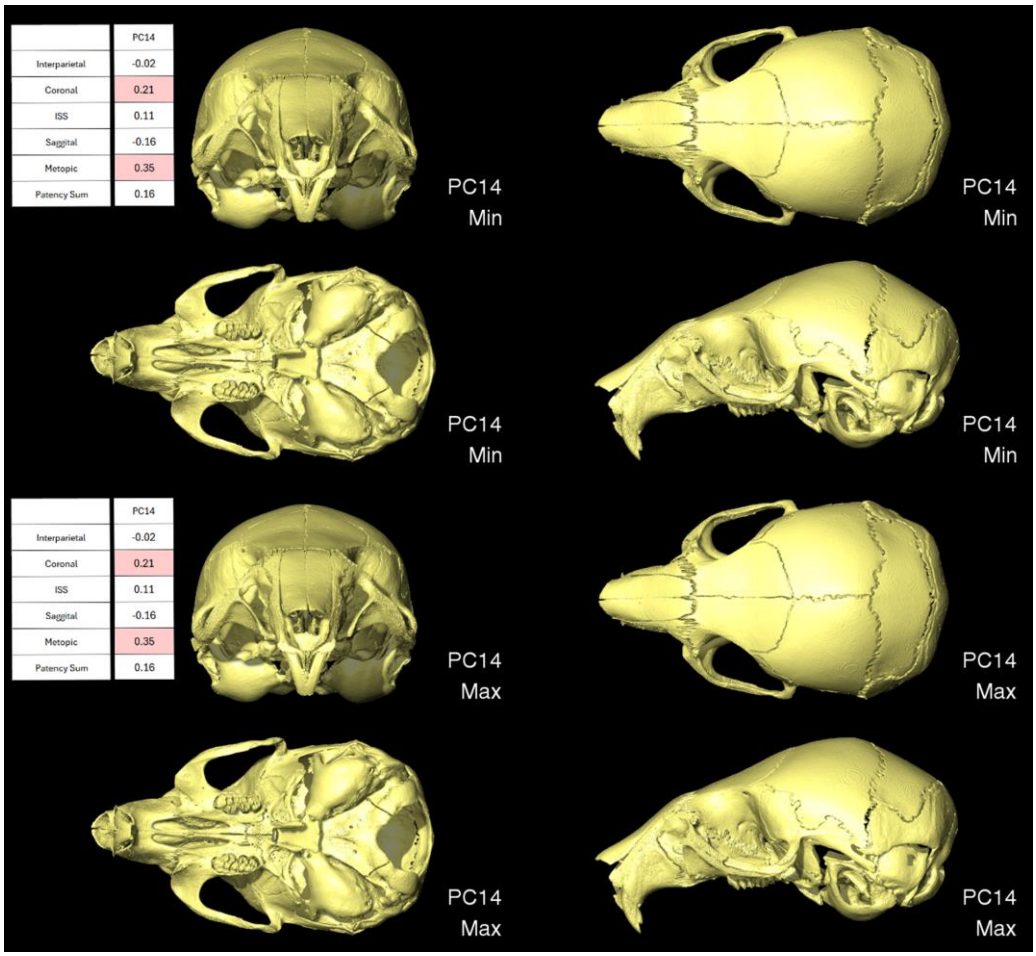
PC14
Interparietal -0.02
Coronal 0.21
ISS 0.11
Sagittal -0.16
Metopic 0.35
Patency Sum 0.16
PC14 Min
PC14 Min
PC14 Min
PC14 Min
PC14
Interparietal -0.02
Coronal 0.21
ISS 0.11
Sagittal -0.16
Metopic 0.35
Patency Sum 0.16
PC14 Max
PC14 Max
PC14 Max
PC14 Max

Figure A3.2. Shapes of the min and max PC shapes for the first 14 PCs (>95% of the shape variation) for P21 MT morphed from a WT skull, with corresponding correlation values from the correlation matrix.

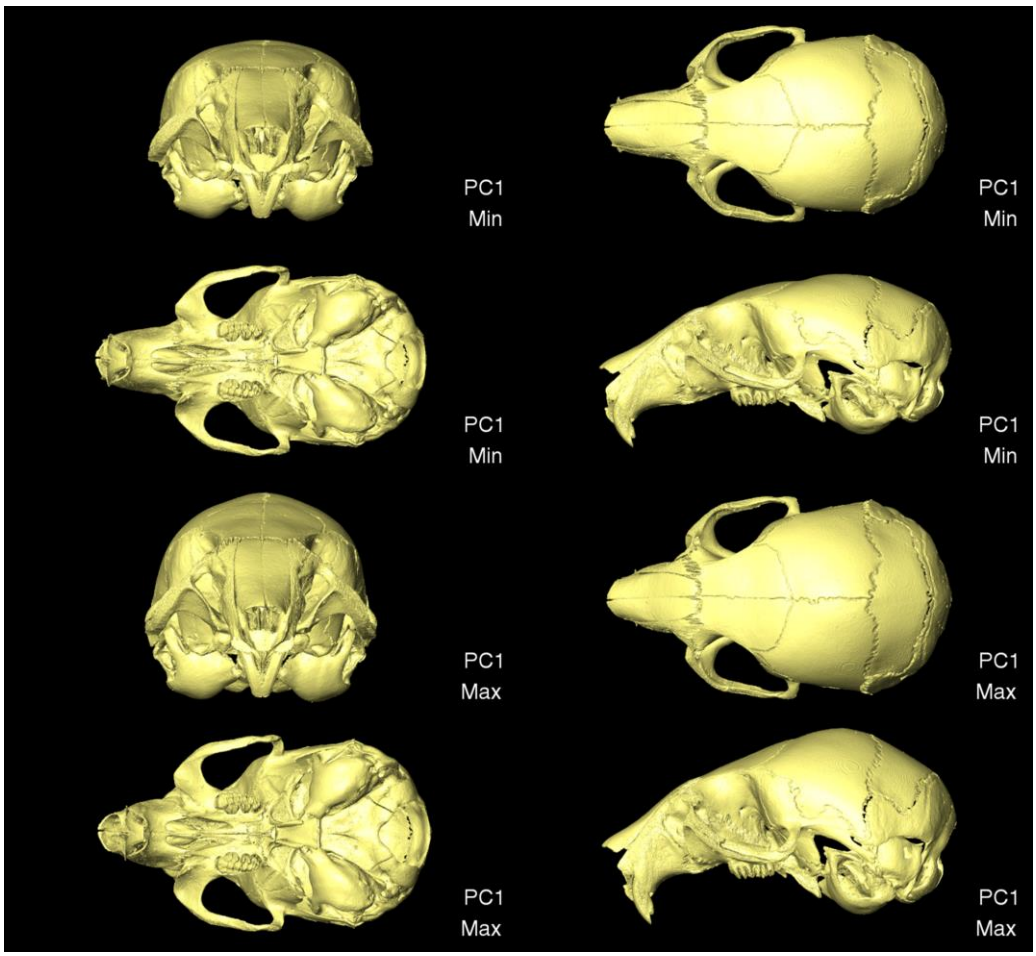
PC1
Min
PC1
Min
PC1
Min
PC1
Min
PC1
Max
PC1
Max
PC1
Max
PC1
Max

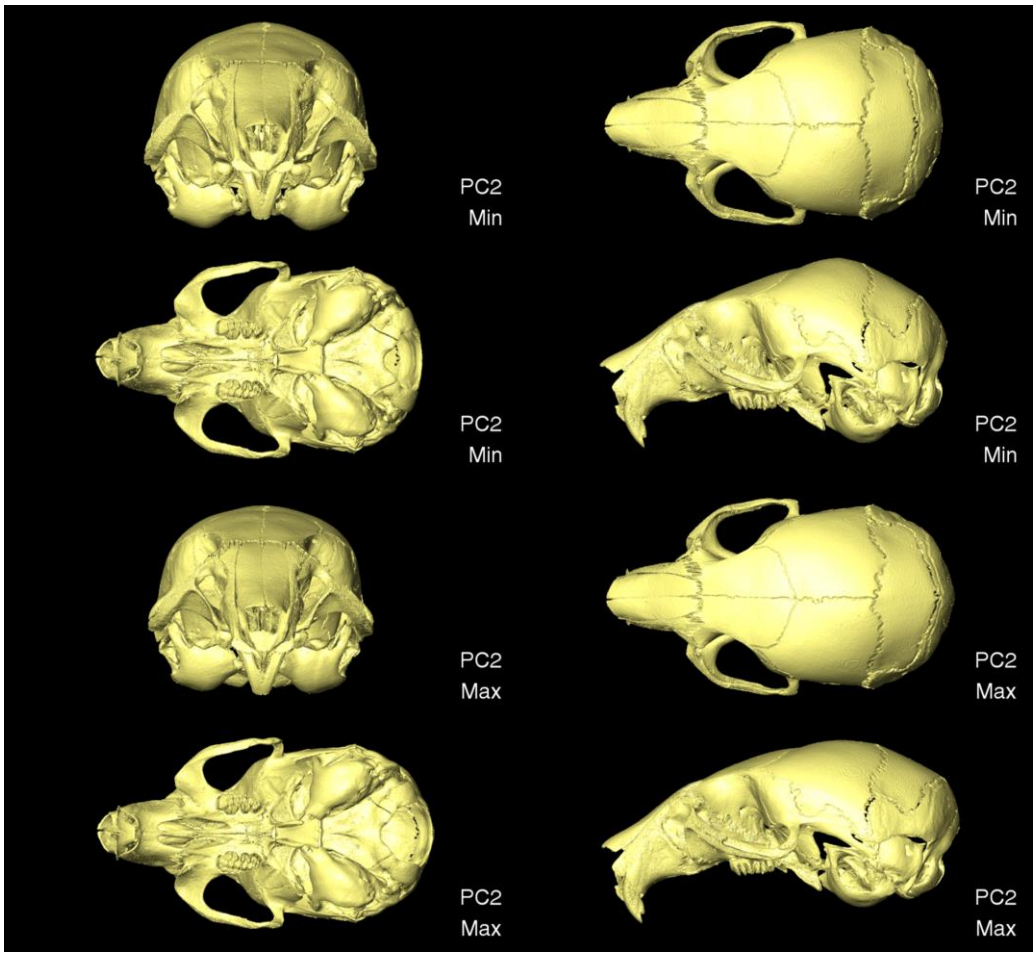
PC2
Min
PC2
Min
PC2
Min
PC2
Min
PC2
Max
PC2
Max
PC2
Max
PC2
Max

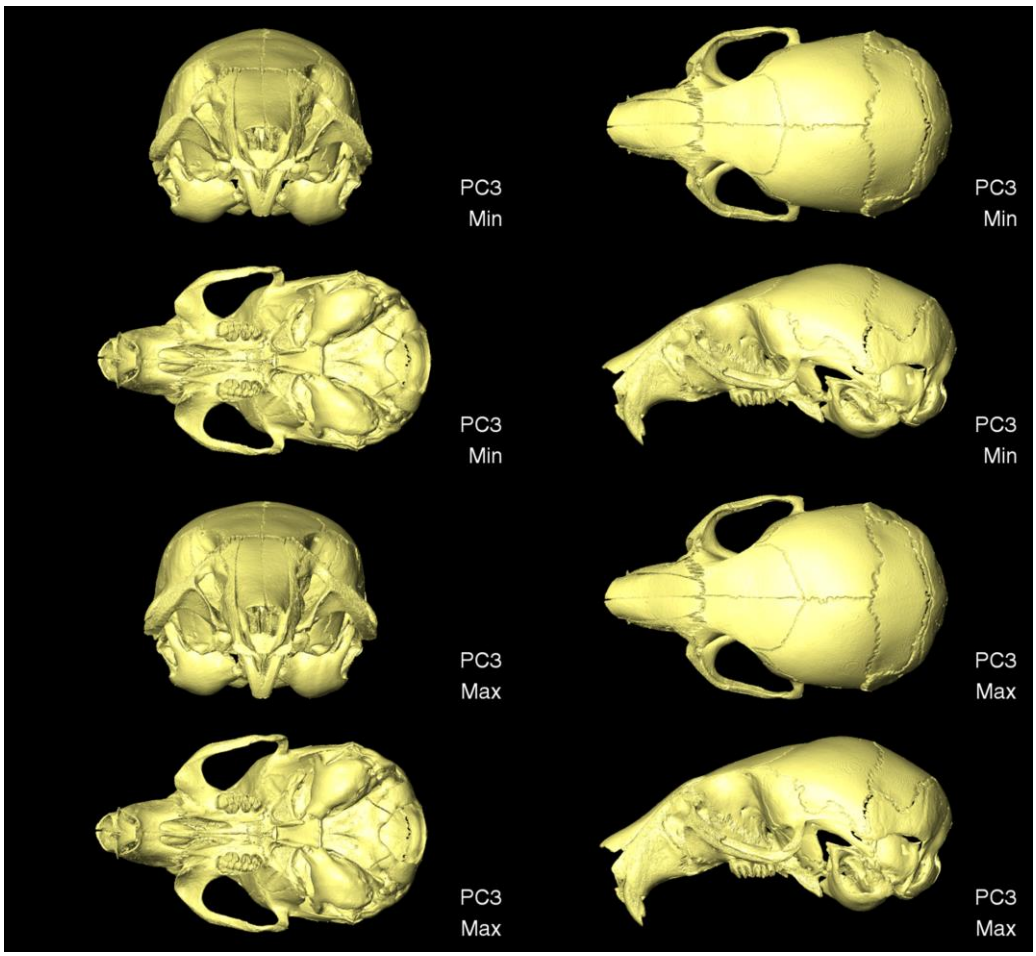
PC3
Min
PC3
Min
PC3
Min
PC3
Min
PC3
Max
PC3
Max
PC3
Max
PC3
Max

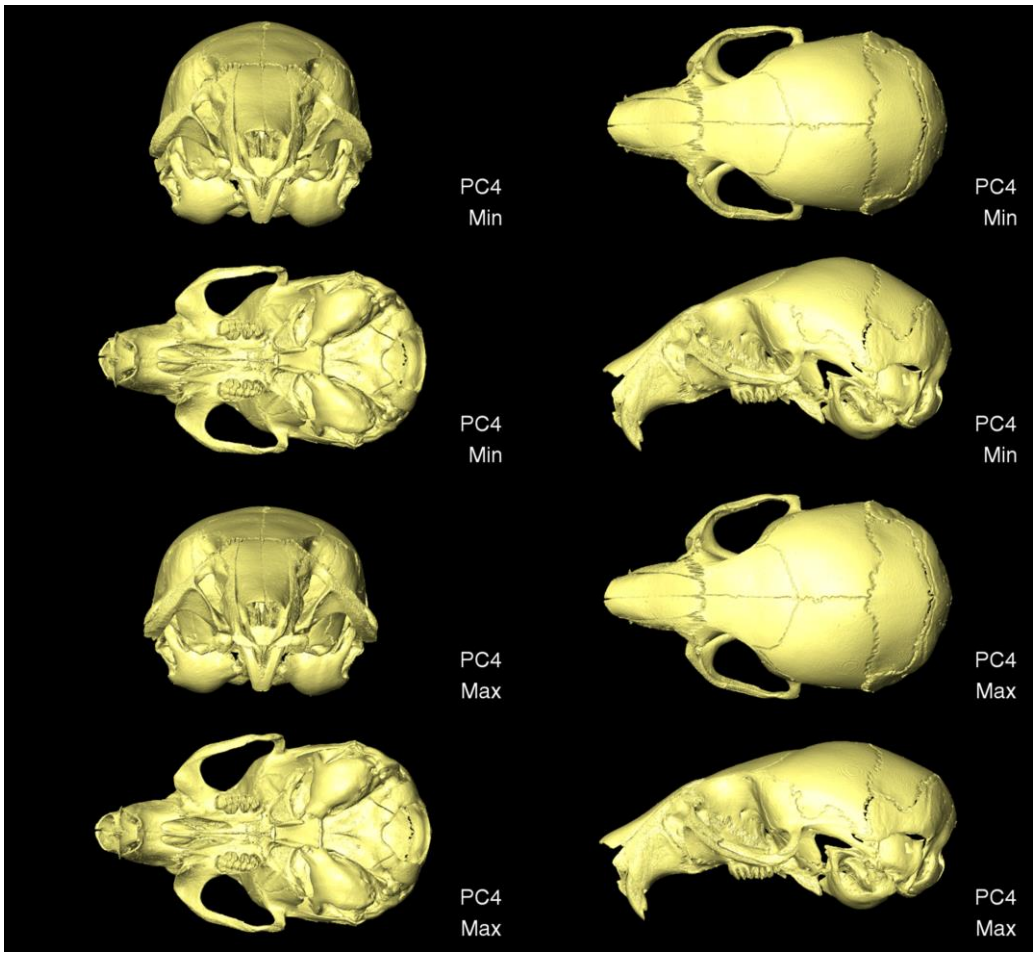
PC4
Min
PC4
Min
PC4
Min
PC4
Min
PC4
Max
PC4
Max
PC4
Max
PC4
Max

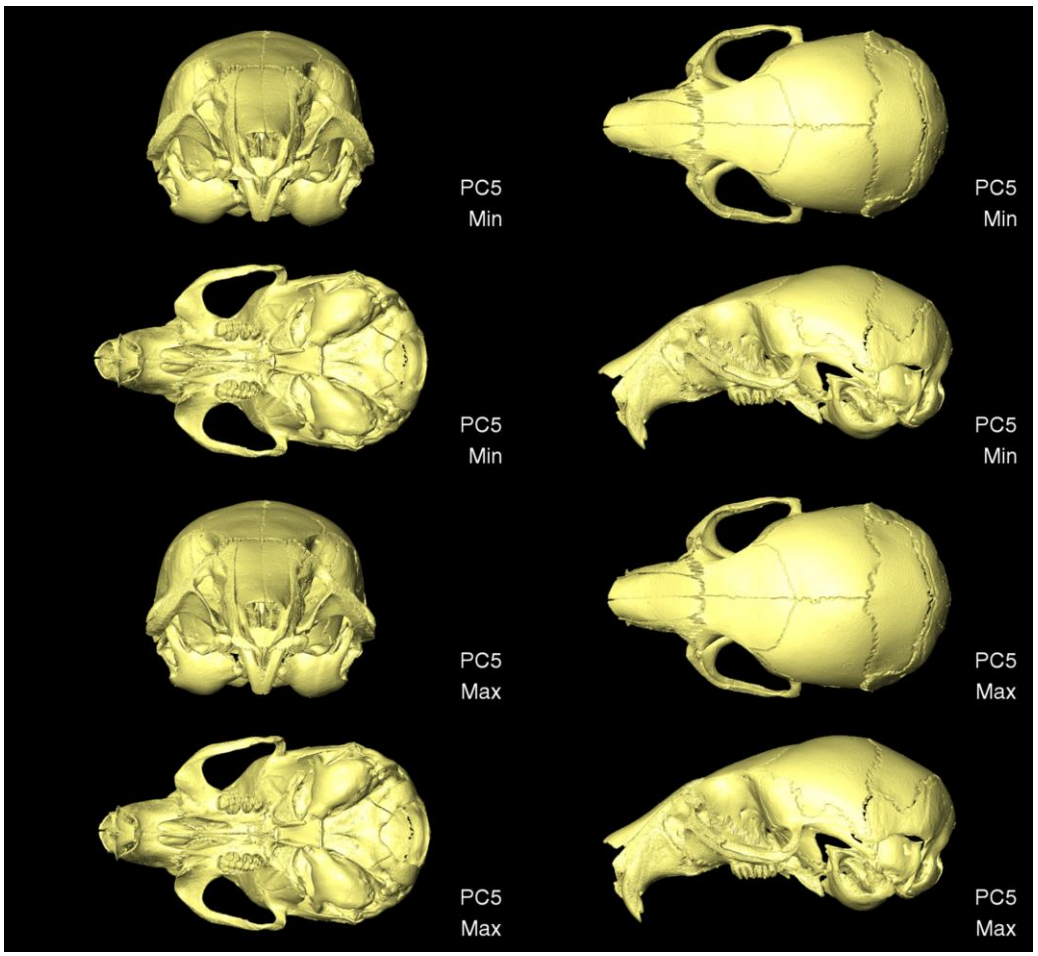
PC5
Min
PC5
Min
PC5
Min
PC5
Min
PC5
Max
PC5
Max
PC5
Max
PC5
Max

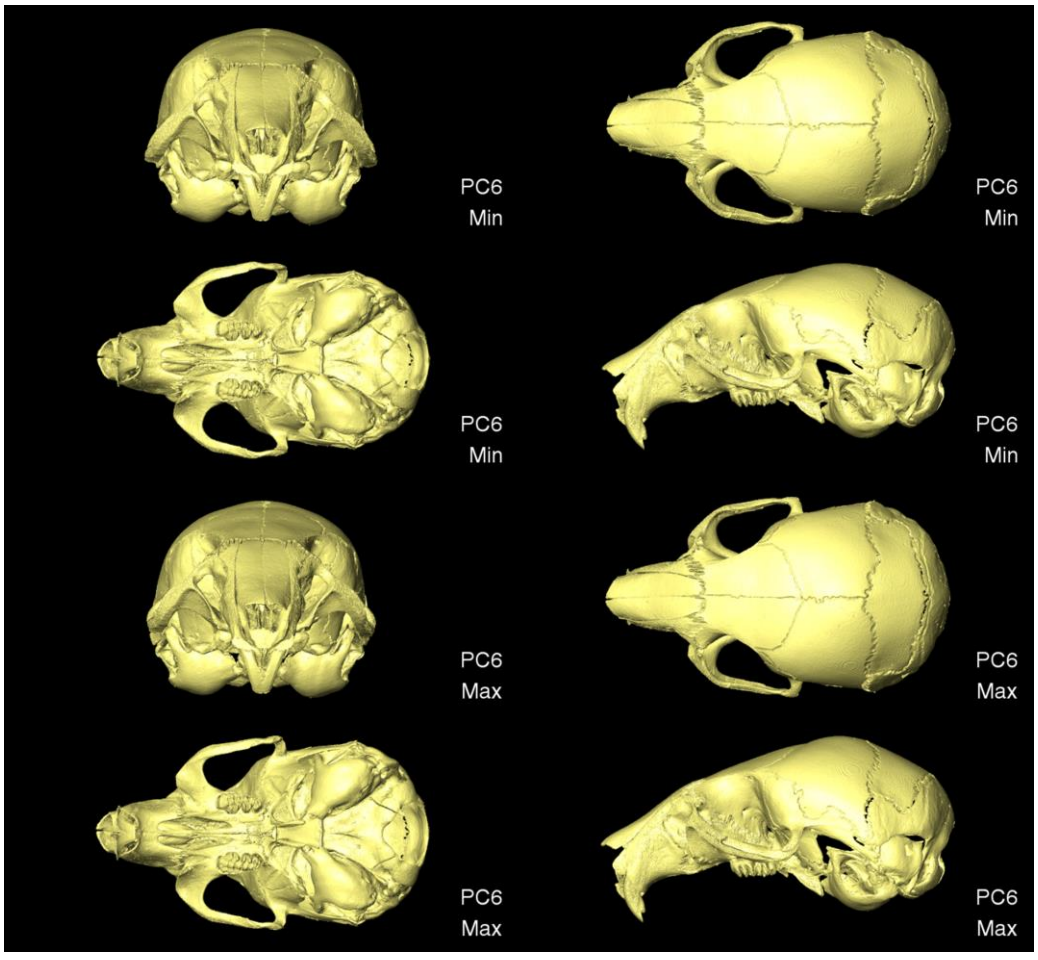
PC6
Min
PC6
Min
PC6
Min
PC6
Min
PC6
Max
PC6
Max
PC6
Max
PC6
Max

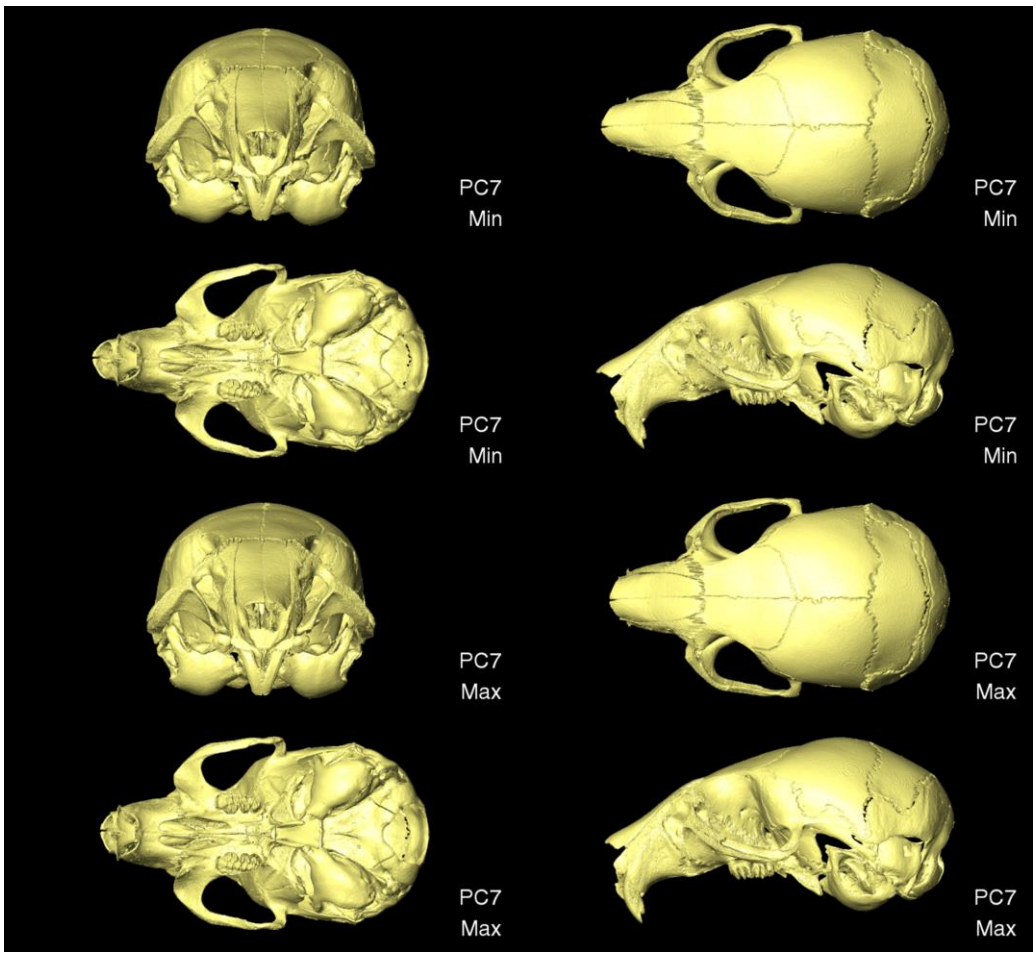
PC7
Min
PC7
Min
PC7
Min
PC7
Min
PC7
Max
PC7
Max
PC7
Max
PC7
Max

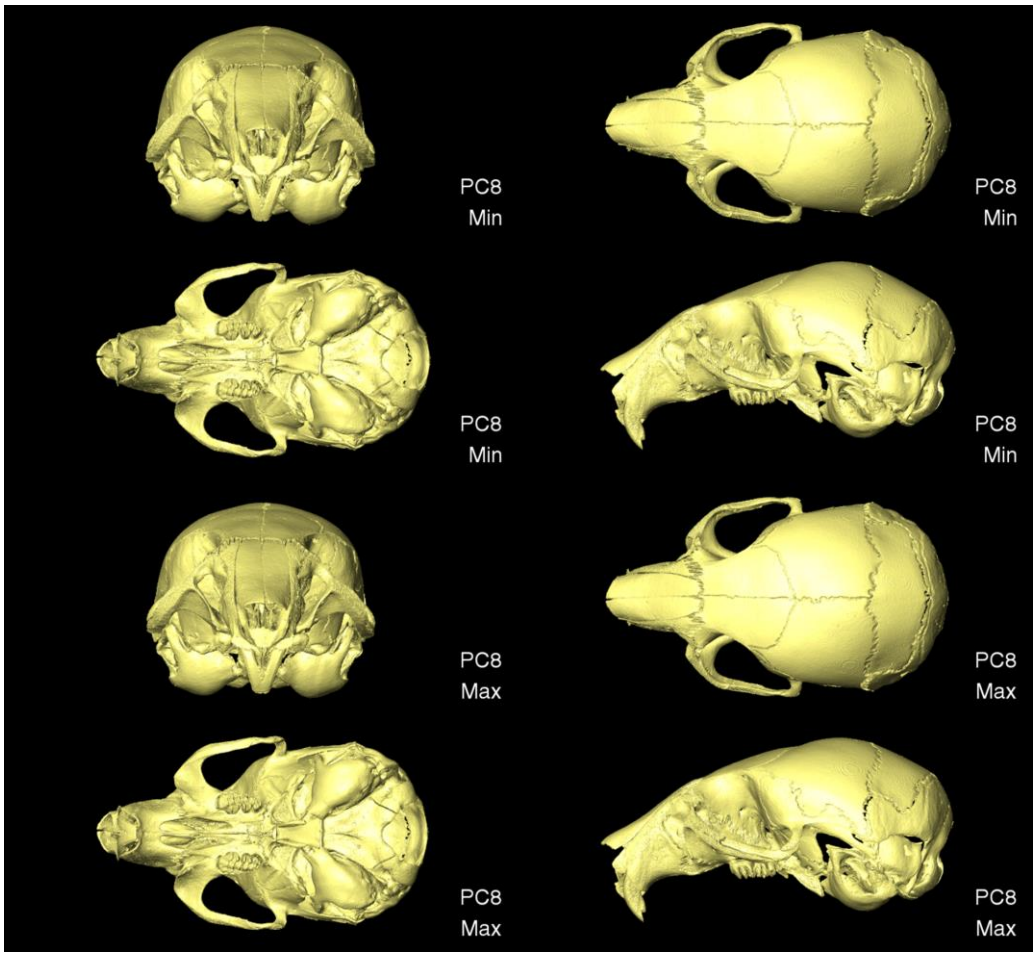
PC8
Min
PC8
Min
PC8
Min
PC8
Min
PC8
Max
PC8
Max
PC8
Max
PC8
Max

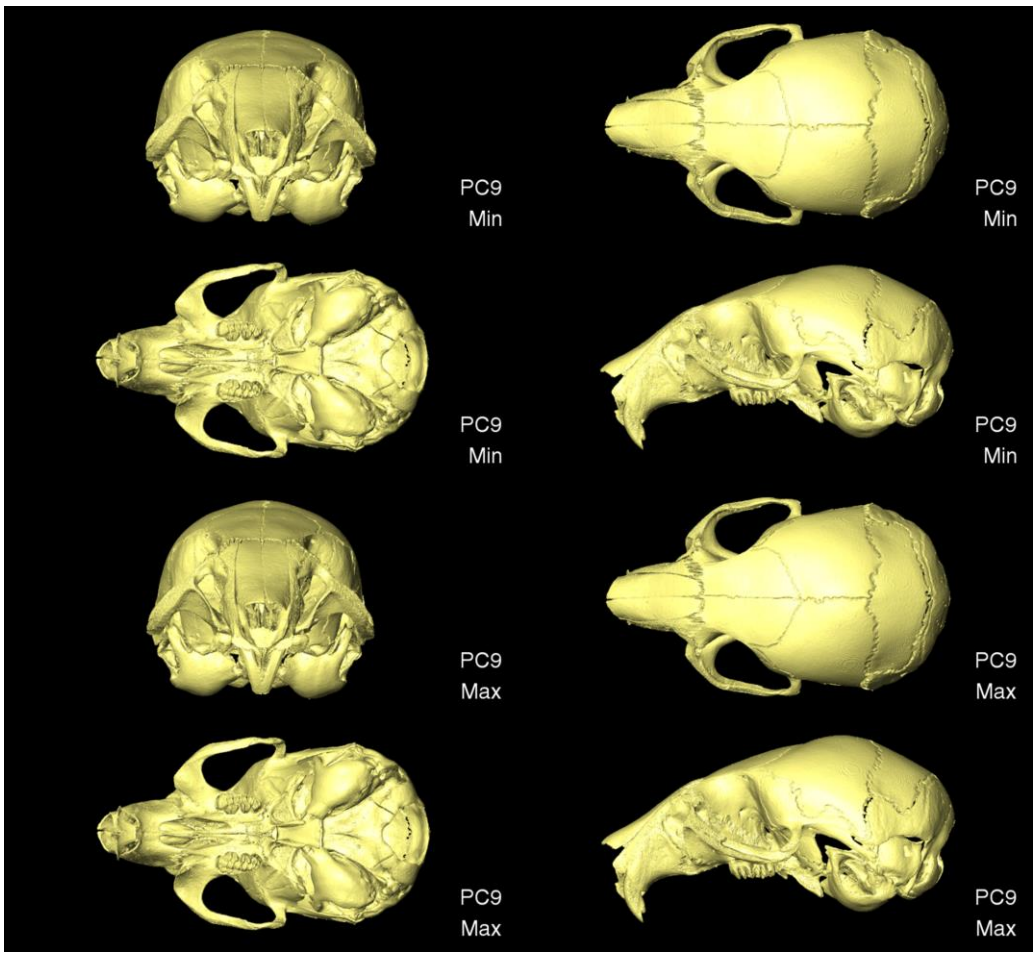
PC9
Min
PC9
Min
PC9
Min
PC9
Min
PC9
Max
PC9
Max
PC9
Max
PC9
Max

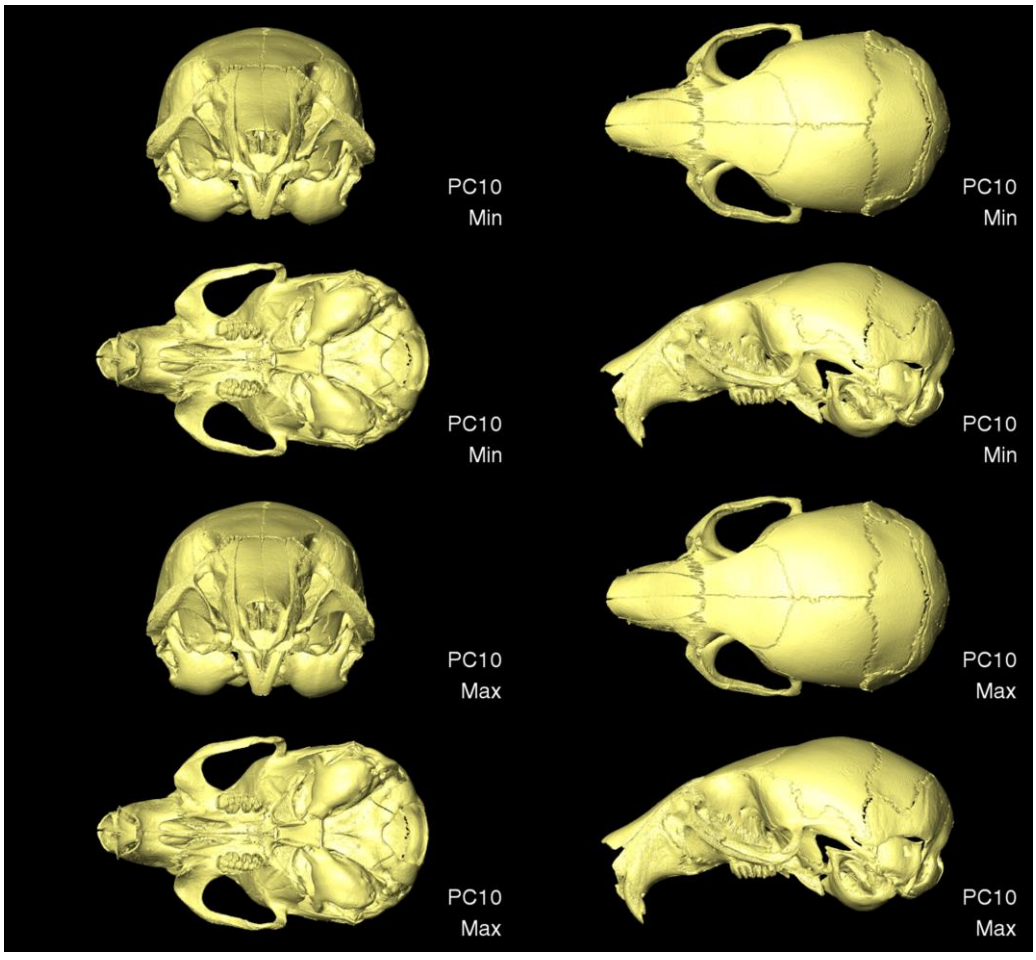
PC10
Min
PC10
Min
PC10
Min
PC10
Min
PC10
Max
PC10
Max
PC10
Max
PC10
Max

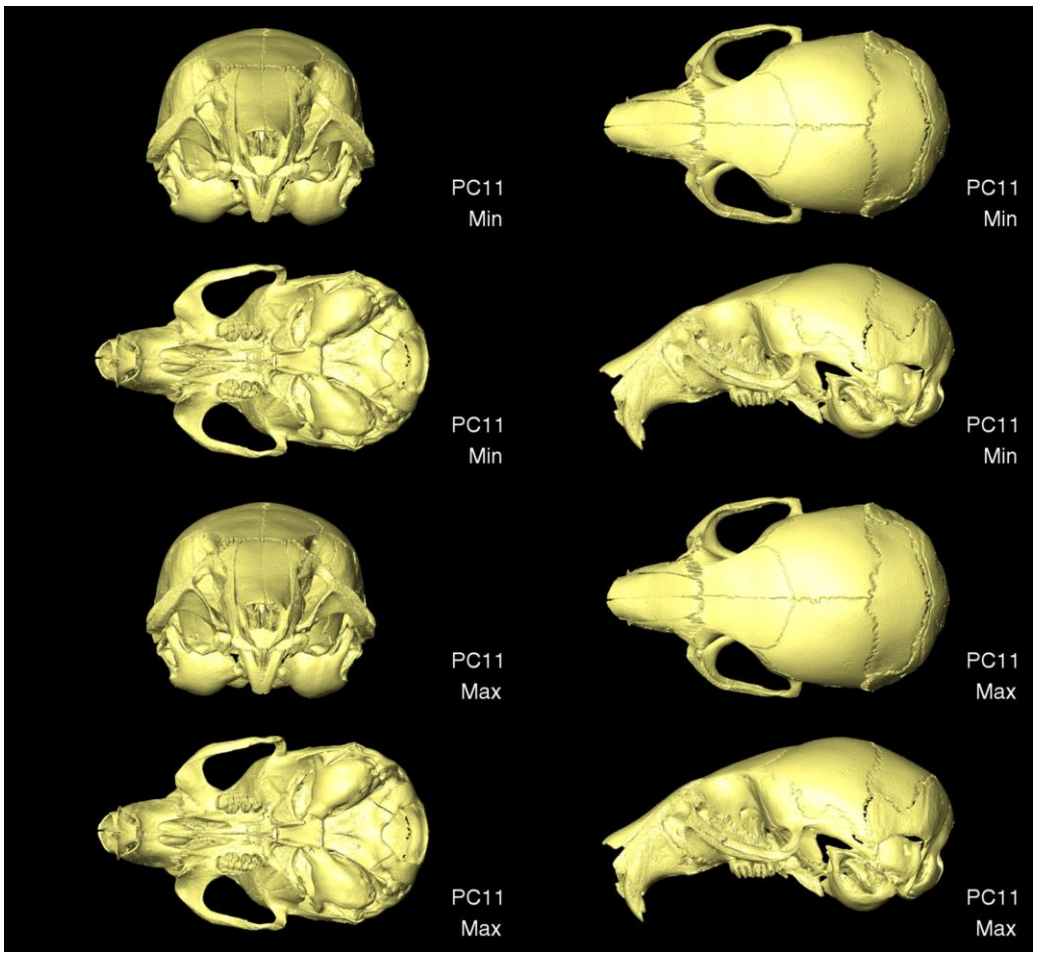
PC11
Min
PC11
Min
PC11
Min
PC11
Min
PC11
Max
PC11
Max
PC11
Max
PC11
Max

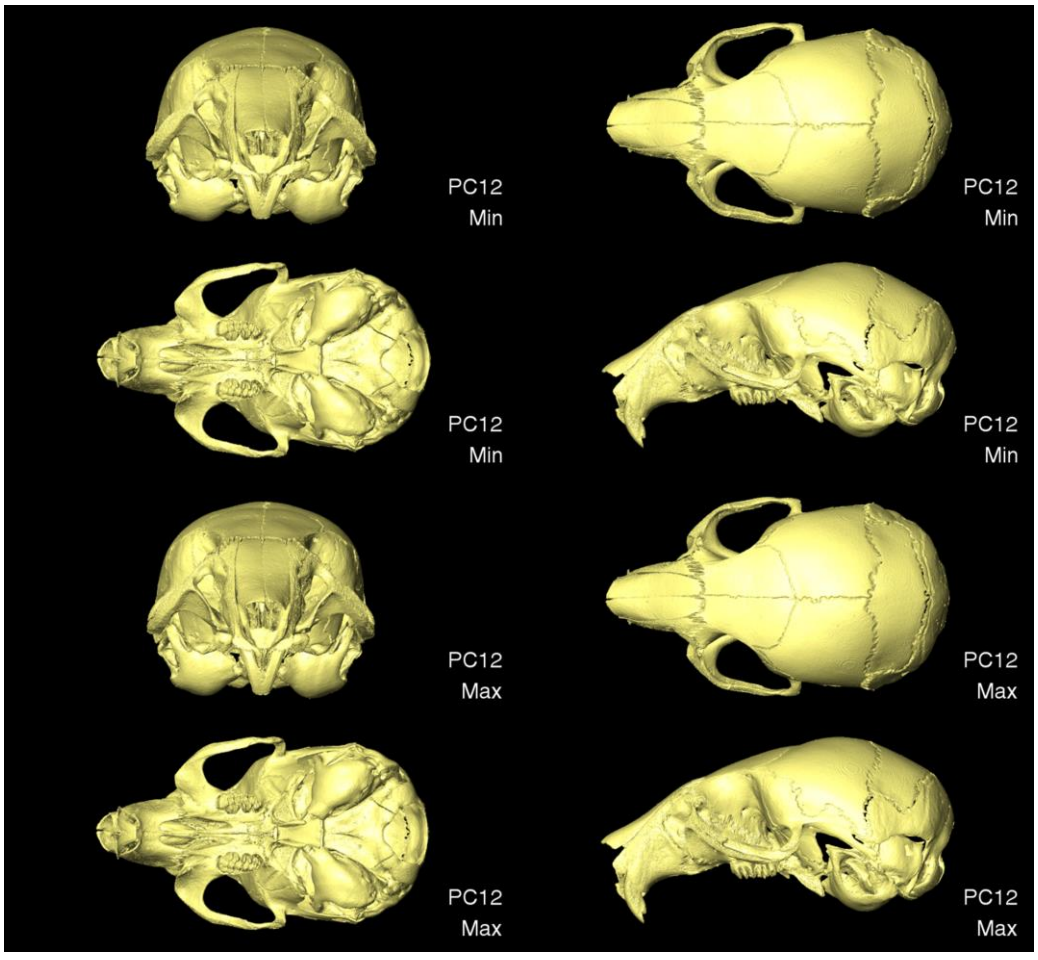
PC12
Min
PC12
Min
PC12
Min
PC12
Min
PC12
Max
PC12
Max
PC12
Max
PC12
Max

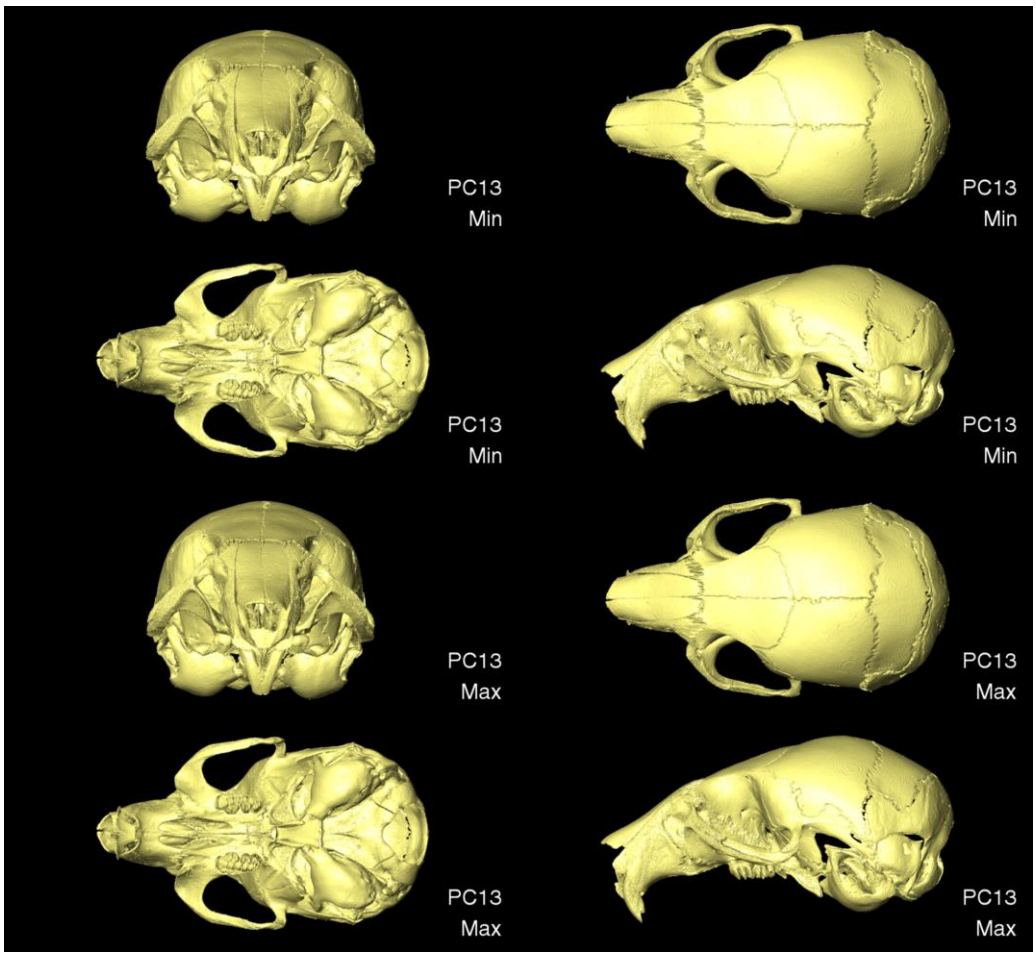
PC13
Min
PC13
Min
PC13
Min
PC13
Min
PC13
Max
PC13
Max
PC13
Max
PC13
Max

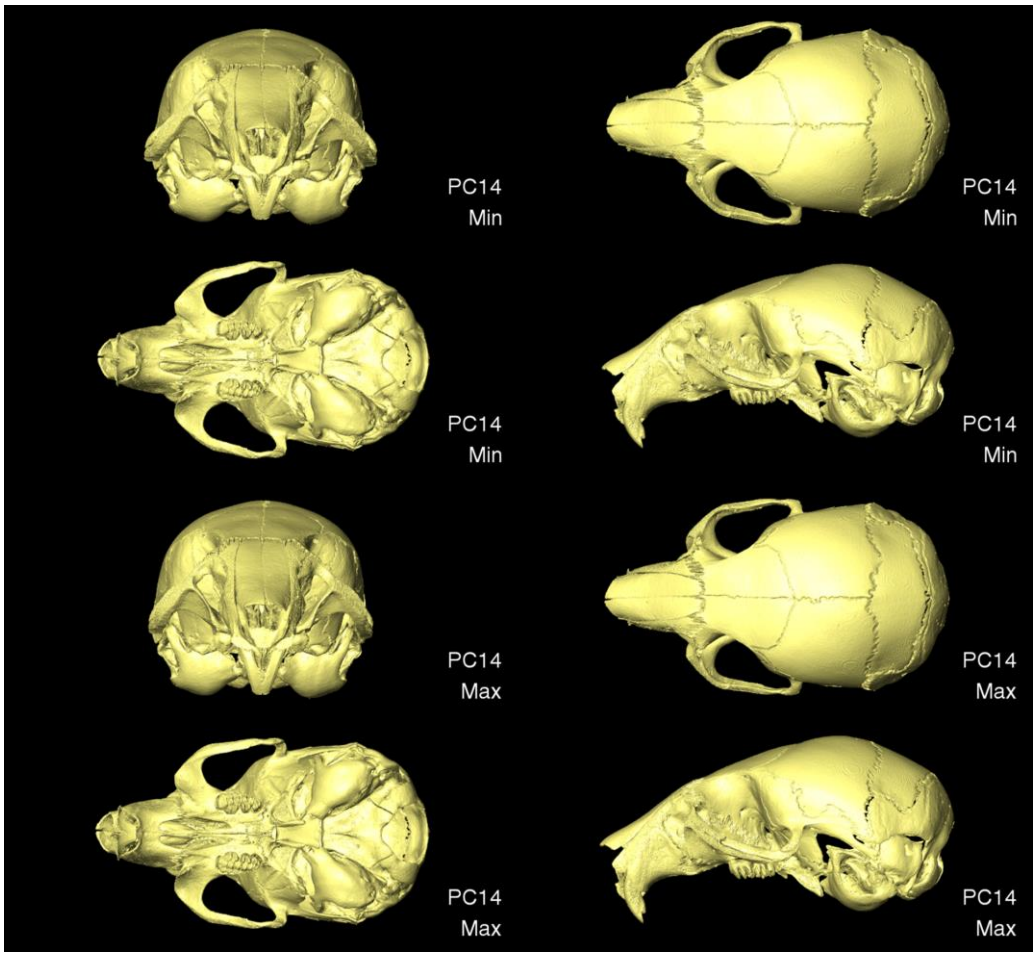
PC14
Min
PC14
Min
PC14
Min
PC14
Min
PC14
Max
PC14
Max
PC14
Max
PC14
Max

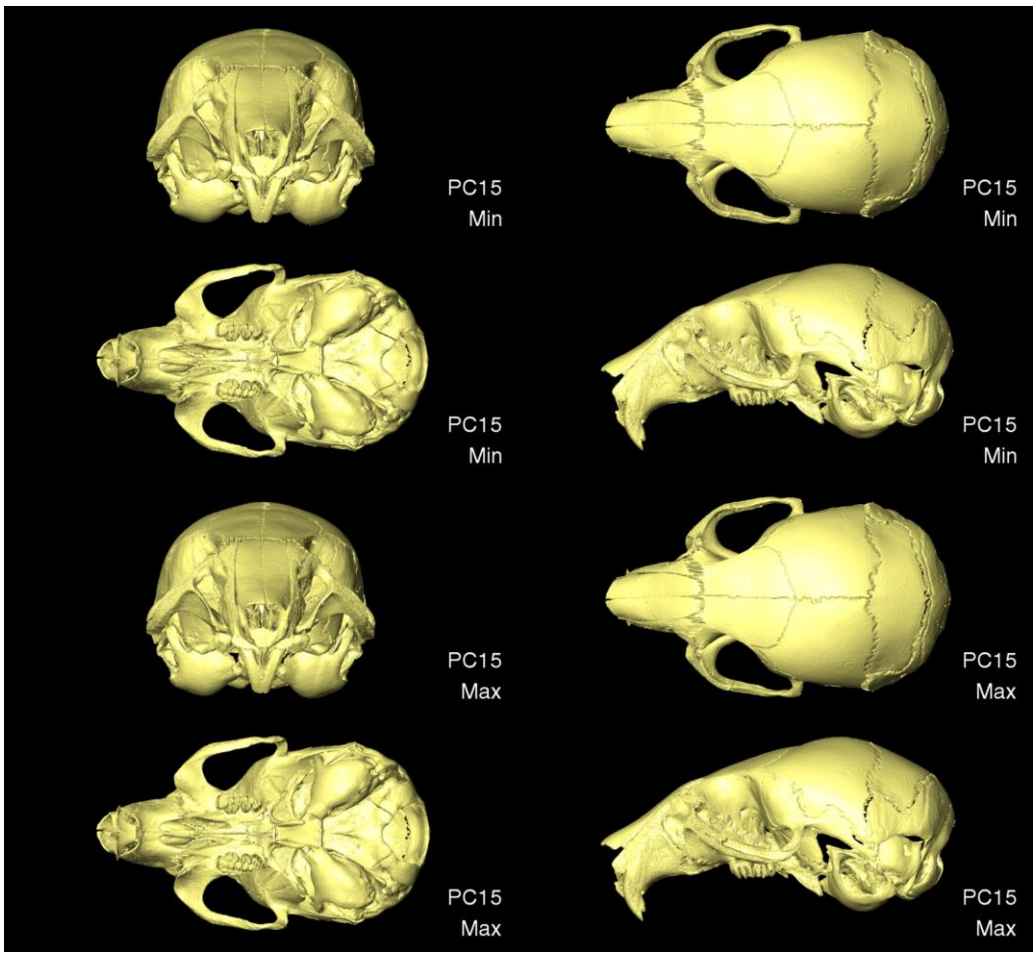
PC15
Min
PC15
Min
PC15
Min
PC15
Min
PC15
Max
PC15
Max
PC15
Max
PC15
Max

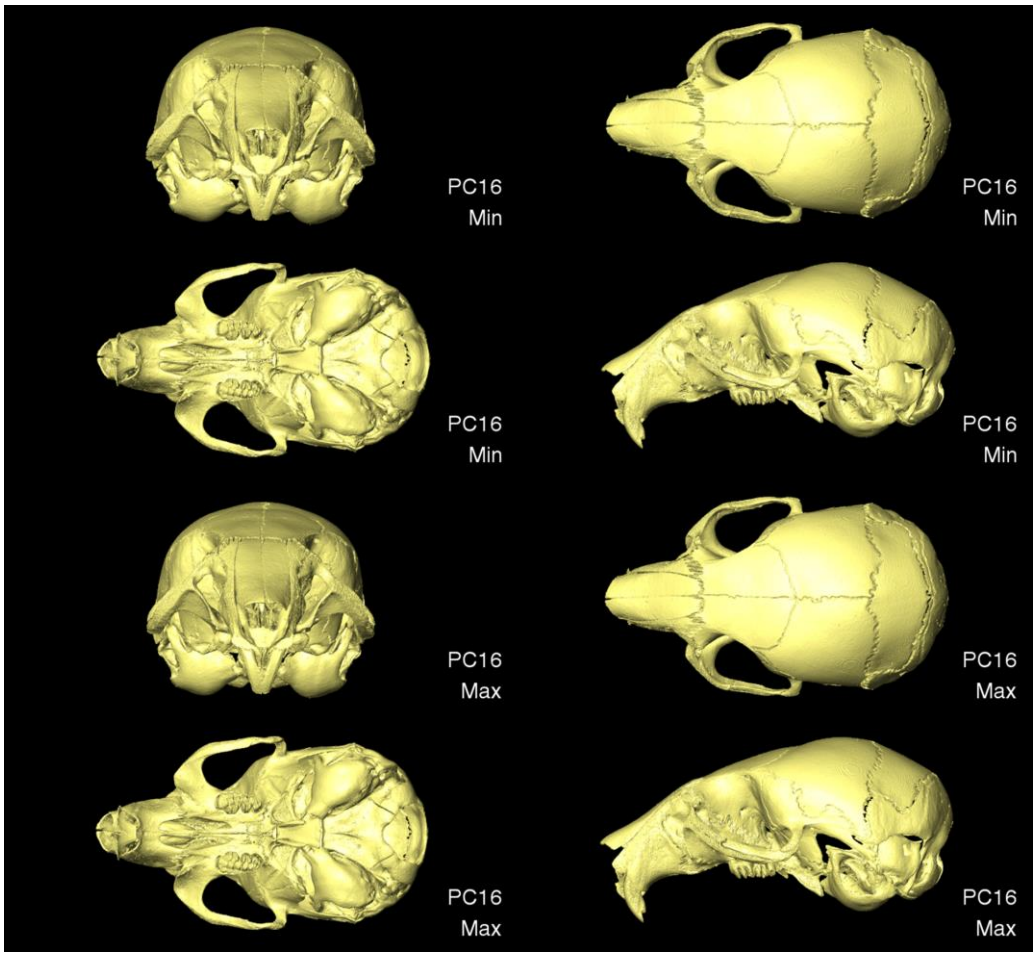
PC16
Min
PC16
Min
PC16
Min
PC16
Min
PC16
Max
PC16
Max
PC16
Max
PC16
Max

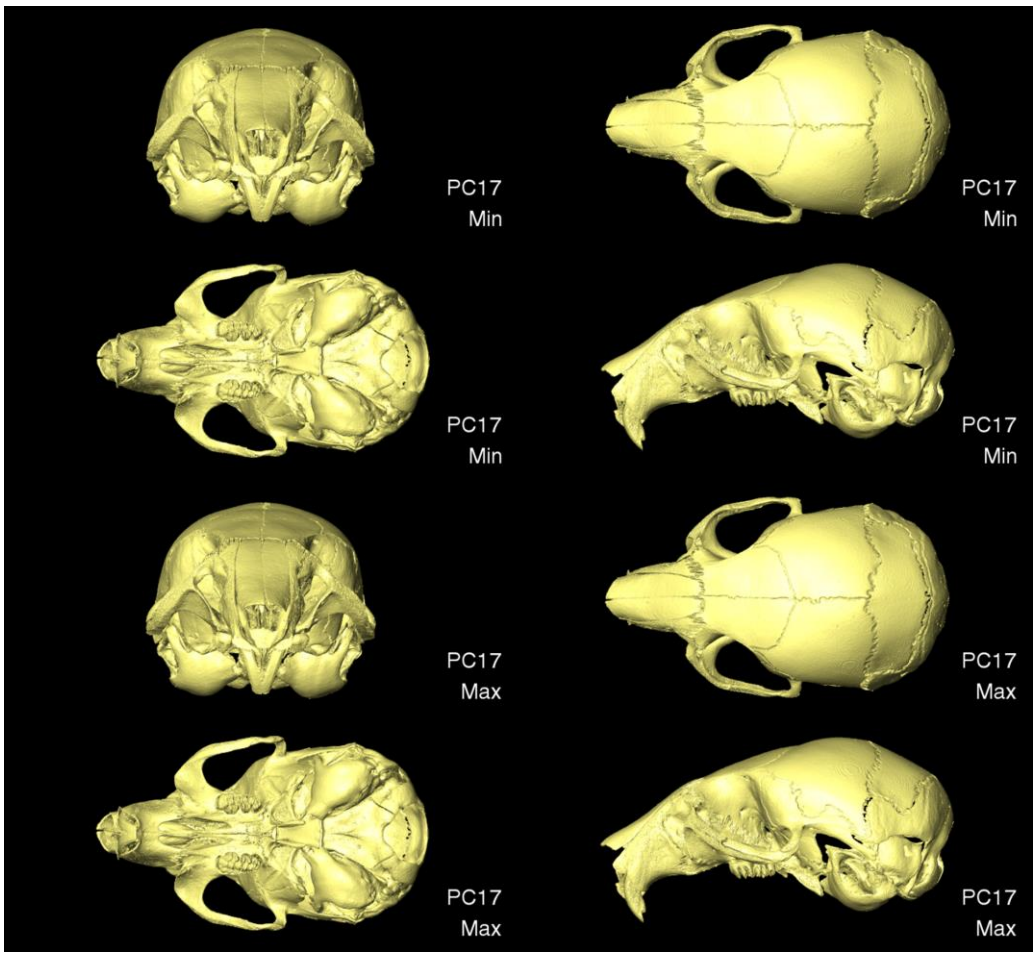

Figure A3.3. Shapes of the min and max PC shapes for the first 17 PCs (>95% of the shape variation) for P42 MT morphed from a WT skull.

Appendix IV List of publications

1. **Didziokas, M.**, Steacy, M., Qiu, T., Liang, C., Pauws, E., Moazen, M. (*In Prep*) *Mouse craniofacial phenotype: Study design implications of litter effects in WT and Crouzon mice and effects of suture fusion on craniofacial shape in Crouzon mice.*
2. Steacy, M., **Didziokas, M.**, Qiu, T., Vithanage, D., Liang, C., Alazmani, A., Moulding, D., Gardner, O., Pauws, E., Moazen, M. (*In Prep*) *Mechanical bone loading effects on morphology and mechanobiology in the coronal suture of Crouzon mice.*
3. Mazzolani, A., Astolfo, A., Buchanan, I., Savvidis, S., **Didziokas, M.**, Moazen, M., Fardin, L., Munro, P., Olivo, A. (2025) *Accurate and noise robust crosstalk removal techniques for edge illumination phase-based x-ray imaging systems.* Optics Express.
4. He, Y., Camaiti, M., Roberts, L., Mulqueeney, J., **Didziokas, M.**, Goswami, A. (*Under Review*) *Introducing SPROUT (Semi-automated Parcellation of Region Outputs Using Thresholding): an adaptable computer vision tool to generate 3D segmentation.* Nature Methods.
5. **Didziokas, M.**, Steacy, M., Qiu, T., Marghoub, A., Alazmani, A., Pauws, E., Moazen, M. (*2025*) *Regional variability in craniofacial stiffness: A study in normal and Crouzon mice during postnatal development.* Biomechanics and Modeling in Mechanobiology.
6. Jiang, Y., Katsura, K. A., Badt, N. Z., **Didziokas, M.**, Dougherty, S., Goldsby, D. L., Bhoj, E. J., Vining, K. H. (*2025*) *Multi-modal characterization of rodent tooth development.* ACS Applied Materials & Interfaces.
7. **Didziokas, M.**, Pauws, E., Kölby, E., Khonsari, R. H., Moazen, M. (2024) *BounTI (Boundary-preserving Threshold Iteration): a user-friendly tool for automatic hard tissue segmentation.* Journal of Anatomy.
8. Liang, C., Marghoub, A., Profico, A., Buzi, C., **Didziokas M.**, van de Lande L., Khonsari, R. H., Johnson, D., O'Higgins, P., & Moazen, M. (2024) *A physico-mechanical model of postnatal craniofacial growth in human.* iScience.
9. Wang. S., **Didziokas, M**., Roscian, M., Evans, S., Rouget, I., Herrel, A., Moazen, M., Souquet, L. (2024) *A comparative analysis of cephalopod beaks puncture abilities using engineering tools.* Marine Biology.
10. **Didziokas, M.**, Jones, D., Alazmani, A., Steacy, M., Pauws, E., Moazen, M. (2024) *Multiscale mechanical characterisation of the craniofacial system under external forces.* Biomechanics and Modeling in Mechanobiology.